Spectroscopy and Dynamics of Fluorescent Protein Chromophore Anions

Ciarán Roger Samuel Mooney

A thesis submitted for the degree of Doctor of Philosophy

UCL

April 2015

I, Ciarán Roger Samuel Mooney confirm that the work presented in this thesis is my own. Where information has been derived from other sources, I confirm that this has been indicated in the thesis.

Abstract

Gas-phase photoelectron imaging spectroscopy has been combined with electrospray ionisation to examine the electronic structure and dynamics of a variety of biologically relevant chromophores. Both nanosecond and femtosecond spectroscopy techniques have been employed and many of these experimental measurements have been complimented by *ab initio* calculations.

The photodetachment spectra of model chromophore anions of Green Fluorescent Protein (GFP) and Cyan Fluorescent Protein (CFP) along with their constituent moieties, phenol and indole, have been recorded at 269 nm and 330 nm. This study provided measurements of the vertical and adiabatic detachment energies of the ground and first excited state radicals of all four molecules.

A detailed nanosecond photoelectron spectroscopy study of the GFP model chromophore anion was then undertaken using a range of wavelengths between 315 nm and 328 nm. This has revealed the interplay between direct and indirect detachment processes and their influence on the photoelectron spectra. A femtosecond time-resolved study of the model GFP chromophore anion was also performed along with *ab initio* calculations to identify key molecular structures. This study revealed that the ultrafast decay dynamics of the gas-phase model anion have similar timescales as those measured in solution. In another study, photodetachment spectra of chemically modified GFP model chromophore anions were measured at 350 nm. The addition of strongly electron donating or withdrawing groups on the phenoxide moiety of the chromophore demonstrates how chemistry can be exploited to tune the electron emission properties the chromophore.

Finally, a study of model chromophore anions of Photoactive Yellow Protein (PYP) was undertaken. This work examined the photoelectron spectra of three isomers of the PYP model chromophore at a wide variety of wavelengths between 315 nm and 364 nm. The vibrationally resolved spectra allow us to identify the predominate anion isomer

produced by electrospray ionisation and highlights the importance of direct and indirect photodetachment pathways in anion spectroscopy.

This thesis is based on the following publications:

Chapter 2:

McKay, A. R., Sanz, M. E., Mooney, C. R. S., Minns, R. S., Gill, E. M., Fielding, H. H. "Development of a new photoelectron spectroscopy instrument combining an electrospray ion source and photoelectron imaging" *Review of Scientific Instruments* **2010**, *81*

Chapter 3:

Mooney, C. R. S., Sanz, M. E., McKay, A. R., Fitzmaurice, R. J., Aliev, A. E., Caddick, S., Fielding, H. H. "Photodetachment Spectra of Deprotonated Fluorescent Protein Chromophore Anions" *Journal Of Physical Chemistry A* **2012**, *116*, 7943–7949

Chapter 4:

Mooney, C. R. S., Parkes, M. A., Zhang, L., Hailes, H. C., Simperler, A., Bearpark, M. J., Fielding, H. H. "Competition between photodetachment and autodetachment of the $2^1\pi\pi^*$ state of the green fluorescent protein chromophore anion" *The Journal of Chemical Physics* **2014**, *140*

Mooney, C. R. S., Parkes, M. A., Zhang, L., Hailes, H. C., Bochenkova, A. V., Fielding, H. H. "Tuning the electron emission properties of the deprotonated green fluorescent protein chromophore anion" *In Preparation* **2014**

Chapter 5:

Mooney, C. R. S., Horke, D. A., Chatterley, A. S., Simperler, A., Fielding, H. H., Verlet, J. R. R. "Taking the green fluorescence out of the protein: dynamics of the isolated GFP chromophore anion" *Chemical Science* **2013**, *4*, 921–927

Chapter 6:

Mooney, C. R. S., Parkes, M. A., Iskra, A., Fielding, H. H. "Controlling Radical Formation in the Photoactive Yellow Protein Chromophore" *Angewandte Chemie International Edition* **2015**, DOI:10.1002/anie.201500549

Acknowledgements

Firstly, I'd like to thank Prof. Helen Fielding for giving me the opportunity to undertake this PhD and for being the eternal optimist to my persistent pessimist. Secondly I'd like to thank Mary, William and Ciara Mooney. Without them I would not be the critical, stubborn and argumentative person I am today. I would like to apologise to Jennifer Harding for not being as fun as I ought to have been, whilst writing up and to say I truly appreciate all her love and support.

At UCL I met many people whom it has been an honour to know but I only have space to name a few. I would like to thank Dr. Roman Spesyvtsev for his friendship and his introduction to Ukrainian culture, Oliver Kirkby for our debates where we put the world to rights and without Dr. Russell Minns I would never have learnt the secret ways of "Slowly Slowly Catchy Monkey" and "Tweaky Tweaky".

The mass spectrometers were, at times, temperamental and uncooperative. John Hill's expertise kept them working reliably enough for me to collect the data in this thesis and for that I will be ever thankful. At times, even the simplest things can cause frustrations but knowing Dr. Michael Parkes was there to help find unplugged cables was reassuring (along with his fellow appreciation for a good balti). I am grateful for the brilliant instruction and unbounded patience of Dr. Alexandra Simperler. Thanks to the project students Lijuan Zhang and Andreas Iskra for their help with the computational and experimental work that makes up this thesis, and also their insightful and "simple" questions that helped point out the gaps in my own understanding.

Finally, all the other members of the Fielding Group and residents of office 121 who have come and gone over my time there. Each one of them has been pleasant to know and work with.

Contents

List of Figures

List of Tables

Chapter 1

Introduction

1.1 Fluorescent Proteins

1.1.1 Green Fluorescent Protein

In the last 50 years green fluorescent protein (GFP) has gone from being discovered as the source of the green glow of a jelly fish, to an incredibly important tool for biological and medical research, revolutionising biomedical science. GFP has undoubtedly led to medical advances and earned three men the Nobel prize for its discovery, characterisation and utilisation.

The story of GFP began with the observation of the green bioluminesence of the jelly fish *Aequorea Victoria*,[7] although the evolutionary reason for developing this ability is not known. The release of Ca^{2+} inside *Aequorea Victoria* interacts with a protein called Aequorin leading to the emission of blue light; this is subsequently absorbed by GFP, leading to the emission of a characteristic green fluorescence with quantum yield of 0.8.[8,9] This rather odd jelly fish was of interest to Osamu Shimomura who in the 1960s, isolated both Aequorin and GFP, the first steps of the rise of GFP.[7]

The discovery of GFP in itself was interesting, but the next critical step came 28 years later with the realisation that other organisms could produce GFP.[10] Martin Chalfie was able to splice the genetic code for GFP into *C. Elegans* deoxyribonucleic acid (DNA)

Figure 1.1: (a) The effect of GFP expression being included in the DNA of c. Elegans can clearly be seen in this photograph, from Chalfie *et al.*[10], (b) Range of different fluorescent proteins and the spectral range available, from Tsien's Nobel Lecture[14]

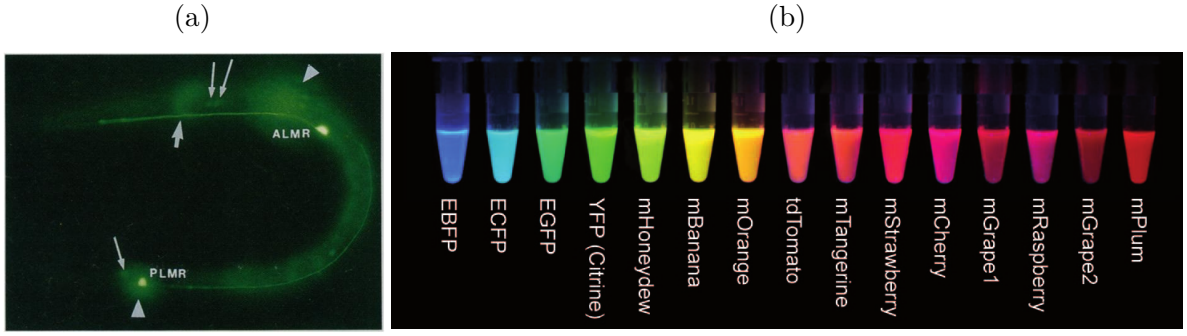

structure which led an otherwise dull worm obtaining the much more interesting ability to glow green! What is also important is that this ability did not adversely affect the worm.[10] The lack of toxicity, and simplicity of conditions required for fluorescence, make GFP an ideal candidate for a fusion tag.[11] This is where GFP is linked with the expression of another gene, allowing observation not only of protein expression but also localisation. The only additional agent required to obtain fluorescent GFP is O_2 in the solution during the folding stage of the protein. No other additional co-factors are required to produce fluorescence.[12,13]

After these two fundamental developments, the final requirement was to make GFP more useful to experimentalists. Roger Y. Tsien developed mutants that increased the spectral range of GFP.[13,15–17] Figure 1.1b shows the colour palette achievable with fluorescent proteins. Development of GFP mutants continues to produce proteins that can fold efficiently at temperatures that are of interest (37 °C) and also are activated by wavelengths that are more convenient to experiments.[8,15,18]

The success of GFP brought it to the attention of other scientists who are now striving to understand the properties of the protein at a more fundamental level, hopefully leading to even more interesting uses and developments of GFP.

The two main structural features of GFP that give rise to fluorescence are the rigid outer structure and the internal chromophore, which can be seen in Figure 1.2 (a and b, respectively).[19,20] Experiments have shown that if the protein becomes denatured and

Figure 1.2: (a) Protein structure of GFP from PDB 1GFL;[19] green arrows show the β-sheets, blue curves show α-helices, white strings are protein strands that have not formed secondary structures, (b) the chromophore of GFP. The wiggly lines denote truncation of links to protein structure.

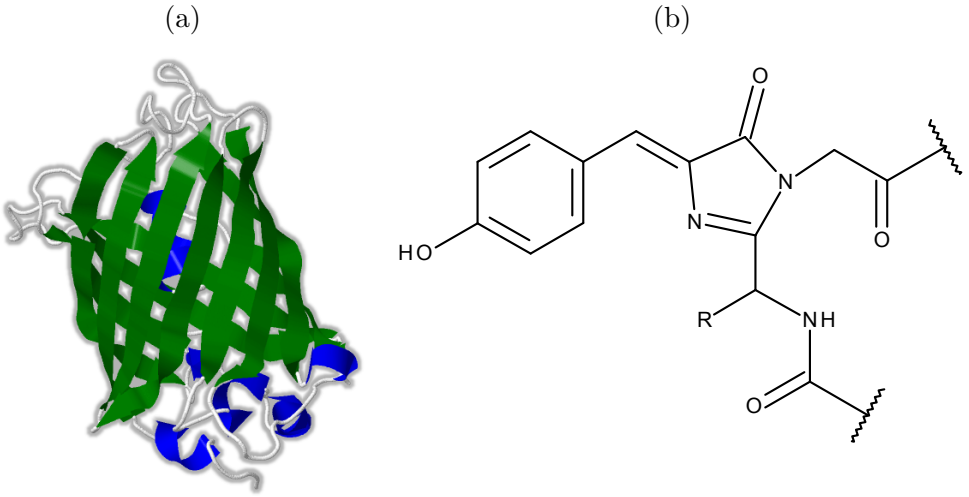

Figure 1.3: Absorbance (solid line) and fluorescence (dashed line) spectrum of GFP in a 50% glycerol solution with 10 mM sodium phosphate buffer (pH 7.0). Absorbance at 398- and 476 nm are the A and B states, respectively. Fluorescence peak at 508 nm is from the I state, see text. Reproduced from Creemers *et al.*[22]

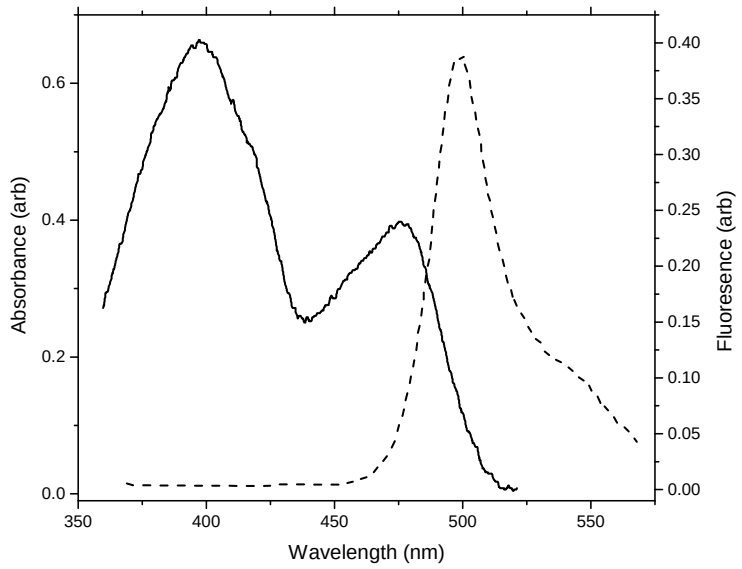

loses its rigid outer structure, the fluorescence is lost too.[21] This leads to the conclusion that the chromophore works in tandem with the protein structure which restricts otherwise accessible radiationless decay to enable fluorescence.

The absorption spectrum of GFP, Figure 1.3 (solid line), gives more information

Figure 1.4: Schematic of the relative position of A, B, and I state energy levels for GFP, along with peak absorbance and fluorescence wavelengths. The green shading shows the states that exists in with the protein in its neutral chromophore conformation, the blue shading depicts the anionic states. The I state exists in the overlap between the two.

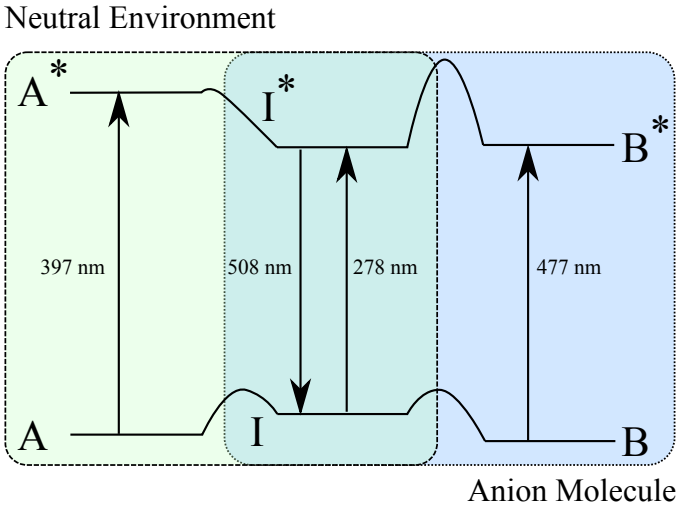

about the nature of this linked relationship between protein and chromophore. Two clear absorbance peaks can be observed for GFP, at 398 and 476 nm.[22] These two features are interchangeable *via* either photo-conversion or through alterations to solution pH.[23,24] With knowledge of the structure of the chromophore it becomes clear that these two absorption maxima can be attributed to two different protonation states of the chromophore, which have been labelled A and B for the protonated and deprotonated states, respectively.[22,23] The deprotonation occurs at the phenol moiety of the GFP chromophore, as phenols are known to be more acidic in their excited state compared to their ground state.[25]

However, neither the A or B state is responsible for the characteristic green fluorescence of GFP, the spectrum of which can be see in Figure 1.3 (dashed line). This was found to be due to a third intermediate state which has been labelled, I.[22,23,25] This has been demonstrated in time-resolved spectroscopy showing that direct excitation of the B state leads to near instantaneous emission from the I state, however there is not an expected return of B absorbance. The I state preferentially re-protonates to form the A ground state. Excitation of the A state leads to a delay in emission from the I state.[23]

Figure 1.5: Structure of pHBDI a commonly used analogue of the GFP chromophore.

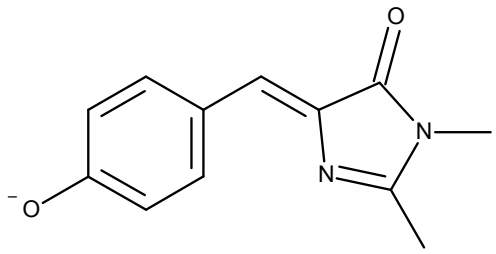

This delay is caused by an excited state conversion process from A to B or I and involves the phenolic proton moving from the chromophore to be sequestered into the protein through a process called excited state protein transfer (ESPT).[23,25,26] The relative energy positions of these states have been measured very accurately using hole-burning spectroscopy at 77 K[22] and a schematic energy level diagram can be seen in Figure 1.4. As mentioned, the acidic nature of the phenol moiety means that excitation of the A state leads to the deprotonated I* state as it is more stable. The model given explains the broad features observed in GFP, however more other studies have extended this model to include more intermediate states[27] to explain the observed "blinking" of GFP under certain conditions.[28]

It is clear that the protein has been studied extensively but it is a very large and complicated system. Investigators have sought to simplify interpretation of the results by performing experiments on a chromophore analogue so as to remove the effects of the protein. Figure 1.5 shows a commonly used GFP chromophore analogue, *p*-hydroxybenzylideneimidazolinone (pHBDI). Measurements of pHBDI's properties in solution have shown that it can also be a protonated neutral, deprotonated anion, or cationic.[20,29,30] Most experiments concentrate on examining the properties of the anion as this is directly relevant to the I state fluorescence, and the B state. The absorption maxima of all the chromophore states in solution are blue-shifted relative to the protein showing the significant effect of interaction with the protein environment.[31] The most striking difference between the chromophore in solution and the protein is the lack of fluorescence, which is analogous to the effect of denaturation of GFP.[20] These observations lead back to the

assumption that the chromophore movement is restricted by the protein, which in turn leads to fluorescence.

The excited state of pHBDI in solution is clearly being deactivated *via* some internal conversion (IC) process preventing fluorescence. This has led to a number of studies that have focussed on finding the nature of this molecular motion.[32–34] These studies found that the fluorescence had a small viscosity dependence, ruling out a radiationless relaxation pathway that possessed a large motion, which would displace a significant volume of solvent.[33] A *hula-twist* has been proposed, with excited state deactivation *via* rotation between the two rings of the chromophore but which is also volume conserving.[33,35,36] The fluorescence of pHBDI in solution also shows a temperature dependence with increasing fluorescence seen at lower temperatures.[20,22,33] The increase in fluorescence occurred when temperatures of the solution was close to the glass temperature of the solvent where viscosity increases significantly, which also suggests restriction of motion is promoting a fluorescent pathway.[33] A detailed study that took account of viscosity at various temperatures found that whilst IC in pHBDI is efficient, there is a small energetic barrier.[33]

If the first stage of studying the properties of GFP was to remove the chromophore from the protein and study it in solution, the next is to remove the solution and study the chromophore in the gas phase. Studying large molecules such as pHBDI in the gas-phase is troublesome due to the likelihood of fragmentation and as such it is only recently that experiments have been built that are able to perform such measurements. These are almost exclusively done using some form of soft ionisation technique (Section 1.3.1). These soft ionisation sources can be configured to produce anions which are of particular relevance to the study of GFP and pHBDI.

One of the first gas-phase measurements of pHBDI was carried out by Nielsen *et al.* using their electrostatic storage ring for atomic physics (ELISA) facility.[37] They measured the production of neutrals, after crossing a beam of anions with a tunable laser beam, to produce an action spectrum of a GFP chromophore. They found that it pos-

sessed an absorption maximum at 479 nm, which bears a striking similarity to the GFP anion absorption band.[37] This led experimenters to infer that, due to the solvent inaccessibility of the protein cavity, the environment around the chromophore may be more akin to the gas-phase than solution. This has since been countered by other experiments that were sensitive to more deactivation channels, such as those of Forbes *et al.* which demonstrated that fragmentation may account for the peak shape.[38,39] This led to a push to measure the direct detachment process of the gas-phase deprotonated p-hydroxybenzylidene-imidazolinone anion ($pHBDI^-$), crucially the ordering of the anion S_1 and radical neutral D_0 energy levels.[2,40,41] Current literature suggests that the anion excitation from S_0 to S_1 is a bound transition, but the detachment to the radical D_0 is very close. Although this picture is complicated by indirect or autodetachment processes which can occur.[41]

An alternative method of understanding the GFP chromophore and the effects of the protein and solvent upon it, is to modelled these systems using computational techniques. A significant amount of theory work concerning the GFP chromophore has been performed modelling the GFP chromophore in the three most relevant conditions, the protein, solution,and the gas phase.[36,42–48]

Work that has sought to understand the effect of the protein on the chromophore have used symmetry adapted cluster (SAC)/SAC-configuration interaction (CI) (SAC-CI) with continuum models[49], SAC-CI with molecular mechanics (MM) that included adjacent protein residues,[50] complete active space self consistent field (CASSCF)/multi-configurational second-order perturbation theory (CASPT2) with a MM model[51] and scaled opposite spin (SOC)-configuration interaction singles and doubles (CIS(D)) with MM.[48]. The earlier work using SAC with contiuum models and adjacent protein residues calculated the excitation energies of the neutral and anionic GFP chromophore anion to be 3.1-3.32 eV and 2.25-2.26 eV,[49,50] respectively, and they compare favourably with the experimentally measured values of 3.1 eV and 2.6 eV. Later calculations using CASSCF/CASPT2 or SOC-CIS(D) with MM produced excitation energies for an anionic

GFP chromophore even closer to the experimental measurements, 2.7-2.8 eV.[48,51]

Calculations using complete active space (CAS)-CI and MM modelled the solution phase excited state decay of a neutral GFP chromophore analogue and showed that the excited decay lifetime is significantly shorter in solution compared to that of the gas-phase,[52] qualitatively agreeing with experimental results.[32] The effects of water micro-solvation on the excitation energies of an anionic GFP chromophore analogue using scaled opposite spin (SOS)-CIS(D), where additional water increased the excitation energy of the S_0-S_1 transition, from 2.61 eV to 2.71 eV.[43] Excitation energies of the anion and radical in solution have been calculated using time dependent density functional theory (DFT) (TD-DFT) with a polarisation continuum model (PCM) model of methanol. They calculated the solution wavelength of the anion and neutral to be 2.95 eV and 3.31 eV, respectively,[53] compared to 2.96 eV and 3.51 ev, experimentally.[29,54]

Gas-phase calculations are appealing because they allow investigators to look at the inherent properties of the GFP chromophore. Early theoretical work on the GFP chromophore attempted to identify the nature of the protonation sites (phenol, imidazole, carbonyl) and states (anion, cation, neutral, zwitterion) of the chromophore in the protein using gas-phase semi-empirical methods.[55–57] This work calculated the gas-phase excitation to be 477 nm and the close agreement with GFP's 480 nm absorption band led investigators to propose it was due to the chromophore being nitrogen imidazole protonated zwitterion.[55] Later work using CASSCF and configuration interaction singles (CIS) found that the zwitterion was an unobservable dark state[36,58], and established the main contributors to GFPs photo-physics was due to the chromophore as the phenol deprotonated anion and neutral (A, B and I states). Vertical excitation energies of anionic GFP chromophore analogues have been calculated using CASPT2 and they predicted it to be of 2.88 eV[58], later investigations using augmented Multi-configurational quasi-degenerate second order perturbation (aug-MCQDPT2) calculated it to be 2.54 eV [2.59 eV, exp].[47] The excited state dynamics of the gas-phase GFP chromophore anion using CASSCF/CASPT2 modelled identified structures that could be responsible for GFPs

fluorescence in the protein and the deactivation pathways in the gas-phase.[46]

Predicting quantitative fundamental gas-phase properties, such as the vertical detachment energy (VDE) or adiabatic detachment energy (ADE), has been carried out by various groups.[42,43,45] Unfortunately, due to the rapid progress of both experimental and theoretical work there has at times been disagreement between theory and experimental. Noticeably, the VDE was predicted to be to be 2.38 eV by [42,45] using equations-of-motion (EOM) methods. Which is significantly different to the experimental measurements, 2.8 eV.[2,40,41] Work that constitutes this thesis has been involved in these on-going discussions and more detail can be found in Chapters 3, 4 and 5.

1.1.2 Photoactive Yellow Protein

When exposed to harmful ultraviolet (UV) light, the bacteria *Halorhodospira halophila* is able to protect itself by moving away to a more hospitable environment.[59] The root of this apparent intelligence is actually due to a protein and a series of photophysical and chemical processes. This negative photoaxis is caused by a single protein which responds to UV light and which eventually triggers a mechanical process to move the entire bacteria to safety. The protein is called Photoactive Yellow Protein (PYP), Figure 1.6, and was discovered in 1984 by T. E. Mayer *et al.*.[60]

The appeal of studying PYP is not just the novel properties that it bestows upon *Halorhodospira halophila* but also its relatively small size, as it consists of only 125 amino acids with a total mass of 14 kDa.[61] The size of PYP makes it an ideal system to study for theoretical and physical scientists trying to understand biologically relevant systems.

The chromophore of PYP is *trans*-4-hydoxycinnamyl (4HCA) and is linked to the protein structure *via* a thiol ester bond. The chromophore is deprotonated in its ground state and resides in a hydrophobic cavity within the protein structure.[62] The chromophore is also hydrogen bonded to surrounding Glu46, Tyr42 and Thr50 amino acid groups. The chromophore of PYP can be seen embedded within the protein in Figure 1.6.

Upon absorption of light PYP goes through a reversible photocycle of which the three

Figure 1.6: Figure showing (left) Photoactive Yellow Protein, structure from the protein database, ID 2QJ5; yellow arrows show the β-sheets, pink curves show α-helices, white strings are protein strands that have not formed secondary structures, and (right) the protein's chromophore anion, *trans*-4-hydoxycinnamyl. The chromophore can be seen within the protein in the top left.

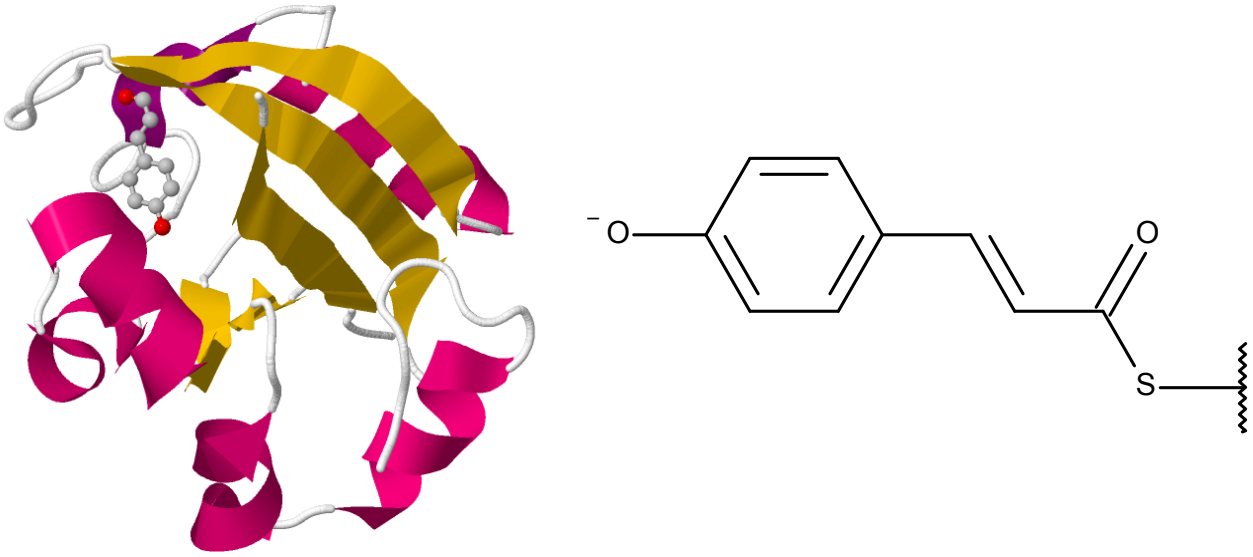

major steps of the PYP photocycle mechanism have been elucidated[63,64] but there are still various sub-steps that have yet to be understood. A simple schematic of the process is presented in Figure 1.7. The three states involved are the ground state, pG, and two intermediate states, I_1 and I_2.* The ground state of *trans*-4-hydoxycinnamyl is the deprotonated *trans* isomer,[66] has an absorption maximum at 446 nm. Upon absorption to its excited state the chromophore isomerises to the *cis* isomer, to form I_1, within 3 ns.[67] The conversion to the *cis* isomer involves a twisting of the thiol carbonyl.[68] The conversion to I_1 causes a red-shift in the absorption spectrum to 465 nm. Next, the I_2 state is formed by a partial unfolding of the protein structure and protonation of the chromophore a surrounding amino group.[66,67] I_2 is formed on a 100s of microseconds time-scale and causes a blue-shift in the absorption maximum to 355 nm. The final step is to reform the ground state by deprotonated, isomerisation back to the *trans* isomer of the chromophore, and re-folding of the protein which all takes place on a millisecond time-scale.[67]

*There are various nomenclatures[64,65] for labelling the states involved. For clarity only one is used in this section.

Figure 1.7: Simplified mechanism of PYP's photocycle showing the three major steps and intermediates (ground state, pG, and intermediates, I_1 and I_2).

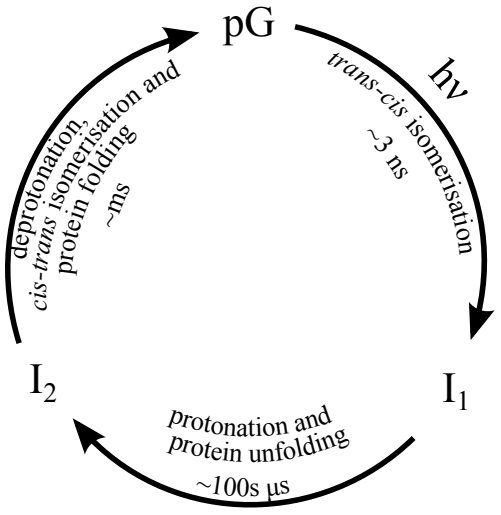

Investigators have looked at the properties of the chromophore in the protein, solution and in the gas-phase both theoretically and experimentally. The chromophore within the protein has been studied by altering the surrounding amino groups. By replacing the hydrogen bonded (Glu46, Tyr42 and Thr50) groups that surround the chromophore with non-hydrogen bonding alternatives it was found that the absorption maximum red-shifted by up to 30 nm.[69,70] This shift was reported to be due to more localisation of electron density onto the chromophore. Theoretical studies show that the overall effect of micro-solvating the isolated chromophore analogue changes the ordering of detached states and bound excitations.[43,71]

When studied in solution or the gas-phase analogues of the 4HCA chromophore are required. There is a small variety of different analogues that have been used which usually possess slightly different structures where the thiol bond to the protein structure would be. These analogues are *para*-coumaric acid (pCA), *trans*-thiophenyl-*p*-ccoumarate (pCT) and *trans*-methyl-*p*-coumarate (pCM).

Gas-phase absorption measurements of deprotonated *para*-coumaric acid (pCA^-) and deprotonated *trans*-thiophenyl-*p*-coumarate (pCT^-), which are alternative 4HCA chromophores, found the absorption maximum to be 430 nm and 460 nm respectively.[72,73]. This is in contrast to solution phase measurements which have found that the absorp-

tion maximums of pCA^- and pCT^- to be 283 nm and 395 nm respectively[72,74] and the PYP absorption maximum at 446 nm. Another model chromophore, deprotonated *trans*-methyl-*p*-coumarate (pCM^-), has been measured with a gas-phase absorption maximum of 432 nm.[75] It has also been observed that *trans*-*cis* isomerisation also occurs in the gas phase.[76] The similarity in absorption maxima and dynamic processes suggest that the environment experienced by the deprotonated chromophore within PYP might be similar to those of the isolated gas-phase model chromophores. The excitation energy of the isolated pCA^- has been calculated to be ∼413 nm.[71,77–80]

1.2 Photoelectron Spectroscopy

Photoelectron spectroscopy (PES) is our view-port into the inner workings of molecular systems. It is a technique with the finesse of a watchmaker's tweezers and the simplicity of a sledgehammer. The selection rules are broad, but vast amounts of information can be encoded in the resulting photoelectrons if you are able to measure them accurately. Experimentally, detecting charged particles is advantageous as they can be detected with great sensitivity using an multichannel plate (MCP) or channeltron.

Other spectroscopic techniques have a raft of selection rules that dictate if particular transitions are forbidden or allowed, which could simplify interpretation. However, transitions that are formally forbidden can be allowed under certain conditions, which can make interpretation complicated. The sledgehammer part of the analogy is that the PES selection rule is that you must remove an electron, and as long as you have enough energy, this is a near certainty. This also means that no state can be "dark" to a photoelectron spectroscopist.

$$A^- + h\nu \rightarrow A^\bullet + e^- \tag{1.1a}$$

$$A^- + h\nu \rightarrow A^{\bullet *} + e^- \tag{1.1b}$$

$$A^- + h\nu \rightarrow A^{-*} \rightarrow A^\bullet + e^- \tag{1.1c}$$

The simplest case is where an electron is removed from the Highest Occupied Molecular Orbital (HOMO). In our case this would be electron detachment from a closed shell anion, A^-, to produce a ground state open shell neutral radical, $A^\bullet$, Equation 1.1a. Although in many experiments the, energy inputted is capable of removing electrons from a number of lower occupied energy levels, producing an excited open shell radical state, $A^{\bullet *}$, Equation 1.1b. It is also possible to create a meta-stable anion state, A^{-*}, which subsequently decays to form the radical and a photoelectron, Equation 1.1c.

As we set the laser wavelength and measure the output parameter, photoelectron kinetic energy (eKE), we can calculate the energy of the system as the difference,

$$\begin{aligned} h\nu &= E(\mathrm{A}^\bullet) + eKE(\mathrm{e}^-) \\ h\nu - eKE(\mathrm{e}^-) &= E(\mathrm{A}^\bullet) \end{aligned} \tag{1.2}$$

The kinetic energy of the detachment is partitioned between the molecule and the electron according to the conservation of momentum. Due to the significant mass difference between the two, nearly all the kinetic energy is carried away by the electron and the velocity of the molecule is ignored. In this introduction to PES, we specifically discuss photoelectron electron detachment rather than ionisation as we are studying anions, however the principles are identical to ionisation of neutrals. Any wavelength can be used in PES and most techniques are classed by the wavelength used, such as X-ray, which detaches electrons from core orbitals, or UV, which detaches electrons from valence orbitals. In our experiments, we exclusively use UV wavelengths.

Figure 1.8 shows a more complicated schematic of photoelectron detachment from

Figure 1.8: Schematic of electron detachment from S_0 to D_0 producing a range of eKEs.

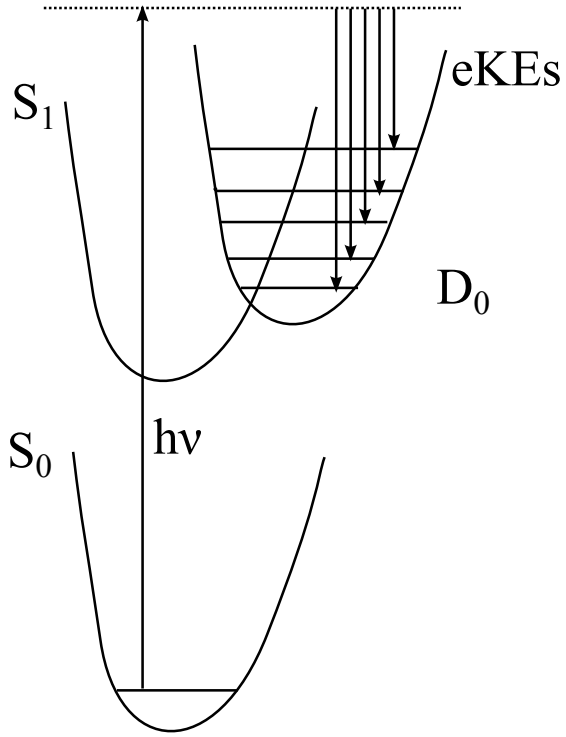

the ground state, S_0, of a closed shell anion to produce an open shell radical in either its ground, D_0, or excited, D_1, states. The varying eKEs that would be produced are not only characteristic of each electronic state of the radical but also of the vibrational modes that are involved. In the example in Figure 1.8, the S_1 state is very close in energy to the D_0 radical such that a vibrationally exited S_1 state could cross over to D_0 and detach an electron. This relative ordering is common in anions meaning that anion electronic absorptions (from S_0 to S_1) can eventually lead to electron detachment.

To continue our previous analogy, whilst the selection rules may be simple, the watchmaker's tweezers are required when the spectra produced need to be unravelled, interpreted and understood. Contrary to what has been stated previously, whilst the presence of all photoelectron peaks in a photoelectron spectrum are allowed, the reality is that the peak shape and intensity is dictated by the overlap of the ground and final states, and can be complicated by a high density of states. This relationship between the initial and final states is quantified by the Franck-Condon factor.[81–83] The probability amplitude of a transition from the initial to final state of a molecule can be described using:

$$R = \int \int \psi'^{*} \mu \psi'' \; dq \; dQ \tag{1.3}$$

Where, R is the overlap between the ground and excited state, ψ' and ψ'' are the wavefunctions for the initial and final state respectively, μ is the electric dipole moment and the entire integral is over electronic and nuclear coordinates, q and Q, respectively. Equation 1.3 can be split into electronic and vibrational components as long as the Born-Oppenheimer approximation (BOA) holds,

$$\begin{aligned} R &= \int \psi_e'^{*}(q,Q)\psi_\nu'^{*}(Q)(\mu_e + \mu_\nu)\psi_e''(q,Q)\psi_\nu''(Q) \; dq \; dQ \\ &= \int \psi_\nu'^{*}(Q) \left[\int \psi_e'^{*}(q,Q)\mu_e \psi_e''(q,Q) \; dq \right] \psi_\nu''(Q) \; dQ + \\ &\quad \int \psi_\nu'^{*}(Q)\mu_\nu \left[\int \psi_e'^{*}(q,Q)\psi_e''(q,Q) \; dq \right] \psi_\nu''(Q) \; dQ \end{aligned} \tag{1.4}$$

Where the subscript e or ν denotes an electronic and vibrational component. The wavefunctions in the second term are orthogonal so the entire second term is zero, which simplifies to,

$$\begin{aligned} R &= \int \psi_\nu'^{*}(Q) R_e(Q) \psi_\nu'' \; dQ \\ R_e(Q) &= \int \psi_e'^{*}(q,Q)\mu\psi_e''(q,Q) \; dq \end{aligned} \tag{1.5}$$

Where, $R_e(Q)$, is the electronic transition moment which in the Frank-Condon approximation can be assumed to be independent of the nuclear coordinates,

$$R = R_e \int \psi_\nu'^{*}(Q)\psi_\nu''(Q) \; dQ \tag{1.6}$$

The Frank-Condon factor is R^2, so a maximum in intensity is observed when the geometries and vibrational modes of the anion and radical are similar. This also means the spread of vibrational modes is small and will produce a narrow feature. Larger changes in geometry between the two states will produce a less intense and broader peaks.

$$\Gamma_{anion} \otimes \Gamma_{\mu} \otimes \Gamma_{radical} \otimes \Gamma_{e^-} \supseteq \Gamma_{tot.sym.} \tag{1.7}$$

For the detachment process to occur the direct products of the anion, radical, transition dipole and electron symmetries must be equal to or contain a totally symmetric representation, Equation 1.7. In practical terms, Equation 1.7 is obeyed by the electron "balancing the equation" and having an angular distribution characteristic of the anion and radical symmetries involved in the detachment process. Using a polarised laser along with a suitable detector (see Section 1.4) it is possible to measure the angular information of the electron and obtain even more information from the detachment. This effect can clearly be seen in the anisotropic photoelectron image of iodide, Figure 2.9(b and d). In this case the detachment is clearly obeying the angular momentum selection rule, $\Delta l = \pm 1$, and detachment from the $^1S_0$ state of I^- to form the $^2P_{1/2}$ or $^2P_{3/2}$ radical states is indicated by the electron projecting onto the detector as a p-wave.

1.2.1 Time Resolved Photoelectron Spectroscopy

Fluorescent proteins are inherently dynamic systems, as they begin by absorbing a photon of one wavelength and finish by emitting another with some unknown intermediate process. PES in itself can provide a detailed picture of the molecules energy level structure but it is limited to a single moment in time. It would be informative to measure how the energy moves around in these molecules so that we can understand the dynamic nature and time-resolved photoelectron spectroscopy (TRPES) is the tool that allows us to accomplish this.

After absorption of a photon, a molecule has multiple pathways which it can follow in order to return to its ground state. Electronic relaxation pathways include intersystem crossing (ISC), IC, Intramolecular Vibrational Energy Redistribution (IVR), fluorescence, phosphorescence, which can be summarised in a Jablonski diagram, Figure 1.9. It can be noted that dissociation and isomerisation are also important decay pathways for many

Figure 1.9: A Jablonski diagram summarising electronic decay pathways after excitation.

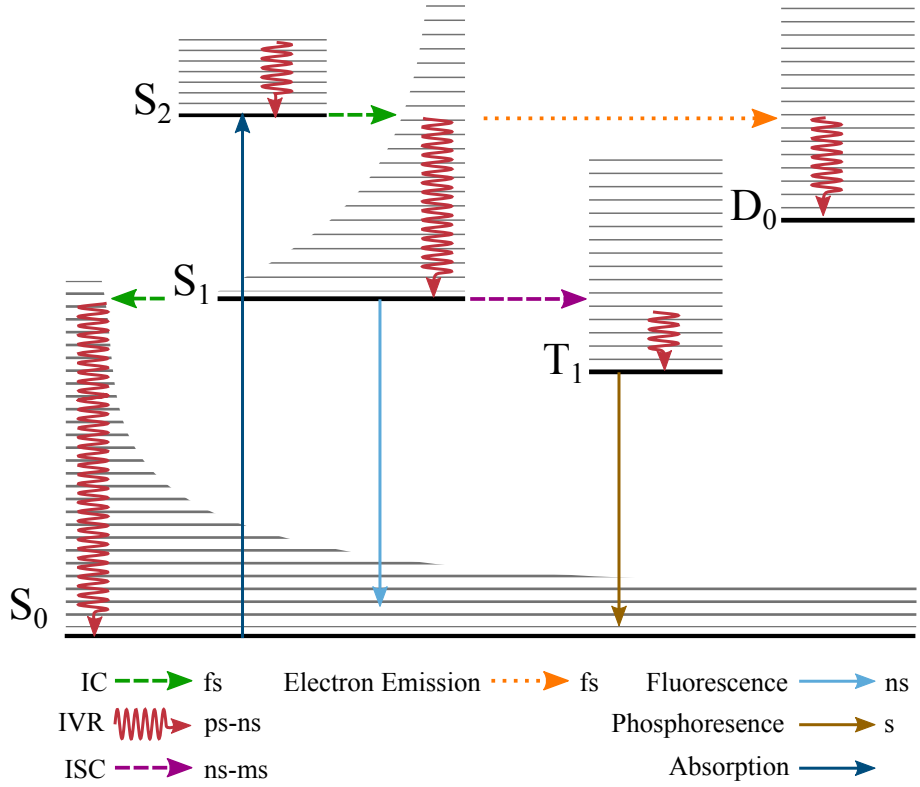

systems. The time-scales of each of these process can range from seconds to femtoseconds, and this will dictate the methods required to observe the process. In our case, the non-radiative intermediate processes of fluorescence proteins mean we wish to study the faster IC, IVR or ISC processes. This is accomplished using femtosecond lasers in a pump-probe configuration pioneered by Ahmed Zewail.[84]

Using two femtosecond lasers pulses in a pump-probe scheme, we can map out the ultrafast dynamics of an excited molecule. Figure 1.10 depicts a schematic of a system being examined using pump-probe TRPES. The molecule is first excited to S_n and subsequently transitions non-radiatively *via* IC to a vibrationally hot lower electronic state S_{n-1}. At some defined time later, the probe laser then projects the relative vibrational populations of S_n and S_{n-1} onto D_0, producing characteristically different photoelectron kinetic energies. By combining a series of successive time delays between the pump and probe pulses, typically from -1 ps[†] to 10 ps, it is possible to build up a characteristic

[†]Negative time used to denote when the probe pulse comes before the pump pulse.

Figure 1.10: A schematic of a pump-probe dynamics experiment. After excitation from a pump laser, the probe laser maps the excited state population onto the radical. The eKEs detected change over time (Δt), from eKE_1 to eKE_2, as the excited state population moves from S_n to S_{n-1}.

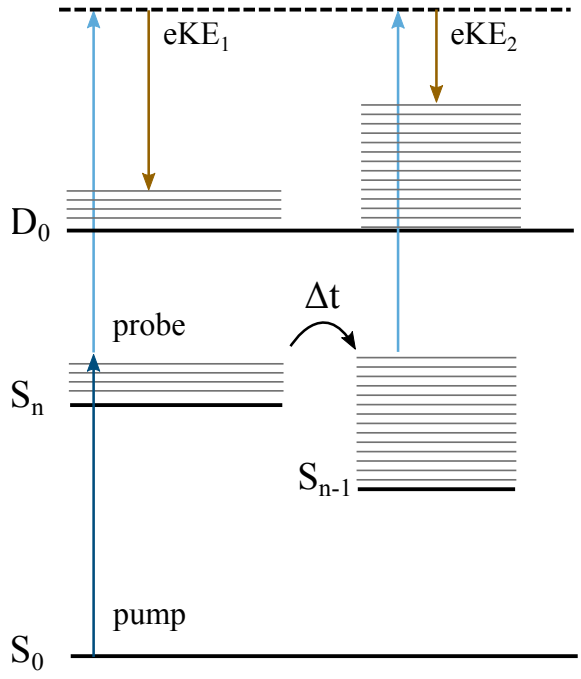

photoelectron kinetic energy map of the molecule.

1.3 Ion Manipulation

To examine the properties of gas-phase properties of ions, we require techniques that allow us to produce, distinguish and store molecular ions. The methods we employ to accomplish in our experiments are introduced in this section. Producing ions consists broadly of two steps, vaporisation and ionisation. In order to vaporise molecules earlier gas phase spectroscopy relied on the high vapour pressures of samples or heating,[85] usually followed by supersonic expansion, to enable the transition from the solid or liquid phase to the gas phase. This was effective for smaller molecules but larger, biologically relevant, molecules tended to have a much lower vapour pressure and decompose on heating thus making the application of these techniques difficult.[86] However, it was not impossible and spectral measurements of DNA bases,[87] and amino acids[88] have been accomplished

using thermal heating. Later work utilised laser desorption to vapourise larger molecules but these were soon superseded by improvements in soft ionisation techniques.[89,90] Once vapourised it is possible to ionise molecules using techniques such as electron ionisation (EI) or photolysis.[91,92] These can be considered "hard" ionisation techniques which leave the ions with a considerable amount of internal energy. Later instrumentation development introduced "soft" ionisation techniques such as electrospray ionisation (ESI) and matrix-assisted laser-desorption ionisation (MALDI).[93]

ESI and MALDI combine the vaporisation and ionisation steps into a single process and the main difference between them is the state in which the molecules are introduced into the ion source. MALDI consists of an analyte suspended in a matrix which is then laser-desorbed. The critical property is that the absorption peak of the matrix is chosen to fit the wavelength of the laser so that the energy is transferred *via* the matrix to the analyte. ESI is the method used in the experiments within this thesis and more details can be found in Section 1.3.1. The discovery and development of MALDI and ESI earned Fenn and Tanaka the Nobel prize.[94,95]

After production of ions, the next step is to isolate or determine which ions are present in the analyte. A lot of experiments involve starting with a mix of molecules to examine and on top of this, most ionisation sources will produce a variety of different species during the ionisation process. In our case, we only ever have a single ion of interest which is then pumped into our ESI apparatus; however even with one molecule it is very likely that ions with a range of mass/charge ratios will be produced. To overcome this issue there are various methods available including 3D quadrupole ion traps, linear quadrupoles and Time-of-Flight (TOF) techniques and research groups have combined various methods of ion selection and manipulation to investigate the gas-phase spectroscopy of biomolecular ions.

The Andersen group used ESI combined with an electrostatic storage ring to record photo-destruction action spectra,[37,72,96] with later modifications able to measure photoelectron spectra.[41] Wang utilises a spectrometer which combines ESI, TOF, a cryogeni-

cally cooled 3D quadrupole trap and a magnetic bottle spectrometer to measure photoelectron spectra.[97] Verlet also used TOF coupled with a velocity map imaging (VMI) spectrometer to measure photoelectron spectra.[98] Jockusch has used a modified commercial ESI mass-spectrometer, which incorporated a 3D quadrupole trap, which stored ions ready to be interrogated by lasers producing photodetachment and photo-fragmentation spectra.[38,39] Dugourd has used ESI combined both a linear quadrupole ion trap and a 3D quadrupole trap in different experiments,[99,100] both apparatus use a laser to produce photodissociation spectra. Using a cryogenically cooled linear quadrupole trap allowed Rizzo to examine molecular ions with both UV and infra-red (IR) lasers, producing double-resonance photodetachment spectra containing vibrational information.[101,102] Zenobi has used Fourier transform ion cyclotron resonance (FT-ICR) to trap ion allowing them to measure the fluorescence spectra of gas-phase ions.[103,104]

A number of the groups mentioned above have used cool traps to control (specficially lower) the internal temperature of ions within their experiments.[97,101,105–107] As electrospray ionisation is operated at room temperature the ions produced can possess an considerable amount of internal energy which can lead to complications in the interpretation of the spectra such as spectral hot-bands,[105] or production of conformers.[102,108] By controlling the temperature of the ions using an ion trap, the effects of temperature on the spectra can be quantified and in the cases mentioned the groups were able to demonstrate improved vibrational resolution, removal of hot-bands[97,105] and analysis of discrete gas-phase conformers.[102]

1.3.1 Electrospray Ionisation

ESI has become an invaluable method for the ionisation of large molecules. Previous techniques such as electron impact would cause large molecules to fragment due to the high energies involved. This made analysis difficult as molecular information would be non-characteristic of the complete molecule. ESI was developed by John Fenn for which he was jointly awarded, along with Koichi Tanaka and Kurt Wüthrich, the 2002 Nobel

prize in Chemistry.[109]

An ESI source is broadly operated as follows: a solution of the molecule is pumped through a capillary (typically micrometres or nanometres in diameter). The capillary is held at a large potential (a few keV), relative to an aperture of a differentially pumped chamber. The potential of the capillary can either be positive or negative depending on the charge of ions required.[110,111] Setting the capillary to a positive potential will produce cations, conversely setting it to a negative potential produces anions. An inert gas which is between 320-350 K is passed over the stream of cations coaxially to aid in the evaporation of solvent molecules. A schematic can be seen in Figure 1.11 (a).

The analyte solution is pumped through the capillary to produce a stream of solution that eventually forms charged droplets, due to Rayleigh instabilities. These charged droplets contain solvent molecules and the molecule of interest. Two mechanisms have been proposed for the formation of the charged final molecule from these droplets, the first was proposed by Dole and the second by Iribarne and Thomson.[112,113] Both models are based on the idea of successive evaporation and "explosion" of the droplets, and differ only in the final step which produces the molecular ion. As solvent molecules evaporate from the droplet surface the electric field of the droplet increases until a critical diameter is reached and the electrostatic repulsion is greater than the surface tension. The droplet explodes into smaller droplets and the process continues until a droplet containing only a single solvent molecule and the charged analyte molecule remains. In the Dole model, the final neutral solvent molecule evaporates leaving the ion, Figure 1.11 (b). In the Iribarne and Thomson model, as the solvent and molecule droplets become smaller the electric field of the droplet increases, and at a critical point the electric field becomes so high that it is able to "lift" the ion molecule from its surface, Figure 1.11 (c). It is worth noting that ESI can not only ionise proteins without fragmentation but with careful choice of solution concentration, solvent and pH, it can leave them in their natural folded states.[114]

Figure 1.11: (a) Schematic droplet formation of solution being pumped through an electrospray tip (b) Dole/Thomson model of ion production (c) Iribarne and Thomson model of ion production. Figures reproduced from Fenn[109]

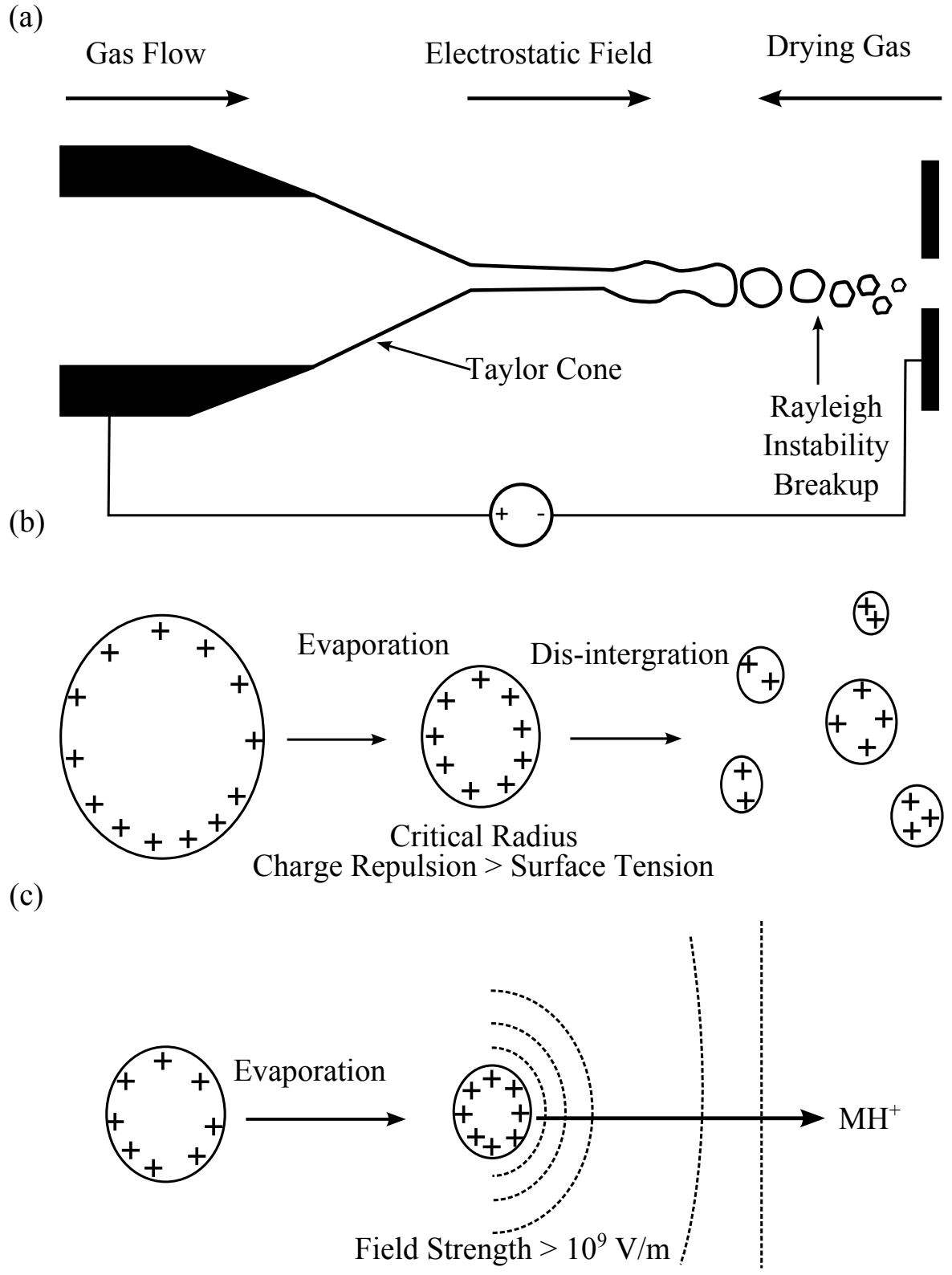

Figure 1.12: Schematic of VMI spectrometer showing pan-caking of Newton spheres. (R) Repller, (E) Extractor, and (G) Ground plates.

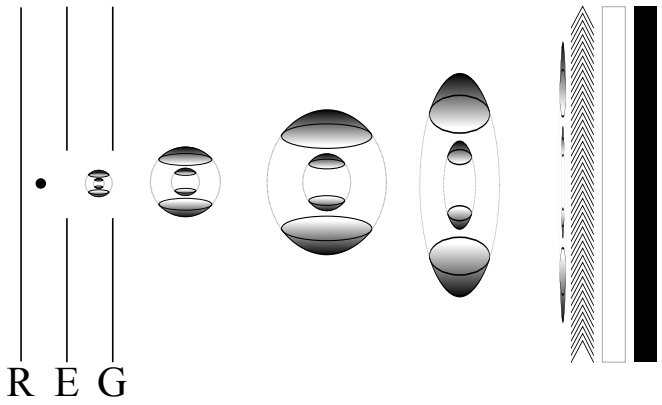

1.4 Velocity Map Imaging

Photoelectron spectroscopy removes an electron from our species of interest which possesses a kinetic energy which is characteristic of the energy level from which the electron was removed from. In an idealised simple system where with a single detachment channel, with no angular propensity, you can easily imagine with each separate detachment that the electrons form an expanding sphere. Unfortunately there are usually multiple detachment processes with each process forming its own characteristic sphere of electrons. Each of these spheres originates in the same place so they have become nested within each other like a set of Russian dolls. Our objective is to measure the ratio of radii between these spheres as they are a direct measurement of the relative energy of each process that created them.

The VMI imaging apparatus allows us to measure the kinetic energy and angular information of a detachment process and the technique was developed by Eppink and Parker.[115] Using a configuration of three parallel plates, each with an aperture, combined with an imaging MCP, phosphor and Charge Coupled Device (CCD) camera, it is possible to build a VMI spectrometer, see Figure 1.12. It is strikingly similar to the classic Wiley-McClaren TOF but without the grids. The three plates, repeller, extractor and ground, are held at a high potential (1000s V). The ratio of the potentials applied to the repeller and extractor is critical and is usually found empirically to be $\sim$0.71. The

Figure 1.13: Schematic of anisotropic 3D Newton sphere becoming "pan-caked" onto a 2D detector.

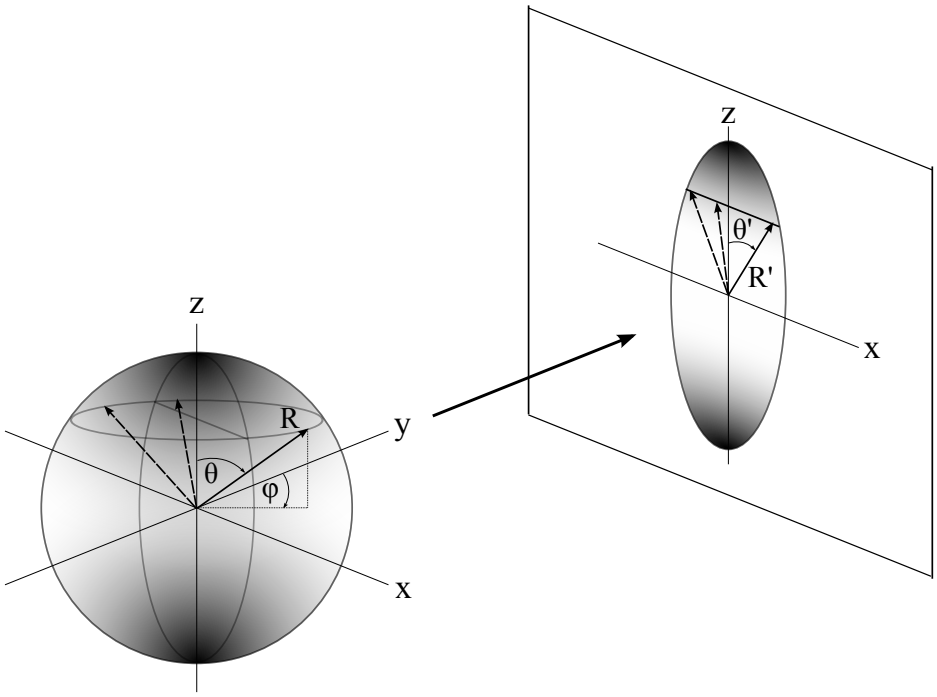

unique property of the VMI ion imaging configuration is that as long as the starting velocity of the electrons (*i.e.* the molecules) is negligible compared to the kinetic energy gained from the electron static field, then the electrons are mapped on to the detector relative to their velocity from the detachment process. Their original position within the interaction region does not affect the final measurement, they are "velocity mapped". The lack of grids not only means means that 100% collection efficiency is possible but that the image is free of distortion. Since its original publication the VMI technique has been used by 100s of groups. The apparatus is easy to construct and gives us two measurable quantities for the cost of a single measurement. Other designs have also been developed, which possess fewer optics and lower voltages[116] or more exotic designs that allow for slow velocity map imaging.[117]

VMI was developed as an ion-imaging technique but can be applied easily to photoelectrons and the principles are the same and in fact simplified because we are only measuring one species. When the electrons are created between the VMI plates, not only is their velocity mapped but they are also time-focused, so that all the electrons arrive

at the detector at the same time. This process is infamously referred to "pan-caking" where the 3D distribution of electrons becomes a 2D image on the flat detector. This process is depicted in Figures 1.12 and 1.13. If we have a single detachment process, which also has a narrow detachment energy distribution (such as removing an electron from an atom) then the radius of the image is a direct measure of the electron's velocity. In the case of molecular PES, we usually have a range of detachment processes and a broad distribution of eKEs and so the larger radii spheres contribute signal towards the centre of the detector where smaller radii spheres also reside. This congests our image and makes interpretation difficult. The result of this can be seen in Figure 1.14, which depicts a slice through the 2D projected image made up of to two Newton spheres. It can be seen from the dashed lines that the signal at larger R is non-zero at the centre, and overlaps with signal from the smaller sphere.

In most experiments the image is even more congested. We require the 3D distribution to measure the radii of the spheres, but we have lost a dimension and only have a 2D image. Fortunately, assuming our VMI spectrometer is working correctly it can be noticed from Figure 1.13 that the sphere has cylindrical symmetry about the z-axis which means there enough information in the 2D image to reconstruct the 3D distribution and therefore the relative velocities. For heavy slow species, such as molecular ions, it is possible to completely side step this issue by designing the TOF so that rather than pan-caking the species at the detector they are spread out in time and the experimentalist needs only to gate the detector on the central portion of the sphere. This then gives a direct measurement of the original sphere without the need for inversion.[118]

1.4.1 Inversion Methods

Two common methods are basis set expansion (BASEX)[119,120] and onion peeling,[121,122] and an overview of their polar implementations is presented in this section. Both push noise towards the centre of the image, which is usually of less interest to the experimentalist. The earlier algorithms for both these methods used Cartesian coordinates but it

Figure 1.14: Slice through a 2D projected image. (Dashed lines) Individual newton sphere contributions (solid line) Summation of dashed line contributions.

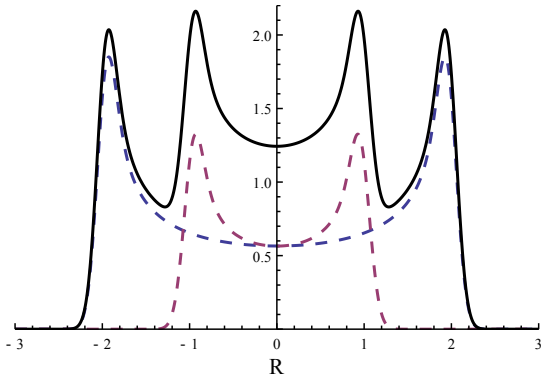

has later been found that converting images to polar coordinates simplifies the calculations. These two methods take completely different approaches for recovering the 3D information and both are used in this thesis.

pBASEX

The BASEX method works from the principle that fitting an appropriate basis functions to the projected image will provide enough information to reconstruct the 3D distribution. BASEX starts from the Abel integral[123], Equation 1.8. Which relates the 2D image, $P(R', \theta')$ to how it is produced from our original 3D sphere, $F(R, \theta)$.

$$\begin{aligned} P(R', \theta') &= 2 \int_{|x|}^{\infty} \frac{r F(R, \theta)}{\sqrt{r^2 - x^2}} \, dr \\ x &= R' \; sin \; \theta' \\ r &= R \; sin \; \theta \end{aligned} \tag{1.8}$$

BASEX works on the principle that the Abel integral can be described using an appropriate set of basis functions,.

$$g_{kl}(R',\theta') = 2\int_{|x|}^{\infty} \frac{r f_{kl}(R,\theta)}{\sqrt{r^2 - x^2}}\, dr$$
$$f_{kl}(R,\theta) = e^{-(R-R_k)^2/\sigma} P_l(cos\ \theta) \tag{1.9}$$

k is the radial pixel from the centre and l is the order of the Legrande Polynomial required. These basis functions allows us to re-write Equation 1.8 as a sum of the contributions of each basis function,

$$P(R',\theta') = \sum_{k=0}^{k=k_{max}} \sum_{l=0}^{l=l_{max}} c_{kl} g_{kl}(R',\theta') \tag{1.10}$$

Along with a conversion of the equations from a continuum to discrete pixels, the original Abel integral equation can now be written in matrix notation,

$$\mathbf{P} = \mathbf{CG} \tag{1.11}$$

Where $\mathbf{P}$ is the 2D image, $\mathbf{C}$ is the matrix of coefficients, and $\mathbf{G}$ is the projection matrix. It is hopefully now clear the the coefficient matrix of Equation 1.11 is a direct representation of the original 3D sphere. To obtain these coefficients requires matrix arithmetic and regression fitting. Computationally, constructing the basis set matrix, $\mathbf{G}$, is time consuming and the number of radial and azimuthal basis functions must be chosen to suit experimental parameters. A larger detector or use of centroiding would necessitate a larger number of azimuthal and radial basis functions in order to accurately reconstruct the Newton spheres from the 2D image. However this cost is traded off against the fact that it only has to be calculated once, and recovered from memory to analyse future images, making it a very quick technique for image analysis.

Polar Onion Peeling

Another inversion technique is onion peeling, which constructs the original 3D distribution by peeling each contribution from the projected 2D image from the outer edge towards the centre, just like peeling an onion. Computationally this method is very fast, giving near to real time results during an experiment. To accomplish this, the outer edge of the projected image is fitted,

$$I(\theta') = N(R') \sum_{n} \beta(R') P_n[cos(\theta')] \tag{1.12}$$

Where $N(R')$ is the intensity coefficient, $\beta(R')$ is the anisotropy coefficient and $P_n[cos(\theta')]$ is the n^{th} order Legrande polynomial also a description of the anisotropy using Legrande polynomials. The 2D projected image can be thought of as the sum of successive functions for each radius, R. A set of idealised basis functions can be generated, $g_{ideal}(R; R', \alpha')$, and scaled using Equation 1.12, to give a 2D projection of the outer contribution, $g_{fit}(R; R', \alpha')$, see Equation 1.13.

$$\begin{aligned} P(R', \theta') &= \int_{0}^{r_{max}} g(r; R', \theta')\ dr \\ g_{fit}(r; R, \theta') &= g_{ideal}(r; R, \theta') N(R) \sum_{n} \beta_r P_n[\frac{R'}{R} cos\ \theta'] \end{aligned} \tag{1.13}$$

This contribution from the outer edge signal can be subtracted from the image to produce a new image, $G^{\ddagger}$, this would be the "peeling" step,

$$G^{\ddagger}(R, \alpha) = G(R, \alpha) - g_{fit}(r; R, \alpha) \tag{1.14}$$

At each stage the fitted intensity and angular information from Equation 1.12 are kept, and are used to construct the original 3D distribution.

1.5 Computational Methods

An experiment, designed properly, provides a result that is robust, testable and repeatable. Although interpretation of these results can be difficult and is certainly open to debate. To aid in this we can use computational methods to model our molecule of interest and compare the results with experiment.

Theoretical chemistry is an area of study in itself, with great effort spent trying to develop new methods, understand the limits of current methods, and explore computationally the properties of molecules that are hard to study experimentally. Using computational chemistry methods we can aid our understanding of experimental results and with software packages such as GAUSSIAN, MOLPRO and MOLCAS,[124–126] along with the increase in computer speed, performing molecular calculations has become much more accessible to the experimentalist. The benefits, as photoelectron spectroscopists, is that we can measure photoelectron eKEs and complement these results with calculations that can give us information about the molecular and electronic structures of anions and radicals that are involved in the emission of photoelectrons.

The work in this thesis employs a number of different methods; Electron Propagator Theory (EPT),[127,128] Møller-Plesset (MP)[129] and CASSCF.[130] They all owe a debt to Hartree-Fock (HF)-Self-Consistent Field (SCF).[131] This was one of the first useful molecular theoretical methods and is the simplest and quickest method available in all chemistry packages. It is nearly always the starting point of many more complicated calculations such as those mentioned above. All computational methods attempt to solve the Schrödinger Equation,

$$H\Psi = E\Psi \tag{1.15}$$

H is the Hamiltonian, Ψ is the wavefunction, and E is the eigenvalue energy. Whilst the Schrodinger equation looks deceptively simple there are two significant challenges to overcome. The first is the Hamiltonian as it includes electron repulsion and nuclear

terms, and the second is finding the exact nature of the wave function.

We shall deal with the second problem first, by Equation 1.16 which allows us a route to discovering a useful wavefunction. If we try successive different wave functions and apply them to the left hand side each improvement should lower the overall energy.

$$\frac{\int \Psi H \Psi \; d\mathbf{r}}{\int \Psi^2 \; d\mathbf{r}} \geq E_0 \tag{1.16}$$

E_0 is the minimum achievable energy, a perfect basis set would converge on the HF limit, which is the minimum energy able to be calculated by the approximations of the HF method. To construct the wavefunction, we choose a set of basis functions. Unfortunately we cannot have an infinite set of them so our wavefunction will always be truncated to some extent leading to inaccuracies in the calculation. Every quantum chemistry software suite constructs the wavefunction from an appropriate basis set. Commonly used sets are either the Pople (also called Gaussian) orbitals or the Dunning basis sets,[132,133] in either case, care must be taken to choose an appropriate set for the system to be studied. In our case, studying anions, it has been shown that basis sets that include diffuse and polarised orbitals are very important to describe the systems.[134]

The next challenge is to find a Hamiltonian we can calculate.

$$H = -\sum_i \frac{\hbar}{2m_e}\nabla_i^2 - \sum_k \frac{\hbar}{2m_k}\nabla_i^2 - \sum_i \sum_k \frac{e^2 Z_k}{r_{ik}} + \sum_{i<j} \frac{e^2}{r_{ij}} + \sum_{k<l} \frac{e^2 Z_k Z_l}{r_{kl}} \tag{1.17}$$

The Hamiltonian is constructed from the effects of electrons and nuclei; the first two terms are the kinetic energy of the electrons and nuclei, respectively; the last three terms are the electron-nuclei attractive potential, electron-electron repulsion and the nuclei-nuclei repulsion potential energy terms, respectively. The terms in the Hamiltonian that cause the problems are the "correlated" potential energy terms of the nuclei and electrons. The fact that the motion of one particle affects the others makes the calculations impossible for anything but the simplest systems, *e.g.* H. The first common approximation is

the BOA which allows us to remove the correlated effects of the nuclei, as they move so slowly compared to the electrons, and leaves us only having to consider the electrons interacting with a static potential due to the nuclei. To find a useful Hamiltonian, the problem is solved by considering the total Hamiltonian being constructed as the sum of individual electron Hamiltonians. The Hartree Hamiltonian is constructed as the sum of individual one-electron Hamiltonians,

$$H = \sum_{i}^{N} f_i \tag{1.18}$$

H is the many body Hamiltonian and f_i is the Fock operator of electron i which is able to take account of the electron repulsion and exchange,

$$\begin{aligned} f_i &= -\frac{1}{2}\nabla_i^2 - \sum_{k}^{nuclei} \frac{Z_k}{r_{ik}} + 2J_i - K_i \\ J_i &= \int |\psi_i(1)|^2 \frac{1}{r_{12}} |\psi_j(2)|^2 \; d\mathbf{r_1} \; d\mathbf{r_2} \\ K_i &= \int \psi_i(1)\psi_j(1) \frac{1}{r_{12}} \psi_i(2)\psi_j(2) \; d\mathbf{r_1} \; d\mathbf{r_2} \end{aligned} \tag{1.19}$$

J_i and K_i are the effects of electron repulsion and exchange, respectively and ψ are spacial-spin wavefunctions. The electron kinetic energy and potential due to the nuclei are still recognisable as the first and second terms, the third term however is where the magic happens. The final term is a result of the work done by Hartree and Fock, and is the potential seen by an electron (i) due to the other electrons. Its exact form is due to the nature of the electron and anti-symmetry requirements. The resulting expectation value for the energy can be calculated using,

$$E = \sum_{i=1}^{N} \epsilon_i - \sum_{i \neq j}^{N} \left[J_i - \frac{1}{2} K_i \right] \tag{1.20}$$

ϵ_i is the energy of i calculated using the Fock operator. The issue here is that each

orbital energy ϵ_i includes accounts for the potential due to ϵ_j, but ϵ_j also accounts for the potential of ϵ_i. So the total potential energy due to the electrons has been double counted which is accounted for by the inner sum.

A problem has now arisen. We can calculate the energy of the system using Equations 1.16 and 1.20 but the equations are dependent on each other. The solution to this problem is to take an initial (educated) guess at the solution to the wavefunction, and plug the result back into the equation. Once successive results are within a certain threshold they are said to be converged and they are described as being self-consistent. This leads to the common name of this methodology, Hartree-Fock Self-Consistent Field theory, HF-SCF. It provides us with a series of absolute energies for each molecular orbital, these are of particular interest to us as we can use Koopmans Theorem to interpret them as detachment energies.

Calculating the detachment energies can be accomplished with a HF calculation. Unfortunately this is a compromised method as the electron correlation is not adequately modelled which will lead to inaccuracies in our calculation. An alternative is to calculate the energy of the system at the beginning and at the end which, would account for the correlation energy and relaxation energy of the process. This calculation has to be incredibly accurate as we are subtracting two numbers and finding a very small difference. Methods that allow us to calculate the detachment energy directly would be advantageous. There are some significant shortcomings with the HF method. The main one being it is a one-electron solution, and only considers the electron exchange in the calculation of the energy. To improve on HF other methods have been developed which account for correlation these include CASSCF (Section 1.5.1), Perturbation Theory (Section 1.5.2) and EPT (Section 1.5.3).

1.5.1 CASSCF

The orbitals that are found by the HF SCF (HF-SCF) method are good as long as the ground state of the molecule is well described by a single configuration of electron orbital

occupations. The method assumes that the occupied orbitals always remain occupied and the unoccupied orbitals always remain unoccupied in some systems this is not always a good approximation. The starting point for CASSCF is that the system is better described by a sum of different occupation energies summed together. This allows us to account for the "non-dynamical" correlation energy that was a limitation of the HF-SCF method.

$$\Psi_{mcscf} = a_1 \left|...\pi_1^2\pi_2^2\pi_3^0\right\rangle + a_2 \left|...\pi_1^2\pi_2^0\pi_3^2\right\rangle \tag{1.21}$$

Where a_1 and a_2 are the relative contributions of each configuration to the overall wavefunction. To accomplish this we could just change the population ordering of the orbitals from the HF-SCF calculation, Equation 1.22a and 1.22b. The problem is that only the occupied orbitals were optimised in the SCF procedure the now occupied virtual orbital is not a good description of the system, Equation 1.22b.

$$\Psi^{HF} = \left|..., \pi_1^2, \pi_2^2, \pi_3^0\right\rangle \tag{1.22a}$$

$$\Psi_{\pi^* \leftarrow \pi} = \left|..., \pi_1^2, \pi_2^0, \pi_3^2\right\rangle \tag{1.22b}$$

$$\Psi^{HF^*}_{\pi^* \leftarrow \pi} = \left|..., \pi_1'^2, \pi_2'^0, \pi_3'^2\right\rangle \tag{1.22c}$$

There is nothing to stop us doing another SCF procedure to find out the nature of this new electron configuration, Equation 1.22c. If we did this for every possible electron ordering combination we would have performed a complete CI calculation and taken account of the effect of all configurations on the molecules ground state energy. This is something that can be done for small molecules but the computational expense is far to great for large polyatomics such as the ones discussed in this thesis. To cut down the computational expense we can make a judgement that there are probably only a limited number of orbitals that make a significant contribution and restrict the possible ordering contributions to a sub-set of orbitals and electrons.

1.5.2 Perturbation Theory

To account for electron correlation we can use perturbation theory by starting with the assumption that our original HF or CASSCF solution was close to the actual answer and that only a small perturbation to this result is required to obtain an improved answer. Perturbation theory breaks down the problem into two components, an unperturbed Hamiltonian we can solve easily, plus some small perturbation which brings us closer to the answer we are looking for.

$$\begin{aligned} (H^{(0)} + \lambda V) \left|\Psi_0\right\rangle &= E \left|\Psi_0\right\rangle \\ H^{(0)}\psi_i &= E_i\psi_i \quad i = 0, 1, 2, ... \end{aligned} \tag{1.23}$$

Equation 1.23 shows $H^{(0)}$ as our Hamiltonian to which we can find the exact wavefunctions, V as our perturbation operator, Ψ_0 is our unperturbed wavefunction and λ as the scaling factor which turns turns our unperturbed Hamiltonian to our Hamiltonian of interest, H. The above also states that solutions of H_0 can form a complete set. For the Hartree-Fock case these choices were first suggested by Moller and Plesset.[129] This has led to many calculations being referred to as MPn, where n is the order of the perturbation. If we set our unperturbed Hamiltonian, $H^{(0)}$, to the sum of our Fock orbitals, given previously in Equation 1.19,

$$\begin{aligned} H^{(0)} &= \sum_{i=1}^{n} f_i \\ H^{(0)}\Psi^{(0)} &= \sum_{i}^{occ} \epsilon_i \Psi^{(0)} \end{aligned} \tag{1.24}$$

It must be stated that the decision to use the sum of Fock energy eigenvalues means that the electron-correlation is completely miscounted as it will count the potential and exchange potential of each twice. To correct this we can set the perturbation operator to calculate the difference between over counting and how it should be counted properly,

$$V = \sum_{i}^{occ} \sum_{j>i}^{occ} \frac{1}{r_{ij}} - \sum_{i}^{occ} \sum_{j}^{occ} J_{ij} - \frac{1}{2} K_{ij} \tag{1.25}$$

Where the first term is the double integral from original Hamiltonian in Equation 1.17, and second term is the method used in the Fock operator, Equation 1.20. Now we have chosen our easy Hamiltonian and a suitable operator it is time to look at the solutions to the perturbation method. We can expand the perturbation operator and wavefunction as a Taylor series,

$$\begin{aligned}(H^{(0)} + \lambda V)\left|\Psi_0^{(0)} + \lambda\Psi_0^{(1)} + \lambda^2\Psi_0^{(2)} + \lambda^3\Psi_0^{(3)} + ...\right\rangle = \\ (E_0^{(0)} + \lambda E_0^{(1)} + \lambda^2 E_0^{(2)} + \lambda^3 E_0^{(3)})\left|\Psi_0^{(0)} + \lambda\Psi_0^{(1)} + \lambda^2\Psi_0^{(2)} + \lambda^3\Psi_0^{(3)} + ...\right\rangle\end{aligned} \tag{1.26}$$

Where $\Psi_0^{(n)}$ and $E_0^{(n)}$ are the n^{th} order perturbed wavefunction and energy correction. We can group the like powers together to find the result of the first, second and third, *etc* order perturbations allowing us to choose the extent we want to calculate the perturbation to,

$$H^{(0)}\left|\Psi_0^{(0)}\right\rangle = E_0^{(0)}\left|\Psi_0^{(0)}\right\rangle \tag{1.27a}$$

$$H^{(0)}\left|\Psi_0^{(1)}\right\rangle + V\left|\Psi_0^{(0)}\right\rangle = E_0^{(0)}\left|\Psi_0^{(1)}\right\rangle + E_0^{(1)}\left|\Psi_0^{(0)}\right\rangle \tag{1.27b}$$

$$H^{(0)}\left|\Psi_0^{(2)}\right\rangle + V\left|\Psi_0^{(1)}\right\rangle = E_0^{(0)}\left|\Psi_0^{(2)}\right\rangle + E_0^{(1)}\left|\Psi_0^{(1)}\right\rangle + E_0^{(2)}\left|\Psi_0^{(0)}\right\rangle \tag{1.27c}$$

After grouping the like powers together we have a set of equations for each of the n^{th} perturbations we can apply to our system of interest. Unfortunately we still have unknowns in our equation the perturbed energy, $E_0^{(0)}$, and perturbed wavefunction, $\Psi_0^{(0)}$. Once we are able to calculate these quantities we can just add the effect of each perturbation to the next to get our final result. By making some approximations and performing the algebra it is possible to construct equations for the second order perturbation energy and the associated wavefunction from the complete set of unperturbed energies and wavefunctions,

$$E_0^{(2)} = \sum \frac{\langle\psi_0| V |\psi_i\rangle^2}{E_0 - E_i} \tag{1.28a}$$

$$\Psi_0^{(2)} = \sum_i c_i \psi_i \tag{1.28b}$$

$$c_j = \sum_{i \neq 0} \frac{\langle\psi_j| V |\psi_i\rangle \langle\psi_i| V |\psi_0\rangle}{(E_0 - E_j)(E_0 - E_i)} - \frac{\langle\psi_j| V |\psi_0\rangle \langle\psi_0| V |\psi_0\rangle}{(E_0 - E_j)^2} \tag{1.28c}$$

Equations 1.28a and 1.28c show that the second order energy and wavefunction can be calculated from the known energies and wavefunctions. Higher order order perturbations can be calculated and are performed routinely, however in most cases the second order perturbation gives improves the HF or CASSCF result without much extra computational cost.[‡] In this work we perform a second order perturbation on a CASSCF result, CASPT2, in order to obtain improved results at certain key geometries, Chapter 5. This theory has its limitations for the perturbation to work the effect must be small and the effects of electron correlation can be significant. Whilst we can calculate higher order perturbations there is no explicit proof that this actually improves the calculated result (unlike for example having a infinite complete basis set *vs* the necessary truncated sets that are used).

1.5.3 Green's Functions Methods

Computational methods that use the Green's function, such as EPT, have the advantage that they can directly compute, without inherent approximations, orbital detachment and attachment energies, quantities that we are keenly interested to aid our interpretation of photoelectron spectra. Green's functions are a method of solving inhomogeneous differential equations, for our purposes a one-body Green's function can be constructed based on the non-interacting HF approximation,

[‡]The first order perturbation is, whilst calculated, not quoted as it is equal to the original HF solution.

$$G_0(x, x', E) = \sum^{occ} \frac{\psi(x)\psi^*(x)}{E - E_a} + \sum^{vir} \frac{\psi(x)\psi^*(x)}{E - E_r} \tag{1.29}$$

It can be seen that the Green's Function above will have poles that are equal to the orbital energies of the Fock orbitals. This unfortunately does not provide us with any improvement over a standard HF method. Although it is reasonable to think that this one-particle HF is a good approximation of an improved many-body Green's function. By obtaining a method to convert a one-body to a many-body Green's Function we could obtain improved answers to our orbital energies. To solve this Dyson introduced a new quantity, the self-energy,

$$G(E) = G_0(E) + G_0(E)\Sigma(E)G(E) \tag{1.30}$$

Where $G(E)$ is the many-body Greens's function, $G_0(E)$ is the one-particle Green's function, and $\Sigma(E)$ is the self-energy. The similarities between the Green's Function methods and perturbation theory can be seen in Equation 1.30. It contains terms we cannot solve,$G(E)$, terms we can solve, $G_0(E)$, and the means to convert the two, $\Sigma(E)$. Unfortunately there is not exact solution to $\Sigma(E)$ but by making appropriate approximations we can hopefully get a better answer for $G(E)$ and subsequently the orbital energies we are interested in. Although there are similarities between the Green's Function method and perturbation theory it must be stated that Equation 1.30 provides an exact solution to the orbital energies if we can solve it exactly of course.

1.6 Conclusion

This chapter has discussed why fluorescent proteins are interesting and how by studying their chromophores in the gas-phase we can aid in the understanding of the complete protein. We have also introduced the components and techniques that we have used to construct our experiment and which are referenced in later chapters. A brief background

to the computational methods that we have used has also being included to help with the appreciation of the results in the experimental chapters. Chapter 2 contains specific details of our experimental apparatus and data analysis. Chapters 3, 4 and 5 present our results for pHBDI$^-$ and Chapter 6 presents our results for various coumaric acid anion isomers.

Chapter 2

Experimental

All the experimental work presented in this thesis employs ESI and VMI to investigate the electronic structure and dynamics of photoactive protein chromophores in their anionic form, in the gas-phase. This chapter provides an overview of the experimental techniques focussing on the experimental apparatus developed at University College London (UCL) that was employed for the work presented in Chapters 3, 4 and 6.

The time-resolved experiments as described in Chapter 5 were carried out using equipment in Dr. Jan Verlet's lab in Durham University and more details of these are presented in Chapter 5.

2.1 Experimental Setup

Our setup consists of a home-built electrospray ionisation photoelectron imaging spectrometer and a nanosecond laser system. The equipment is based on a Waters quadrupole time-of-flight (Q-ToF) mass spectrometer which were modified to replace the perpendicular reflectron TOF with a VMI photoelectron spectrometer. During the course of the experiments the apparatus was modified to improve signal/noise and resolution. In earlier experiments the machine that was used a Ultima API model, the second machine was a Global model. The earlier Ultima had been modified to include to increase the

Figure 2.1: A schematic diagram of the electrospray ionization (ESI) and photoelectron spectroscopy imaging apparatus. (1) ESI ion source; (2) ion tunnels; (3) quadrupole mass selector; (4) ion trap entrance lens; (5) linear hexapole ion trap; (6) ion trap exit lens; (7) acceleration, focus and x-y steering; (8) potential switch; (9) baffles; (10) laser beam; (11) VMI plates; (12) μ-metal shielding; (13) MCP; and (14) CCD camera. Liquid N_2 cold trap, not shown, which is positioned above the VMI plates, outside the μ-metal shielding.

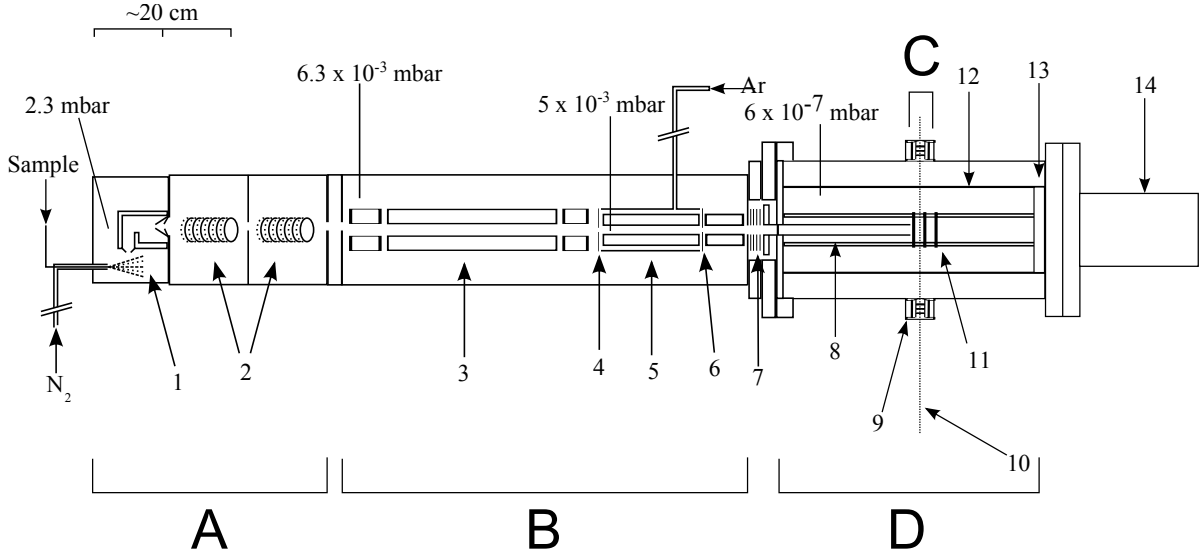

mass/charge range using a modified radio frequency (RF) supply along with other modifications which are described in this chapter. The second Global model was fitted with a standard lower mass range RF quadrupole supply. Other than the RF supply differences, the two mass spectrometers follow exactly the same design.

2.1.1 Electrospray Quadrupole Mass Spectrometer

Briefly, sample solutions are directly infused from a syringe pump (Harvard Apparatus 55-2222) into the ESI capillary. The evaporation of the highly charged droplets is assisted by the application of heated drying gas that is directed coaxially along the ESI capillary. The resulting ions are mass selected and guided into the hexapole ion trap. Ions pulsed out of the ion trap are guided and focused into the detachment zone of a photoelectron imaging spectrometer where they interact with a laser pulse. The resulting photoelectrons are accelerated toward a position sensitive detector where they are imaged using a CCD camera. Sections A and B were adapted from the commercial Q-ToF. Section D was

designed and built in-house. The detailed design, modification, and operation of the instrument are described in the sections below.

Anion production

For the work presented in Chapters 3 and 5 the GFP and cyan fluorescent protein (CFP) chromophores were synthesised using the method reported by Voliani *et al.*.[135] and their structures were confirmed using nuclear magnetic resonance (NMR). Phenol and indole were purchased from Sigma-Aldrich and used without further purification. The modified pHBDI molecules used in Chapter 4 were synthesied by Ms. Zhang following the method reported by Jaffrey *et al.*[136] with some alterations.[137] The various PYP chromophores as described in Chapter 6 along with phenol and indole used in Chapter 3 were purchased from Sigma-Aldrich and used without any purification.

Solutions of the molecule of interest are prepared and drawn into a syringe (SGE 25 μl or Hamilton 10 ml) ready for use in the electrospray. The concentration of the solutions was usually between 100 μM – 1 mM. Most solutions were made up with methanol but, depending on the solubility of the molecule, an alternative solution of water and methanol (1:9) was used. Concentrated ammonia (28%) was added dropwise to make the solution pH = 11, this ensured the anionic forms of the molecules were predominant in the solutions. We found that a single drop in a 50 cm^3 solution was adequate for our experiments. These solutions are pumped into the electrospray apparatus at a rate of 5-20 μL/min *via* a 0.25 mm internal diameter polyether ether ketone (PEEK) line.

The production of anions by electrospray is aided by dry nitrogen which is used as a nebulising and desolvation gas. The temperature of the capillary and the flow rate of the desolvation gas can be controlled. For our experiments, the temperature was set to 300 °C and the desolvation flow rate was 100 l/hr. This was found to produce the most intense and stable anion beam.

The ESI interface comprises of a standard Z-spray source[138] fitted with an electrospray probe (Figure 2.1). This configuration consists of an electrospray and a heated

source block which are orientated at right angles to each other. The source block has an aperture into the differentially pumped chamber. This perpendicular arrangement is to cut down on the amount of background ions and decrease the pumping requirements of the apparatus.[138] The position of the probe can be adjusted relative to the entrance to the vacuum chamber. The source block temperature was set to 120 °C for all our experiments. Once ions have passed though the source block aperture they are guided to the mass selection part of the apparatus by a pair of RF transfer lenses.

Quadrupole mass filter and linear hexapole ion trap

Quadrupole mass filters (QMFs) are a very common method of separating ions by their mass/charge ratio usually in preparation for the ions to be investigated by another technique. Commonly used in combination with a TOF spectrometer and in smaller, simpler, instruments they are simply employed with an ion source at one end of the QMF and some sort of detector at the other. More complicated designs have multiple QMFs in sequence which allow for scanning, along with parent or child mass spectrometry methodologies. In our experiment we use a single QMF to filter out our ions of interest before passing them into our spectrometer. An extension of the QMF is the 3D ion trap, which can be used to store ions as well as filter them in a similar way to a QMF.[139]

Their construction and operation are deceptively simple, only requiring four parallel cylindrical rods and an RF supply, see Figure 2.2. Technically the rods should be hyperbolic but in practice circular rods are adequate. The rods are connected in pairs and the supplies are configured such that an opposite field is applied to each pair, Equation 2.1.

$$U + V cos(\Omega t) \tag{2.1}$$

Where V is the zero-to-peak amplitude of oscillation, Ω is the frequency, t is time. U is the Direct Current (DC) offset and, for example, is positive for the x-axis rods, and negative for the y-axis rods. A QMF works from the principle that an oscillating electric field between the four rods will induce a "wobble" to ions as they travel through

Figure 2.2: Schematic diagram of quadrupole mass filter assembly, wiring and ion trajectory

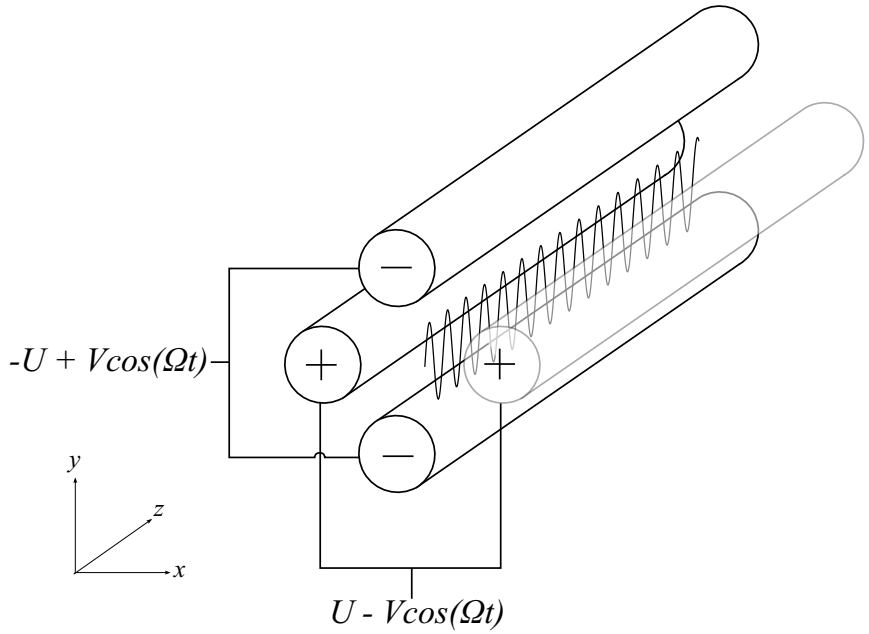

the QMF. If the frequency and magnitude of the oscillations are chosen correctly then only the ions with a specific mass/charge ratio will maintain an oscillating but stable trajectory from one end to the other with the other ions being ejected from the QMF. Ions with m/z values above and below the set value will have unstable trajectories and either hit a rod or leave the QMF entirely.

Each of the rods acts as a high or low pass filter, with ions that sit between the two filters being allowed through the QMF. An example can be described with a cation, along with a positive offset (U). In one plane, xz for example, the net positive field of the rods means that the ions will stay near the centre of the assembly. The RF potential will accelerate the light ions more significantly and so eventually the amplitude of their "wobble" will cause them either to hit a rod or leave the QMF assembly. On the other hand heavier ions will also begin to wobble but due to their larger mass these will increase at a slower rate and so remain close to the centre of the QMF assembly. Overall the xz rods are acting as a high-pass filter. In the opposite plane, yz for example, the ions will both be attracted towards the negatively biased rods. The RF potential will again affect the lighter ions more significantly but this time move them back towards the centre of

the QMF assembly allowing them to pass through the QMF. Heavier ions will not be as affected by the RF potential and will eventually hit a rod or leave the QMF assembly. Overall the yz rods are acting as a low-pass filter.

Understanding whether an ion will have a stable or unstable trajectory requires us to understand the nature of the forces being imposed on the ion. Using Mathieu's equations two parameters can be derived a, q, see Equations 2.2 and 2.3.*[140] Where m is the mass of the ion, and e the charge of an electron. These two parameters link the properties of the QMF and mass/charge of the ions. An ion is said to be stable when the value of β is an integer.

$$a_x = \frac{8eU}{m_0^0\Omega^2} \tag{2.2}$$

$$q_x = \frac{-4eV}{m_0^0\Omega^2} \tag{2.3}$$

$$\beta_x \approx \sqrt{(a_x + \frac{1}{2}q_x^2)} \tag{2.4}$$

Figure 2.3 (a) shows an ideal stability diagram for a QMF. The axis, (a_u, q_u), are a combination of stability for each pair of rods. The two light shaded regions depict the stability curve for an ion in between a single pair of rods. Where these two curves cross, darker shading, shows the region of a_u and q_u where the ion is stable in both dimensions. It can be noted that the dark shaded region is symmetric about q_u. Only those ions which sit in the middle of each filter's range will have a trajectory that reaches the end of the QMF. This would be a fixed mass-range operation, filtering a specific mass. If the ratio of U/V is altered over time then the ions that are able to pass through are also changed, building up a mass spectrum.

To scan a QMF in order to obtain a mass spectrum the U/V parameters must be

*An equivalent set of equations can be defined for the QMF, the y,z-axis where $a_y = -a_x$ and $q_y = -q_x$

Figure 2.3: (a) Graph of ion stability regions within a quadrupole mass filter, (b) Graph showing stability regions for three ions of different mass (solid lines), where $M_1 < M_2 < M_3$ and quadrupole scanning profile (dotted line).

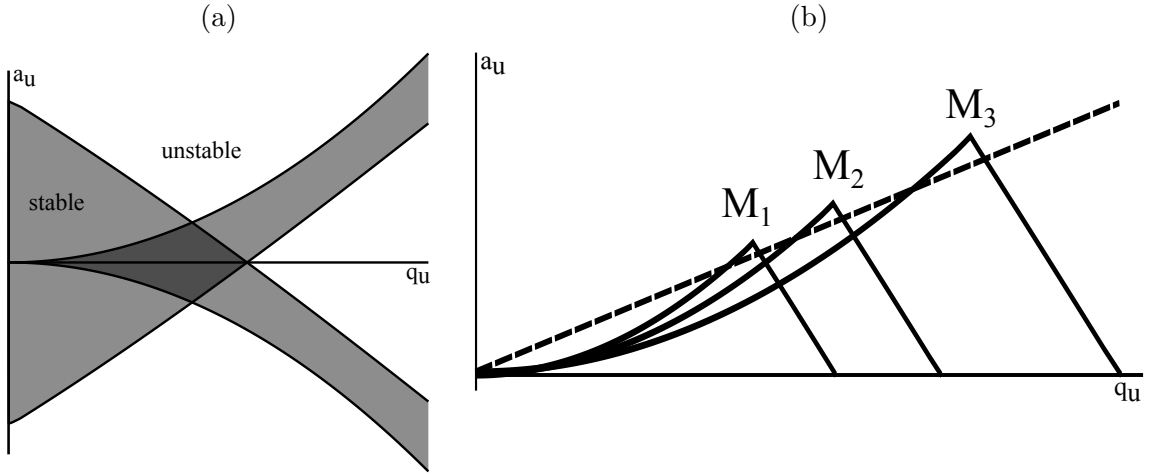

altered to allow successive ions through. Figure 2.3 (b) shows the stability diagram for three different mass ions, M_1, M_2 and M_3 and a path of U/V parameters that will trace stable regions for each mass. The stability regions of all three ions overlap so there are areas where the QMF will allow all ions to have stable trajectories. In order to select a mass appropriate q_u, a_u parameters are chosen so that only the top narrow section of their associated stability curves are probed. This is depicted in Figure 2.3b as the dashed line this does have the effect of reducing the ion throughput.

In our experiment a quadrupole mass filter is used to select ions of interest and ensure that only a single mass/charge ratio is present in the ion beam after electrospray ionization (Figure 2.1(3)). Earlier experiments used a Q-ToF Ultima API which had been modified to increase the upper mass range from from 4000- to 32000 m/z. This modification included a new RF coil, control electronics, modified control software, and ion optics in the quadrupole and collision cell. The new RF coil lowered the RF supply frequency, increasing the maximum mass/charge range. In order to control the new RF coil, the control electronics were modified and the personal computer (PC) control software had to be reconfigured. Within the chamber the entrance and exit lenses to the collision cell were replaced with lenses that had smaller apertures. The reduced frequency modification reduced the mass resolution of the quadrupole mass filter to ∼5.7.

Later experiments used a Q-ToF Global with a standard high frequency RF supply. This higher frequency supply, coupled with larger aperture ion optics, increased the number of ions in the ion packet for lower mass-charge molecules. The difference in number of ions between the two experiments is ∼4,000 ions/s for the high mass range configuration compared to 10,000-30,0000 ions/s for the low mass range.

In order to increase the ion density and couple the continuous beam of ions produced in the ESI source with our pulsed laser source, we have incorporated a linear hexapole ion trap after the quadrupole mass filter (Figure 2.1(5)). The linear hexapole trap was modified from the original RF hexapole collision cell in the both of the Q-ToF mass spectrometers used. This cell consists of six parallel rods connected to an RF supply of 300 kHz. The rods are surrounded by an aluminium cylindrical sleeve and capped at both ends with two stainless steel entrance and exit lenses with pinhole apertures of 3 mm. A gas line lies 5 mm behind the entrance lens and allows the cell to be filled with argon to operating pressures of up to $\sim 5\times10^{-3}$ mbar. The application of pulsed DC potentials on the entrance and exit lenses and argon pressures of 5×10^{-3} mbar allows the original hexapole ion guide to function as a linear hexapole ion trap, as first described by Chernushevich.[141] Singly charged ions enter the trap with a kinetic energy of 6.2 eV and the majority of this translational energy is removed by the application, from a bench top power supply, of a DC voltage of -5.8 V to the entrance lens. The exit lens is maintained at -3 V, which is sufficient to prevent leakage of ions from the cell from either aperture. Ions are trapped for approximately the repetition time of the experiment (for our 20 Hz experiments, this is 49.96 ms). The trap is then opened for 10–40 μs by increasing the exit lens voltage from -3 to +30 V to extract the ions, before returning to the original trapping voltage. Figure 2.4 shows a schematic of potentials on the ion trap lenses and how these change during a trapping cycle.

It is not trivial to measure the absolute ion yield[142] and calculations using SIMION[143] can be unrealistic and cumbersome; however, we are able to make an estimate. Measurements of the current produced from the continuous ion beam indicate that 9.4×10^{7} iodide

Figure 2.4: A schematic of the potentials experienced by the ions as they pass through the linear hexapole ion trap when the potential switch is off. Solid lines show the trapping potentials; the dotted lines show the extraction potentials. The dashed line shows the potential experienced by ion before it enters the linear hexapole ion trap. The vertical axis is plotted on a log scale.

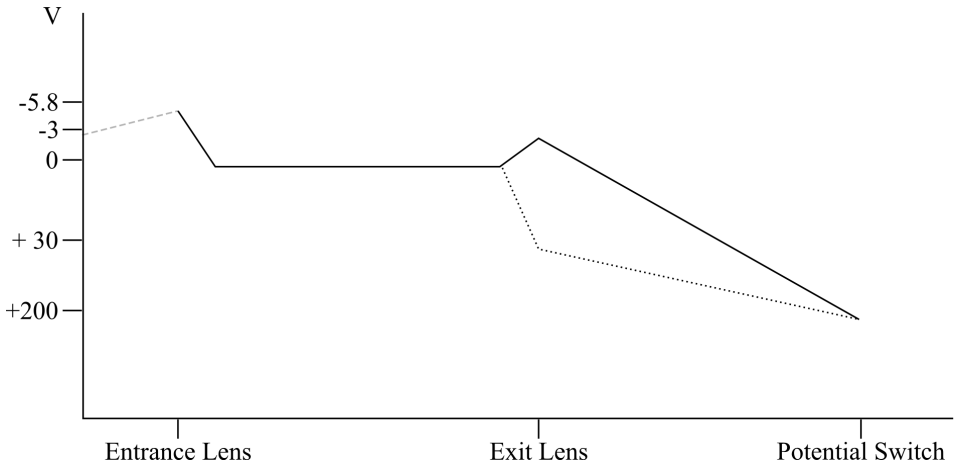

Figure 2.5: A graph showing the number of I^- anions in the linear hexapole ion trap as a function of the trapping time. The ion counts are integrated over 10 s. Dots = experimental data, solid line exponential growth, $y = 99.4 - 87.2e^{-x/7.6}$. The trap is almost at capacity after 30 ms.

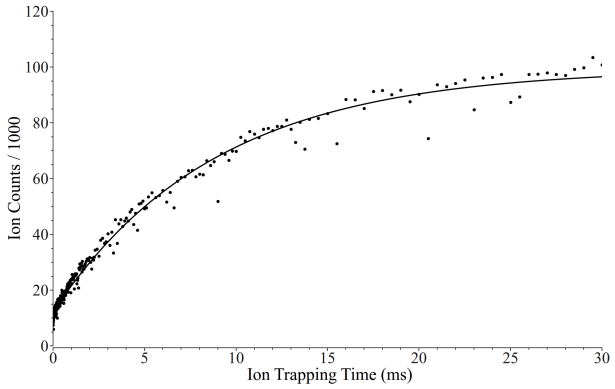

anions are produced per second and successfully transferred from the ESI source to the linear hexapole ion trap. The original developers of the linear hexapole ion trap scheme[141] and other detailed studies on linear quadrupole traps quote >95% trapping efficiency.[144] Assuming a modest trapping efficiency of 20% and a trapping cycle of 20 Hz, we estimate that for I^- anions we have $\sim 10^6$ ions in a bunch per trapping cycle.

The time taken to fill the ion trap was measured by varying the length of time that the entrance lens of the ion trap was at a potential that allowed the ions to enter the

trap (Figure 2.5). We determined that the potential required to stop ions, with collision energy 6.2 eV, entering the trap was -11 V and we confirmed that -6 V was the optimum voltage to allow these ions to pass into the trap. The trap filling time was increased in microsecond increments and the total ion signal at the VMI MCP was measured for 10 s for each data point. Figure 2.5 shows that by 30 ms the trap is beginning to approach capacity.

2.1.2 Photoelectron Imaging

We use photoelectron imaging (PEI) to record photoelectron spectra and photoelectron angular distributions (PADs) simultaneously. The ionization continuum provides a template for observing nuclear and electronic structure: the nuclear (vibrational) structure can be observed *via* Franck–Condon distributions in the PES, and the electronic structure can be observed *via* Koopman's type correlations dictate which electronically excited states of the neutral molecule are formed during the photodetachment of an electron from the anion and are distinguished by photoelectron energy. In addition, the PAD may provide complementary detail about the electronic configuration at the point of photodetachment, which allows the electronic symmetry to be determined.

In our instrument, we employ the VMI method, pioneered by Eppink and Parker[115] as a revolutionary modification of the imaging technique originally developed by Chandler and Houston.[145] Photoelectrons are accelerated in a DC electric field and imaged on a position sensitive detector. When the electrode potentials are set to values that satisfy the requirements for velocity-mapping,[115] a particular initial electron velocity will correspond to a specific position on the detector. To deduce the PES and PAD from the two-dimensional image recorded at the detector, requires the original three-dimensional PAD to be reconstructed. There are a number of methods available to do this.[119,120,122,146,147] In our group we employ an image inversion program that uses polar basis set expansion (pBASEX),[120] which deals well with the background noise which we have as a result of sending the anions and electrons along the same axis.

Figure 2.6: SIMION ion trajectory simulations of I^- in the potential switch (PS)/VMI region of the apparatus. The top and middle figures show 3D views of ion trajectories (black) when the PS is off (+200 V) and on (-1000 V), respectively. The ions are unable to overcome the repeller potential barrier when the PS is off (top), but are able to cascade into the VMI region when the PS is turned on (middle). The bottom figure is a 2D view of the ion trajectories showing how the PS focuses the ion beam in the interaction region. Repeller (R), extractor (E), and ground (G) plates are set at -870, -623 and 0 V, respectively.

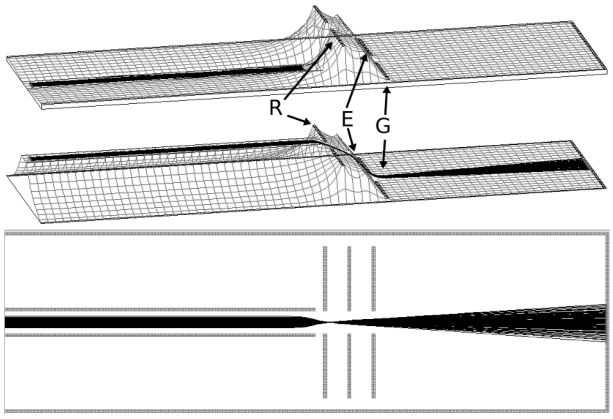

The photoelectron imaging spectrometer consists of a vacuum chamber housing a potential switch, VMI optics and a liquid nitrogen cold trap. The chamber is pumped by a 1000 l/s Maglev turbomolecular pump (Leybold MAG W1300) maintaining a background pressure of 6×10^{-7} mbar. The potential switch (Figure 2.1(5)) consists of a tube lens that is 178 mm long, 15 mm external diameter and 10 mm internal diameter. The tube lens extends to within 3 mm of the VMI repeller plate. When the PS is off, the ions are unable to overcome the potential barrier of the VMI optics, but when the PS is turned on the potential barrier is removed and the ions cascade into the VMI region (Figure 2.6).

The VMI optics are based on the Eppink and Parker design[115] and consist of a set of three polished parallel field plates (repeller, extractor, and ground) separated by 15 mm with PEEK spacers (Figure 2.1(11) and 5). Each plate has a diameter of 105 mm, with a 15 mm hole in the centre for ions to pass through. We found that the optimal voltage ratios for producing focused images were: extractor/repeller = 0.72-0.70 with repeller/potential switch = 0.87. The extractor/repeller ratio varied depending on the experiment. Only the extractor was varied to find the focus with the repeller/potential switch ratio left fixed. The potentials for the repeller and extractor plates was supplied

Figure 2.7: A schematic diagram of the velocity map imaging configuration, with dimensions. Diagram shows: (1) potential switch; (2) repeller; (3) extractor; (4) ground plates; (5) laser path; (6) ion packet; (7) MCP; (8) phosphor screen; and (9) CCD camera.

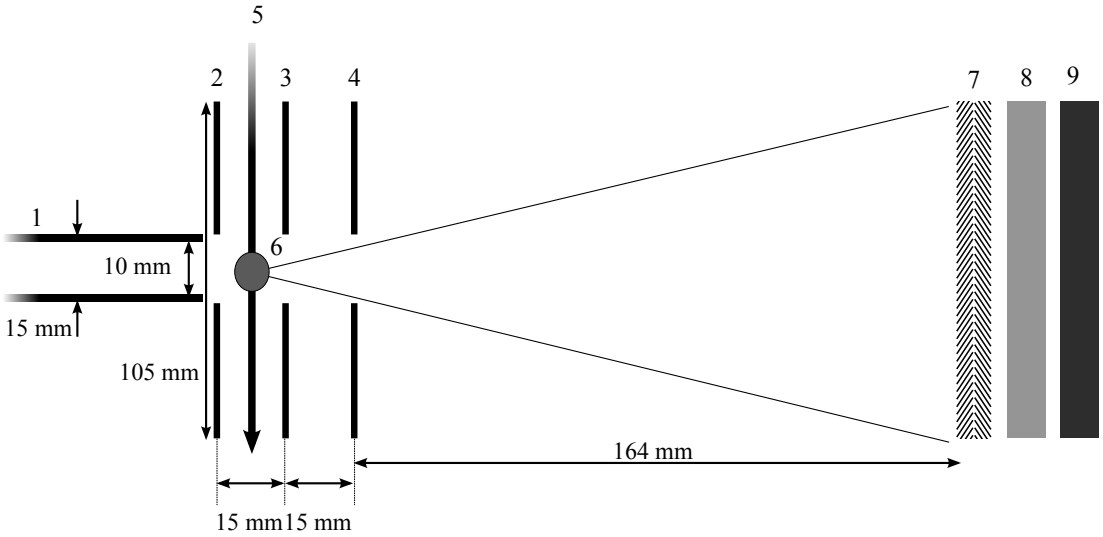

from a pair of Stanford Research Systems PS325s. The photoelectrons are accelerated through a 164 mm field-free region (surrounded by a single layer of μ-metal shielding) and collected by a commercial imaging detector (Photek, East Sussex, UK) comprising a pair of microchannel plates backed by a phosphor screen (Figure 2.1(13)) set to a potential of 4500 V. The front and rear MCPs were set to 850- and 450 V respectively, and pulsed using by applying a 500 V offset to the rear plate. A CCD camera (Basler A312f) (Figure 2.1(14)) detects the light emitted from the phosphor and the images are collected on a PC using commercial software (IFS32). The detector was gated to collect only signal from the photoelectrons, which arrive at the detector before the anions.

Ion selection, storage, and coupling with photoelectron imaging

A number of research groups have designed instruments that couple ESI with photoelectron spectroscopy.[97,148–150] Often, ion storage mass spectrometry is utilized to allow operation at repetition rates, which are convenient for use with many laser systems. Frequently, a quadrupole ion trap is inserted in the ion beam and used to accumulate ions before they are expelled, using high voltages, into the field-free region of a time-of-flight mass spectrometer, which is collinear with the ion trap. In this arrangement, referenc-

ing the ion beam to ground is impossible, *i.e.*, the time-of-flight has to be floated at a high potential, and further manipulation of the ion packet is difficult. One solution is to unload the quadrupole ion trap at low voltages and then use perpendicular ion extraction for the time-of-flight.[97] The novelty of our instrument is that, instead of using field-free time-of-flight to deliver the ion packet, we eject the ions using low voltages into a collinear PEI spectrometer. The exiting ion packet is then focused using an RF-only hexapole, steered and focussed using electrostatic *x,y*-deflectors, then re-referenced using a potential switch which allows the ions to pass into the high voltage photodetachment region of our PEI spectrometer (see Figure 2.1).

We control the ion beam (by turning on or off the Transistor-Transistor Logic (TTL) pulses that control the timing of the PS) using software that we have interfaced with the data acquisition software running on a PS. During data acquisition, half of the time is spent collecting a laser only background and the other half is spent collecting the signal resulting from the interaction of the laser with the anions. This has the advantage that we can subtract appropriate backgrounds should the laser power fluctuate. The timing of the PS and MCP triggering is optimised to reduce the ion background to an acceptable level. If this could not be obtained a complementary ion only background is also acquired, then scaled for subtraction from the signal image. The laser-only (and ion-only) backgrounds is then subtracted from the overall signal to produce a final photoelectron image.

2.1.3 Timing sequence and overall operation

Operation of the instrument requires careful synchronization of all four of the main activities: trapping and releasing the ions, switching the ion potential, overlapping the laser and ion beams, and timing the camera so that the photoelectrons are detected without the negative ion background. The master trigger in the experiment is a DG535 (Stanford Instruments) pulse generator which produces a 20 Hz pulse train for the nanosecond laser experiments. Triggers from this delay generator are sent to the laser system, the imaging electronics and a second DG535 which provides triggers for the ion trap and potential

Figure 2.8: Experimental timing sequence for I^- experiment: (1) initial trigger event (T = 0); (2) ion trap opening period (T_1 = 40 μs); (3) potential switching period (ion trap-PS delay, T_2 = 10 μs; PS on duration, T_3 = 12 μs); PS on period, T_3; (4) camera opening triggered (camera delay, T_4 = 2.1 μs); and (5) laser delay between laser triggered and detected at interaction region (T_5 = 2.15 μs). T_4 and T_5 are adjusted for each experiment.

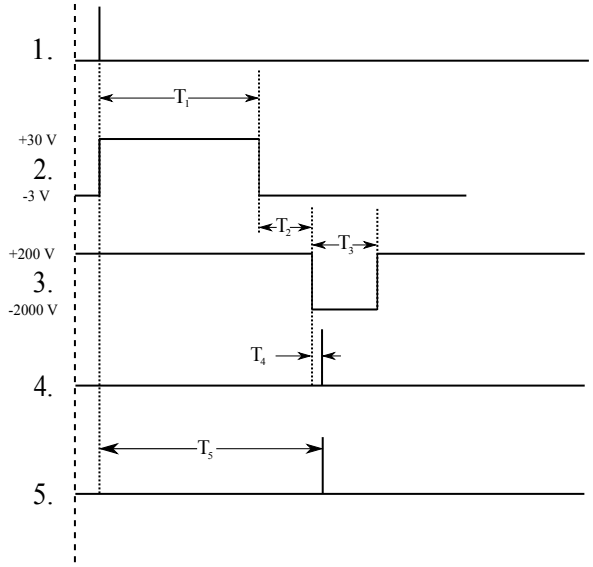

switch.

ESI provides a continuous source of ions which are subsequently trapped. Trapping allows us to maximize the ion density in our beam at the laser interaction region and allows the photoelectrons produced in the experiment to be detected with a minimal background from other negative ions. The trap opening/closing waveform is controlled by triggering a HP 8116A function generator, whose output is amplified by a Tabor wideband amplifier. The trap is opened for 10-40 μs by increasing the exit lens voltage from -3 to +30 V to extract the ions from the trap, before returning to the original trapping voltage.

Downstream, from the trap the potential switch facilitates the transfer from the low voltage mass spectrometer side of the machine into the high voltage photoelectron spectrometer. The potential switch optic is pulsed using a DEI PVX-4140 triggered by one of the DG535s. The start of the cycle begins with the potential switch at the same voltage as the final transfer optics in the mass spectrometer ($\sim$200 V) until all the ions released from the trap are contained within its volume. The potential switch is then

quickly (within 20 ns) ramped up to a high negative voltage, with the exact value depending on the absolute values of the repeller and extractor voltages required for the particular experiment being performed. The potential switch is then maintained at this voltage until the imaging cycle is complete before it is returned to its default state. The potential switch has the added advantage of providing an ion focus at the laser ion beam interaction region, as can be seen in the bottom panel of Figure 2.6.

The imaging detector is triggered after the potential switch ramped up and remains on until a few tens of nanoseconds after the laser pulse has passed through the system. This delay provides enough time for the electrons to reach the detector, but it is too short for the residual negative ions remaining in the beam to reach the detector. The laser timing can then be adjusted to maximize the overlap between the ion and laser beams. A schematic representation of all the timings is presented in Figure 2.8. Absolute values for the delays between the trap opening, the potential switch ramp, and laser beam trigger depend on the mass/charge ratio of the ion species being studied.

2.1.4 Photoelectron Imaging Spectrometer

The photoelectron velocity distribution is recovered from the two-dimensional images using pBASEX.[120] The code outputs a slice through the reconstructed 3D photoelectron distribution that gave rise to the experimental image. The photoelectron kinetic energy is proportional to r^2, where r is the distance from the centre of the image. Photoelectron spectra are then converted from a velocity to an energy distribution by multiplying the integrated photoelectron count by the $1/r$ Jacobian factor. The photoelectron angular distribution can also be obtained from the output of the pBASEX code. The PAD following one-photon ionization of an isotropic ensemble of closed shell species using plane polarized light takes the form $I(\theta) \propto 1 + \beta P_2(cos\theta)$, where θ is the angle between the laboratory frame z-axis and direction of ejection of the electron, β is the anisotropy parameter[151] and $P_2(cos\theta)$ is the second-order Legendre polynomial.

A raw photoelectron image following photodetachment of I^- is presented in Figure 2.9,

Figure 2.9: (a) Raw photoelectron image of the I^- anion at 4.61 eV, acquired for 360 000 laser shots (left), and a slice through the centre of the inverted image (right). The inner ring corresponds to 0.6 eV photoelectrons leaving iodine in the $^2P_{1/2}$ electronically excited state and the outer ring corresponds to 1.5 eV photoelectrons leaving iodine in the $^2P_{3/2}$ electronic ground state. (b) Corresponding photoelectron kinetic energy spectrum of I^- at 4.61 eV showing the $^2P_{1/2}$ and $^2P_{3/2}$ states of iodine (black line) and the anisotropy β (red line). The FWHM is ∼60 meV for 0.6 eV photoelectrons and ∼120 meV for 1.5 eV photoelectrons. (c) Raw photoelectron image of the I^- anion at 3.93 eV, acquired for 24 000 laser shots (left), and a slice through the centre of the inverted image (right). The ring corresponds to 0.88 eV photoelectrons leaving iodine in the $^2P_{3/2}$ electronic ground state. (d) Corresponding photoelectron kinetic energy spectrum of I^- at 3.93 eV showing the $^2P_{3/2}$ state of iodine (black line) and the anisotropy β (red line). The FWHM is ∼35 meV for 0.88 eV photoelectrons. The photoelectron kinetic energy spectra are normalised to the most intense point. The laser polarisation is vertical (from the top to bottom of the images).

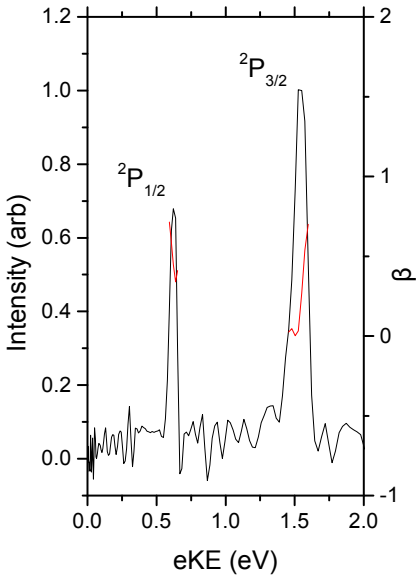

(a)

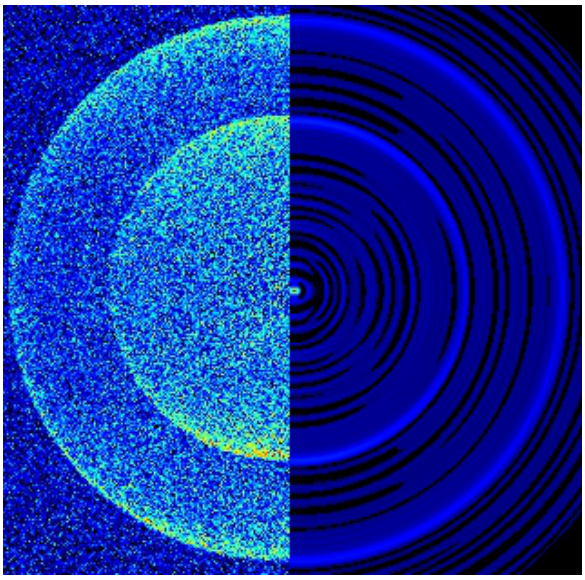

(b)

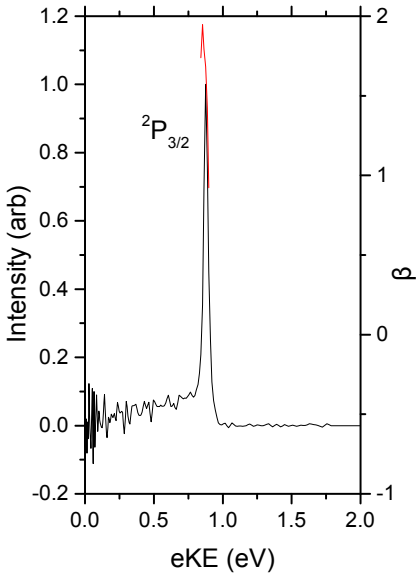

(c)

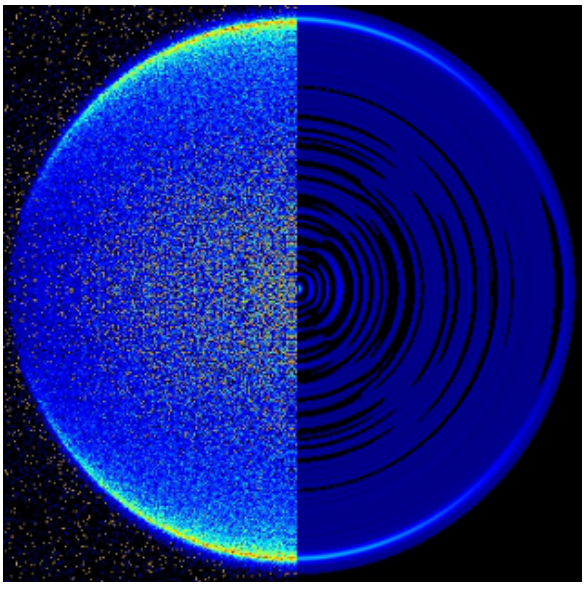

(d)

Figure 2.10: Graph showing normalised iodide photoelectron spectra taken at 315 nm acquired with different centroiding factors. Each curve is offset but normalised to the most intense point. 1× Centroiding (black), 2× Centroiding (red), 4× Centroiding (blue).

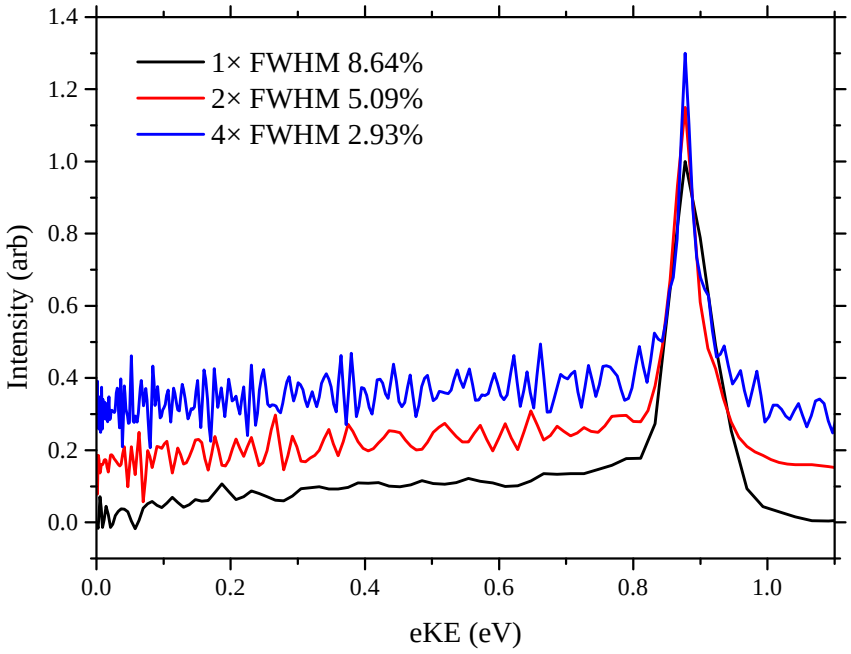

Table 2.1: A table showing the memory requirements for different pBASEX basis functions typicall used in non-centroided image inversion.

Centroiding	Legendre	Radial Bins	Azimuthal Bins	Basis Functions	Memory (MB)
1x	2	256	256	128	128
2x	2	512	512	256	1024
4x	2	1024	1024	512	8192

together with the inverted image obtained using the pBASEX program and the corresponding photoelectron spectrum. The equipment calibration was checked at least once a day before beginning a data acquisition. In later work the calibration of the equipment was checked between each change of molecule before continuing.

When necessary, images were collected using centroiding in order to increase the resolution.[152] of the experiment. Choice of centroiding factor (2×, 4×, *etc*) depends on two factors, the time required for image acquisition and the size of basis set required for the inversion.

Each increase in centroiding factor (2×, 4×, 8×) increases the size of the final image, compared to the original, by the square (4×, 16×, 64×). This means the time taken to acquire an image with similar counts across the new centroided image, compared to the original image, also increases by the square.

Figure 2.10 shows an iodide photoelectron spectrum obtained using three different factors of centroiding. The 1× and 2× spectra were acquired for the same amount of time (10 mins), the 4× spectra was acquired for twice as long (20 mins). There is a noticeable narrowing of the iodide peak from 8.6 % to 5.1 % full-width half maximum (FWHM) between the spectra acquired with 1× and 2× centroiding respectively. There is also a significant increase in the amount of noise along the low kinetic energy portion of the spectra. The effect of the 4× centroiding is also to produce a still narrower peak 3 % FWHM but also with a much more significant amount of noise. Considering the increase in resolution verses the time taken to acquire and resultant noise it was decided that 2× centroiding offered the best compromise.

One of the fundamental advantages of pBASEX over alternative algorithms is that it uses pre-generated basis functions to speed up the inversion calculation. However the validity of the inversion result depends on the number of basis functions used for an image of a given size. Using centroided images our experiments requires a larger basis set. This requirement of a new basis set presents another problem with respect to the PC memory requirements. When analysing a centroided image the memory requirements to perform the inversion are easily calculated. Table 2.1 shows the memory requirements for different basis sets, based on the recommended parameters for the pBASEX method for a non-centroided image. For the simplest image acquisition, using 1× centroiding, the computer memory requirements of basis set are not significant (128 MB). However, scaling the parameters for 2×, or 4× centroided images increases the memory requirements to 1024 MB and 8192 MB respectively. Whilst inverting a 2× centroided image would be possible on a normal desktop PC this would not be trivial for a 4× centroided image.

To overcome this, the number of azimuthal bins was decreased as the number of radial functions was decreased. This significantly reduced the amount of memory required for the inversions, as can be seen by the numbers in Table 2.2. The effect of this would be to allow us to fit the radial intensities adequately, obtaining electron velocities, at the expense of accurately

Table 2.2: A table showing the memory requirements for different pBASEX basis functions with reduced Azimuthal bins. The effect of these basis sets on inversions of centroided images can be seen in Figure 2.11.

Set No.	Legendre	Radial Bins	Azimuthal Bins	Basis Functions	Memory (mb)
1	2	512	16	256	32
2	2	512	32	256	64
3	2	512	64	256	128

Figure 2.11: Graph the effect of using different sized basis sets to invert an iodide image at 315 nm using pBASEX. Sets correspond to those presented in Table 2.2. Each curve is offset but normalised to the most intense point.

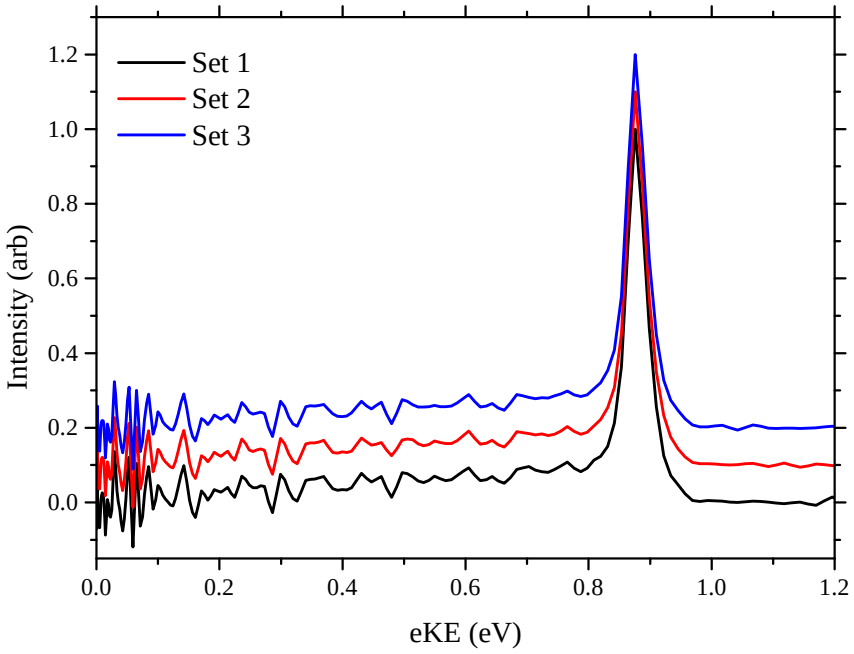

fitting the anisotropy in the image. As most of the data we have collected shows no anisotropy this was deemed to be an acceptable cost. As can be seen in Figure 2.11 a reduction in the number of azimuthal bins has no significant impact on the inverted iodide energy spectrum.

Some of our images possessed a distortion due to an imperfection in the alignment of the potential switch with the VMI field plates, causing a distortion of the focussing fields in the interaction region. To avoid this distortion broadening our spectra, the image was analysed in quarters. Each quarter was analysed separately to see which provided the smallest FWHM whilst maintaining a circular image. In those experiments with distorted images this was found to be the bottom left quarter.

Figure 2.12: Uncertainty in energy calibration of an inverted VMI image.

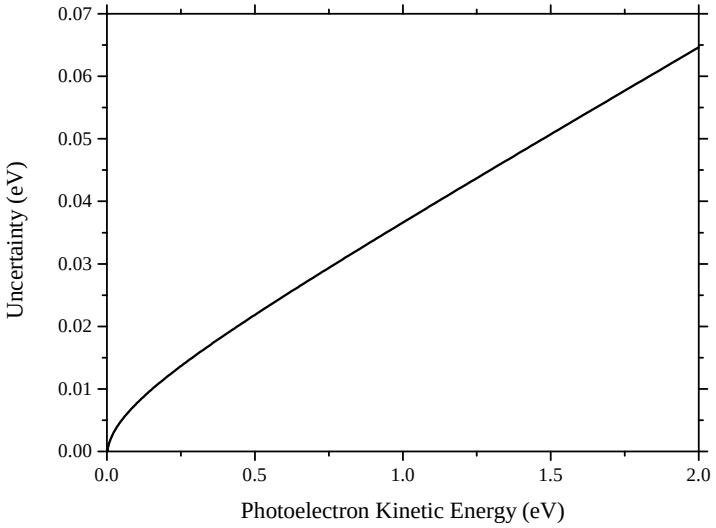

The resolution of the photoelectron imaging detector is defined in terms of the resolution of the photoelectron velocity, Δv. Since the photoelectron kinetic energy $\propto v^2$, the energy resolution is higher for the lower kinetic energy photoelectrons. Figure 2.9b illustrates the resolution of the instrument. The I^- photodetachment spectrum shows two clear peaks centred at 0.6- and 1.5 eV, corresponding to the $^2P_{1/2}$ and $^2P_{3/2}$ spin-orbit states of the neutral iodine atom. The $^2P_{3/2}$ peak appears broader due to the decreased resolution of the instrument at higher photoelectron kinetic energies: for our imaging detector the peak width is ∼60 meV for 0.6 eV photoelectrons and ∼90 meV for 1.5 eV photoelectrons. The bandwidth of the nanosecond laser pulses is ∼0.05 cm^{-1} (0.006 meV) which is less than the resolution of the PEI spectrometer.

Uncertainties in VMI data analysis can come from three areas, uncertainty in photodetachment energy of you calibration molecule, laser wavelength and inversion centre choice. The uncertainty in the photodetachment energy of I^- has been measured to be 3.0590±0.0001 eV[153] and the uncertainty wavelength of the photodetachment laser in our experiment is 0.0002 nm, measured using the WS-7 Wavemeter.[154] This leads to an error in the kinetic energy of the photodetatched electron of 0.0001 eV across 315-364 nm.

The pBASEX image inversion algorithm requires the centre of the acquired image to be chosen. As this is done by eye so there is the possibility of incorrectly choosing the appropriate centre. This is procedure is performed twice; once for the calibration image and once for the

Figure 2.13: Figure showing the photodetachment spectrum of o-Coumaric acid measured at 315 nm (black) with example measurements of peak maximum, FWHM, and threshold fitting lines (red).

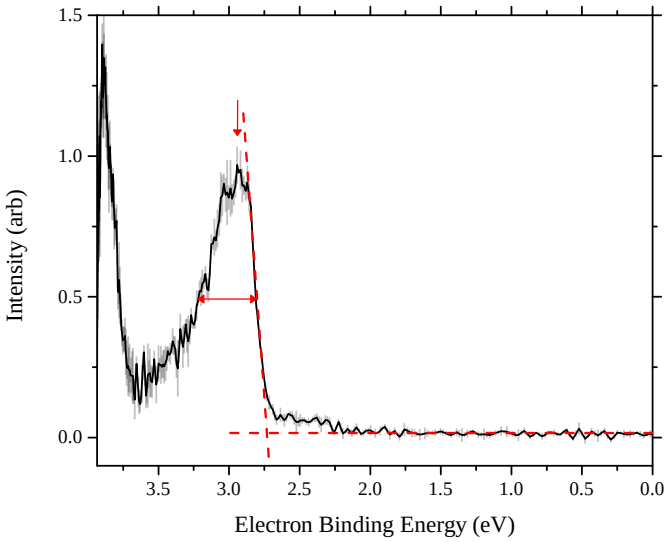

image of the molecule of interest. The suitability of a chosen centre point is firstly done by eye as the inverted calibration spectra will show a poorly resolved broad peak, secondly the FWHM of the I^- peaks are compared and the narrowest is assumed to be the most appropriate centre. Our experience shows that anything more than a few pixels off can significantly impact the inverted spectra, so a conservative error of ± 5 pixels is chosen as the possible error in choosing the centre. The conversion of spectra from a velocity to an energy scale causes the associated error along the x-axis to be non-uniform, the largest errors occur further away from the zero. For example, the expected error due to calibration and inversion is 0.065 eV at 2.000 eV when using $2\times$ centroiding and a 315 nm laser. Figure 2.12 shows the non-uniform nature of the uncertainty across the x-axis due to the conversion from velocity to energy.

Earlier experiments acquired VMI images for approximately 20 minutes, these images were summed together into a single image in order to obtain the final image which would be inverted to produce a spectrum. This was the technique used for the data presented in Chapters 3. In later acquisitions each image was still acquired for approximately 20 minutes but each image was saved separately and over a typical experimental acquisition 3-5 images would be collected. Each image would be inverted based on an iodide calibrations measured before the experimental

acquisitions begun. The resulting spectra would be compared to produce a mean and standard deviation for the intensity value at each radial position. The result of this analysis can be seen as the faint lines on Figure 2.13 and the data presented in Chapters 4 and 6.

The error in peak maxima was found by first identifying the point with greatest intensity in a given region. Once identified, adjacent data points were inspected to find alternative data points who standard deviation would also place them at the same intensity. The data point which was the furthest away was then taken as the uncertainty in the intensity maximum. The error in the FWHM of a peak was determined by first finding the FWHM at the most intense data point. The corresponding FWHM was then found for standard deviation maximum and minimum of the most intense data point.

The spectra measured using our equipment is usually unable to resolve vibrational features of the detachment spectra without vibrational resolution our ability to assign unequivocally the ADE of our molecules of interest is difficult. Therefore, we attempt to assign a lower limit instead and accomplish this by measuring the threshold of the rise in the first photodetachment peak of a molecule. To accomplish this we perform two separate linear fits one of the background at high kinetic energies and the high kinetic energy edge of a photodetachment peak, the intercept of these two linear fits provides the threshold. The standard deviation of each intensity data point is used as a weighting factor in the linear fits. The final uncertainty of the intercept is a combination of the uncertainty of the two linear fits, along with the systematic uncertainty from the experiment.

The photoelectron count-rate is ∼10 kHz and this value can be used to estimate the number of anions in the laser interaction region: $\text{count} - \text{rate} = \sigma N l F$, where σ is the photodetachment cross section, N is the anion number density, l is the interaction length, and F is the photon flux. Assuming 5 mJ of weakly focused 315 nm radiation ($F = 7.91\times10^{15}$ photons/pulse), a photodetachment cross section of $\sigma \approx 10^{-17}$ cm^2,[155] and an interaction length of $l \approx 15$ mm, we can calculate that the anion number density must be $N \approx 4200$ anions/cm^3 for a count-rate of 175 Hz (ion pulsing operating at 20 Hz). If the laser interaction volume is ∼0.25 cm^{-3}, the number of anions in the laser interaction region is ∼1000.

Figure 2.14: A schematic diagram showing the 315–364 nm (top) and 210 nm beam lines (bottom). (M) Aluminium mirror; (P) Periscope; (DM) Dichroic mirror; (BD) Beam dump; (L) Lens; (BBO) β-barium borate crystal; (KDP) potassium dihydrogen phosphate crystal.

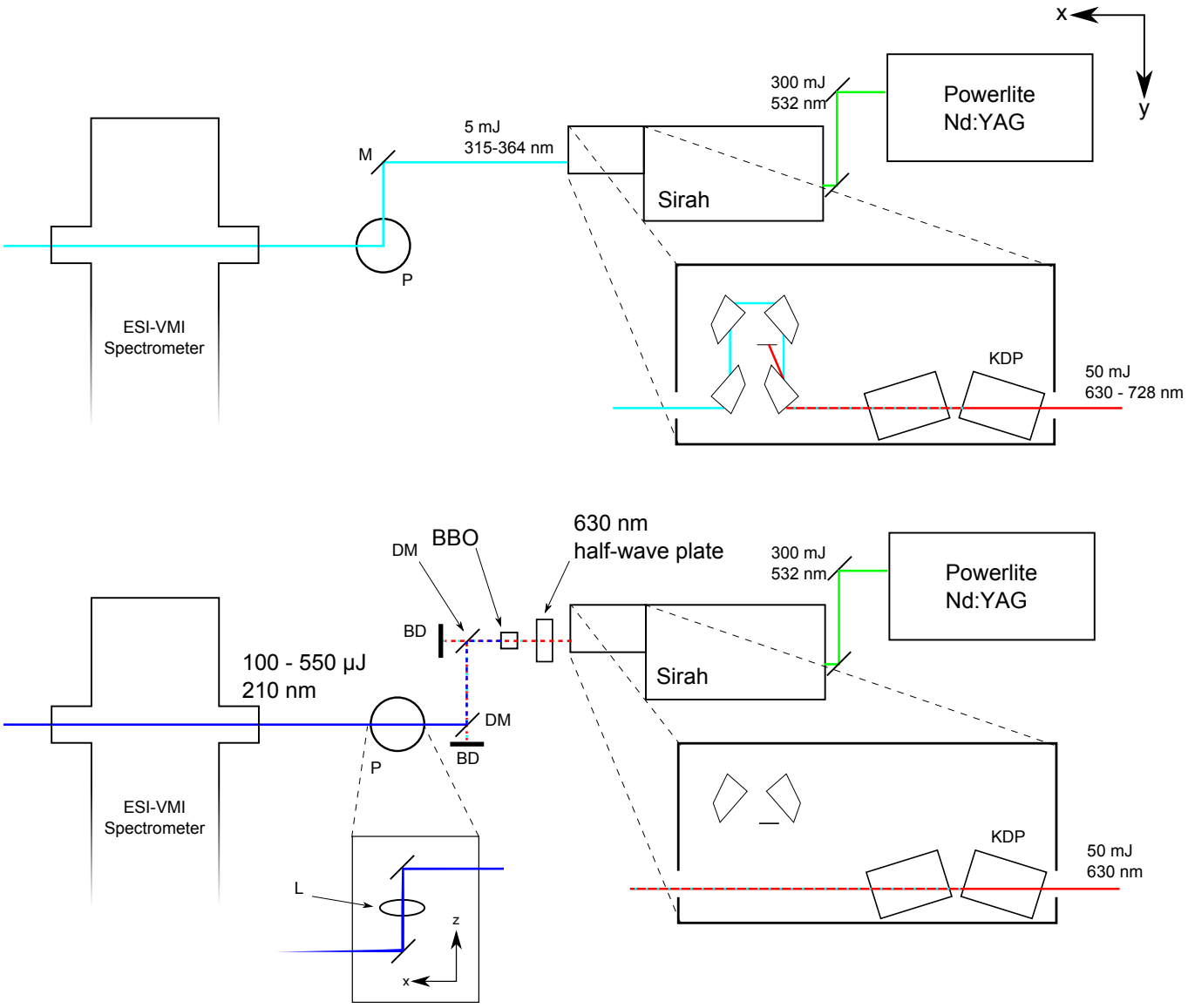

2.1.5 Nanosecond Lasers

The photodetachment spectra presented in Chapters 3, 4 and 6 were recorded using a combination of nanosecond laser configurations to generate 210 nm, 269 nm, 315–328 nm and 350–364 nm. All laser wavelengths were measured to within 0.2 pm using an interferometer based wavelength meter (SNIIMS Type WS).

The 315–328 nm and 350–364 nm ranges were produced using the same optical setup and equipment. To generate 315–328 nm and 350–364 nm, DCM and pyridine 2 laser dyes in

methanol were used, respectively. A schematic of both beam lines is shown in Figure 2.14. First, 300 mJ from the 2nd harmonic of a Nd:YAG (Continuum Powerlite 8020) was used to pump a Sirah (Cobra-Stretch D-24) dye laser to produce 50 mJ of 630–728 nm light. This was then frequency doubled using a potassium dihydrogen phosphate (KDP) crystal to produce either ∼5 mJ of 315–328 nm or 350–364 nm, depending on the dye used, with a pulse duration of ∼6 ns. The doubled light was then separated from the fundamental using a set of Pellin-Broca prisms. A vertical laser polarisation (perpendicular to the laser table) was required for our experiments so the electric field of the light is parallel to the plane of the VMI detector. To obtain the correct laser polarisation, the doubled light was sent through a periscope assembly with the mirrors orientated at 90° to each other. The linewidth of the Sirah dye laser is quoted as 0.181 cm^{-1}, equivalent to ∼0.022 meV which is less than the resolution of our detector.

A similar set up was used to generate 210 nm light with some modifications and additions. First, 300 mJ from the 2nd harmonic of the Nd:YAG was used to pump the Sirah dye laser to produce ∼50 mJ 630 nm light. This was then frequency doubled using a KDP crystal. Two of the Pellin-Broca prisms were removed so that the frequency doubled and fundamental light remained co-axial. Both beams were passed through a 630 nm waveplate to rotate the 630 nm light to a vertical polarisation to match the frequency doubled light before mixing. Both beams were then mixed in a β-barium borate (BBO) crystal to produce ∼100–500 μJ 210 nm light, with a pulse duration of ∼6 ns. To filter out the 210 nm light from the two residual beams the optics in rest of the beam line, up to the chamber, were dichroic mirrors optimised for 200 nm. The mixing process produced 210 nm light with vertical polarisation appropriate for our experiment. The 210 nm light was focussed before entering the chamber to minimise laser background. This was achieved by placing a lens (100 mm focal length) between the periscope mirrors.

The 269 nm light was created in a two-step process. A schematic of the beam line can be seen in Figure 2.15. First, 230 mJ of the frequency-doubled output of the nanosecond Nd:YAG laser, operating at 20 Hz, was used to pump a dye laser (Continuum ND6000) operating with fluorescein 548. This produced laser pulses at 544 nm, pulse energy ∼15 mJ, and pulse duration of ∼6 ns. The output from the dye laser was then mixed with 20 mJ of the 532 nm radiation from the Nd:YAG laser in a BBO to create pulses at ∼269 nm with pulse energy of ∼4 mJ. The

Figure 2.15: Schematic diagram of 269 nm beam line. (M) Aluminium mirror; (P) Periscope; (DM) Dichoric mirror; (BD) Beam dump; (L) Lens; (BBO) β-barium borate crystal.

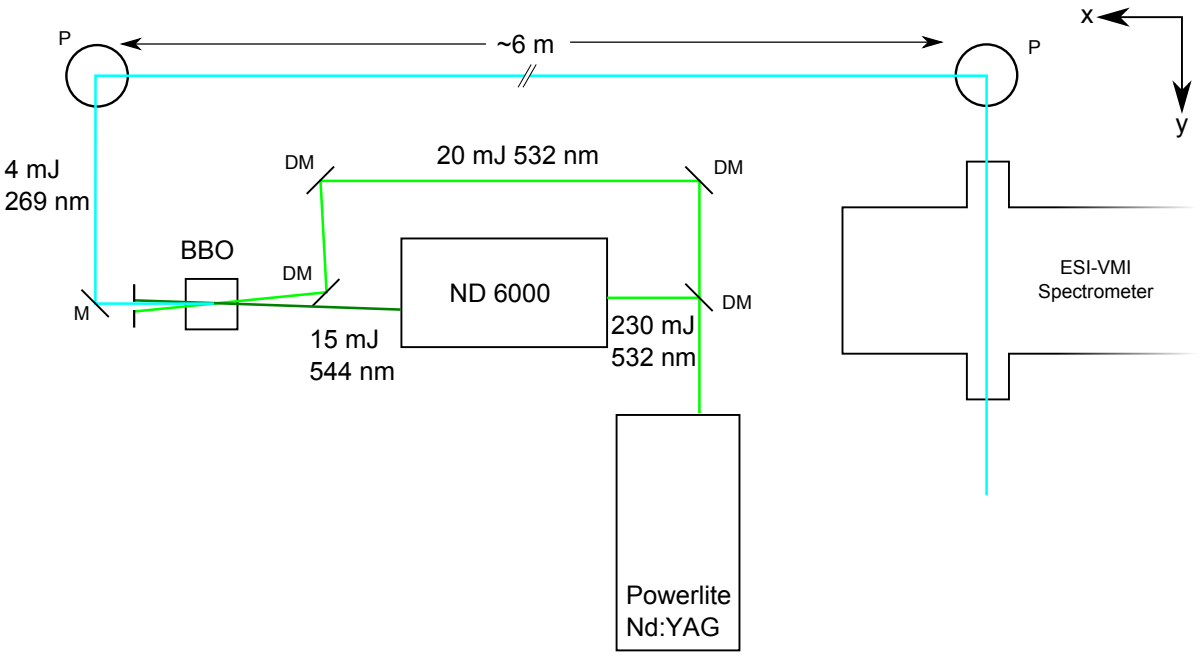

laser power at the apparatus was ~0.9 mJ per pulse. The linewidth of the Sirah dye laser is quoted as 0.08 cm^{-1}, equivalent to ~0.010 meV which is less than the resolution of our detector.

2.2 Conclusions and perspectives

We have developed a new and versatile photoelectron imaging instrument for investigating the spectroscopy and dynamics of anions in the gas-phase. There is increasing interest in obtaining photodetachment energies of species that can be placed in the gas-phase using electrospray ionization, and we anticipate that our instrument will provide new and exciting research opportunities to investigate not only anions of biological interest, but also other species that can be taken from the solution phase (organic and inorganic anions).

We also have plenty of opportunities to increase the versatility of the instrument. Ultimately, our aim is to use this instrument, not only for isolated biological chromophores, but also to study chromophores within their native proteins that require non-covalent interactions to maintain their structure. This is the reason for the modified RF supply of the Ultima API Global allowing it to operate at a reduced frequency of 300 kHz extending the mass range of its quadrupole

filter from 4000 to 32000 m/z. Conventional ESI is not well suited to preserving non-covalent interactions: the generation of ions requires the surface tension of the solvents to be overcome and evaporation of the droplets produced requires heat or high flow rates of curtain gas, both of which serve to disrupt fragile interactions. To solve this problem our instrument already has a nanospray electrospray ionisation (nanoESI)[156,157] capability. NanoESI uses borosilicate or quartz capillaries, with tip orifice diameters of around 1-4 μm, which are made conductive by coating with gold, or inserting a thin metal wire down the length. A lower voltage of $\sim$1.5 kV is applied to generate an electrospray and a backing gas is used to initiate the flow. The flow rate in nanoESI is approximately 20 nl min^{-1}, two orders of magnitude lower than that used in ESI; this low flow rate allows long analysis times from small volumes of sample ($\sim$30 mins from 1-5 μl). NanoESI offers more than just the advantages of a low flow source, the smaller droplets produced (<200 nm in diameter) easily evaporate generating ions. This negates the use of heating or high flow rates of curtain gas and facilitates the use of solutions with higher surface tensions, such as water and aqueous buffers, allowing proteins to remain 'native-like' in conformation, and thus preserving the non covalent interactions.

Another of our aims is to employ time-resolved photoelectron spectroscopy to study the ultrafast dynamics of biological chromophore anions, as isolated species and in their native protein environments.

Chapter 3

Photodetachment spectroscopy of biological chromophore anions

3.1 Introduction

As a result of GFPs importance in the life sciences, there have been numerous spectroscopic and theoretical studies focused on improving our understanding of the photochemistry and photophysics of GFP, and its analogues;[23,158,159] however, there are still unanswered questions. For example, there is still some debate surrounding the interpretation of photo-destruction action spectra,[37,39,160,161] and until recently,[40,41] the photodetachment energy had not been measured directly, despite its being crucial in determining whether anionic chromophores of fluorescent proteins can function as light-induced electron donors.[45,162] To address this, we have recorded photodetachment spectra of the isolated GFP chromophore anion and of one of its analogues to determine VDEs and to estimate ADEs.

Wild-type GFP displays two absorption bands around 395 and 480 nm, ascribed to the neutral and deprotonated anionic forms of the chromophore, respectively.[8,23] Excitation of either form results in fluorescence at 508 nm, originating from the anionic chromophore (the neutral form deprotonates upon excitation).[23,25] The fluorescence of GFP is lost when the protein is denatured, but it is recovered when refolded.[163] Furthermore, the chromophore of GFP has been found to be non-fluorescent in solution[163] and in the gas phase[38] but to show strong

Figure 3.1: Structures of model GFP (a) and CFP (b) chromophores.

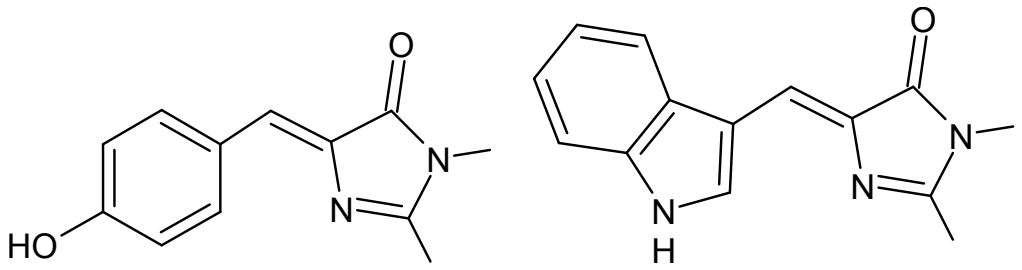

(a) (b)

fluorescence when cooled to 77 K.[163] Fluorescence of the chromophore occurs when efficient non-radiative decay through fast internal conversion is prevented[164] at low temperatures or by the protein environment.

The environment of the chromophore in the protein is crucial in defining its optical properties. The absorption bands of the model chromophore pHBDI (Figure 3.1a) in solution are shifted with respect to those observed in the protein, irrespective of the solvent.[54] However, investigations of the deprotonated anion of the model GFP chromophore in the gas phase using photo-destruction action spectroscopy in the ELISA found the maximum of the absorption band to be 479 nm (2.59 eV), which is remarkably close to the absorption maximum of wild-type GFP.[37] This led to the suggestion that the protein environment of the chromophore is very similar to the gas phase and that the electronic structure of the chromophore is not modified significantly by interactions with surrounding amino acid side chains or water molecules. Subsequent photo-destruction spectra of isolated deprotonated chromophore anions in a modified quadrupole ion trap recorded a maximum in the absorption spectrum around 482.5 nm (2.57 eV), similar to the ELISA measurements.[38] These results were interpreted in terms of $S_1 \leftarrow S_0$ excitation in addition to a contribution from direct photodetachment. Electronic structure calculations suggest that the protein environment has a relatively small effect on the excitation energy of the bright absorbing state and lowest-lying triplets, but that it results in a significant increase in the vertical detachment energy.[48]

An interesting class of GFP analogues is the CFPs. In CFPs, the tyrosine amino acid at position 66 is mutated to tryptophan, which results in an indole group replacing the phenol group in the neutral chromophore (Figure 3.1b). This substitution modifies the absorption and

emission properties of the proteins, which are also influenced by changes in the amino acid residues interacting with the chromophore in the protein. One of these analogues, labelled W7, has a broad absorption band with two maxima, at 434 and 455 nm, and a broad fluorescence band with a strong emission around 476 nm and a weaker emission around 505 nm, that is, blue-shifted with respect to GFP.[8] It is believed that these absorption features originate from the neutral and anionic (deprotonated) forms of the chromophore, with a mechanism analogous to that shown by GFP. No explanation has been provided so far for the double emission. The gas-phase investigation of the model deprotonated anionic chromophore of CFP showed that it absorbs at 459 nm (2.71 eV), which is very similar to one of the absorption maxima of analogue W7, and led to the lower energy absorption of W7 being assigned to the anionic form.[165]

It is important to obtain detailed spectroscopic information for isolated fluorescent protein chromophores if we are to understand fully the processes that determine the specific characteristics of various analogues and to evaluate correctly the role of the protein environment. Moreover, the information yielded by gas-phase experiments on isolated chromophores provides important benchmarks for electronic structure calculations.[36,42,45,46,166] A detailed understanding of the electronic properties of fluorescent proteins and their chromophores is an essential first step toward designing efficient fluorescent proteins for specific roles. For example, photodetachment has been proposed as a channel for deactivation of the electronically excited deprotonated GFP chromophore anion in the gas phase, which theory has predicted to lie above the vertical photodetachment energy.[42] It has been proposed that this deactivation channel is related to the potential for GFPs to behave as light-induced electron donors in the presence of suitable electron acceptors.[162] Donation of electrons from GFPs following illumination with blue light at 488 nm is associated with photoconversion to a red-fluorescence-emitting state, which is referred to as oxidative redding.[162] A different photoconversion process that also results in red fluorescence of GFP under anaerobic conditions has also been reported.[167,168] This anaerobic redding was observed to be enhanced when UV light was used to induce photoconversion. Neither of these photoconversion processes has been explained at the molecular level, although a possible mechanism for oxidative redding involving the anionic GFP chromophore, its doublet radical (singly oxidized species), and cation (doubly oxidized species) has been proposed.[45] Bodganov *et al.* suggested that anaerobic redding may involve a radical chromophore of GFP.[162] Although

it has been found that a large variety of GFPs undergo oxidative redding, the cyan and blue analogues possessing chromophores in which tyrosine66 has been replaced by tryptophan or histidine, respectively, do not exhibit this photoconversion process.[162]

In the work presented in this chapter, we have employed photoelectron spectroscopy to measure the photodetachment energies of the deprotonated anions of both the GFP and CFP chromophores presented in Figure 3.1. To benchmark our measurements for these fluorescent protein chromophore anions and as a step toward understanding the differences arising from the chemical nature of the chromophores, the deprotonated phenol and indole anions have also been investigated.

3.2 Methods

3.2.1 Experimental Section

The photodetachment spectra are plotted as a function of eKE and electron binding energy (eBE): eBE = hν – eKE. The VDE for anionic systems is the energy required to remove an electron without any geometric change between the anion and the resulting neutral species, and it is usually taken to correspond to the eBE value at the maximum intensity in each photoelectron band. The adiabatic electron affinity (EAa) (or adiabatic photodetachment energy) is the energy difference between the lowest vibrational state of the neutral species and the lowest vibrational state of the anion. Extracting an accurate value for EAa from a photodetachment spectrum requires vibrational resolution. In an unresolved photoelectron spectrum, the upper limit for EAa is the VDE, and lower limits for EAa have been approximated by estimating the onset of the photodetachment signal[169] or by fitting a straight line through the high eKE edge of the unresolved peak.[170] In this work, we estimate values for EAa by modeling the photodetachment spectra and fitting to the measured VDE.

3.2.2 Computational

Density-functional-based electronic structure calculations of the deprotonated anions and their corresponding neutral radicals were carried out using the GAUSSIAN09 package.[124] Geometries

were optimized using the Meta-generalized Gradient Approximation (GGA) hybrid functional TPSSh[171] together with the 6-311++G** basis set. The vertical photodetachment energies were determined from an EPT calculation of correlated ionization with the aug-cc-pVDZ basis set on the optimized geometries of the anions. The suitability of the computational methodology was judged by employing a variety of functional forms and comparing them with our experimental data, details of which are provided in the Appendix B.

We estimate the EAa associated with the $D_0 \leftarrow S_0$ process in all chromophores by modeling the photodetachment spectra at 300 K using the program EZspectrum.[172] As input for this program, we used the *ab initio* optimized geometries of the anion and radical in their ground electronic states, and their frequencies and normal mode vectors were calculated at the TPSSh/6-311++G** level, details of which are provided in Appendix B.0.1. We determined the value of EAa by fitting the calculated vertical detachment energy to the experimental value. Assuming that the uncertainty in our experimental VDE values (±0.1 eV) is significantly larger than errors in the frequency calculations (±0.02 eV), we expect the error in EAa to be around 0.1 eV. This method was benchmarked for phenol. Using the experimental electron affinity of 2.253 eV,[173] our calculated VDE is 2.30 eV, which is in good agreement with our experimental value of 2.37±0.10 eV determined from the photoelectron spectrum recorded at 269 nm (4.61 eV) (see below and Figure 3.3).

3.3 Results and Discussion

Photoelectron spectra of deprotonated model GFP and CFP chromophore anions are presented in Figure 3.2. The photoelectron spectrum of the deprotonated model GFP chromophore has been recorded at both 269 nm (solid line) and 330 nm (dashed line). Both exhibit a strong asymmetric feature centered around 2.85 eV eBE, corresponding to photodetachment from the electronic ground state of the anion to the electronic ground state of the neutral radical. The VDE is measured to be 2.85±0.10 eV following photodetachment at 269 nm (4.61 eV) and has a value closer to 2.90 eV following photodetachment at 330 nm (3.76 eV). In the 269 nm spectrum, we also observe a second peak that is centered around 4.08±0.10 eV eBE, which is attributed to the first excited electronic state of the neutral radical. This peak is relatively broad, suggesting

that there is a larger geometry change between the ground electronic state of the anion and the first electronically exited state of the radical than there is between the ground electronic state of the anion and the ground electronic state of the radical. The energy difference between the ground and first excited states of the neutral deprotonated GFP chromophore radical, at the equilibrium geometry of the ground state of the anion, is 1.23±0.20 eV.

The photoelectron spectrum of the deprotonated CFP chromophore shows some similarity to that of the deprotonated GFP chromophore. It has a strong feature around 2.9 eV eBE arising from photodetachment from the electronic ground state of the anion to the electronic ground state of the neutral radical. The VDE is measured to be 2.88±0.10 eV following photodetachment at 269 nm (4.61 eV). We observe a second peak that is centered around 3.96±0.10 eV eBE, corresponding to the first electronically excited state of the neutral radical. We also see the start of a third peak in the photoelectron spectrum at around 4.5 eV, corresponding to the second electronically excited state of the neutral radical. We cannot determine the VDE of this state. The energy difference between the ground and first excited states of the neutral deprotonated CFP chromophore radical, at the equilibrium geometry of the ground state of the anion, is 1.08±0.20 eV.

The assignments of the features in the photoelectron spectra of the model deprotonated GFP and CFP chromophore anions are supported by *ab initio* calculations. The VDEs are reasonably well predicted by single-point EPT/aug-cc-pVDZ calculations on the TPSSh/6-311++G** optimized geometries (Table 3.1). Average errors for this type of calculations are around 0.25 eV.[174]

For the deprotonated GFP chromophore anion, our calculations yield a VDE of 2.592 eV, which is in reasonable agreement with our measurements. Higher-level calculations predict a VDE of 2.54 eV.[42,45] Our measured VDE lies within the range of possible values predicted by photo-destruction action spectroscopy.[38] In fact, the inferred electron detachment spectrum obtained from a photodissociation action spectrum recorded by Forbes and Jockusch[38,39] shows some similarity to our spectrum. In the action spectrum, there are two overlapping peaks: a sharp peak whose maximum lies at 482.5 nm (2.57 eV) and a broad peak that appears to extend from 465 to 400 nm (2.67 eV – 3.1 eV) with a maximum around 450 nm (2.8 eV). Comparison with our data suggests that the broad peak with a maximum around 2.8 eV might correspond to photodetachment to the ground electronic state of the neutral radical. The sharp peak with

Figure 3.2: Photodetachment spectra of the deprotonated model GFP chromophore anion (top) at 269 nm (4.61 eV) (solid line) and 330 nm (3.76 eV) (dashed line) and the photodetachment spectrum of the deprotonated model CFP chromophore anion (bottom) at 269 nm (4.61 eV). The vertical lines are the spectra calculated using ezSpectrum (see text), and the solid red line is the result of convolution with a Gaussian FWHM of 0.3 eV. (The background signal is set to zero and spectra are normalized to the most intense data point. The solid line is a moving average of data points. The scale of the electron kinetic energy corresponds to the spectra recorded at 269 nm (4.61 eV).)

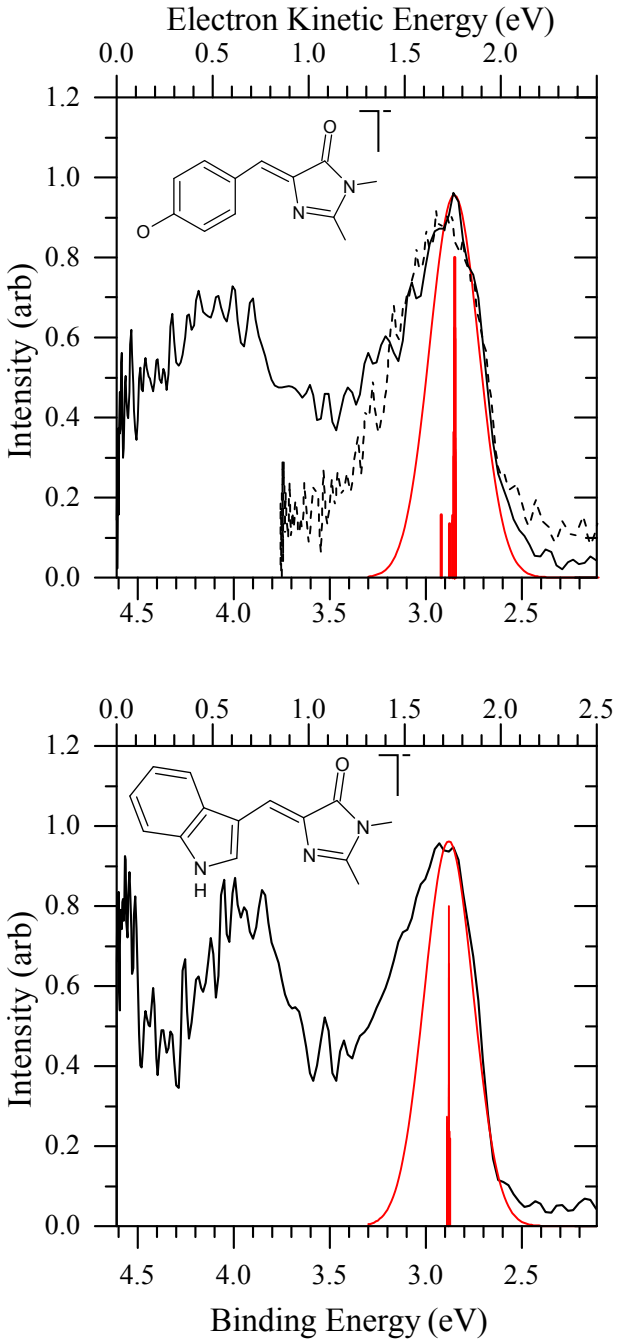

a maximum at 2.57 eV is assigned as the $S_1 \leftarrow S_0$ transition of the anion. Our VDE is also similar to two other recent measurements.[40,41]

For the deprotonated CFP chromophore anion, NMR spectra revealed the presence of two isomers: cis and trans about the exocyclic C=C double bond.[175] As confirmed by additional NMR measurements both isomers show a trans configuration about the exocyclic C–C single bond (cis–trans-CFP and trans–trans-CFP in Figure B.1 in Appendix B).[175] These isomers coexist in an 8.2:1 ratio in methanol-d_4 solution favouring the cis–trans isomer. Thus, we ran EPT calculations for the deprotonated anions of both cis–trans and trans–trans isomers of CFP, which gave VDEs of 2.598 eV and 2.608 eV, respectively, in reasonably good agreement with our experimental value (see Table 3.1).

The photoelectron spectra for deprotonated GFP and CFP chromophore anions were simulated using ezSpectrum[172] and plotted in Figure 3.2 as stick spectra. These were convoluted with Gaussians with FWHM = 0.3 eV (determined by benchmarking this method against the photoelectron spectrum of the deprotonated phenol anion) to fit the low eBE edge of the experimental photoelectron spectra (see Figure 3.2) and used to determine EAa. Using this procedure, the EAas are estimated to be 2.80±0.10 eV for GFP and 2.88±0.10 eV for CFP. Unlike the photodetachment spectrum for phenol (see below), well-resolved vibrational progressions are not predicted by the simulations for either deprotonated chromophore anion. The difference between the simulated VDE (spectral maximum) and EAa is only 0.05 eV for GFP with our level of calculation, which considered only limited excitations of vibrational modes within a harmonic approximation. Sophisticated high-level calculations place the VDE – EAa difference at 0.15 eV.[45] If we consider this VDE – EAa difference, the estimated value for EAa would be 2.70±0.10 eV for the deprotonated GFP chromophore anion. In either case, the value for EAa is greater than the $S_1 \leftarrow S_0$ excitation energy predicted from photo-destruction spectra.[39]

In contrast to the calculated spectra, the peaks in the experimental photodetachment spectra corresponding to $D_0 + e^- \leftarrow S_0$ are asymmetric for both GFP and CFP deprotonated chromophore anions. The peaks rise more steeply on the low eBE side then fall gently on the high eBE side (see Figure 3.2). One possible explanation for this is that there is a competing population of vibrationally excited states of higher electronically excited states of the anion, which subsequently undergo IVR, followed by autoionization, or even IC to the dense mani-

Table 3.1: Experimental and calculated photodetachment energies of the deprotonated chromophore anions (eV). [a]eBE at maximum electron intensity in the photoelectron spectra (Figures 3.2 and 3.3). [b]Determined by single-point EPT/aug-cc-pVDZ calculations on the TPSSh/6-311++G** optimized geometries of the anions. [c]Cis and trans refer to the exocyclic double bond; they are cis–trans and trans–trans isomers in Figure B.1 in Appendix B

	VDE		
Chromophore	experiment[a]		theory[b]
GFP	2.85±0.10		2.592
CFP	2.88±0.10	cis[c]	2.608
		trans	2.598
Phenol	2.37±0.10		2.177
Indole	2.58±0.10		2.43

fold of vibrational states belonging to lower electronically excited states, followed by IVR and autoionization.

The profiles of the peaks corresponding to $D_0 + e^- \leftarrow S_0$ in GFP are also different for the photoelectron spectra recorded at 269 (4.61 eV) and 330 nm (3.76 eV): the low eBE sides of the spectra look the same, but the high eBE side falls more rapidly in the 330 nm spectrum. The second excited state of the isolated GFP chromophore anion has been predicted to lie around 4.38 eV,[43] so it is possible that competing excitation of the second excited state, with subsequent IC/IVR or IVR, and then autoionization is the cause of the increased photoelectron signal on the high eBE side of the peak in the 269 nm spectrum. It is worth noting that because the low eBE sides of both peaks fit the profile obtained by convoluting the calculated photoelectron spectrum with a Gaussian FWHM = 0.3 eV, it is unlikely that single-photon resonances with electronically excited states of the neutral radical are having any effect on the photoelectron spectrum. The best fit of the profile to both spectra is obtained when the modeled spectrum is centered at 2.85 eV, so our best estimate of the VDE for the deprotonated GFP chromophore anion is 2.85±0.10 eV.

The anionic GFP and CFP model chromophores employed in this work can be considered as consisting of two moieties: an imidazolinone unit and a phenol (GFP) or indole (CFP) unit. To gain insight into the chemical nature of the photodetachment process in the fluorescent protein chromophore anions, we have also recorded photodetachment spectra of the deprotonated phenol and indole anions. Their photoelectron spectra are presented in Figure 3.3. The spectra are

very similar: each has a relatively narrow, intense peak at lower eBE and a broader peak at higher eBE. The sharp peaks correspond to detachment from the electronic ground state of the deprotonated anion to the electronic ground state of the neutral radical, and the broad peaks correspond to the photodetachment process from the electronic ground state of the anion to the first electronically excited state of the neutral radical.

For phenol, the VDE corresponding to the $D_0 \leftarrow S_0$ process is measured to be 2.37±0.10 eV at 269 nm (4.61 eV) which, as discussed in Section , is in agreement with the literature value.[173] For indole, the VDE corresponding to the $D_0 \leftarrow S_0$ process is measured to be 2.58±0.10 eV at 269 nm. There is also a second band in the spectrum centered at 3.61±0.10 eV, which corresponds to photodetachment to the first excited electronic state of the radical. The photoelectron spectra for phenol and indole simulated using ezSpectrum[172] are also plotted in Figure 3.3. Using our fitting procedure, the EAa for indole is determined to be 2.54±0.10 eV. Calculations for phenol and indole chromophores were performed in the same manner as for the fluorescent protein chromophores, and the calculated VDEs are in good agreement with the experimental values (see Table 3.1).

The photoelectron spectra of all four chromophores are characterized by an intense, relatively narrow peak at lower binding energies and a weaker, broader feature at higher binding energies. This suggests that the geometries of the excited states of the radicals differ more than those of the ground states from the corresponding electronic ground states of the deprotonated anions. The fact that the photoelectron spectra share similar features suggests that electron detachment might be governed by the phenol/indole moieties in the GFP/CFP chromophores, respectively. The VDEs of the GFP and CFP model chromophore anions are slightly higher than those of the phenol and indole anions, respectively. This might be an indication that the higher conjugation and delocalization introduced by the imidazolinone unit stabilizes the negative charge of the anions, increasing the photodetachment energies of the model fluorescent protein chromophores.

Further insight can be obtained by examining the molecular orbitals involved in the photodetachment processes, calculated using the EPT/aug-cc-pVDZ method on the TPSSh optimized geometries (Figure 3.4). Comparison between the HOMOs of the phenol and deprotonated GFP chromophore anions shows that the HOMO of the phenol anion closely matches the shape of the HOMO of the deprotonated GFP chromophore anion on the phenol moiety. For the CFP

Figure 3.3: Photodetachment spectra of the deprotonated phenol anion (top) and the deprotonated indole anion (bottom) at 269 nm (4.61 eV). The vertical lines are the spectra calculated using ezSpectrum (see text), and the solid red line is the result of convolution with a Gaussian of FWHM 0.3 eV. (The background signal is set to zero, and spectra are normalized to the most intense data point. The solid line is a moving average of data points.)

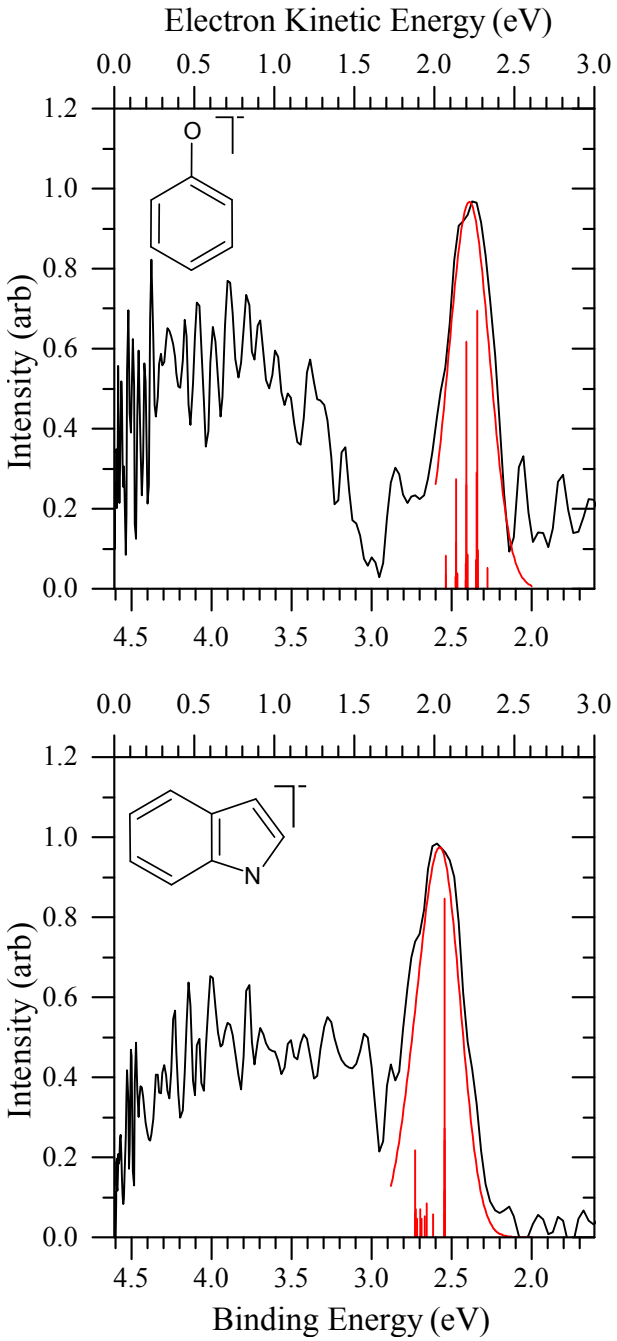

model chromophore anion, the shape of the HOMO on the indole moiety is almost exactly the same as the HOMO of the indole anion. In the HOMOs of both GFP and CFP model chromophores, there is also significant mixing of the phenol or indole moieties' π character with the

Figure 3.4: HOMOs of the deprotonated model GFP chromophore anion (top left), model CFP chromophore anion (bottom left), deprotonated phenol anion (top right), and deprotonated indole anion (bottom right), determined from the EPT/6-311++G** calculations using TPSSh optimized geometries.

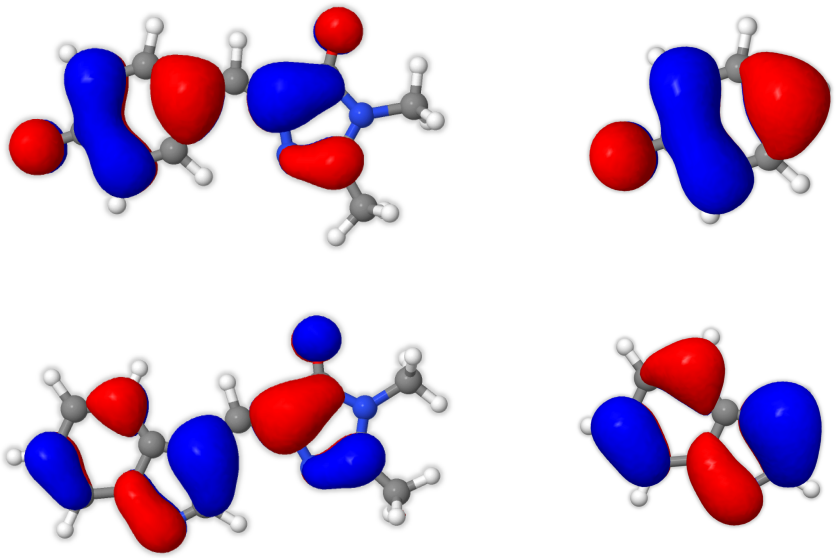

π character of the imidazolinone moiety. The HOMOs of both fluorescent protein chromophores exhibit essentially the same electronic density on the imidazolinone unit. This is consistent with our suggestion that photodetachment from the ground state of the chromophore anions to the ground state of the radicals might be dictated by the differences between the phenol and indole moieties of the chromophores.

Returning to the suggestion that photodetachment is a possible channel for deactivation of the electronically excited deprotonated GFP chromophore anion in the gas phase, our measurements suggest that the VDE lies above the $S_1 \leftarrow S_0$ transition (predicted to lie at 2.57 eV).[39] Our estimates for the EAa indicate that this is also likely to lie above the $S_1 \leftarrow S_0$ transition. Concerning the possibility of the isolated chromophores' being involved in oxidative redding,[45,162] the adiabatic detachment energies estimated in our work suggest that radical formation is not likely to be possible following irradiation with a single photon of 488 nm light (2.54 eV) for either chromophore, since both the measured VDEs and estimated EAas of the deprotonated GFP and CFP model chromophore anions are above the $S_1 \leftarrow S_0$ absorption maxima deduced from action photo-destruction spectra: 2.57 eV (482 nm) for GFP[37] and 2.70 eV (459 nm) for CFP.[41]

3.4 Conclusions

We have employed photoelectron imaging spectroscopy to record the photoelectron spectra of deprotonated GFP and CFP chromophore anions. We observe evidence of competition between direct photodetachment and autoionization following excitation and subsequent IVR, or IC and IVR, of vibrationally and electronically excited states of the anion lying above the photodetachment threshold. We determine the VDEs of the deprotonated GFP and CFP chromophore anions to be 2.85±0.10 and 2.88±0.10 eV, respectively. We have also estimated the EAas by calculating the photoelectron spectra using *ab initio* calculations to determine the geometries and vibrational frequencies of the ground electronic state of the anions and corresponding neutral radicals, giving values of 2.80±0.10 eV and 2.88±0.10 eV, for GFP and CFP, respectively. Our data and methodology has been benchmarked against the photodetachment spectrum and analysis of the deprotonated phenol anion, previously measured with vibrational resolution.[173] Calculated VDEs at the EPT/aug-cc-pVDZ level are in reasonable agreement with the experimental values. The orbitals calculated using this method for the deprotonated GFP and CFP chromophore anions differ in their phenol and indole moieties, which in turn are very similar to the HOMOs of deprotonated phenol and indole anions, respectively. Despite the fact that there has been a great deal of effort directed toward understanding the photophysics and photochemistry of fluorescent protein chromophores, there is still some debate regarding the interpretation of experimental observations following the absorption of visible and ultraviolet light in the isolated chromophores. Our experimental photoelectron spectra of the deprotonated GFP and CFP chromophore anions provide new reference data as a benchmark for improving theory and our understanding of the response of these chromophores to UV light and also as a step toward understanding possible deactivation channels of the optically bright S_1 states of this biologically significant family of chromophores.

We have measured VDE and ADE of the smallest building block, the chromophore, of the quintessential fluorescent protein, GFP. We also benchmarked calculations against photodetachment measurements of multiple chromophore anions and showed that current theoretical methods produce results that are in close agreement with experimental results. Measuring these fundamental properties and understanding the photophysics and photochemistry of the chro-

mophores in isolation will will hopefully lead to improvements in the design and application of fluorescent proteins in the field of imaging.

Chapter 4

Photodetachment Processes and Spectral Tuning of the GFP Chromophore anion

4.1 Introduction

A number of recent photoelectron spectroscopy and theoretical studies of gas-phase pHBDI have also shown that following excitation to the first electronically excited state of the deprotonated anion, $1^1\pi\pi^*$, direct and indirect photodetachment processes compete with internal conversion and fragmentation.[40,41,176] Photoelectron spectra presented previously in Chapter 3 suggested the existence of competing electron emission pathways at higher photodetachment energies, however this was not investigated in any detail. Here, we investigate in detail the competition between direct photodetachment and autodetachment of the $2^1\pi\pi^*$ state of the anion at these higher photodetachment energies, in the range 350–315 nm, within the $2^1\pi\pi^*$ –S_0 absorption band (Figure 4.1).

The chromophore, the workhorse of GFP, has been examined intensively and the literature contains many studies subjecting pHBDI to various experimental conditions. These include solution phase studies,[177] viscosity and solvachromatism studies,[33,54,178] gas-phase measurements,[2,37,39,40,176,179] theoretical measurements[42,45,46,48] and time-resolved femtosecond mea-

Figure 4.1: Schematic energy level diagram illustrating the excitation scheme in the pHBDI$^-$ detachment spectra. The vertical axis marks the vertical excitation energy of the $1^1\pi\pi^*$ state of the anion[46] and the vertical detachment energy (Table 4.1).

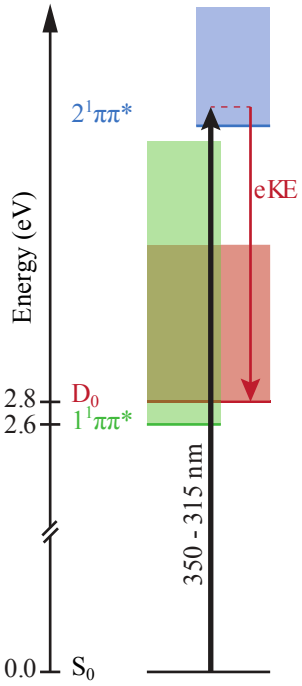

surements.[5,177] All this work relies on altering the experimental condition or technique to explore the properties of the chromophore of GFP. We have decided to taken an alternative approach which is to change the structure of chromophore itself in order to explore its fundamental characteristics.

Whilst there are many studies of the GFP chromophore there are only a few papers studying the effect of chemical modifications of GFP chromophore in the literature. Tolbert *et al.* investigated the effect of increasing the length of an alkyl chain attached to the phenolic oxygen in solid state pHBDI derivatives.[180] They observed a blue-shift with increasing wavelength due to a decrease in interaction between the chromophore and the lattice.[180] The same group also examined the well-known non-fluorescence of pHBDI in solution.[20] The lack of fluorescence is understood to be the result of the deactivation of the excited state by *cis-trans* rotation about the ring bridging bonds[5,178] and they have showed that by chemically fixing the conformation of pHBDI with Zn^{2+} or BF_2 the fluorescence returns.[181,182]

Unfortunately, gas-phase studies of chemically modified pHBDI are more rare. Nielsen *et al.* have measured the action spectrum of a modified pHBDI with an *ortho*-bromine attached to

Figure 4.2: Structures of (a) DM-HBI$^-$, (b) pHBDI$^-$ and (c) DF-HBI$^-$ used in this study.

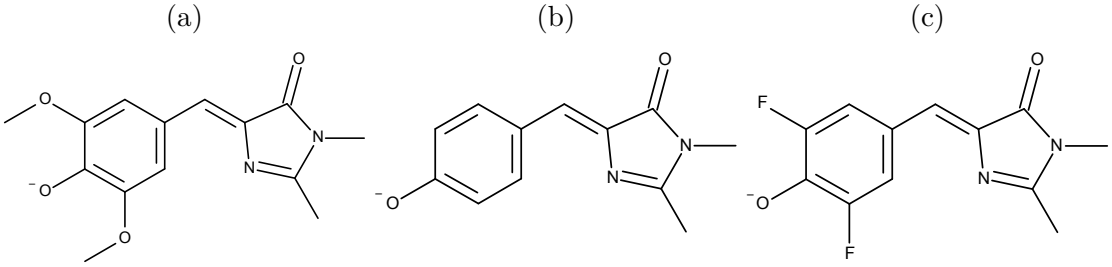

the phenol ring. The authors were unable to observe a difference between the gas-phase action spectrum of this bromide derivative and that of pHBDI.[183,184]

We intend to study the extreme effects of electron donating and electron withdrawing groups on the electronic structure of pHBDI$^-$, using methoxy and fluoride groups, respectively. These groups produce difluoro-hydroxybenzylidene-imidazolinone (DF-HBI) and dimethoxy-benzylidene-imidazolinone (DM-HBI) which can be seen in Figure 4.2. These methoxy and fluoride substituted GFP analogues were originally developed as a solution to a practical problem of detecting small molecules. They were designed to be used in tandem with a novel ribonucleic acid (RNA) sequence called "Spinach" in order to act as a fluorescent probe.[136,185] Beyond the brief study of DF-HBI and DM-HBI in solution as part of the development of the "Spinach" experimental technique, to the best of our knowledge no other in-depth studies of their properties have been undertaken.

For our purposes it can be noted that the addition of fluoride and methoxy groups to pHBDI to produce DF-HBI and DM-HBI induces significant but opposite effects to the molecular system. Where, in deprotonated dimethoxy-benzylidene-imidazolinone anion (DM-HBI$^-$), the methoxy groups are able to donate electrons *via* the π system increasing electron density of the central molecular structure compared to pHBDI$^-$ and, in deprotonated difluoro-hydroxybenzylidene-imidazolinone anion (DF-HBI$^-$), the fluoride groups are able to inductively remove electron density *via* the σ-structure. Studying both these extreme examples of pHBDI will allow us to better understand the effect of modifying the chromophore and hopefully allow for more targeted spectral tuning of this model GFP chromophore and thus ultimately the electronic structure of GFP itself.

4.2 Results

Figure 4.3 shows photodetachment spectra for pHBDI$^-$ measured at 350 nm, 328 nm and 315 nm. Each spectrum displays a single resolved asymmetric peak. The threshold of the peaks remains consistent across all wavelengths, 2.58-2.59 eV eBE. The spectra show an overall trend of increasing FWHM of the peaks with increasing wavelength, from 0.32 eV at 350 nm to 0.79 eV at 315 nm.

Calculations were undertaken within the group to produce a simulated photodetachment spectra, VDE, ADE and vertical excitation energy (VEE) to aid with the interpretation of the photodetachment spectra that were measured. At the time of writing only the calculations for pHBDI$^-$ were completed due to the complexity of calculating the same quantities for DF-HBI$^-$ and DM-HBI$^-$. All the calculations were carried out using GAUSSIAN09[124] and its included methods. Geometries and frequencies for the anion and radical of pHBDI$^-$ were optimised with B3LYP/6-311++G(3df,3pd). The simulated stick spectrum spectrum in Figure 4.3 (top, red lines) was calculated using the GAUSSIAN09 Franck-Condon method. The simulated spectrum included the first 500 vibrational states of the anion and were composed of up to 3 normal modes whose Boltzmann populations were $\geq$10% of the ground vibrational state. The vibrational temperature of the anions was assumed to be 300 K. Gaussian convolutions of the simulated stick spectrum are discussed in Section 4.3.

The VDEs were obtained using the EPT method with the outer valence Green's function (OVGF) propagator[186,187] and a 6-311++G(3df,3pd) basis set. The suitability of this method was determined by comparing photodetachment energies calculated using different basis sets with experimental measurements of the VDE, Appendix B.1.2, and benchmarking against the high-resolution photoelectron spectrum of the phenoxide anion. The EPT/6-311++G(3df,3pd) method gives a VDE of 2.280 eV for the phenoxide anion, which is within 1% of the experimental value of 2.253$\pm$0.0006 eV reported by Gunion *et al.*[173] The ADE was calculated as the difference between the absolute energies of the anion and radical optimised geometries. Table 4.1 summarises our calculated VDE and ADE results along with experimental measurements.

The VEEs of the singlet excited electronic states of pHBDI$^-$ were calculated using the

[†]oscillator strength

Figure 4.3: Figure showing experimental photodetachment spectra for pHBDI at 350 nm, 328 nm and 315 nm. A set of simulated photodetachment spectra, calculated using GAUSSIAN09 is depicted in the experimental 350 nm spectrum. The stick spectrum is the output from a GAUSSIAN09 FC calculation, the red and blue curves are Gaussian convolutions of the stick spectrum with 400 cm^{-1} and 1800 cm^{-1} FWHMs, respectively.

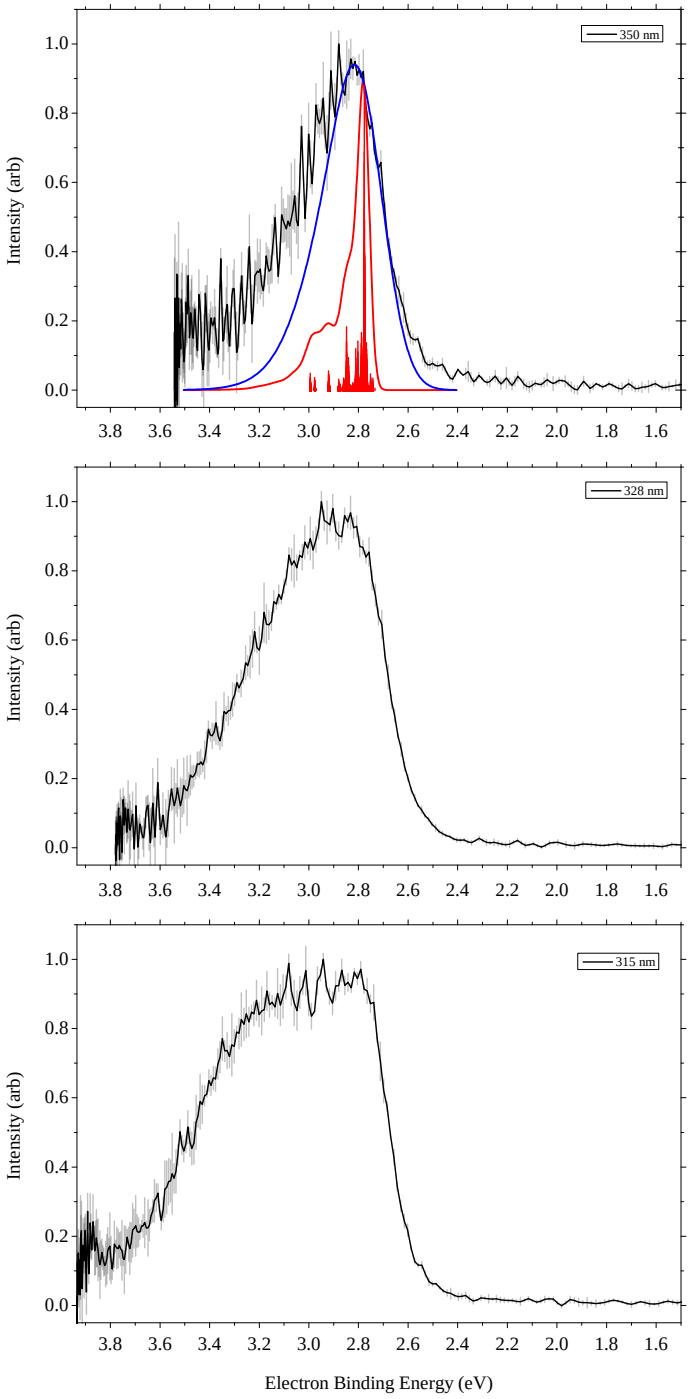

Table 4.1: Calculated VDE and ADE (0-0 transition) for D_0-S_0 detachment, together with experimental photoelectron spectrum measurements. A description of the experimental measurements is provided in the text. Calculations performed by Prof. H. Fielding.

Method	Quantity	eBE (eV)	Reference
EPT/6-311++G(3df,3pd)	VDE	2.777 (0.874)†	
B3LYP/6-311++G(3df,3pd)	ADE	2.775	
PES (350 nm)		2.82±0.10	Toker *et al.*[41]
PES (355 nm)		2.68±0.1	Chapter 3
PES (330 nm and 269 nm)		2.85±0.10	Horke *et al.*[40]

Table 4.2: Predominant Transition Contribution, VEEs and oscillator strengths of the first two $^1\pi\pi^*$ excited states of pHBDI$^-$. Calculations performed by Prof. H. Fielding.

State	Predominant Transition Contribution	VEE (eV)	f
$1^1\pi\pi^*$	0.69(57–59)	3.128	1.050
$2^1\pi\pi^*$	0.62(57–69)	4.391	0.058

CAM-B3LYP/6-311++G(3df,3pd) method. The long range corrected version of B3LYP using coulomb attenuating method (CAM) was chosen for its potential to describe excited states with charge-transfer character.[188] The transitions with oscillator strengths, f, greater than 0.002 found by these calculations is summarised in Table 4.2.

Figure 4.4 shows photodetachment spectrum for deprotonated anions of pHBDI, DM-HBI and DF-HBI, measured at 328 nm. Overall it can be seen that the spectrum for each deprotonated chromophore anion displays a single resolved peak. The key features are described below and are summarised in Table 4.3.

The photodetachment spectra for DM-HBI$^-$, Figure 4.4 (top), shows a single resolved asymmetric feature and the onset of a second feature at high eBE. The threshold of the peak was fitted and found to be 2.52 ± 0.19 eV eBE. The peak intensity and FWHM of the feature were measured to be 2.71 ± 0.17 eV eBE and 0.41 ± 0.10 eV, respectively. The second high eBE feature begins to rise at ∼3.55 eV eBE but the entire peak is not resolved.

The photodetachment spectrum for pHBDI$^-$, Figure 4.4 (middle), shows a single resolved asymmetric feature. The threshold of the peak was fitted and found to be 2.57 ± 0.10 eV eBE. The peak intensity and FWHM of the features were measured to be 2.95 ± 0.13 eV eBE and 0.59 ± 0.10 eV, respectively.

The photodetachment spectrum for DF-HBI$^-$, Figure 4.4 (bottom), shows a single par-

Figure 4.4: Figure showing photodetachment spectra for pHBDI$^-$ (top), DM-HBI$^-$ (middle) and DF-HBI$^-$ (bottom) measured at 328 nm.

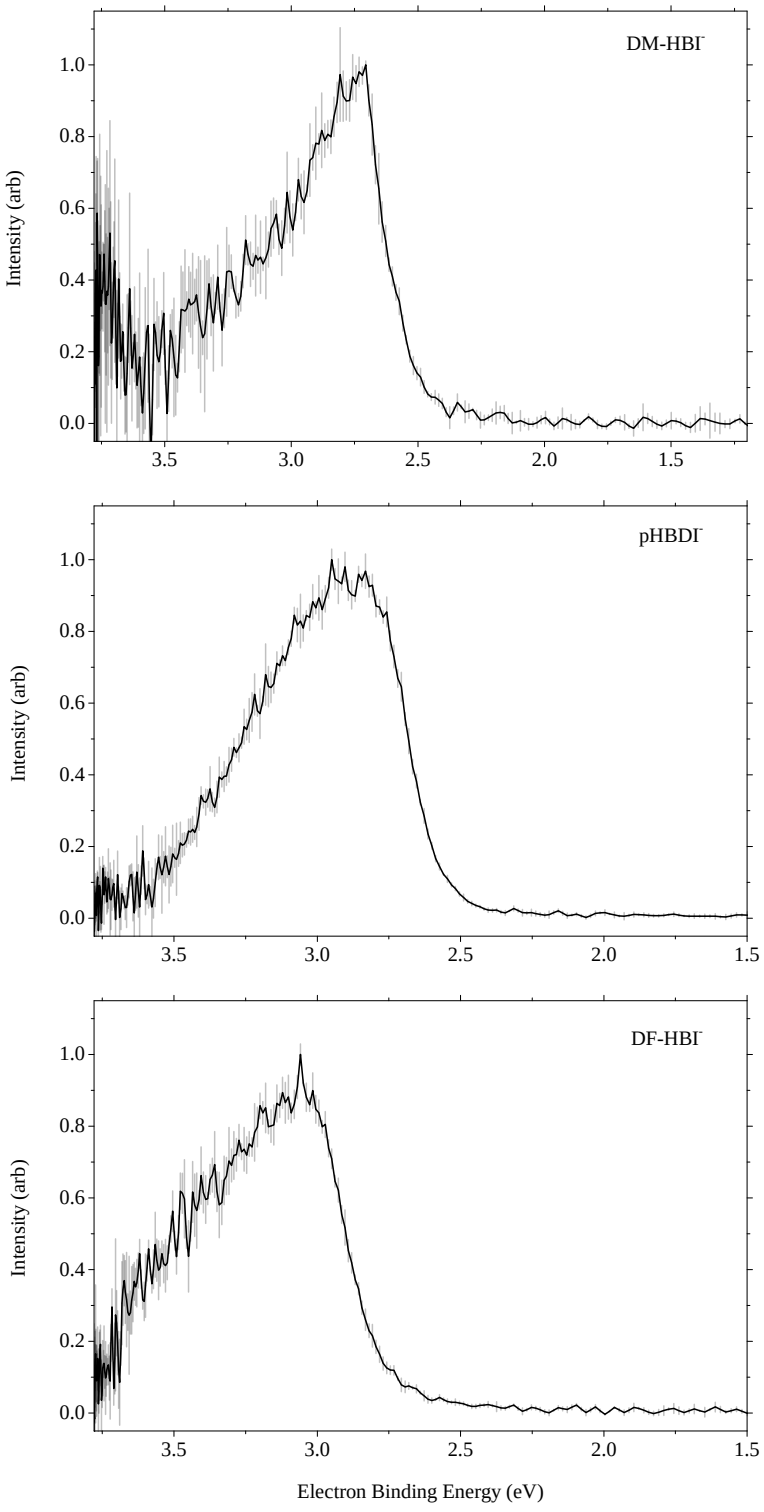

tially resolved asymmetric feature. The threshold of the peak was fitted and found to be 2.77 ± 0.09 eV eBE. The peak intensity and FWHM of the feature were measured to be

Table 4.3: Table summarising results from photoelectron spectra of DM-HBI$^-$, pHBDI$^-$ and DF-HBI$^-$.

Chromophore	Wavelength (nm)	Threshold (ev)	Peak (ev)	FWHM (ev)
DM-HBI$^-$	328	2.52 ±0.19	2.71 ±0.17	0.41 ±0.10
pHBDI$^-$	315	2.58 ±0.10	2.94 ±0.21	0.79 ±0.10
	328	2.57 ±0.10	2.95 ±0.13	0.59 ±0.10
	350	2.59 ±0.13	2.88 ±0.11	0.32 ±0.12
DF-HBI$^-$	328	2.77 ±0.09	3.06 ±0.07	0.54 ±0.10

Figure 4.5: Raw velocity map images for (a) DM-HBI$^-$, (b) pHBDI$^-$ and (c) DF-HBI$^-$ measured at 315 nm. Laser polarisation is in the vertical axis.

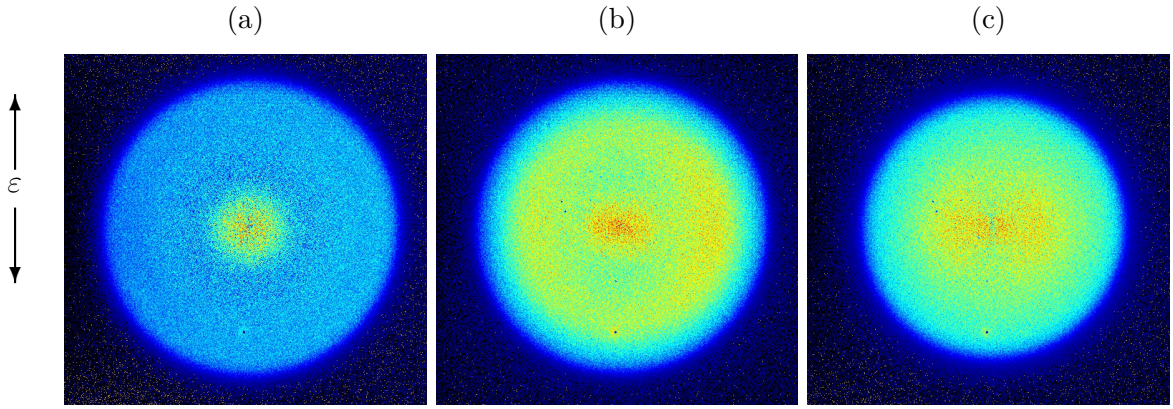

3.06 ± 0.07 eV eBE and 0.54 ± 10 eV, respectively.

It should be noted that whilst DF-HBI$^-$ and pHBDI$^-$ photodetchment peaks have the similar FWHMs it is clear that they have very different peak shapes. The peak in the spectrum of DF-HBI$^-$ has a high energy shoulder compared to that of pHBDI$^-$.

Figure 4.5 shows the raw VMIs measured at 315 nm for DM-HBI$^-$, pHBDI$^-$ and DF-HBI$^-$. For DF-HBI$^-$, Figure 4.5c, it can be seen that the electron photodetachment is anisotropic at the centre of the image and is perpendicular to the laser axis. The image for pHBDI$^-$, Figure 4.5b, also possibly shows electron photodetachment anisotropy in the outer yellow band, again perpendicular to the laser axis. However DM-HBI$^-$, Figure 4.5a, shows no anisotropy in the electron photodetachment. For both pHBDI$^-$ and DF-HBI$^-$, attempts were made to quantify this apparent anisotropy but the statistics were too low to produce a meaningful result.

4.3 Discussion

We begin by discussing the results for pHBDI$^-$ first, as we have a greater wealth of data at our disposal, and the comparison of pHBDI$^-$ with DF-HBI$^-$ and DM-HBI$^-$ is discussed later in this section.

The spectrum of pHBDI$^-$, Figure 4.3, shows the characteristic single direct photodetachment peak from the HOMO to produce the ground state neutral radical. It can be seen that as the photodetachment wavelength decreases that the peaks FWHM increases from 0.32 eV to 0.79 eV and at 315 nm the spectral profile is clearly not that of a simple Franck-Condon envelope. There is a new feature centered around 3.2 eV eBE and there is also some evidence of vibrational structure in the range 2.9–3.1 eV. This suggests that autoionisation of a higher lying excited state of the anion is contributing to the photoelectron spectrum. This is characteristic of increasing autodetachment caused by an excited anion state. This suggests that all three wavelengths are above the excited anion state, and that they are being widened due to increased cross-section of the anion excited state. Due to autodetachment complicating the spectrum it is hard to accurately determine the VDE, but as the 350 nm spectrum is much narrower it would not be unreasonable to suggest ∼2.8 eV eBE as the closest estimate, which is in reasonable agreement with other measurements.[2,40]

To assist with the interpretation of the photoelectron spectra and to understand the role of the different electronic states, we have calculated the VDE, using the EPT method, and the ADE (Table 4.1). These values are compared with the electron binding energy corresponding to the maximum intensity in the experimental photoelectron spectrum, determined by fitting the calculated photoelectron spectrum convoluted with a Gaussian to the experimental spectrum recorded at 350 nm (see Figure 4.3 (top)), and other experimental values reported in the literature.[2,40,41]

The calculated VDE is 2.78 eV, whilst lower than the maximum intensity in the experimental photoelectron spectrum (2.8±0.1 eV), is within the experimental errors of all previously reported experimental measurements. Toker *et al.* reported a value of 2.68±0.1 eV, which they determined by fitting a Franck-Condon envelope to an experimental photoelectron spectrum recorded at 355 nm.[41] Their Franck-Condon envelope was calculated by taking a Fourier

Figure 4.6: Figure showing the main ground-state CAM-B3LYP/6-311++G(3df,3pd) orbitals involved in the transitions to the $1^1\pi\pi^*$ and $2^1\pi\pi^*$ states (Table 4.2).

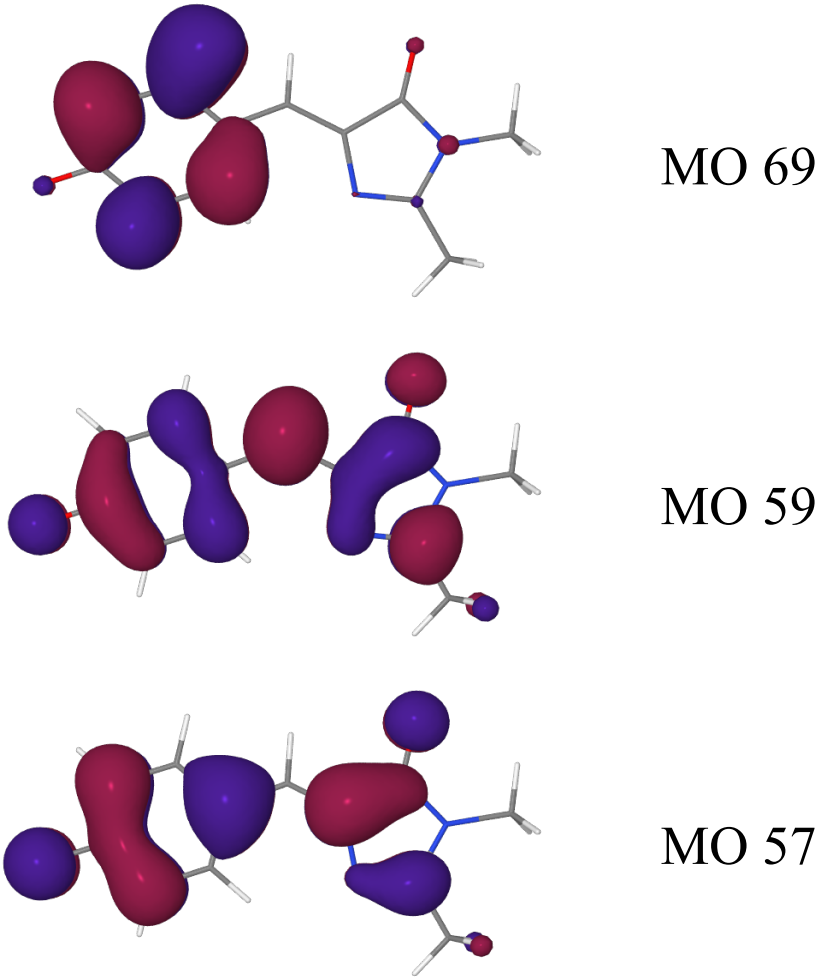

transform of Lax's autocorrelation function using PBE0/aug-cc-pVDZ optimised geometries and frequencies. Horke and Verlet reported a value of 2.8±0.1 eV, based on measuring the maxima in photoelectron spectra recorded at 355 nm, 268.1 nm, and 201.5 nm.[40] In Chapter 3 we reported a value of 2.85±0.1 eV, based on fitting a Franck-Condon envelope calculated using ezSpectrum[172] to experimental photoelectron spectra recorded at 330 nm and 269 nm. Our calculated VDE is very close to the value reported recently by Bravaya and Krylov which was calculated using the ωB97X-D/aug-cc-pVTZ method with ωB97X-D/cc-pVTZ optimised geometries (2.76 eV).[44]

To identify the electronic state responsible for the broadening on the high eBE side of the photoelectron spectra, calculations were carried out within the group to calculate the VEEs

Figure 4.7: Schematic of multiple photodetachment pathways from the same photodetachment wavelength producing three different electron kinetic energies. (left) Direct detachment from S_0 to D_0, (middle) indirect autodetachment from S_0 to D_0 *via* S_1, (right) VAD to D_0 from S_1, after excitation from S_0 to S_1. In this schematic, $eKE_1 > eKE_2 > eKE_3$.

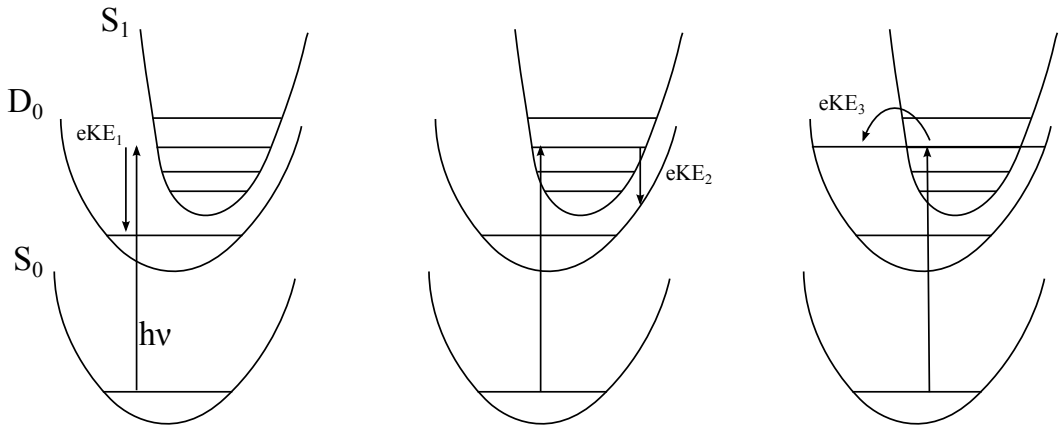

of the singlet excited states of the anion, Table 4.2. The CAM-B3LYP/6-311++G(3pd,3df) molecular orbitals (MOs) involved in these transitions are presented in Figure 4.6. The HOMO (MO 57) is delocalised across the whole molecule. It has two out-of-phase π bonds across the central C-C-C bridge, with a node at the central C-atom, and a pair of out-of-phase delocalised π orbitals on the phenoxide ring. The first singlet excited state is dominated by a transition from the HOMO to MO 59 and involves a $\pi^* \leftarrow \pi$ transition on the central C-C-C bridge. The calculated VEE (3.1 eV) is in line with values determined at similar levels of theory,[48] although it is higher than those reported from action spectroscopy measurements[37,38] and higher levels of theory.[42,46,189]

The second singlet excited state with appreciable oscillator strength is dominated by a transition from the HOMO (MO 57) to MO 69. As can be seen in Figure 4.6, MO 57 is delocalised across the whole molecule and has two out-of-phase π-bonds on the phenoxide unit, whereas MO 69 has two π^*-bonds on the phenoxide ring and has virtually no electron density on the imidazolinone unit. This indicates that the transition involves a $\pi^* \leftarrow \pi$ transition on the phenoxide ring and charge-transfer from the imidazolinone unit to the phenoxide ring. The calculated VEE is 4.4 eV, which is reasonably close to the maximum in the action absorption spectrum of $pHBDI^-$ (310 nm or 4.0 eV) recorded at the ELISA facility.[190] Thus, we believe the most likely explanation for the broadening on the high eBE side of the photoelectron spectrum

is resonant excitation of the $2^1\pi\pi^*$ state followed by vibrational motion within the $2^1\pi\pi^*$ and autodetachment (Figure 4.7(middle)). In this case, the profile of the experimental photoelectron spectrum will reflect the Franck-Condon overlap between the ground electronic state of the anion (S_0), the $2^1\pi\pi^*$ state of the anion and the ground electronic state of the neutral radical (D_0), in addition to a contribution from direct electron detachment (the Franck-Condon overlap between S_0 and D_0). Following resonant excitation of the $2^1\pi\pi^*$ state, ultrafast dynamics through conical intersections between the $2^1\pi\pi^*$ state and lower electronic excited states of the anion may compete with autodetachment from the $2^1\pi\pi^*$ influence the shape of the photoelectron spectrum.

In order to determine if other processes are also contributing to the photoelectron spectra, we have calculated the photoelectron spectrum corresponding to direct photodetachment from the ground electronic state of the anion to D_0. Figure 4.3 (top) shows the calculated photoelectron stick spectrum. The most intense line in the spectrum is the 0-0 transition at 22387 cm^{-1} (2.78 eV). The experimental instrument resolution is $\sim$5% and corresponds to a FWHM of 0.05 eV at 1 eV eKE (2.5 eV eBE) and 0.02 eV at 0.5 eV eKE (3 eV eBE). To compare the low eBE edges of the calculated spectrum and the experimental spectrum recorded at 350 nm, the calculated spectrum is convoluted with Gaussians with FWHM of 400 cm^{-1} (0.05 eV), Figure 4.3 (top, red curve).

Although our calculated spectrum does not include the high density of low intensity transitions on the high eBE tail of the spectrum,[41] the overall profile is very similar to those obtained by Toker *et al.*[41] and by Bravaya and Krylov.[44] However, the calculated spectrum convoluted with an instrument resolution of 400 cm^{-1} FWHM is considerably narrower than the experimental photoelectron spectrum recorded at 350 nm (FWHM=0.32$\pm$0.12 eV). It is also worth noting that this calculated spectrum is narrower than the experimental photoelectron spectrum recorded at 355 nm by Toker *et al.* (FWHM 0.25 eV).[41] We find that a Gaussian function of 1800 cm^{-1} (0.22 eV) FWHM is required to fit the low eBE edge of the 350 nm spectrum. This is consistent with the instrument function of 0.18 eV (1460 cm^{-1}) FWHM that Bravaya and Krylov found necessary to reproduce the 355 nm photoelectron spectrum of Toker *et al.*.[44] Even with this unrealistically broad instrument function, the experimental spectrum recorded at 350 nm is broader than the calculated spectrum on the high eBE side, indicating that resonant

excitation of the $2^1\pi\pi^*$ state followed by vibrational motion and autodetachment is competing with direct photodetachment at 350 nm (Figure 4.7 (middle)).

The broadening of the spectrum on the low eBE (high eKE) side of the spectrum does not change with wavelength in the range 350–315 nm. This suggests that it is not controlled by Franck-Condon overlap between the $2^1\pi\pi^*$ state of the anion and the D_0 state of the radical, *i.e.*, autodetachment followed by resonant excitation of the $2^1\pi\pi^*$ state. We believe the most likely explanation is vibrational decoherence, or intramolecular vibrational energy redistribution, within the high density of vibrational energy levels in the D_0 state of the radical. The calculated photoelectron stick spectrum (Figure 4.3 (top)) assumes that the vibrational states have infinite lifetime. If there were rapid decoherence or IVR in D_0, the D_0 lines would have a spectral width corresponding to their decoherence lifetime. Modelling the D_0-S_0 Franck-Condon spectrum and convoluting with Gaussians of FWHM 1800 cm^{-1} is equivalent to an instrument function with FWHM 400 cm^{-1} and a lifetime broadening of FWHM 1400 cm^{-1} (corresponding to a lifetime of around 10 fs). This 10 fs timescale is also remarkably similar to the effective vibrational decoherence timescale deduced from analysis of the decay of the autocorrelation function used to calculate the $1^1\pi\pi^*$-S_0 absorption spectrum above ∼2.75 eV where the electron emission active modes are excited directly.[41]

The small peak visible in the 315 nm spectrum around 3.9 eV eBE (∼50 meV eKE) merits some discussion (Figure 4.3 (bottom)). Similar low eKE features have been observed in spectra recorded around 500 nm and have been attributed to vibrational autodetachment (VAD) from the resonantly excited $1^1\pi\pi^*$ state[41,176] or thermionic emission following internal conversion back to S_0.[40] In order to investigate the origin of this feature, we have calculated the VEE of the first excited electronic state of the neutral radical at the optimised geometry of the anion. We find that this state arises predominantly from ionisation out of MO 55 and has a VEE of 1.562 eV, which translates into a VDE of 4.339 eV. This is very close to the VEE of the $2^1\pi\pi^*$ state of the anion and also to the VDE to D_1 determined by measuring peak maxima in our earlier photoelectron spectra,[2] and thus we conclude that the small peak visible around 3.9 eV is likely to arise from direct detachment to D_1 or from VAD from the $2^1\pi\pi^*$ state of the anion to D_1.

It is clear that the chemical modifications to the pHBDI sub-structure has a significant effect

on the detachment spectra. The effect can be seen broadly in some overall trends in the gas-phase photodetachment spectra. The threshold detachment, peak energies and peak FWHMs increase from DM-HBI$^-$→ pHBDI$^-$→ DF-HBI$^-$ (Table 4.3) and this same trend can be seen in the peaks of the UV/visible solution phase measurements, Figure B.2(bottom).

Although the peak and thresholds for DM-HBI$^-$ and DF-HBI$^-$ have been measured with a single spectrum for each it is difficult to come to a definitive quantity for VDE and ADE. We can state that the VDE of both species is unlikely to be higher than our measured peak which provides an upper limit, and that the ADE is unlikely to be lower than our measured peak threshold. It can be noted that the maximum difference between the anion absorption peak in solution and the threshold photodetachment energy for DM-HBI$^-$ and DF-HBI$^-$ in the gas phase is only 0.07 eV and 0.16 eV, respectively. This similarity suggests it is likely that the gas-phase S_1 absorption is very close to the S_0-D_0 detachment energy, which has been noted for pHBDI$^-$.[2,38,39,176]

Figure 4.4 shows that at 328 nm the spectra for all the deprotonated chromophore anions possess a single resolved peak. This feature is most likely to be produced by a direct detachment of an electron from the HOMO to the neutral radical in its ground electronic state, Figure 4.7 (left). The only spectra to differ is that of DM-HBI$^-$ which has the onset of an extra feature at high binding energy, which could be indicative of either a VAD process, Figure 4.7 (right), or a direct detachment process to an excited radical state. pHBDI$^-$ and DF-HBI$^-$ have have no other features and significantly there is no signal towards the centre of the VMI image, *i.e.* at high eBE, for these deprotonated chromophore anions. The lack of a peak at low eKE for DF-HBI$^-$ suggests that at 328 nm we are not close to detaching to a radical excited state of the chromophore. As mentioned previously for pHBDI$^-$ a second detachment peak does not appear until 315 nm. There is a clear trend in the VDE of DM-HBI$^-$, pHBDI$^-$ and DF-HBI$^-$ from 2.71 eV to 3.06 eV. This trend can be explained *via* the differing effects of the fluoride and methoxy substituents on the anion and radical states.

To understand the root of the differences between these anions we have to discuss the opposing effects of the methyl and fluoride substituents on the pHBDI$^-$ structure. Firstly, it is worth noting that the electron donating/withdrawing effects of both substituents are limited to the phenol moiety of the pHBDI$^-$ structure. The fluoride groups are removing electrons *via*

Figure 4.8: Resonance structures and distribution of partial charges in the phenol moiety of pHBDI$^-$ for the anion (top) and radical (bottom). R = CH_2-imidazolinone.

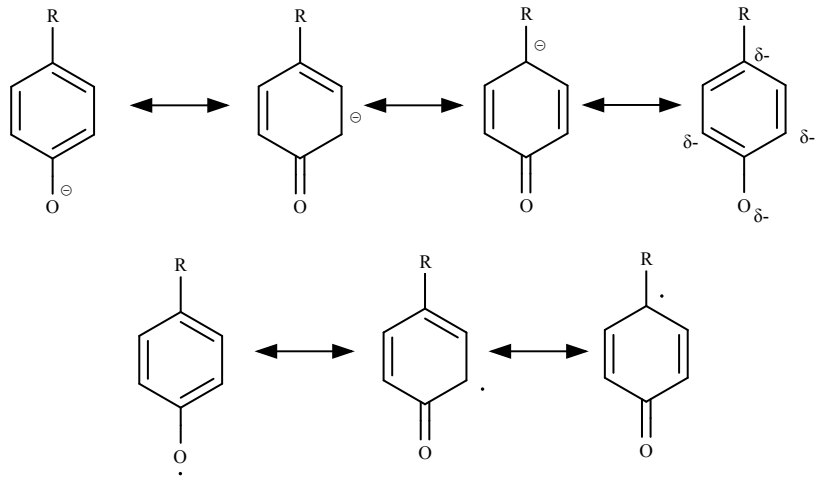

Figure 4.9: Resonance structures of DF-HBI$^-$ phenol moiety for the anion (top) and radical (bottom). R = CH_2-imidazolinone.

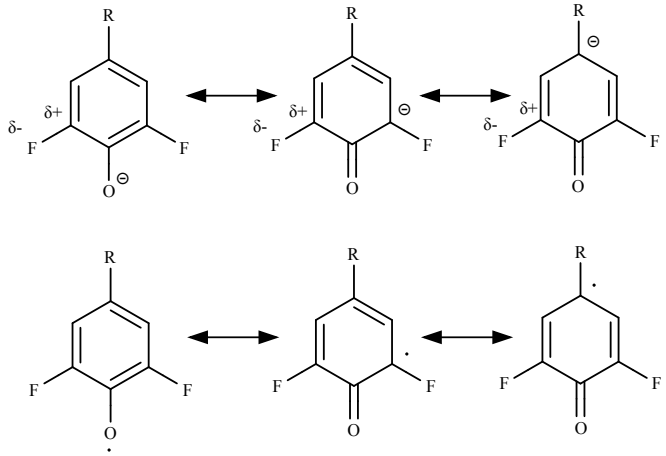

the σ-structure of the system and therefore is not an extended effect. The methoxy groups are donating electrons *via* the π system but their positions on the ring constrains the conjugation so they cannot interact with the extended π-structure of the chromophore anion. In both cases we can state that the effects are limited to the phenol moiety of both DF-HBI$^-$ and DM-HBI$^-$.

The resonance structures of pHBDI$^-$ can be seen in Figure 4.8 (top) and shows that an overall partial negative charge can be found at the ortho- and para- positions. The fluoride groups of DF-HBI$^-$ stabilises this excess negative charge at the ortho- and para- of the anion by withdrawing electron density inductively, Figure 4.9 (top), lowing the energy of the ground S_0 state. It is clear that the electron withdrawing fluorides have a significant effect on the

Figure 4.10: Resonance structures of DM-HBI$^-$ phenol moiety for the anion (top) and radical (bottom). R = CH_2-imidazolinone.

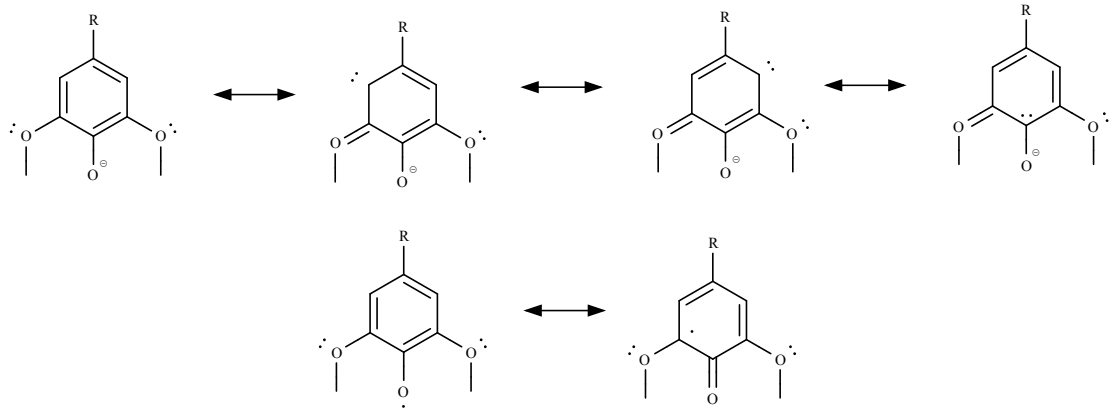

gas-phase photodetachment spectra which is in contrast with the observation of Nielsen *et al.*, who employed a single bromide group substitution compared to our use of two, much more electronegative, fluorides.[183] The two methoxy groups of DM-HBI$^-$ at the ortho- position of the phenol moiety destabilises the excess charge of the anion due to the increased electron density being pushed onto the phenol ring *via* resonance, Figure 4.10 (top), increasing the energy of the S_0 state.

The radical state produced in our experiment also possess resonance structures mimicking the resonance structures of the anion, Figure 4.8 (bottom). However, the stabilising effects of the fluoride and methoxy substituents has swapped in the radical state. The effect of the two fluoride groups on the radical destabilises D_0 by withdrawing electrons from the electron "poor" ortho- and para- carbons of the phenol moiety, Figure 4.9 (bottom), increasing the energy of the D_0 state. The radical of DM-HBI can form a captodative radical, Figure 4.10 (bottom), where the methoxy groups work in tandem with the oxygen to stabilise the D_0 *via* resonance decreasing the energy of the state. Using these observations along with our experimental VDE measurements, we can construct an energy level diagram of the S_0 and D_0 states of all three deprotonated chromophore anions, Figure 4.11, which demonstrates this DM-HBI<pHBDI<DF-HBI trend.

The asymmetry and variation in peak widths show that alternative process are occurring for the different anions. The width of the anion peaks increases significantly between DM-HBI$^-$ and DF-HBI$^-$. These differences could be due to a significant difference in geometry between the S_0 and D_0 states, comparatively differing amounts of autoionisation between the

Figure 4.11: Schematic energy level diagram showing the effects of the substituents on the S_0 and D_0 energy levels for DM-HBI$^-$, pHBDI$^-$ and DF-HBI$^-$. Energies for each chromophore are the photodetachment peak energies, Table 4.3.

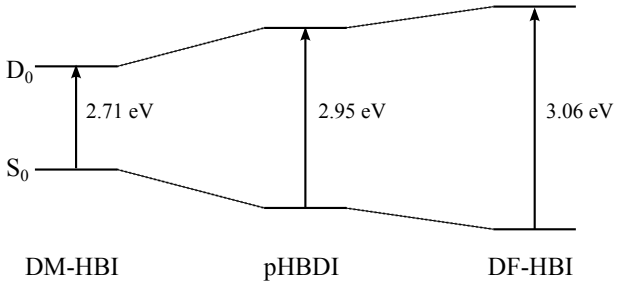

all three deprotonated chromophore anions or a mixture of the two. As already stated the $2^1\pi\pi^*$ state of pHBDI$^-$ increases the photodetachment peak width with increasing wavelength. The increase in the photodetachment peak of DF-HBI$^-$ also suggests, that at 328 nm, more indirect autodetachment is occurring due to an excited anion state. Conversely, it suggests that for DM-HBI$^-$ at 328 nm there is no excited anion state nearby. Work is underway to simualte the photodetachment spectra of DM-HBI$^-$ and DF-HBI$^-$ which should provide us with information about anion and radical gemoetry changes. Even though the FWHM of pHBDI$^-$ and DF-HBI$^-$ are similar it is clear that their peak shapes are different with DF-HBI$^-$ having a shoulder on the higher binding energy side of the peak. It can also be seen from the VMI image of DF-HBI$^-$, Figure 4.5c, that there is a noticeable amount of anisotropy. This anisotropy is not uniform across the image, suggesting that there are two processes one giving rise to the peak and the other its shoulder. Although it is possible to see this apparent anisotropy in the image, attempts to quantify it were inconclusive due to low statistics.

As noted DM-HBI$^-$ possess an extra feature, see Figure 4.4 (top) at high eBE which could be the result of either a direct detachment to an excited state of the radical or a VAD process involving an excited anion state. With just a single spectrum at one wavelength and no corresponding gas-phase measurement of the absorption spectra or calculations available for DM-HBI$^-$ it is difficult to distinguish between the two processes. It can be seen from the basic solution phase spectra, Figure B.2(bottom), that there is a small rise in the solution phase absorption spectra of DM-HBI$^-$ at 328 nm. This suggests there is some anion absorption at this wavelength in solution. A lack of anisotropy in the centre of the VMI image of DM-HBI$^-$, Figure 4.5(a), also supports the argument that the peak is due to VAD process. Unfortunately

neither observation unambiguously assigns the peak as either direct detachment to an excited radical or VAD.

4.4 Conclusion

We have measured the photodetachment spectrum of pHBDI$^-$, a model for the GFP chromophore, between 315-350 nm, and calculations were performed to complement these experimental results. These two approaches are able to demonstrate the increasing importance of autodetachment at shorter wavelengths in pHBDI$^-$. At all photon wavelengths, direct detachment from S_0 to D_0 is an important electron emission channel but resonant excitation of the $2^1\pi\pi^*$ state, followed by autodetachment to D_0, is also significant. At 315 nm, the D_1 detachment channel is accessible and we see evidence for either direct or indirect electron detachment to this channel. We attribute the overall broadening of the photoelectron spectra to rapid ($\sim$10 fs) vibrational decoherence, or ultra-fast intramolecular vibrational energy redistribution, within the high density of vibrational energy levels of the D_0 state of the neutral radical.

We have measured the photodetachment spectra at 328 nm for two chemically modified GFP chromophore anions, DF-HBI and DM-HBI, and compared them to a commonly used model GFP chromophore anion, pHBDI. The modifications were chosen to be chemical extremes which demonstrate the possible tuning properties of electron donating and withdrawing modifications. It was shown that the gas-phase threshold and peak photodetachment energies follow the same trend as solution phase maximum absorptions and a chemical reasoning for the observations was presented. We propose a relative energy level diagram for DM-HBI$^-$, pHBDI$^-$ and DF-HBI$^-$, derived from consideration of resonance effects in the S_1 and D_1 states. Our observation of the effect of electron withdrawing groups is different to the literature of similarly modified GFP chromophore anions, which could not measure an appreciable difference.[183]

To gain a better understanding of the effects of these kinds of chemical modifications to the electronic structure of the anion, a more comprehensive study needs to be undertaken. This would require not only more photodetachment spectra but also gas-phase absorption measurements. It has been supposed that the differences between the modified GFP chromophore anions detachment spectra are due to the effect of autodetachment and relative altering of ex-

cited state energy positions. This would be an interesting subject for theory work and efforts are under way to simulate the detachment spectra for DF-HBI$^-$ and DM-HBI$^-$. With an improved understanding of the subtleties of these chemical groups on the photochemical properties of chromophore anions it would also aid in future targeted modifications to the chromophore structure.

Chapter 5

Dynamics of the isolated GFP chromophore anion

5.1 Introduction

Despite the fact that there have been numerous experimental and theoretical investigations of the fundamental photophysics and photochemistry that underpin the photobiology of GFP,[23,28,159,191] the role of the protein environment around the central chromophore is still not completely understood. It has been suggested that the environment of the chromophore inside the protein is similar to that *in vacuo*,[37–39] however the isolated chromophore was found to be non-fluorescent,[38] and the dominant pathway for excited state relaxation in the gas-phase still remains an open question.

The fluorescence of GFP is lost when the protein is denatured but returns upon renaturation or cooling below the glass transition temperature.[34] In solution, the chromophore was found to be virtually non-fluorescent,[20] which has been attributed to a fast non-radiative decay channel becoming accessible. Interestingly, the absorption maximum of the chromophore in solution varies with the choice of solvent, but the excited state lifetimes show relatively little dependence on the solvent, except for extremely viscous solvents, such as glycol, in which the excited state lifetime becomes significantly longer.[178,192,193] Consistent with experiment, theoretical investigations indicate that the ultrafast non-radiative decay observed in solution involves motion on

Figure 5.1: The structure of deprotonated pHBDI$^-$, a model for the GFP chromophore, with the atomic numbering and torsional angle, ϕ, referred to in this chapter.

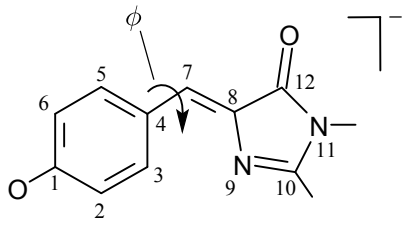

the excited state surface away from the fluorescent state (FS) *via* rotation about the C4-C7 bond (torsional angle ϕ, Figure 5.1), followed by internal conversion to the ground state.[46,178] This rotation appears to be inhibited in the protein environment, making fluorescence from the excited state the primary decay channel. High viscosity solvents or freezing below the glass transition temperature similarly prevent free rotation around ϕ, leading to the observed slowing down of the non-radiative decay.[193,194]

The electronic absorption spectrum of the isolated pHBDI$^-$ chromophore is similar to that of the native protein in its anionic form.[37] This suggests that the protein environment does not induce significant differences in electronic character or excitation energy between the ground and first excited singlet $\pi\pi^*$ state around the Franck-Condon (FC) region in the chromophore. While the similarities in absorption spectra of the isolated chromophore and the chromophore within the protein environment are striking, their decay pathways are clearly different because in the gas-phase, the chromophore is non-fluorescent. This leads to the question of how, and on what timescale, the isolated chromophore decays, which is the focus of this work.

We probe directly the electronic relaxation pathway of an isolated model GFP chromophore anion (pHBDI$^-$, Figure 5.1) following excitation to the first electronically excited $\pi\pi^*$ state, S_1. Using anion time-resolved photoelectron spectroscopy,[195,196] we track the evolution of excited state population and interpret our results with the help of *ab initio* calculations. The results reveal that sub-picosecond dynamics are occurring on the S_1 excited state followed by internal conversion. Our results are remarkably similar to the dynamics observed in solution.[33,177,178] Our calculations suggest that the excited state undergoes rapid (sub-picosecond) motion from the FC region towards a twisted intermediate (TI), which subsequently undergoes internal converion to the anion ground state, as has previously been suggested to explain the dynamics in solution.[46,178] The decay mechanism *in vacuo* and in solution appear identical, despite theoret-

ical studies that suggest otherwise.[194]

5.2 Experimental

Full details of the experimental apparatus have been reported previously and only details pertinent to the current experiment are given here.[116,149] Anions were transferred into the gas-phase by electrospraying a 1 mg/ml solution of pHBDI in 90:10 methanol:water, with NaOH added dropwise until a colour change from pale-yellow to dark yellow was observed. Anions were subsequently trapped in a ring electrode trap, and injected co-linearly into a Wiley-McLaren time-of-flight mass spectrometer at 500 Hz repetition rate. Isolated $pHBDI^-$ were observed as a single peak at 219 Da and the laser-ion delay adjusted such that only $pHBDI^-$ were intersected by femtosecond pump and probe laser pulses in the centre of a VMI setup.[115,116] Photoelectrons were collected in the direction mutually perpendicular to the ion and laser beams. Photoelectron images were acquired for approximately $2{\times}10^5$ laser shots per delay and the resulting images were deconvoluted using the polar onion-peeling routine;[122] yielding photoelectron spectra and angular distributions. The VMI spectrometer was calibrated using photodetachment from I^- and has a typical eKE (resolution ΔeKE/eKE of 5%).

The excitation (pump) and detachment (probe) laser pulses were derived from a commercial Ti:Sapphire oscillator and amplifier system (Spectra Physics Tsnuami and Spitfire XP Pro). Pump pulses at 500 nm were obtained by sum-frequency generation of the output from an optical parametric amplifier with the fundamental 800 nm. Typical pump-probe intensities in the interaction region were on the order of 2×10^{10} W cm^{-2}. Pump and probe pulses were delayed relative to each other using an optical delay line and a cross-correlation with FWHM of 130 fs was measured in a thin β-barium borate crystal.

Isolated $pHBDI^-$ molecules are excited with 500 nm (2.48 eV) femtosecond laser pulses, just below the maximum of the $S_1 \leftarrow S_0$ transition (Figure 5.2).[37–39] This excitation energy is resonant with the S_1 excited state but below the maximum in the direct photodetachment around 2.7-2.9 eV,[2,40,41] thus minimising direct and indirect electron loss channels in the anion. Excited state population is subsequently projected into the photodetachment continuum after a delay t, using an 800 nm (1.55 eV) probe pulse. Photoelectron images are recorded for a series

Figure 5.2: Energy level diagram of pHBDI$^-$ and excitation scheme employed in this work. Population is transferred into the S_1 excited state with a 500 nm (2.48 eV) photon, and the S_1 population probed at 800 nm (1.55 eV). Shown in the top right are two representative photoelectron spectra, recorded when the probe arrives before the pump ($t < 0$, green) and with both pulses temporally overlaid ($t = 0$, red). Both spectra show a large, non-dynamic feature at low eKE due to indirect electron detachment from the anion (see text for details). The peak at eKE = 1.96 eV, requires at least two photons and is consistent with resonant two-photon detachment *via* the S_1 excited state. The pump-probe signature of the excited state is observed as a broad feature peaking at $eKE = 1.1$ eV.

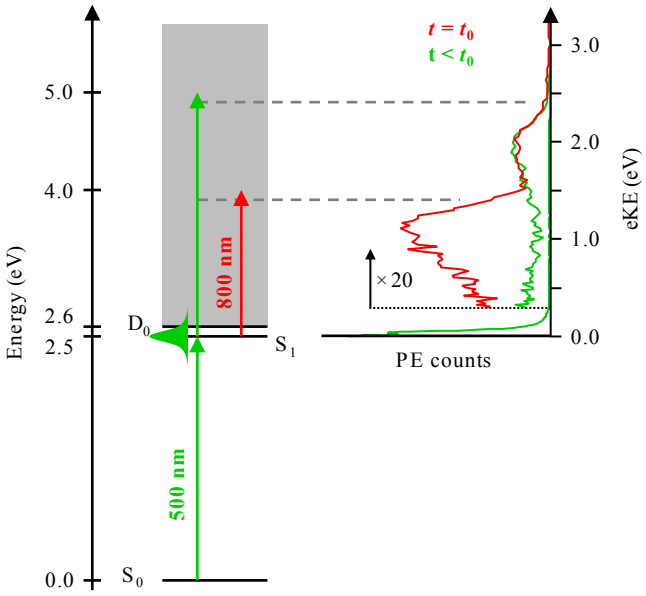

of pump-probe delays.

5.3 Computational

The molecular geometries along the excited state reaction coordinate of a simplified model GFP chromophore anion with a hydrogen terminated imidazole group (deprotonated *p*-hydroxybenzylidene-imidazolinone (HBI$^-$)) were determined by a potential energy surface (PES) scan calculation. The simplified model chromophore was chosen to reduce computational expense as removal of the methyl groups is unlikely to have a significant effect on the energetics of the chromophore.[197]

We employed the CASSCF level of theory with a 6-31G* basis set[46] using MOLPRO 2010.1.[125] Ideally, the complete active space should include all p-orbitals antisymmetric to the molecular plane, which would require CASSCF(16/14), a calculation with 16 electrons in 14 orbitals. To reduce the computational cost, we employed an incomplete active space of 12

electrons in 11 orbitals.[46] The 3 orbitals and 4 electrons that were excluded were considered to have least influence on the conjugation and were the lowest and highest benzene valence π-orbitals on the phenol moiety (*i.e.* the lowest HOMO and the highest Lowest Unoccupied Molecular Orbital (LUMO)) and the lone pair on the N11 atom. A two-root (S_0, S_1) state-average procedure was used to avoid CASSCF convergence problems in all calculations. The CASSCF PES scan calculation was performed on the GFP chromophore anion for the torsional angle ϕ. Once we obtained the anion geometries, we reduced the number of electrons by one to be able to calculate single-state CASSCF energies for the radical of the same geometry in its ground D_0 state.

To improve the energy profile of the CASSCF calculations, single-state, single-point, CASPT2 calculations were performed with the ANO-pVDZ basis set for both the anion and radical at key geometries using MOLCAS7.6.[125,126,198,199]

5.4 Results

Figure 5.2 shows two representative photoelectron spectra, with the probe pulse arriving before the pump ($t < 0$, green line), and when pump and probe are overlapped temporally ($t = 0$, red line). The former is identical to a pump-only photoelectron spectrum, indicating that the probe alone is not resonant with any transition within the chromophore. This spectrum shows a large feature at eKE < 0.2 eV, arising primarily from indirect electron loss following excitation of the S_1 state at 2.48 eV.[2,39–41] A second feature, centred at eKE = 1.96 eV, requires at least two photons and is consistent with resonant two-photon detachment *via* the S_1 excited state, as seen previously in single-photon photoelectron spectra of $pHBDI^-$.[40] When pump and probe are temporally overlapped, an additional photoelectron feature can be discerned at eKE = 1.1 eV. Given the probe energy of 1.55 eV, this feature is consistent with excitation of the S_1 state by the pump pulse, followed by detachment with a probe photon. Hence, this feature is a direct measure of the population in the S_1 state.

Time-resolved photoelectron spectra are shown in Figure 5.3(top), with pump-only and probe-only signals subtracted from pump-probe spectra, leaving only the time-resolved S_1 excited state photoelectron signal as a function of time. For clarity and later comparison, Fig-

Figure 5.3: Time-resolved photoelectron spectscopy results for pHBDI$^-$ following excitation of the S_1 excited state at 500 nm (2.48 eV) and probing with 800 nm (1.55 eV). (top) Experimental photoelectron spectra as a function of pump-probe delay; (middle) Contour plot of the data shown in (top); (bottom) Simulated time-resolved photoelectron data, modelled using the timescales and coefficients extracted from the global fitting procedure described in the text.

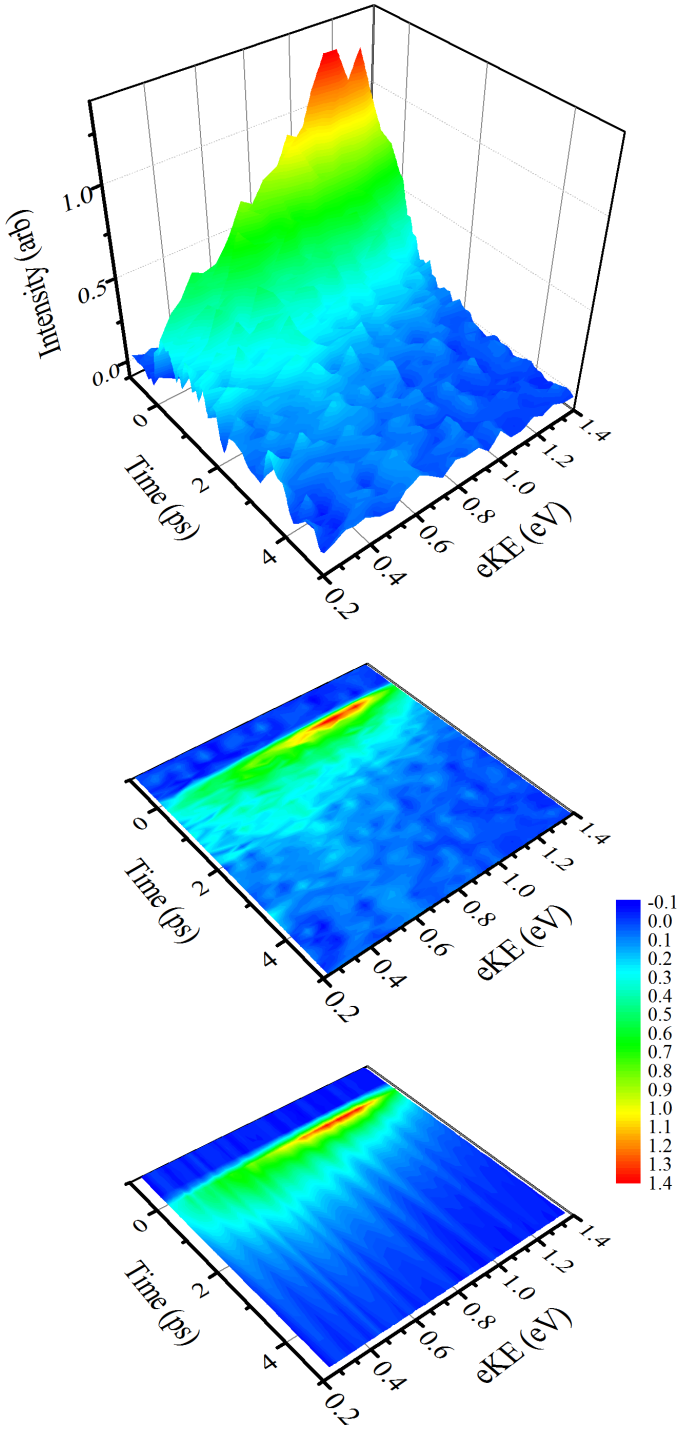

Figure 5.4: Spectral components of the fast ($c_1(eKE)$, 330 fs, blue trace) and slow ($c_2(eKE)$, 1.4 ps, red trace) decay coefficients extracted from the data using Equation 5.1. The sum of the two components (black trace) represents the photoelectron spectrum of the initially excited state, that decays on a 330 fs timescale.

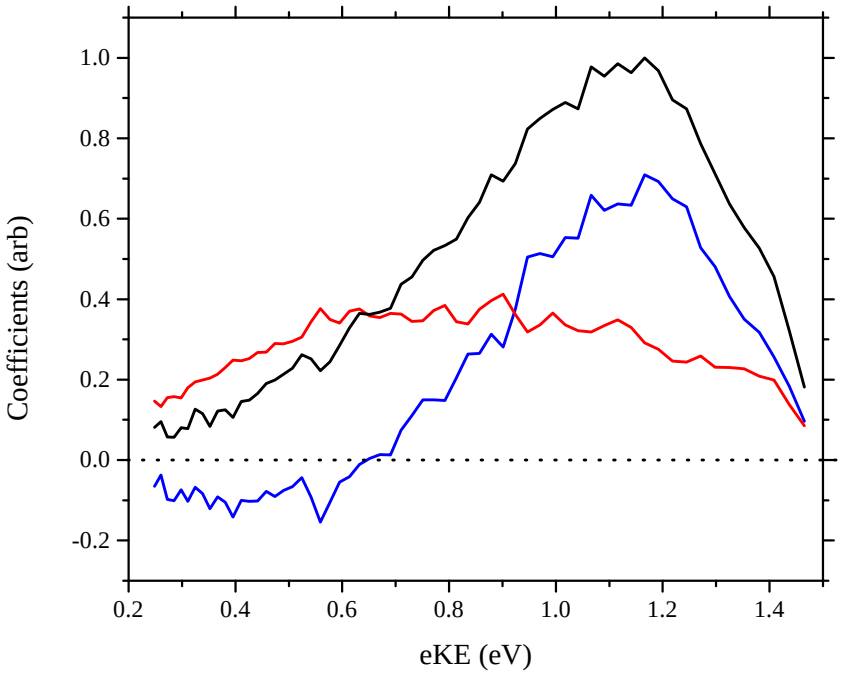

ure 5.3(middle) is a contour map of the same data. A rapid rise in photoelectron signal is observed at $t = 0$, with maximum intensity at eKE = 1.1 eV. The photoelectron spectrum at $t = 0$ is asymmetric with a decaying tail towards low eKE. With increasing pump-probe delay the high eKE side of this feature decays on a sub-picosecond timescale, leaving a broad feature centred around eKE = 0.6 eV, which subsequently decays on a picosecond timescale.

The observed dynamics were fitted to a sum of exponentially decaying spectral profiles convoluted with a Gaussian cross-correlation function, $g(t)$,

$$S(eKE, t) = \sum_i g(t) \otimes c_i(eKE) e^{\frac{-t}{\tau_i}} \tag{5.1}$$

where the coefficients $c_i(eKE)$ represent the intensity of the i^{th} decay at a given eKE, and τ_i is its corresponding lifetime. Two contributions were sufficient to fit the time-resolved data set and the resultant lifetimes are $\tau_1 = 330$ fs and $\tau_2 = 1.4$ ps. The resultant $S(eKE, t)$

is plotted in Figure 5.3(bottom), and reproduces the experimental data (Figure 5.3(middle)) remarkably well, with an adjusted $R^2 = 0.98$ (see Appendix B.2). The spectra of the individual fit coefficients, $c_1(eKE)$ and $c_2(eKE)$, are shown in Figure 5.4, where positive values indicate exponential decay and negative values indicate exponential growth at the respective timescales.

The spectrum obtained for $c_1(eKE)$, corresponding to a timescale of 330 fs, shows a decay of intensity in the spectral region eKE $>$ 0.6 eV, while concomitantly a rise is observed for eKE $<$ 0.6 eV. This suggests an evolution along the excited state potential energy surfaces with a characteristic lifetime of 330 fs, from a point along S_1 producing photoelectrons with high eKE to a point leading to photoelectrons with lower eKE. The remaining population, described by the coefficient $c_2(eKE)$, has a broad eKE distribution peaking around 0.6 eV (Figure 5.4) and a lifetime of 1.4 ps. The spectral shape of this feature shows no further changes as indicated by the fact that only a single timescale is required to reproduce the spectrum at long delays. The photoelectron spectrum associated with the 330 fs timescale can be reconstructed by summing the coefficients of the fit (see Appendix B.2) and this is shown in Figure 5.4 as a solid blue line.

The decay times and their relative weights obtained from the global fit have also been used to reproduce the total integrated photoelelctron signal as shown in (Figure 5.5). The fast and slow decaying components clearly show the origin of the bi-exponential decay that has also been observed in solution and the overall fit is in excellent agreement with the experimentally measured photoelectron signal. At long times, however, the total integrated photoelectron signal does not decay to zero. Instead, about 2% of the photoelectron signal at $t = 0$ remains and decays on a timescale exceeding the current experiment (10 ps). This residual signal indicates that a very small fraction of the population remains in the excited state.

5.5 Discussion

To interpret the photoelectron spectra, we have performed *ab initio* calculations of a model GFP chromophore anion, HBI^-. Specifically, we have calculated the energy of the S_0, S_1 states and the neutral D_0 state at a number of key geometries along the potential energy surface of the S_1 excited state. A summary of the results from our calculations is provided in Figure 5.6. In agreement with previous studies,[46,178] we identify three key geometries along the minimum

Figure 5.5: Integrated photoelectron spectra of the initially excited state that decays on a 330 fs timescale (blue), the longer lived state whose population rises with a 330 fs timescale and decays on a 1.4 ps timescale (red) and the total integrated photoelectron spectrum (black) together with experimental data (black circles).

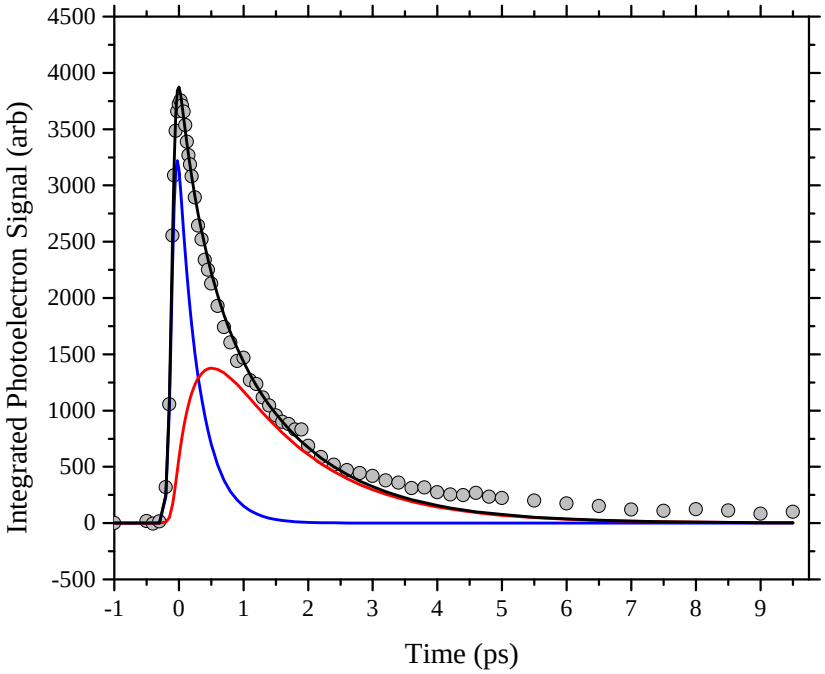

energy path of the S_1 excited state: the FC geometry corresponds to the geometry initially excited from S_0; the FS is a shallow minimum on S_1; and a TI in which rotation about the central C4-C7 bond (ϕ, Figure 5.1) by 90° has occurred. Note that an additional TI geometry can be accessed by rotation about the C7-C8 bond. This process was found to possess a small potential barrier in the gas-phase, making ϕ torsion the more likely deactivation pathway, although not necessarily exclusive.[46]

The FC and FS geometries are connected primarily by a stretching of the allyl C-C bond occuring on a timescale of tens of femtoseconds.[46] Calculated S_1 potential energy surfaces indicate that the surface connecting the FC and FS is rather flat along the minimum energy path.[46] Our calculations show that the geometry change from FC to FS induces only a small change in the D_0 energy, suggesting that the photoelectron spectra of the FC and FS geometries are similar. Moreover, based on the timescale associated with motion from FC to FS, both geometries will be populated during the laser excitation. Hence we conclude that the photoelectron

Figure 5.6: Schematic potential energy curves of S_1 and D_0 along the reaction coordinate from FC $\rightarrow$ FS $\rightarrow$ TI, together with the CASPT2 calculated energies and the CASSCF (S_0, S_1) state-averaged orbitals at FC and TI. After TI, decay back to the D_0 anion ground state is likely to occur by internal conversion.

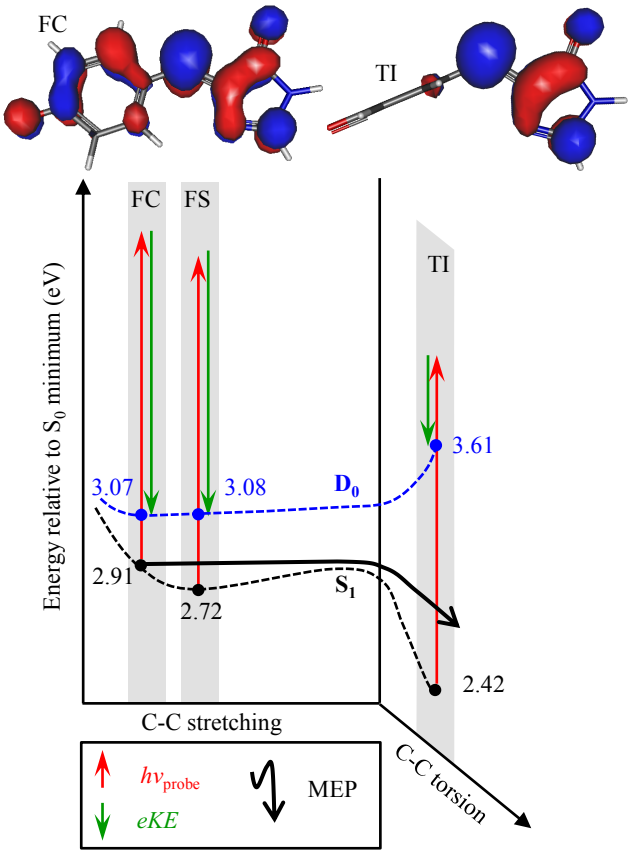

spectrum corresponding to the fast lifetime (τ_1 = 330 fs) corresponds to a combination of the photoelectron spectra of FC and FS (Figure 5.4, blue trace).

After the formation of the FS geometry, theory predicts the presence of a negligible (0.02 eV) barrier between the FS and TI. This motion involves a significant change in reaction coordinate on the S_1 state, as initial stretching of the C-C-C bridge is replaced by a rotation about weakened bonds. From our calculations, this motion leading from FS to TI is associated with a significant stabilisation of S_1 by 0.48 eV with respect to the energy of the FC geometry, which is in qualitative agreement with Olivucci *et al.*[46] and quantitative agreement with more recent calculations.[197] Concomitantly, the energy of D_0 increases by 0.54 eV along this mode with respect to the energy of the FC geometry, as indicated in Figure 5.6. This picture is in excellent agreement with the observations in Figure 5.3(top,middle) and Figure 5.4: after the decay of the initial geometries on the S_1 state, a new feature emerges at a lower eKE, redshifted by

0.5 eV, and broadened substantially. The spectral shift can be attributed to the increase in energy of the D_0 surface and the extra width to the divergence of the potential energy surfaces, likely leading to a broadened Franck-Condon window for photodetachment. The TI will be formed vibrationally hot as the internal energy must be conserved in the gas-phase. We have not performed a Franck-Condon analysis as the effective temperature is non-Boltzmann and the mode distribution unknown.

The conceptual picture of the dynamics of the isolated GFP chromophore anion is as follows. Initial excitation leads to the formation of the FC state, which evolves to the FS state within the time resolution of our experiment (sub-100 fs). From the FS state the system undergoes a rotation about the C-C-C bridge on a 330 fs timescale, consistent with timescales observed for similar motions in biological chromophores such as rhodopsin.[200] The TI subsequently decays on a 1.4 ps timescale, most likely by internal conversion to the S_0 ground state in a single exponential fashion. Unlike the initial motion from the FC/FS to TI geometries, the decay of the TI in the S_1 state does not involve spectral changes. After decay from the TI, some population still remains on the excited state, presumably in the TI geometry. The lifetime of this trapped population exceeds 10 ps, however, this is not likely to lead to significant fluorescence as the TI geometry is only weakly fluorescent. Alternatively, this long-time signal could arise from the lowest triplet state populated by inter-system crossing from the S_1 state. The weak photoelectron spectrum attributed to this slow decay is too noisy to provide insight into its origin.

The decay lifetimes found by global fitting are in remarkable quantitative agreement with the excited state dynamics of $pHBDI^-$ in solution, as measured by fluorescence up-conversion, where a bi-exponential decay with characteristic lifetimes of 340 fs and 1.1 ps was observed in methanol.[33,177,178] The timescales were found to be almost insensitive to polarity[178] or viscosity,[177] with the exception of very large viscosities, which lead to a substantially longer lifetime of the excited state.[193] The dynamics were interpreted as a fast initial motion along a vibrational coordinate on the S_1 state, followed by intramolecular vibrational redistribution and decay from the formed intermediate. Our mechanistic model is consistent with these experiments and comparison with our quantum chemistry calculations leads us to interpret the second step as a rotation about one of the C-C bonds in the bridge. The similarity between the gas-phase and

solution also hints at the minor role that autodetachment from S_1 plays in the decay dynamics, a pathway that is energetically inaccessible in solution. This is in agreement with recent photoelectron spectroscopic results on $pHBDI^-$.[2,40,41] Furthermore, our spectra do not show any evidence for such dynamics (at eKE < 0.1 eV), although the resultant signals would be expected to be small and on a large background. Nonetheless, even if competitive autodetachment was taking place, one might expect that only the timescales would be affected and the spectral features arising from S_1 photodetachment would remain mostly unchanged.

Previous theoretical studies have suggested a difference in the decay pathways accessible to the chromophore in solution and in the gas-phase. Specifically, in solution, both rotation about the C7-C8 or C4-C7 bonds are barrierless. In the gas-phase, a barrier to rotation about C7-C8 leads to a preferential deactivation pathway involving C4-C7 rotation.[46] However, the most striking difference is the energy gap between the S_0 and S_1 states following rotation about either bonds. In solution, the TI associated with rotation around the C4-C7 bond has a much larger S_0-S_1 gap than in the gas-phase and also significantly larger than the TI formed following rotation of the C7-C8 bond. Hence, it was concluded that rotation about the C7-C8 bond will lead to more rapid decay in solution. Rotation about the C4-C7 bond would lead to a bottleneck in the dynamics and some population could remain trapped on the excited state. From our experimental data, the remarkable qualitative and quantitative agreement between the measured excited state decay in solution and *in vacuo* would suggest that similar relaxation pathways are accessed in both environments, although we cannot definitively assign the rotation to a specific bond.

The striking insensitivity of the relaxation dynamics to the environment is surprising for two reasons. Firstly, the maximum of the gas-phase absorption spectrum of the anion GFP chromophore is very similar to that of GFP within the protein.[37,161] In contrast, the absorption spectrum in solution is blue shifted by $\sim$0.3 eV in water[20] and suggests that either the FC structures may be different or that electronic states are destabilised or stabilised to differing extents in solution. One might expect that this would have some bearing on the excited state dynamics, although it should be pointed out that the coincidence of the gas-phase and protein absorption spectra may be accidental and result from a cancelation between blue-shifting and red-shifting interactions in the protein. Secondly, it is well-known that when the environment

is the GFP β-barrel protein, the dynamics are on a nanosecond timescale[23] and have slowed down by 3 orders of magnitude with respect to the isolated chromophore dynamics determined here. This is at odds with the observed insensitivity of the environment on the excited state dynamics. In the protein, the weakly fluorescent TI is almost never reached and the chromophore is trapped in the FS geometry. In both the gas-phase and solution, the chromophore leaves the FS geometry on a 330 fs timescale to form the TI intermediate *via* a negligible barrier.[46,178] The observed discrepancy points to a large influence of the protein environment on the S_1 excited state potential energy surface. The TI is accessed *via* a rotation about the bridging C-C bonds, which appears to be dramatically restricted if the chromophore is embedded in the protein barrel. On the imidazole side, the chromophore is covalently bound to the protein, while the hydroxy-anion is restricted by hydrogen bonds.[8,19,201] From the comparison of the dynamics of the GFP chromophore in the gas-phase and in water, it is clear that the solvation of the phenoxy anion and H-bonding alone are insufficient to cause significant changes in excited state dynamics. In terms of covalent bonding, the addition of bulky groups on the GFP chromophore does influence the dynamics, but by less than one order of magnitude.[164] Hence, it must be the concerted action of the protein on both sides of the chromophore that restricts the motion, leading to a large barrier on the S_1 state that prevents the TI from being formed and thus establishes fluorescence as the primary decay channel.

5.6 Conclusions

We have measured the ultrafast relaxation dynamics of an isolated model GFP chromophore using time-resolved photoelectron spectroscopy. The resulting deactivation pathway was found to proceed *via* two distinctive coordinates. Initially, the excited state evolves from the FC region to the FS geometry, on timescales faster than the time resolution of the current experiment. From the FS a rotation about the bridging C-C bond leads to the formation of a twisted intermediate geometry on a timescale of 330 fs. This subsequently undergoes internal conversion to the anionic ground state in 1.4 ps. These results are in quantitative agreement with measurements of the same chromophore in solution and suggest that a similar relaxation pathway is operative.

A key feature of the current experiment is that we have essentially measured the photoelectron spectra of the transient intermediates in the GFP chromophore. The FC/FS and the TI geometries are represented by the photoelectron spectra shown in Figure 5.4. These photoelectron spectra will serve as important benchmarks for quantum dynamics calculations of the involved intermediate species. Moreover, the S_1 potential energy surface can be refined in conjunction with excited state dynamics calculations, providing an important step towards a complete understanding of the photophysics of the GFP chromophore. This goal lies at the heart of understanding the photophysics and photochemistry that underpin the fluorescence properties of GFP. Moreover, it is only through the deep insight provided in the current experiment that one may hope to develop the predictive capabilities of new biological probes with finely tuned properties.

Chapter 6

A Gas-Phase Study of PYP Chromophore Analogue Isomer Anions

6.1 Introduction

The rather sensible self-preservation behaviour of *Halorhodospira halophila* has been mentioned in Chapter 1. The workhorse of this behaviour is the 4HCA chromophore, which is found within the protein PYP. In order to understand the properties of this chromophore various analogues have been studied. In this chapter we chose to study the pCA analogue, Figure 6.1 (right). pCA is the simplest and smallest molecular model for the 4HCA chromophore, making it an ideal candidate for experimental and theoretical work. The work presented here, studies the isolated PYP chromophore and employs pCA^- as a model. We also investigate the effect of structural changes to the model chromophore anion by looking at the *ortho-* and *meta-* isomers, Figure 6.1 (left and middle).

All three coumaric acid isomers, studied in this chapter, have the problem of two deprotonation sites, one at the carboxylic acid group and another on the phenol group. Deprotonation of the carboxylate is the lower energy state in solution due to the solvent's ability to stabilise the negative charge.[77] However, in the gas phase, deprotonation at the phenol moiety is the

lower energy state due to resonance stabilisation across the phenol and alkyl bonds leading to a stabilisation of 13 kcal mol^{-1}.[79] Using ESI causes a conundrum as to which of the two protonation states is formed in the gas-phase, as pCA is in solution initially. In solution the carboxylate form of pCA^- is more stable and presumably more abundant, but is transferred to the gas-phase, where the phenolate form is favoured. Previous experimental gas-phase measurements stated that there was a significant amount of the phenolate present in the gas-phase from an ESI source, however these studies were inconclusive about the amount of carboxylate also present.[72] Calculations also suggest that the the VDE should be 2.92 eV for the phenolate, compared to 3.91 eV for the carboxylate.[77]

It has been noted that for many isolated model chromophores in their anionic forms, the vertical excitation energy is very close to the vertical detachment energy.[71,77] This produces a metastable excited state where autoionisation is an important process in the photodetachment of an electron from an anionic molecule.[202] This property has been observed in other anionic fluorescent protein chromophore molecules such as the pHBDI anion which has been used as a model for the chromophore of GFP.[2,42] Previous work has calculated the VDE and found it to be between 2.6-2.9 eV, this range was ascribed to competing processes of VAD and direct detachment.[75]

6.2 Results

Photodetachment velocity map images were collected for deprotonated *ortho*-coumaric acid (oCA), *meta*-coumaric acid (mCA), and pCA at 315 nm, 328 nm, 350 nm and 364 nm and analysed using the methods detailed in Chapter 2. The resulting photodetachment spectra are

Figure 6.1: Molecular structures of the *trans*-4-hydoxycinnamyl model chromophores, o-, m- and p-Coumaric (left to right) acid phenolate anion.

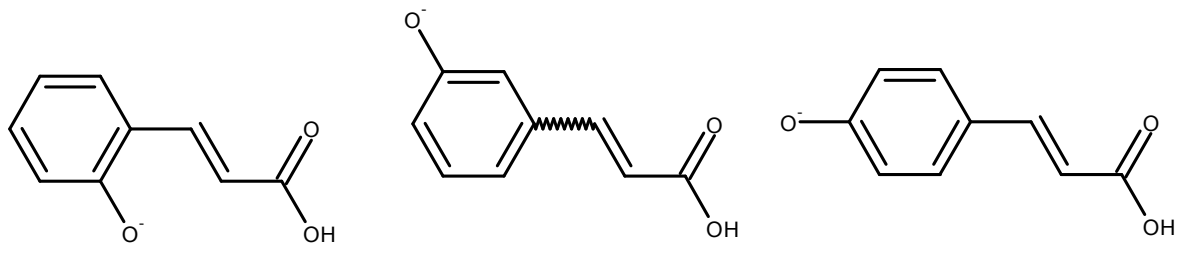

Figure 6.2: Photodetachment spectra of o-, m- and p-Coumaric acid plotted against electron kinetic energy at various wavelengths; 315 nm (cyan), 328 nm (blue), 350 nm (green) and 364 nm (red). The areas beneath the spectra are normalised. The faint lines are the standard deviations for each datapoint and their derivation is described in Chapter 2.1.4.

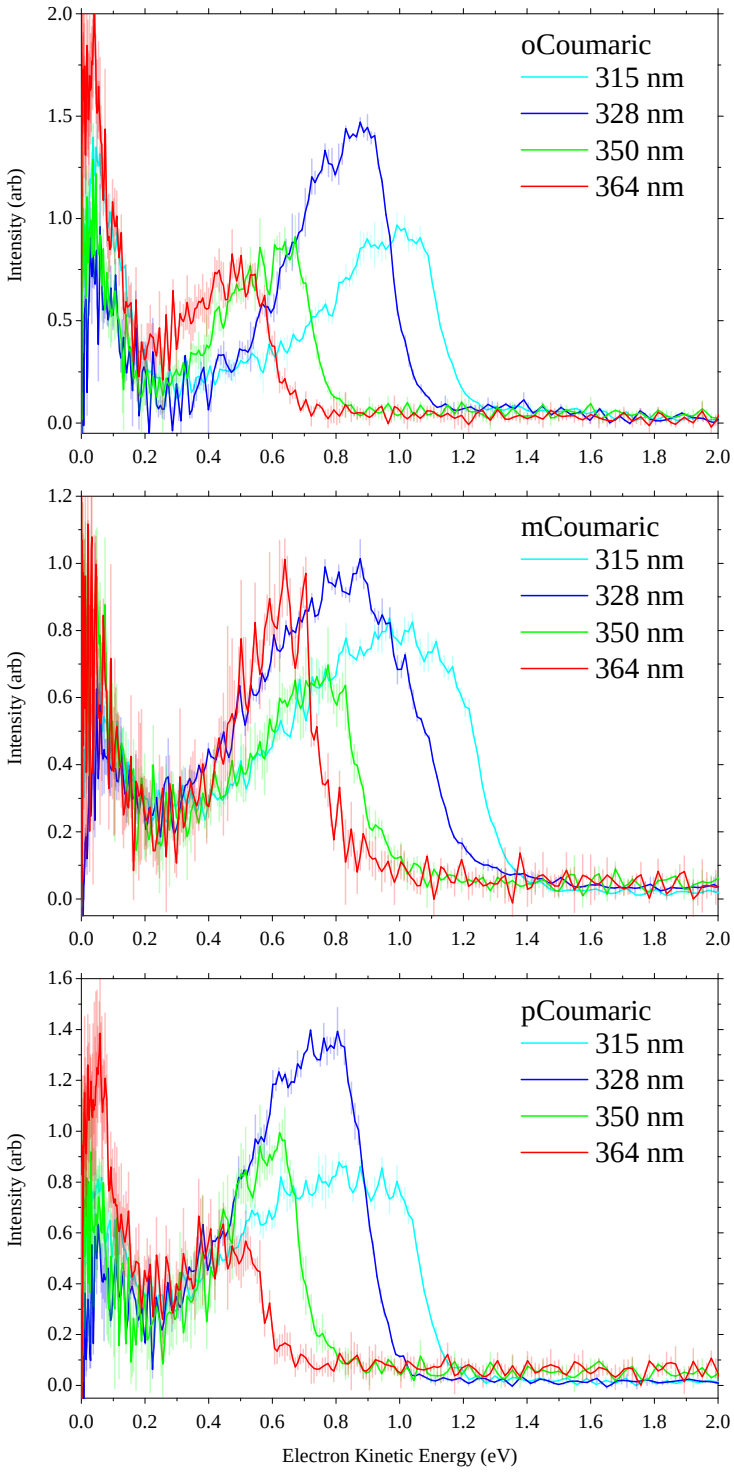

presented in Figures 6.2 and 6.3 with the spectra plotted against a eKE and eBE, respectively. The spectra in Figure 6.2 have been normalised on area, whilst those in Figure 6.3 have been normalised on the peak intensity of the low eBE feature.

Here, we report the eBE of the maxima of the lowest eBE (highest eKE) peaks for each chromophore and photodetachment wavelength. We also report the photodetachment threshold by fitting the background, and a straight line along the lower eBE edge of the lower eBE peak and taking the intercept. These quantities are reported in Table 6.1.

6.2.1 Experimental Photodetachment Spectra

All the spectra shown in Figure 6.2 exhibit similar features for each isomer at each wavelength. Each spectrum has a single, broad, resolved high eKE peak with no obvious vibrational features and a partially resolved low eKE feature. The width and shape of the high eKE peak varies with wavelength for each isomer, however the low eKE feature begins to rise at 0.2 eV for all isomers and its magnitude, relative to that of the higher eKE peak varies with wavelength. There is a shift in the onset of the high eKE feature to lower eKE with increasing wavelength, as would be expected from the decreasing photodetachment available energy available.

Figure 6.2 (top) presents the photodetachment spectra of deprotonated *ortho*-coumaric acid (oCA^-). As expected, the position of the high eKE features shifts to lower eKE with longer wavelength. The most intense high eKE peak is at 328 nm, peaks from 315 nm, 350 nm and 364 nm have similar peak heights as one another. The low eKE feature shows a rough trend towards higher intensity at longer wavelengths but the position, ∼0-0.2 eV, does not alter.

Figure 6.2 (middle) presents the photodetachment spectra of deprotonated *meta*-coumaric acid (mCA^-). The shape and position of the high eKE feature changes dramatically from 315 nm to 364 nm but with no clear trend. The low eKE feature at ∼0-0.2 eV shows a consistent intensity and width across all the wavelengths.

Figure 6.2 (bottom) presents the photodetachment spectra of pCA^-. Again, there is a shift in the position and onset of the high eKE feature to lower eKE with longer wavelength. The most intense detachment peak is observed at a photodetachment wavelength of 328 nm. The low eKE feature shows a rough trend towards higher intensity at longer wavelengths but, again,

the position, ∼0-0.2 eV, does not change.

Figure 6.3 presents the photodetachment spectra for deprotonated oCA, mCA, and pCA at 315 nm, 328 nm, 350 nm and 364 nm plotted against eBE. Once plotted as a function of eBE, and normalised to the maximum intensity of the low eBE feature, more significant trends become apparent. It can be seen that for each wavelength each isomer has an identical threshold for the higher eBE feature although some of the features change shape significantly towards high eBE as a function of photodetachment wavelength.

Figure 6.3 (top) presents the photodetachment spectra for oCA^-. At each photodetachment wavelength, the threshold for detachment to the ground state of the radical is the same, 2.74-2.75 eV. The energy positions, FWHM and shapes of the low eBE feature are also similar for all photodetachment wavelengths.

Figure 6.3 (middle) presents the photodetachment spectra for mCA^-. At each wavelength, the threshold for detachment to the ground state of the radical is the same, 2.56-2.59 eV. There is a transition between the energy positions and shapes of the peak intensity of the low eBE feature as the photodetachment wavelength decreases. At lower photodetachment wavelengths (364 nm and 350 nm) the intensity maximum is at 2.77 eV and the FWHM is 0.24-0.38 eV and higher photodetachment wavelengths (328 nm and 315 nm) the intensity maximum has shifted to 2.90-2.97 eV and its FWHM increased to 0.60-0.70 eV.

Figure 6.3 (bottom) shows the photodetachment spectra for pCA^-. At each photodetachment wavelength, the threshold for detachment to the ground state of the radical is the same, 2.78-2.81 eV. Again, there are different maximum intensities and shapes associated with the low eBE feature. At low photodetachment wavelengths (364 nm and 350 nm), the features overlap and have similar widths (0.26-0.27 eV). As the photodetachment wavelength increases, the features FWHM increases substantially, from 0.42 eV to 0.68 eV and the features peak intensity shifts, from 3.06 eV to 3.13 eV.

The peak maxima, thresholds and FWHMs from the spectra presented in Figure 6.3 are summarised in Table 6.1.

Figure 6.4 presents the relative percentage area of the low eKE feature at 0-0.2 eV as seen in Figure 6.2. The low and high eKE features are clearly mixed to a greater or less extent depending on wavelength and isomer so the cut-off for integration was chosen for each isomer

Figure 6.3: Photodetachment spectra of o-, m- and p-Coumaric acid plotted against electron binding energy at various wavelengths; 315 nm (cyan), 328 nm (blue), 350 nm (green) and 364 nm (red). The spectra are normalised to the peak of the low eBE feature. The faint lines are the standard deviations for each datapoint and their derivation is described in Chapter 2.

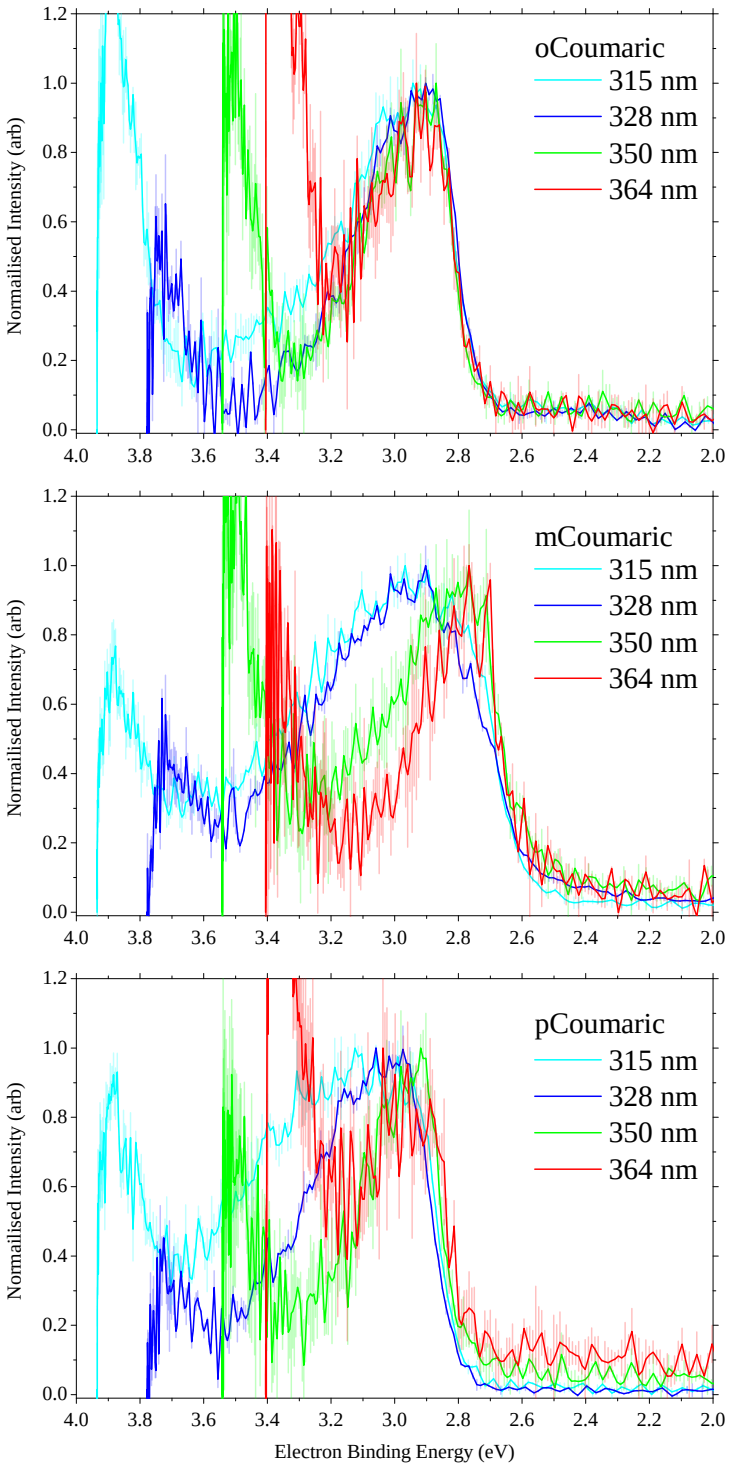

Table 6.1: Summary of measured properties of the low eBE feature for o-, m- and p-Coumaric acid at 315-, 328-, 350-, and 364 nm. These are threshold energy, position of intensity maximum and FWHM of the low eBE feature. The energies are derived from the eBE spectra, Figure 6.3.

Isomer	Wavelength (nm)	Threshold (ev)	Intensity Maximum (ev)	FWHM (ev)
ortho	315	2.737 ±0.320	2.94 ±0.07	0.41 ±0.166
	328	2.736 ±0.037	2.90 ±0.02	0.36 ±0.094
	350	2.754 ±0.230	2.87 ±0.11	0.28 ±0.135
	364	2.754 ±0.330	2.93 ±0.04	0.29 ±0.138
meta	315	2.594 ±0.295	2.97 ±0.07	0.70 ±0.133
	328	2.560 ±0.056	2.90 ±0.11	0.60 ±0.141
	350	2.590 ±0.220	2.77 ±0.15	0.38 ±0.193
	364	2.598 ±0.586	2.77 ±0.07	0.24 ±0.119
para	315	2.782 ±0.175	3.13 ±0.18	0.68 ±0.133
	328	2.804 ±0.196	3.06 ±0.08	0.42 ±0.092
	350	2.784 ±0.357	2.92 ±0.11	0.26 ±0.094
	364	2.808 ±0.508	3.04 ±0.15	0.27 ±0.303

Figure 6.4: Graph showing the ratio between integrated low kinetic energy feature and high kinetic energy feature of o-, m- and p-Coumaric against wavelength. The eKE area integrated was from 0 eV eKE to 0.18 eV, 0.27 eV and 0.24 eV for o-, m- and p-Coumaric, respectively. The higher eKE peak for each isomer was from those cut-offs mentioned to 2 eV.

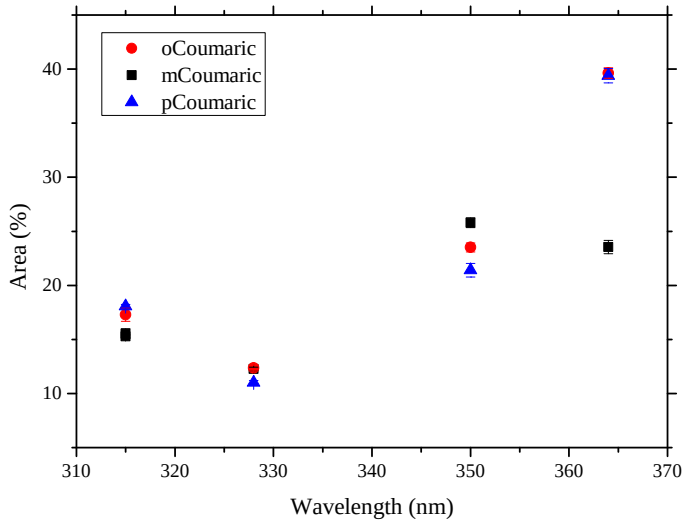

as the minimum between the two features. The eKE area integrated was from 0 eV eKE to 0.18 eV, 0.27 eV and 0.24 eV for oCA^-, mCA^- and pCA^-, respectively. The higher eKE peak for each isomer was from these cut-offs to 2 eV. Overall, Figure 6.4 shows that all the coumaric acid isomers shows a negative trend with a small increase in the proportion of low eKE peak

Figure 6.5: Isomers of mCA^-, (left) *s-cis trans meta*-Coumaric acid (mCA^--1) and (right) *s-trans trans meta*-Coumaric acid (mCA^--2).

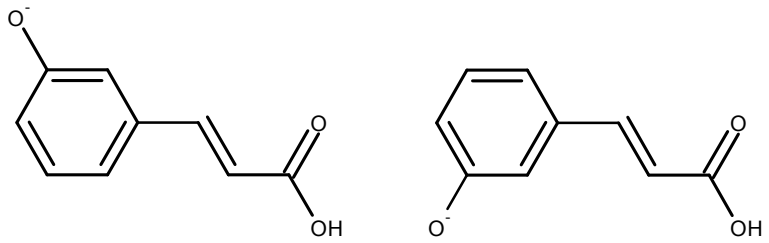

at 315 nm. oCA^- and pCA^- show a similar trend over all four wavelengths going from ∼40% at 364 nm to ∼17% at 315 nm. mCA^- has a significantly lower percentage, 24%, at 364 nm than oCA^- and pCA^-. At 350-, 328- and 315 nm mCA^- shows the same trend as oCA^- and mCA^-. mCA^- rather than a more gradual change shows a step change from >20% at 350 nm and 364 nm, to <20% at 315 nm and 328 nm.

6.2.2 Simulated Photodetachment Spectra

To aid with the interpretation of the photodetachment spectra from $D_0 \leftarrow S_0$ of oCA^-, mCA^- and pCA^- were simulated using GAUSSIAN09 and EZspectrum.[124,172] The geometries and frequencies for both the anion and the radical for the molecules in Figure 6.5 were calculated at the B3LYP/aug-cc-pVDZ level using GAUSSIAN09, and the results were checked for imaginary frequencies. It should be noted that for mCA^- the rotation of the phenol group was undefined in our sample, hence our experiments would have measured the photodetachment spectra of both isomers. To account for this we have simulated the spectra for both possible isomers *s-cis trans meta*-Coumaric acid (mCA^--1) and *s-trans trans meta*-Coumaric acid (mCA^--2), Figure 6.5. The results of these calculations were then used as the input to EZspectrum to produce simulated photoelectron detachment spectra with a molecular temperature of 300 K. Vibrations were visualised from the results of the GAUSSIAN09 calculations and are numbered from $\nu = 0$. The vibrational modes are numbered from $\nu = 0$, consistent with the output of the EZspectrum calculation.

EZspectrum produces a stick spectrum of relative energies and Franck-Condon overlap integrals. As our instrument cannot resolve fine vibrational structure, to compare the simulated spectra with our experimental detachment spectra we need to convolute each stick with a Gaus-

sian profile. The 364 nm mCA^- photodetachment spectra was selected to compare with a set of simulated stick spectra convoluted with various Gaussian widths. The photodetachment spectrum of mCA^- was chosen as it is expected to produce the least complicated detachment spectrum with a minimal influence from other detachment processes besides that of direct $D_0 \leftarrow S_0$ detachment. Figure 6.6 shows the photodetachment spectrum of mCA^- plotted against eKE with the result of a simulated photoelectron spectra of *meta*-Coumaric-1 using a Gaussian convolution of widths of 10 meV, 25 meV and 40 meV (24 meV, 59 meV, 94 meV FWHM, respectively).

It can be seen from Figure 6.6 that using a convolution Gaussian width of 10 meV produces a spectrum that is still too well resolved and that using a convolution Gaussian width of 40 meV produces a featureless peak. It was decided that at convolution Gaussian width of 25 meV gave a good compromise between too much and too little vibrational detail.

Figure 6.7 shows the stick spectra produced using EZspectrum along with 25 meV Gaussian convolutions to produce a simulated photodetachment spectrum for oCA^- (top), mCA^--1 (middle-left), mCA^--2 (middle-right) and pCA^- (bottom) plotted against their respective experimental 364 nm photodetachment spectra. EZspectrum produces a simulated photoelectron spectrum from the overlap of vibrational modes between the anion and radical states and plots the results on a relative (not an absolute) energy scale. In order to compare the EZspectrum output with our experimental data the simulated spectra need to be shifted in energy which was done by eye. The simulated spectra were shifted by 2.865 eV, 2.700 eV, and 2.875 ev for *ortho*-, *meta*-, *para*-Coumaric acid, respectively.*

Figure 6.7 (top) shows that the simulated S_0-D_0 photodetachment spectrum of oCA^- is dominated by the $\nu = 11$ vibrational mode, with the most intense detachment peak arising from the 0-0 transition. The $\nu = 0$ mode of the anion and radical is an out of plane bending motion across the entire molecule. The $\nu = 11$ mode of the anion is an out of plane bending motion across the entire molecule, the same mode in the radical is dominated by a ring breathing motion. A figure of these vibrational modes for the anion and radical can be seen in Figure 6.8.

*Since submitting the thesis analysis by the research group found that using the calculated ADE from B3LYP/aug-cc-pVTZ calculations to shift the simulated spectra gave excellent agreement for *meta*-Coumaric acid. Using the same procedure for *ortho*- and *para*-Coumaric acid leads to the simulated spectra predicting greater photoelectron intensity at higher than possible eKEs, this was ascribed to rotation about single bonds within each of these isomers. [6]

Figure 6.6: Graphs comparing simulated photoelectron spectra convoluted with a range of Gaussian widths compared to m-Coumaric acid. (black line) mCA^- Photodetachment spectra at 364 nm, (red line) simulated photoelectron spectrum of deprotonated mCA^-. (top) Simulated spectra convoluted with a Gaussian width of 10 meV, (middle) 25 meV and (bottom) 40 meV. Simulated spectra were calculated with EZspectrum at 300 K.

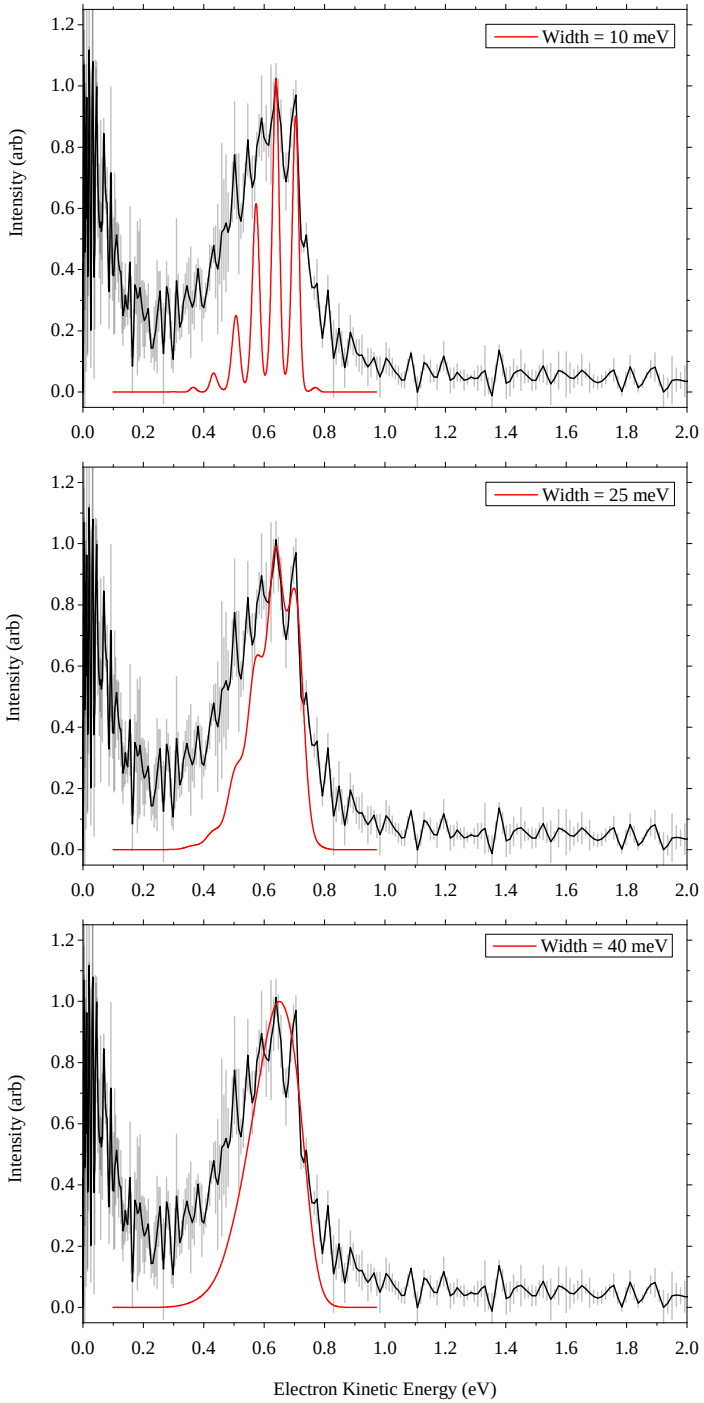

Figure 6.7: Graphs showing *ortho*- (top), *meta*- (middle) and *para*-Coumaric (top) 364 nm photodetachment spectra (red line) at 364 nm plotted against eBE, simulated stick spectrum (black sticks), and convoluted simulated spectrum (black line). The two isomers of mCA^-, mCA^--1 and mCA^--2 are plotted on the middle-left and middle-right, respectively. Simulated spectra were shifted, by eye, by 2.865 eV, 2.700 eV, and 2.875 ev for *ortho*-, *meta*-, *para*-Coumaric acid, respectively.

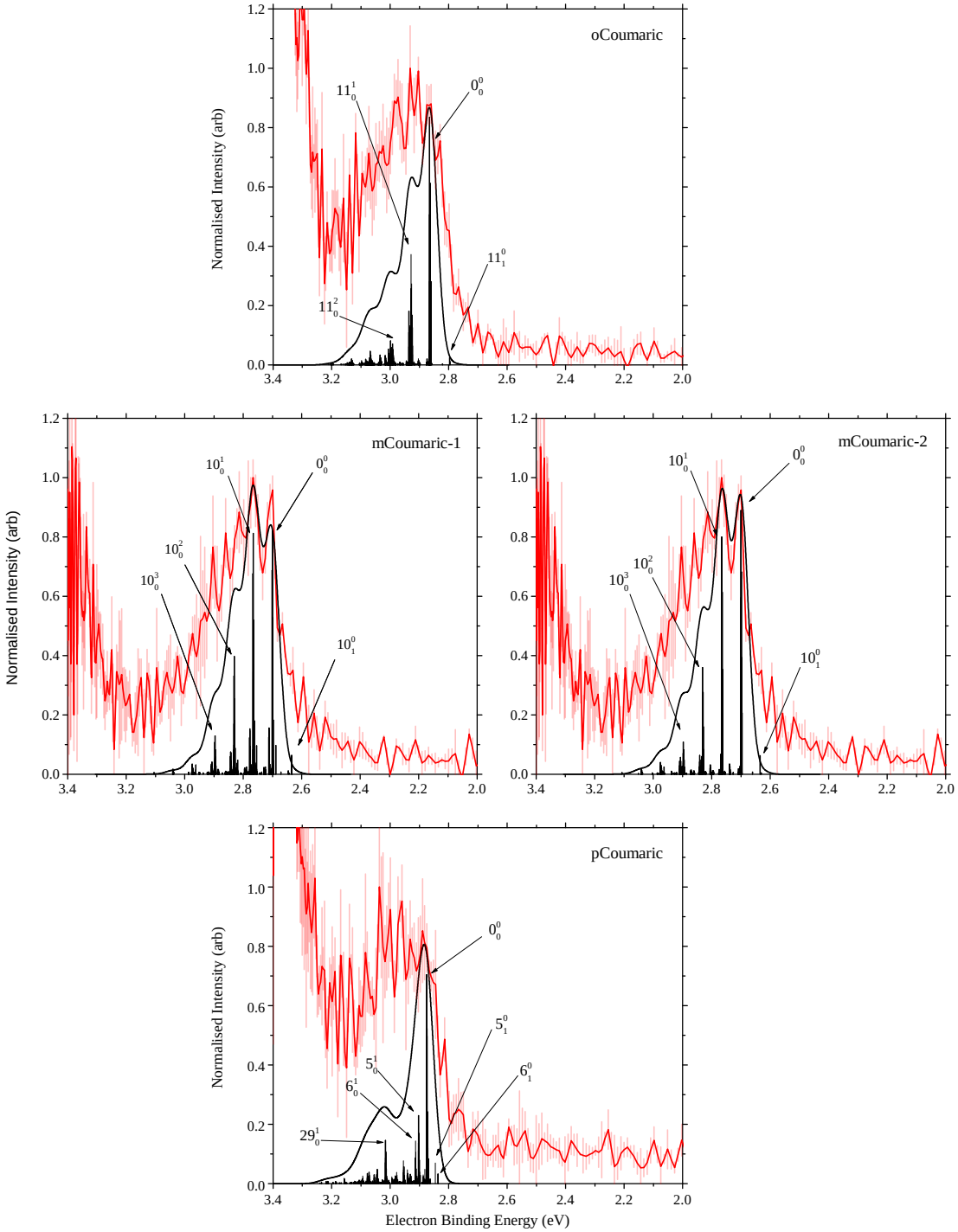

Figure 6.8: Figure showing the $\nu = 0$ and 11 vibrational modes of oCA$^-$ anion and radical.

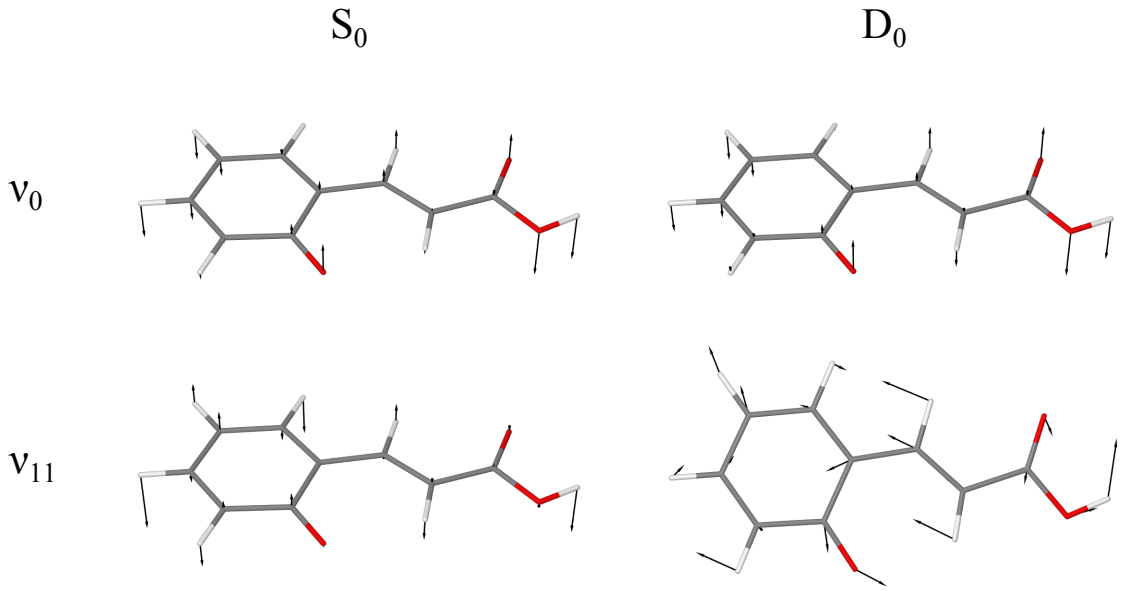

Figure 6.9: Figure showing the $\nu = 0$ and 10 vibrational modes of mCA-1$^-$ anion and radical.

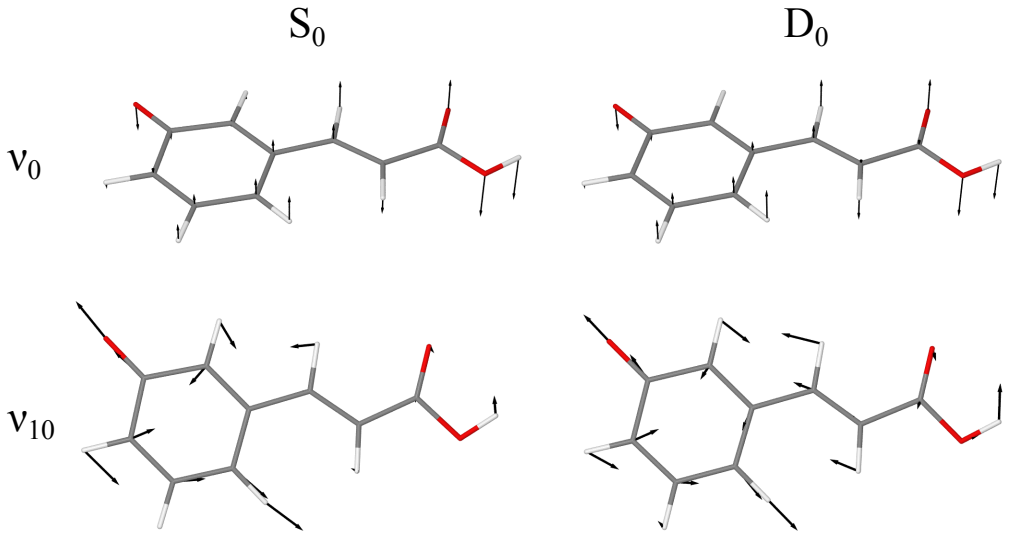

Figure 6.7 (middle) shows that simulated S_0-D_0 photodetachment spectrum of mCA$^-$ is entirely dominated by the $\nu = 10$ vibrational mode for both mCA$^-$-1 and mCA$^-$-2. The most intense detachment mode from the simulation, for both isomers, is the 0-0 pathway; however upon convolution, the $\nu = 10$ 0-1 transition appears more intense. The high eBE tail of the convoluted simulated spectrum is significantly less intense that than the 364 nm spectrum. There is good agreement between the two most intense peaks of the simulated spectrum and those of the experimental 364 nm photodetachment spectrum. Noting the relative intensity of

Figure 6.10: Figure showing the $\nu = 0$ and 10 vibrational modes of mCA-2$^-$ anion and radical.

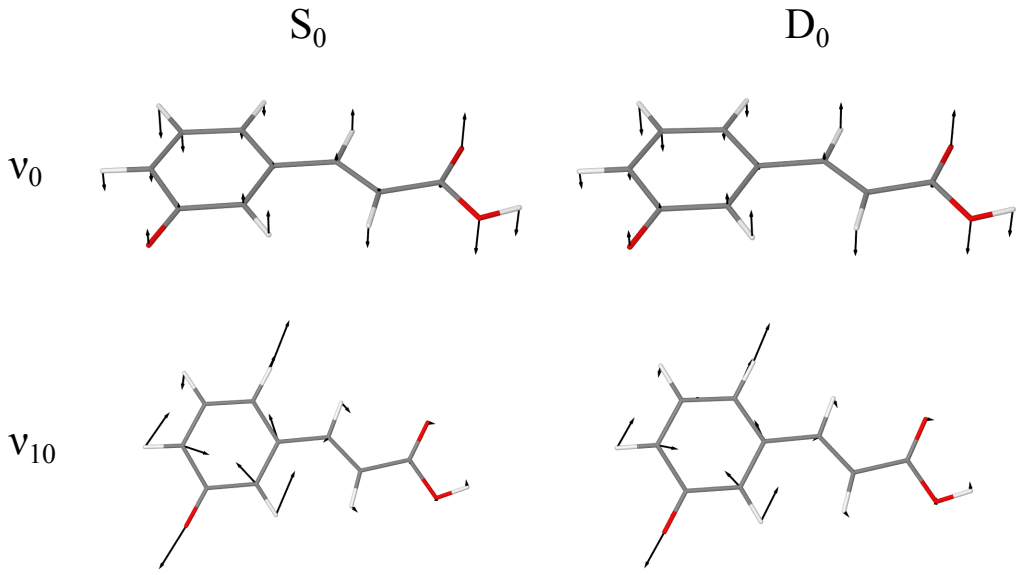

the 10_0^1 and 0_0^0 peaks of the simlation, it can be seen that the agreement between these two simulated peaks and the experimental data is marginally better for mCA$^-$-2 then for mCA$^-$-1. The $\nu = 0$ vibrational mode of the anion and radical for both mCA$^-$ isomers concists of an out-of-plane bending mode. The $\nu = 10$ vibrational mode of the anion and radical, for both mCA$^-$ isomers, is dominated by an in plane ring stretching mode. A figure of the vibrational mode for the anion and radical of mCA$^-$-1 and mCA$^-$-2 can be seen in Figures 6.9 and 6.10, respectively.

Figure 6.7 (bottom) shows that simulated S_0-D_0 photodetachment spectrum of pCA$^-$ is composed of a mix of different vibrational modes, $\nu = 0$, 5, 6 and 29. There is relatively poor agreement between the simulated and 364 nm experimental result. The simulated spectrum is dominated by a single 0-0 transition. The $\nu = 0$ vibrational mode of the anion and radical is an out of plane bending mode. The $\nu = 5$ vibrational mode of the anion and radical is an out of plane bending mode and an in plane stretching mode, respectively. The $\nu = 6$ vibrational mode of the anion and radical is an identical in plane stretching mode. The $\nu = 29$ mode of both the anion and radical is an in plane bending motion across the entire molecule. A figure of these vibrational modes for the anion and radical can be seen in Figure 6.11. It is noted that the $\nu = 5$ and $\nu = 29$ vibrational modes of the pCA$^-$ anion and radical are similar to the $\nu = 6$ and $\nu = 29$ modes of the oCA$^-$ anion and radical, respectively.

Figure 6.11: Figure showing the $\nu = 0$, 5, 6 and 29 vibrational modes of deprotonated pCA^- anion and radical.

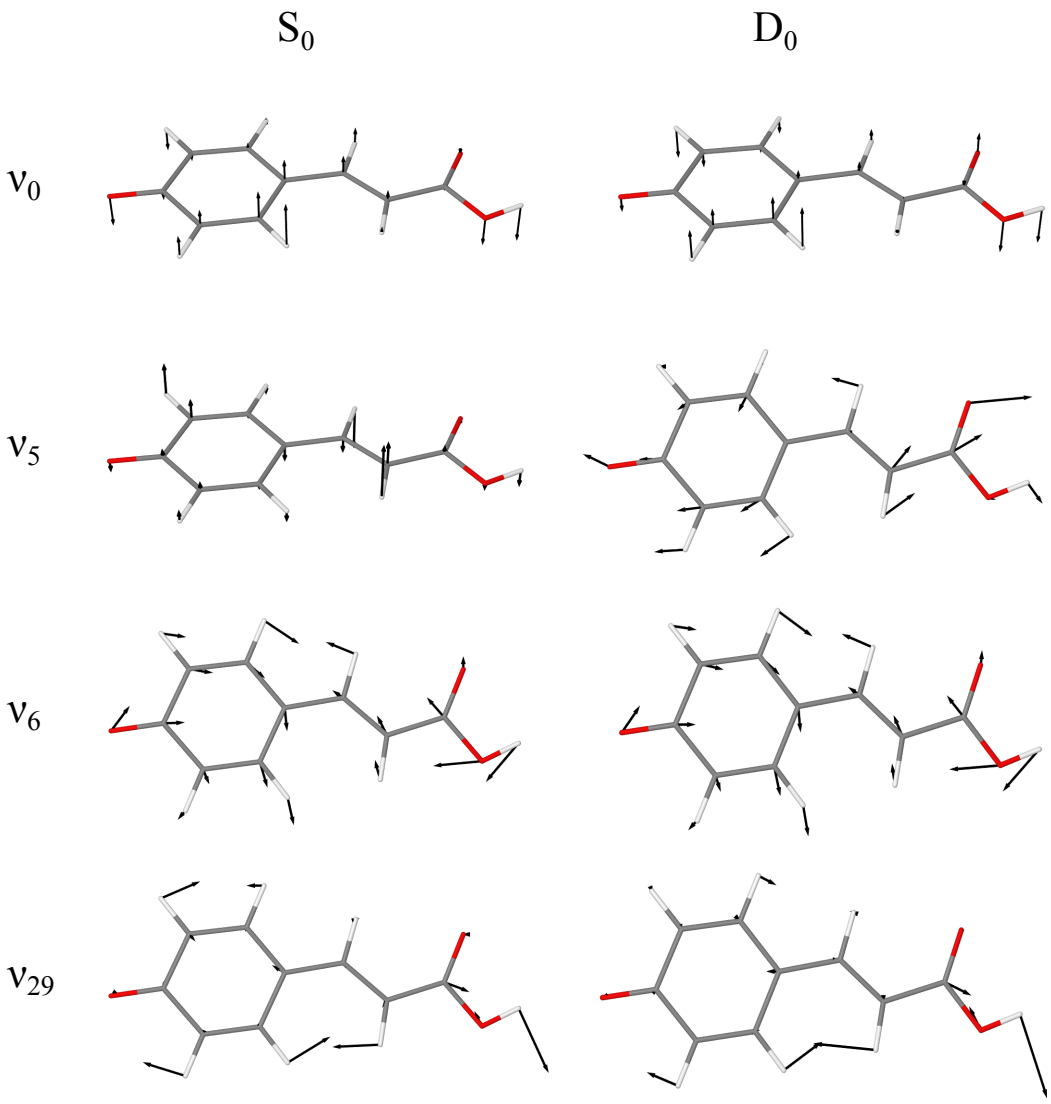

6.3 Discussion

The first question to ask is, whether the phenolate or carboxylate isomer is formed by the coumaric acids using the ESI source in our experiment? The measured threshold and peak detachment energies for pCA^- were found to be between 2.78 - 2.81 eV and 2.92 - 3.13 eV respectively. These are very close to the ADE and VDE predicted by Krylov *et al.* of 2.72 eV and 2.92 eV.[77] The peak maxima and thresholds that we measure are both significantly less than the predicted detachment energy required to form the neutral from the carboxylate anion,

3.91 eV,[†] and in agreement with other experimental and theoretical studies for the energy required to produce the neutral radical from pCA^- in its phenolate anion form, ∼2.9 eV.[75–77,79] Although our measurement does not unambiguously distinguish between the phenolate and carboxylate forms it would suggest that the phenolate isomer is dominating the spectra.

As we are also studying the *ortho-* and *meta-* isomers of coumaric acid, it was necessary to perform calculations to see the difference in detachment energies between their associated phenolate and carboxylate isomers.[203] These calculations were carried out in our group and a summary of results can be seen in the Appendix C.0.4. The calculations found that the VDE for the oCA^- phenolate and carboxylate were 2.76- and 4.71 eV, respectively, and that the VDE for the mCA^- phenolate and carboxylate were 2.74- and 4.85 eV, respectively. These calculations show the same trend that was found by Krylov *et al.*[77] for pCA^- where the vertical detachment to form the ground state radical from the phenolate anion is significantly less, 1-2 eVs, than the energy required for the carboxylate anion. The peak photodetachment energy for oCA^- and mCA^- were measured to be between 2.87-2.94 eV and 2.77-2.97 eV respectively. Comparing these experimental results with these calculations suggests that again the phenolate isomer is the predominant species in the gas phase for oCA^- and mCA^-.

Figure 6.12 shows action spectra for deprotonated *ortho*-methyl-coumaric acid ($oCMe^-$), deprotonated *meta*-methyl-coumaric acid ($mCMe^-$), deprotonated *para*-methyl-coumaric acid ($pCMe^-$) measured by Rahbek.[75] These coumaric acid analogues are unable to form carboxylate isomers due to the methyl group in place of the carboxylate proton, and as stated above, we believe that the phenolate isomer predominates in our experiments with the coumaric acid isomers. The substitution of the proton for a methyl group should not significantly impact the π-system of the coumaric acid, which is likely to be dominating our results. So the methyl coumarates and coumaric acids are similar enough that we believe we are justified in using Figure 6.12 to understand the detachment processes of the coumaric acids measured in this work.

All the spectra, for all the isomers, in this work possess a low eKE feature between 0-0.2 eV, which does not change energy with photodetachment wavelength, see Figure 6.2. This would suggest that the low eKE electrons are being created by the same process for all the isomers at

[†]Appendix C.0.4

Figure 6.12: Action absorption spectra of oCMe$^-$, mCMe$^-$ and pCMe$^-$ showing the first second and third absorption bands as identified by Rahbek.[75] The labels of the peaks 1, 2, 3 are equivalent to our labels, S_1, S_2 and S_3, respectively.

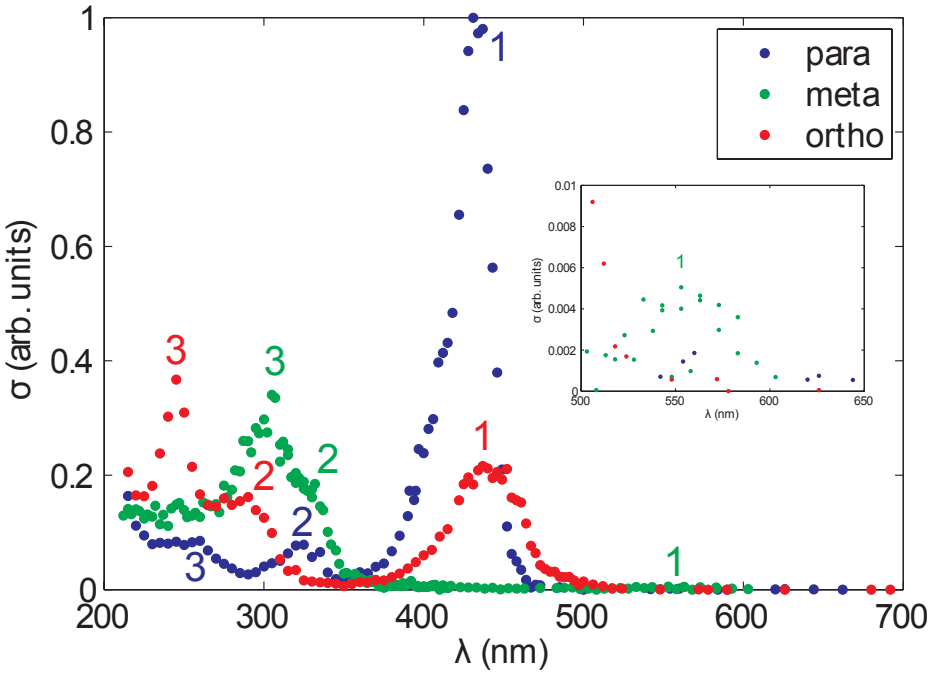

all wavelengths. Thermionic emission or VAD have been proposed as an explanation in pCMe$^-$ for a peak between 0-0.2 eV,[75] as the gas-phase $S_1 \leftarrow S_0$ transition of pCA$^-$ has been calculated to be very close to its VDE.[43] However the fast timescale of the electron photodetachment rules out thermionic emission as a possible detachment pathway,[75] which led the authors to conclude that VAD was the cause of the low eKE feature. The similarities between the low eKE feature measured in our experiments and those of Rahbek suggest that VAD is occurring and that its relative importance varies as a function of coumaric acid isomer.

We note that there is a change in the ratio between the low eKE peak and high eKE peak, see Figure 6.4, which hints at a change in propensity between the indirect processes and direct processes for the different isomers at varying wavelengths. There is a minimum in the ratio between the two peaks for all isomers at 328 nm and comparing this to the photodetachment spectra in Figure 6.2 it can be seen that for oCA$^-$ and pCA$^-$ that this minimum coincides with the most intense direct photodetachment peak. In fact, an overall trend in the peak height can be seen from shorter to longer wavelength, peaking at 328 nm for both isomers. There is no equivalent trend apparent in the photodetachment spectra of mCA$^-$, which is likely due to

Figure 6.13: Schematic of energy levels for deprotonated *ortho*-, *meta*-, and *para*-coumaric acid. Arrows depict experimental photodetacment energies, 315 nm (cyan), 328 nm (blue), 350 nm (green) and 364 nm (red). Energy levels are derived from this work and the work of Rahbek,[75] see text for more details.

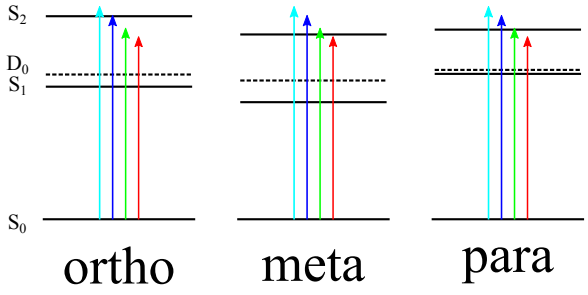

the fact that peaks 2 and 3 in Figure 6.12 are very close together. It can be seen at longer wavelengths that there is significantly more indirect photoelectron detachment *via* VAD for all the isomers. It can also be seen at 364 nm that oCA$^-$ and pCA$^-$ have a similar ratio of indirect/direct detachment, ∼40%, which is significantly more than mCA$^-$, 24%. This could be due to the different relative cross sections for absorption to the S_1 state of each isomer. This can be seen in Figure 6.12 where the intensity of the action absorption peak 1 for pCMe$^-$ and oCMe$^-$ are on the same order of magnitude, whereas the mCMe$^-$ peak is 100× smaller.

At all wavelengths and for all coumaric acid isomers, the higher eKE peak, see Figure 6.2, is a result of direct detachment from the ground state of the deprotonated anion to the equivalent deprotonated radical. Detachment to the ground state radical, D_0, is the most probable result as this has been calculated to be 2.92 eV for pCA$^-$, compared to 4.54 eV for vertical detachment to D_1.[77] Detachment to the first excited state of the radicals for mCA$^-$ and oCA$^-$ is also unlikely as the VDE required has been calculated to be significantly higher, see Appendix C.0.4.

It can be seen from both Figures 6.2 and 6.3, that the shape of the detachment spectra is dependant on wavelength. We propose that detachment to produce these peaks is a direct process but one that involves autodetachment *via* the anion S_1 and S_2 states. By comparing our results in Figure 6.3 with those of Rahbek[75] in Figure 6.12 it is apparent there is a correlation between the photodetachment peak shapes change and action spectroscopy peaks.

Figure 6.13 shows a schematic representation of the deprotonated anion and radical states ground and excited states for oCA$^-$, mCA$^-$ and pCA$^-$. The positions of the anion levels (S_0, S_1, S_2) were taken as thresholds from Figure 6.12, positions of the radical ground state were

taken as thresholds from Figure 6.3.

In Figure 6.3 (top) it can be seen, that regardless of wavelength, the threshold for detachment of oCA^- to the ground state of the deprotonated radical does not alter and that the overall shape of the peak does not change significantly. As the wavelength increases more of the higher binding energy tail is revealed at higher binding energy, and the peak becomes slightly wider. As the peak shape does not change significantly it suggests that the same process is producing the peak at all wavelengths. It can be seen from Figure 6.13 that only the 315 nm experiment is able to populate at just above threshold of the S_2 of oCA^-, and that the rest of the wavelengths used are beneath the S_2 threshold. This shows that for oCA^-, autodetachment is predominantly *via* S_1 and only the 315 nm spectra would be expected to show any effect from S_2.

In Figure 6.3 (middle) it can be seen that regardless of wavelength, the threshold for detachment of mCA^- to the ground state of the deprotonated radical does not alter. The peak shape alters significantly between 328 nm and 350 nm with the peak shape becoming wider below 350 nm. Figure 6.13 shows that the threshold for the S_2 state of oCA^- is only just below the 350 nm light and that both 328 nm and 315 nm are significantly above the S_2 threshold. The significant change in peak shape between 328 nm and 350 nm seems to be as a result of the inclusion of more S_2 character in the autodetachment process.

In Figure 6.3 (bottom) it can be seen that regardless of wavelength the threshold for detachment of pCA^- to the ground state of the deprotonated radical does not alter. The peak shape alters significantly between 350 nm and 328 nm, and again between 328 nm and 315 nm. Figure 6.13 shows that the threshold for the S_2 state of oCA^- is only just below the 350 nm light. Both 328 nm and 315 nm are significantly above the S_2 threshold. The change in peak shape from 350 nm to 328 nm is caused by the inclusion of S_2 in the autodetachment process. Unlike mCA^- though another significant peak shape change occurs at 315 nm. This may be due to states that are not clear from the action spectra of $mCMe^-$.

In our analysis of the photodetachment spectra, we have been careful not to ascribe the peak intensity of the peaks in the photodetachment spectra as the VDE of the respective molecules. As shown, the peak shape and intensity can vary significantly depending on the isomer and, more critically, because of the absorption profile of the gas-phase anion. Measuring the anion photodetachment spectra alone would not allow one to be sure that detachment is a

simple direct process not involving anion states. This has implications for other gas-phase anion systems as the detachment energy is frequently very similar to the absorption maximum. Due to the changing peak shape it is hard to measure an accurate VDE from a single wavelength. Especially if the energy coincides with a particularly strong absorption of the ground state anion.

For coumaric acid the S_1 and S_2 are important states to consider when modelling the detachment spectra and measuring the VDE. From the small range of wavelengths in this work we cannot confirm this but, using theory can help us understand the processes that are involved.

It can be seen from Figure 6.12 that $mCMe^-$ has the smallest cross-section for its first excited anion state. Our hypothesis would suggest that would mean the detachment spectra for mCA^- with the longest wavelength would be most similar to a direct detachment process that involves the smallest amount of autodetachment *via* S_1. It can be seen from Figure 6.7 (middle-left and middle-right) that the simulated spectra for mCA^- has very good agreement with the measured 364 nm spectra. It can also be seen from Figure 6.7 (top and bottom) that the simulated photodetachment spectra for oCA^- and pCA^- do not agree as well with their 364 nm photodetachment spectra. This is due to the much larger absorption cross sections of the S_1 states in oCA^- and pCA^- as seen in Figure 6.12. This supports our hypothesis that S_1 is having a significant effect on the detachment profile of oCA^- and pCA^-, but not mCA^-.

To aid with our interpretation of the experimental photodetachment spectra we simulated the spectra that would be produced by direct detachment from S_0 to D_0 of all the coumaric acid anion isomers. We have compared our simulated spectra to the experimental spectra taken for all isomers at 364 nm as at this wavelength there would be the least contribution from any anion excited states, Figure 6.7. The agreement between the oCA^- and pCA^- spectra is poor, demonstrating that a simple direct detachment from S_0 to D_0 does not well describe the detachment process. The agreement between the simulated and experimental spectra for mCA^- is much better.

The simulated spectra in Figure 6.7 (middle-left and middle-right) also shows that the smaller features on the low eBE feature are the result of vibrational modes of mCA^-. The simulated detachment spectra of mCA^--1 and mCA^--1 are very similar but demonstrate the same overall characteristics. It is clear from both of the simulated spectra in Figure 6.7 (middle)

that the 0-0 detachment of mCA^-, whilst the most intense of the stick profiles, does not coincide with the maximum intensity peak in the 364 nm spectrum after a Gaussian convolution. This would mean that the VDE of mCA^- is actually the slightly less intense of the two peaks, 2.70 eV eBE rather than 2.77 eV eBE. It is worth mentioning that similarity between the simulated spectrum and the experimental spectrum for mCA^- at 364 nm whilst not identical is striking. This shows that detachment at 364 nm is dominated by direct detachment from S_0 to D_0 with coupling between identical vibrational modes as seen in Figures 6.9 and 6.10.

It is also noticeable that the spectra calculated for pCA^- is very similar to that calculated for $pCMe^-$ although the assignment of the simulated spectra position is significantly different.[75] This would suggest that the D_0-S_0 detachment is similar for both of the molecules.

The most intense transition given by the simulated photodetachment photodetachment spectra, for all the pCA isomers, is the 0-0 transition. Examining this vibrational mode, Figures 6.8, 6.9, 6.10, 6.11, it is clear that the vibrational motion is the same for all the isomers, an out-of-plane bending mode. The effect of the different O^- phenyl positions is making very little difference to the S_0-D_0 detachment pathway. The 0-0 transition and vibrational mode is the only shared characteristic of the isomers. The other significant vibrational modes for each of the isomers do no seem to share any similarity. The judgement of similarity, or lack of, between the different isomers vibrational modes must be taken in the context of oCA^- and oCA^- poor agreement with the experimental data. The simple S_0-D_0 detachment model used in the simulations does not effectivly account for the effects of excited anion states on the photodetachment spectra.

6.4 Conclusion

We have measured the photoelectron spectra for oCA^-, mCA^-, pCA^- using our anion photoelectron imaging spectrometer. We are able to observe the effects of direct and indirect detachment processes. We observe that VAD is occurring in all isomers of coumaric acid at the photodetachment energies we employed. We also note the change in peak profile and position of peaks due to direct photodetachment which depends on wavelength. We propose that this shift in peak shape and position is caused by autodetachment to D_0 occurring *via* the S_1 and

S_2 states of the anion. This shift in peak shape and position makes it hard to assign VDEs for the coumaric acids from the experimental spectra. The exception to this is mCA^-, due to the low absorption cross-section of it's first excited state which allowed the low eBE edge of the photodetachment spectra to be dominated by the Franck-Condon overlap between the ground anionic and radical states. The observation of vibrational modes in the photodetachment spectra of mCA^- were assigned, with the aid of computational work, allowing us to measure the VDE to be 2.70 eV eBE.

This propensity to detach *via* anion states is likely to be present with other chromophore anions and in order to measure the VDE an understanding of the absorption profiles of the anions and detachment spectra at various wavelengths would be required. A single measurement at a single wavelength is unlikely to be a complete picture.

In this work, we have had to rely on action spectra of $oCMe^-$, $mCMe^-$, $pCMe^-$, recorded by another group, to understand the photodetachment spectra of coumaric acid. This is not ideal and work is already under way to modify the experiment so that action spectra can be acquired in conjunction with photoelectron images. It is hoped that our own action spectra will be similar to that recorded by Rahbek and support our assumptions of energy level positions.

A theoretical analysis has been performed, using *ab initio* methods, to support our hypothesis of S_1 being a minor contribution to detachment in mCA^-. These calculations only considered the S_0 and D_0 states and our hypothesis requires the inclusion of S_1 and S_2 in the detachment profile simulations too. Calculations that involve these states would allow a better understanding of the peak profiles measured here, reveal underlying structure and allow a more accurate measurement of the VDE and ADE.

Our calculations and experiment have also supported the assumption that the phenolate rather than the carboxylate isomer is predominately formed by pCA using ESI and that this is also true for oCA and mCA.

Chapter 7

Outlook and Summary

We have developed a new instrument that combines VMI and ESI to measure the gas-phase electronic structure and dynamics of a wide variety of molecular anions.[1] This has been used successfully to measure the photodetachment spectra of a range of biological chromophore anions. When the work presented in this thesis began, there were few gas-phase experimental measurements of biological chromophore anions.[26,37,38] It was a field ripe for study and in a period of a few years the body of literature has grown to include multiple gas-phase measurements of model GFP and PYP chromophores complemented by numerous theoretical studies.[1–3,5,39,42–46,176]

We have studied model chromophores of GFP and CFP with nanosecond photoelectron spectroscopy and have measured the excited state decay of a GFP model chromophore using femtosecond time-resolved photoelectron spectroscopy.[1,2] Our first photodetachment measurements of the GFP and CFP model chromophores allowed us to identify the energy required to detach a single electron leaving the corresponding neutral radical in its ground and excited electronic states. Comparing these two chromophores allowed us to measure the effect of the phenol and indole moieties on each chromophore.[1] Both GFP and CFP contain an imidazolinone moiety which was not covered in our studie and for completeness the contribution of this imidazolinone moiety to the photodetachment spectra of both these chromophores should be investigated. We also identified that the VDE of the gas-phase GFP chromophore anion was above that of its $S_1 \leftarrow S_0$ transition. This was a starting point that initiated other studies of the model GFP chromophore anion from which it became apparent that there are still a number of

different processes that are needed to be untangled before the photophysics of the model GFP chromophore anion could be fully understood.

Our femtosecond time-resolved measurements have identified the intermediate excited states and dominant decay pathway, *via* a twisting of the briding bonds, of an isolated GFP model chromophore anion. The lifetimes of the gas-phase decay are in qualitative agreement with the same molecule in solution suggesting in both environments the decay pathway is the same. Identifying the radiationless relaxation route of the isolated chromophore will lead to better understanding of how the rigid structure of GFP prevents the excited state twisting motion.

We have highlighted the importance of indirect detachment *via* higher lying excited $1^1\pi\pi^*$ states of a model GFP chromophore at a wide range of wavelengths.[3] We found that between 350 nm and 315 nm resonance excitation of the $2^1\pi\pi^*$ state of the model GFP chromophore anion followed by autodetachment was an important pathway influencing the shape of the detachment spectra. We have also examined the effect of chemical modification on the photoelectron emission properties of the chromophore.[4] By introducing electron donating and electron withdrawing groups to the phenol moiety of the model GFP chromophore anion structure we were able to modify the VDE. The electron donating group destabilised the S_0 state and stabilised the D_0 state to give an overall decreased in the VDE compared to that of the unmodified GFP chromophore anion. The electron withdrawing group stabilised the S_0 state and destabilised the D_0 state to give an overall increase in the VDE compared to that of the unmodified GFP chromophore anion. It would be interesting to compaore if the effects seen in this work are similar to other electron donating and withdrawing groups. This includes not only the effect of weaker or stronger electron withdrawing or donating groups but whether what the effect of inductive or resonance effects would be. We noted possible anisotropy present in the photodetachment spectra of $pHBDI^-$ and DF-HBI^- but were unable to quantify the amount due to poor statitics, it would be interesting and relatively simple to reacquire these images for a longer period in order to confirm and quantify this observation.

PYP has been identified as an ideal candidate for studying biological anionic systems thanks to its comparatively small size (125 amino acids *vs.* 238 amino acids in GFP) and its chromophores molecular simplicity. We carried out a detailed study of the model PYP chromophore at a wide range of wavelengths and using three different isomers.[6] We also performed *ab ini-*

tio calculations to aid the interpretation of these results. The excited anion states have been demonstrated to have significant influence in the photodetachment spectra and thus accurate models of the photodetachment spectra must include these states in theoretical methods. Future complementary work could include measuring the action spectra of these coumaric acid isomers or to measure the photodetachment spectra of other model PYP chromophores. Such as the methoxy-courmaric acid chromophore where the carboxylate group has been replaced with a methoxy group, simplifying the deprotonation and providing a closer analogue of the actual PYP chromophore.

All the anionic chromophores studied in this thesis showed the effects of the anions excited states and the profound influence they had on the profile of the detachment spectra. We have used off-the-shelf computational methods to simulate the $S_0 \leftarrow D_0$ detachment spectra. These calculations only included the anion and radical ground states but to truly reproduce experimental results the effects of the S_n states of the anions must be included. Collaborators in Aarhus are currently working on simulating the effect of excited anion states on photodetachment spectra for the chemically substituted GFP chromophores. Any progress in this area could also be applied to our experimental results for the PYP chromophore anion.

There is still scope for improvement and development of our instrument and the experiment to enable us to collect a wider variety of data. We have identified that anion excited states must be considered when evaluating photodetachment spectra of biological chromophore anions. Our experiment lacks the ability to measure these but it does have the potential to accomplish these measurements, so we intend to add the capability to our experiment to measure photoelectron action spectra. We also have access to tunable femtosecond lasers which can be employed to measure time-resolved photodetachment spectra, to accomplish this would require improvements to the efficiency of data collection, due to the increased number of spectra that would need collecting. The internal ion temperature is currently an uncontrolled and critical variable in the experiments presented here. The inclusion of either measurement or control of ion temperature, *via* our linear ion trap, would allow us to quantify or exclude the effects of ion temperature on photodetachment spectra.

More ambitious extensions to the equipment, using nanospray, could enable us to transfer whole proteins into the gas-phase, this would be an exciting step in gas-phase biological

spectroscopy.[156,157] Measuring the photodetachment spectra of GFP or PYP in their entirety and being able to compare them with the isolated chromophore will hopefully allow a fuller understanding and greater exploitation of both proteins. Needless to say that a time-resolved measurement of the protein would be even more fascinating. There are some obstacles to be overcome such as cost, efficiency and spectral resolution but these are solvable problems. There is also the possibility of performing gas-phase measurements of the solution characteristics of these molecules using newly developed liquid jets,[204] and such experiments are currently being built in the group.

Appendix A

Error analysis

As mentioned in Chapter 2 the uncertainty in the energy calibrated x-axis is non-uniform due to the converting the axis from being proportional to velocity to proportional to energy. The table below demonstrates the difference in relative error associated with this conversion.

Values in the energy are scaled to the 152^{nd} pixel, which is the maximum of the I^- detachment peak at 315 nm. The relative error is calculated as the percentage of the expected value (Px^2) and difference between the squared value offset by five pixels and four pixels. This difference can be measured in either direction however the values converge to within a 0.01% difference by 0.1 eV.

Table A.1: Table showing estimated systematic errors due to choice of inversion centre. Reference against I^- image which has photodetachment energy 3.0590±0.0001 eV using photodetachment laser at 315±0.0002 nm. $\Delta(\mathrm{Px}-5)^2 = (\mathrm{Px}-5)^2_n$ - $(\mathrm{Px}-5)^2_{n-1}$

Px	Px^2	$(\mathrm{Px}-5)^2$	$\Delta(\mathrm{Px}-5)^2$	$\mathrm{Px}^2/[\Delta(\mathrm{Px}-5)^2]\%$	E (eV)	Err (eV)	Err × 2 (eV)
0	0	25	-	-	0	-	-
1	1	16	-9	900.00	0.000041	0.000365	0.000731
2	4	9	-7	175.00	0.000162	0.000284	0.000568
3	9	4	-5	55.56	0.000365	0.000203	0.000406
4	16	1	-3	18.75	0.000649	0.000122	0.000244
5	25	0	-1	4.00	0.001015	0.000043	0.000086
6	36	1	1	2.78	0.001461	0.000045	0.000090
7	49	4	3	6.12	0.001989	0.000125	0.000249
8	64	9	5	7.81	0.002597	0.000206	0.000412
9	81	16	7	8.64	0.003287	0.000288	0.000575
10	100	25	9	9.00	0.004059	0.000369	0.000739
⋮	⋮	⋮	⋮	⋮	⋮	⋮	⋮
219	47961	45796	427	0.89	1.946505	0.031575	0.063149
220	48400	46225	429	0.89	1.964322	0.031821	0.063643
221	48841	46656	431	0.88	1.982220	0.032069	0.064138
222	49284	47089	433	0.88	2.000200	0.032318	0.064635
223	49729	47524	435	0.87	2.018260	0.032567	0.065135
224	50176	47961	437	0.87	2.036402	0.032818	0.065636
225	50625	48400	439	0.87	2.054624	0.033070	0.066140
226	51076	48841	441	0.86	2.072928	0.033323	0.066646

Appendix B

Green Fluorescent Protein

Figure B.1: Stereoisomers of CFP about the exocyclic double bond

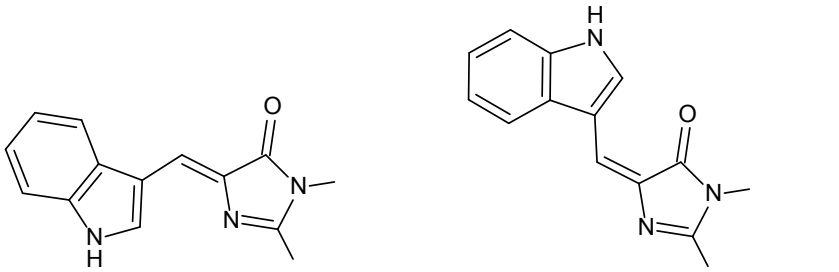

(a) *cis-trans*-CFP (b) *trans-trans*-CFP

Table B.1: Comparison of DFT optimised geometries for EPT calculations (eV)

Chromophore	Geom. Opt.	EPT Method	
		EPT/aug-cc-pVDZ	EPT/6-311++g**
GFP	B3LYP/6-311++G**	-2.582	-2.444
	TPSSh/6-311++G**	-2.592	-2.453
cis-CFP	B3LYP/6-311++G**	-2.604	-2.474
	TPSSh/6-311++G**	-2.608	-2.478
trans-CFP	TPSSh/6-311++G**	-2.598	-2.472
Phenol	B3LYP/6-311++G**	-2.166	-1.986
	TPSSh/6-311++G**	-2.177	-1.996
Indole	B3LYP/6-311++G**	-2.424	-2.539
	TPSSh/6-311++G**	-2.425	-2.273

B.0.1 Geometries

TPSSh/6-311++G** optimised geometries of the deprotonated anions employed in the EPT calculations and ezSpectrum simulations presented in the paper.

GFP

Atom	X	Y	Z
H	2.38145	-2.50316	0.00005
O	-2.57543	-2.32701	-0.00022
H	0.11816	-2.10617	-0.00016
H	4.73735	-1.75625	0.0004
C	2.61675	-1.43918	0.00013
H	-4.79061	-1.42538	0.00052
C	-2.2862	-1.12232	-0.00069
C	3.92514	-1.03403	0.00035
C	0.20603	-1.01939	-0.00016
C	1.52309	-0.51546	0.00002
C	-1.03028	-0.38715	-0.00041
C	-4.67537	-0.33852	0.00042
N	-3.25333	-0.08629	-0.00003
H	-5.1604	0.07545	-0.89123
H	-5.15989	0.07558	0.89228
C	4.29311	0.37295	0.00058
O	5.4884	0.76277	0.0004
C	1.86275	0.87663	0.00001
N	-1.28395	0.99314	-0.00057
C	-2.58035	1.12882	-0.00029
C	3.16643	1.29611	0.00021
H	1.04958	1.59477	-0.00017
H	3.40851	2.35611	0.00016
H	-3.94273	2.54733	-0.88387
C	-3.30138	2.43564	-0.00002
H	-3.94215	2.5473	0.88426
H	-2.56044	3.23578	-0.00025

Trans-CFP

Atom	X	Y	Z
C	-3.196457	1.222311	0
C	-2.439872	0.044992	0
C	-3.095434	-1.222283	0
C	-4.491216	-1.303177	0
C	-5.232394	-0.119765	0
C	-4.590286	1.132347	0
C	-1.019729	-0.259484	0
C	-0.982318	-1.700481	0
N	-2.180857	-2.273072	0
C	0	0.696188	0
C	1.392171	0.61767	0
C	2.285656	-0.525546	0
N	3.56805	0.072095	0
C	3.405064	1.455406	0
N	2.151463	1.803809	0
O	2.132894	-1.756692	0

C	4.543535	2.430991	0
C	4.765107	-0.740579	0
H	5.516974	1.935055	0
H	4.491219	3.076448	0.882826
H	4.491219	3.076448	-0.882826
H	5.649537	-0.102128	0
H	4.783999	-1.385421	-0.884263
H	4.783999	-1.385421	0.884263
H	-0.340853	1.732371	0
H	-2.714943	2.198002	0
H	-5.188342	2.040341	0
H	-6.318816	-0.163051	0
H	-4.979485	-2.273935	0
H	-0.071206	-2.286529	0

Cis-CFP

Atom	X	Y	Z
C	3.24657	1.0414	0
C	2.44604	-0.10724	0
C	3.05673	-1.39854	0
C	4.44856	-1.53022	0
C	5.23231	-0.37479	0
C	4.63555	0.89986	0
N	2.10579	-2.41691	0
C	0.93071	-1.79677	0
C	1.01884	-0.36162	0
C	0	0.59708	0
C	-1.38135	0.44809	0
N	-2.09342	-0.75918	0
C	-3.35804	-0.44588	0
N	-3.5716	0.93072	0
C	-2.30603	1.56692	0
O	-2.17344	2.80035	0
C	-4.79691	1.69947	0
C	-4.4626	-1.45942	0
H	-5.45334	-0.99937	0
H	-4.38416	-2.10226	0.88237
H	-4.38416	-2.10226	-0.88237
H	-5.65849	1.03074	0
H	-4.83951	2.34292	-0.88461
H	-4.83951	2.34292	0.88461
H	0.3133	1.64126	0
H	2.80103	2.03377	0
H	5.26622	1.78549	0
H	6.31642	-0.45738	0
H	0.00098	-2.35285	0
H	4.90099	-2.51824	0

Phenol

Atom	X	Y	Z
O	-2.35144	0	0.00029
C	-1.07878	0	-0.00069
H	-0.83065	-2.1553	0.00009

H	-0.83065	2.1553	0.00009
C	-0.28773	-1.21159	-0.00009
C	-0.28773	1.21159	-0.00009
C	1.10162	-1.20057	0.00013
C	1.10162	1.20057	0.00013
H	1.63824	-2.15076	0.00034
H	1.63824	2.15076	0.00034
C	1.83081	0	0.00005
H	2.91751	0	0.00027

Indole

Atom	X	Y	Z
H	-0.97173	2.51821	-0.00001
H	2.08108	2.12509	-0.00007
C	-0.93976	1.42871	0
C	1.66579	1.1234	-0.00004
H	-3.08215	1.22272	0.00001
C	0.29416	0.74782	-0.00001
C	-2.12695	0.70061	0.00001
H	3.45448	-0.19925	0.00013
C	2.37155	-0.08845	0.00009
C	0.30922	-0.70278	0
C	-2.10908	-0.71475	0.00002
N	1.58521	-1.19826	-0.00007
H	-3.05125	-1.2599	0.00001
C	-0.90443	-1.41402	0.00001
H	-0.88993	-2.50231	-0.00001

TPSSh/6-311++G** optimised geometries of the deprotonated radicals employed in the ezSpectrum simulations presented in the paper.

GFP

Atom	X	Y	Z
H	2.39066	-2.52108	0.00009
O	-2.54711	-2.31638	-0.0002
H	0.11769	-2.13545	-0.00012
H	4.74857	-1.73525	0.00031
C	2.62215	-1.45934	0.00011
H	-4.826	-1.38721	0.00043
C	-2.29222	-1.12363	-0.00048
C	3.91767	-1.0381	0.00024
C	0.21275	-1.05155	-0.00011
C	1.52679	-0.52942	0.00001
C	-1.00097	-0.3869	-0.00026
C	-4.67845	-0.30645	0.00028
N	-3.24091	-0.08379	-0.00005
H	-5.13991	0.12208	-0.89278
H	-5.13954	0.12229	0.89344
C	4.24544	0.38623	0.00034
O	5.42325	0.78675	0.00033
C	1.82579	0.87707	0.00001
N	-1.2427	0.97247	-0.00036
C	-2.55187	1.1121	-0.0002

H	0.99627	1.57383	-0.00009
C	3.11601	1.31489	0.00014
H	3.35679	2.37281	0.00013
H	-3.88991	2.52953	-0.88312
C	-3.25017	2.42578	-0.00003
H	-3.88953	2.5295	0.88335
H	-2.50649	3.2212	-0.00017

Cis-CFP

Atom	X	Y	Z
C	3.22866	1.15554	0
C	2.45636	-0.00488	0
C	3.07405	-1.2786	0
C	4.45249	-1.41037	0
C	5.22431	-0.23613	0
C	4.62344	1.02586	0
N	2.11458	-2.32321	0
C	0.9482	-1.74115	0
C	1.02722	-0.27412	0
C	0	0.65531	0
C	-1.3779	0.40821	0
N	-2.01291	-0.8054	0
C	-3.31144	-0.54951	0
N	-3.6037	0.79626	0
C	-2.37824	1.49597	0
O	-2.26797	2.71339	0
C	-4.88366	1.49209	0
C	-4.33564	-1.63372	0
H	-5.35725	-1.25491	0
H	-4.19254	-2.2655	0.88081
H	-4.19254	-2.2655	-0.88081
H	-5.69575	0.76768	0
H	-4.9581	2.1237	-0.88747
H	-4.9581	2.1237	0.88747
H	0.26309	1.71082	0
H	2.77192	2.14085	0
H	5.24466	1.91517	0
H	6.30698	-0.31028	0
H	4.91545	-2.39092	0
H	0.02302	-2.3025	0

Phenol

Atom	X	Y	Z
O	-2.30372	0	-0.00019
C	-1.04604	0	-0.00009
H	-0.85678	-2.1644	-0.00004
H	-0.85678	2.1644	-0.00004
C	-0.29053	-1.23937	-0.00001
C	-0.29053	1.23938	-0.00001
C	1.08688	-1.22493	0.00008
C	1.08688	1.22493	0.00008
H	1.64437	-2.15611	0.00012
H	1.64437	2.15611	0.00012

C	1.78424	0	0.00013
H	2.86923	0	0.00022

Indole

Atom	X	Y	Z
H	0.99757	2.50801	0.00007
H	-2.03487	2.14336	-0.00012
C	0.95738	1.42318	0.00006
C	-1.63533	1.13706	-0.00011
H	3.10021	1.17517	0.00006
C	-0.26348	0.74216	0
C	2.14111	0.66879	0.00005
H	-3.46577	-0.16992	0.00015
C	-2.38494	-0.08737	0.00008
C	-0.29562	-0.68335	-0.00002
C	2.09734	-0.72532	0.00001
N	-1.62437	-1.16727	-0.00006
H	3.02533	-1.28769	0
C	0.86836	-1.42356	-0.00002
H	0.83917	-2.5076	-0.00004

B.1 Modified GFP Chromophore Anions

B.1.1 Solution Phase Absorption Spectra

Figure B.2 shows a UV/visible absorption spectra obtained by Lijuan Zhang whilst working in the Fielding research group. Ms. Zhang also synthesised the three molecules studied in Chapter 4, pHBDI, DF-HBI and DM-HBI. They were synthesised following a literature synthesis detailed in the work of Jaffrey *et al.*.[136]

Details of the experimental methodology of the solution UV/visible absorption measurements are as follows as taken from Ms. Zhang's undergraduate project report.

> Methanol (MeOH) solvent was purchased from Aldrich. Acid and alkaline aqueous solutions were prepared from deionized water and hydrochloric acid (∼37%, Aldrich) and sodium hydroxide pellets (Aldrich). The recrystallized products were prepared separately in various methanol-water (1/1 vol) solutions at different pH values: 1.00, 7.24/7.53, 13.00. Ultraviolet-visible (UV-vis) spectra were measured on a Lambda 25 UV/VIS spectrophotometer supplied by Perkin Elmer precisely.

Figure B.2: UV/Vis absorption spectra for DM-HBI (black), pHBDI (red) and DF-HBI (blue) at pH 1 (top), 7 (middle) and 13 (bottom). Measurements taken in 1:1 MeOH:H_2O.

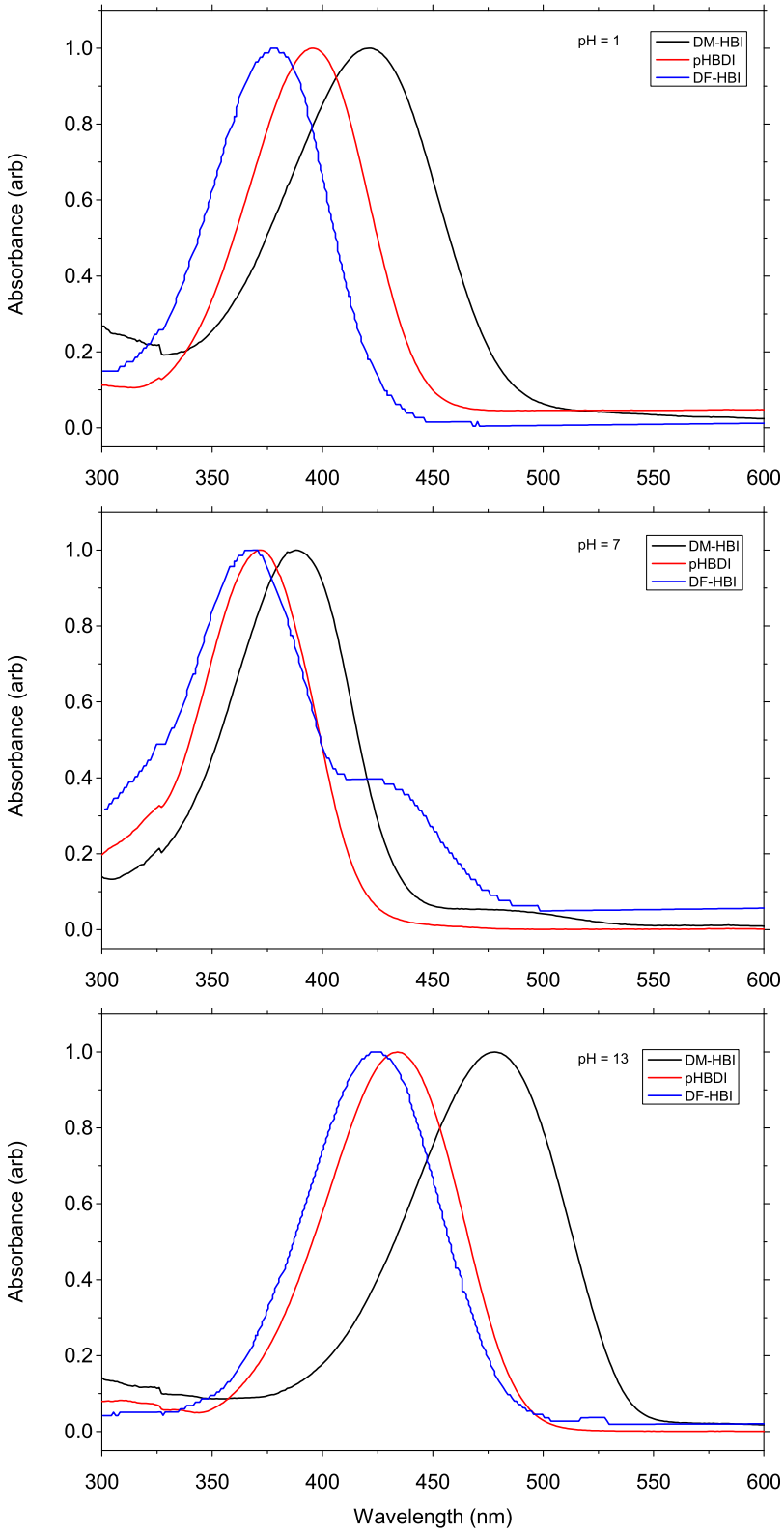

B.1.2 Calculation Benchmarks

Table B.2: D_0-S_0 VDEs and pole strengths (in parentheses) for pHBDI$^-$.

Method	Geometry	eBE/eV
EPT/6-311G	B3LYP/6-311G	2.08 (0.88)
EPT/6-311++G(d,p)	B3LYP/6-311++G(d,p)	2.44 (0.88)
EPT/6-311++G(3df,3pd)	B3LYP/6-311++G(3df,3pd)	2.78 (0.87)
EPT/6-311G	cam-B3LYP/6-311G	2.06 (0.88)
EPT/6-311++G(d,p)	cam-B3LYP/6-311++G(d,p)	2.43 (0.88)
EPT/6-311++G(3df,3pd)	cam-B3LYP/6-311++G(3df,3pd)	2.76 (0.88)
EPT/6-311G	ωB97X-D/6-311G	2.05 (0.88)
EPT/6-311++G(d,p)	ωB97X-D/6-311++G(d,p)	2.42 (0.88)
EPT/6-311++G(3df,3pd)	ωB97X-D/6-311++G(3df,3pd)	2.75 (0.88)

B.2 Femtosecond Experimental Analysis

Figure B.3: A plot of the difference between the experimental and modelled photoelectron spectra, Figures 5.3(a) and (b) in the paper. The numerical scale is the same as that shown in Figure 5.3; however the colour scale has been adjusted to make the features more visible.

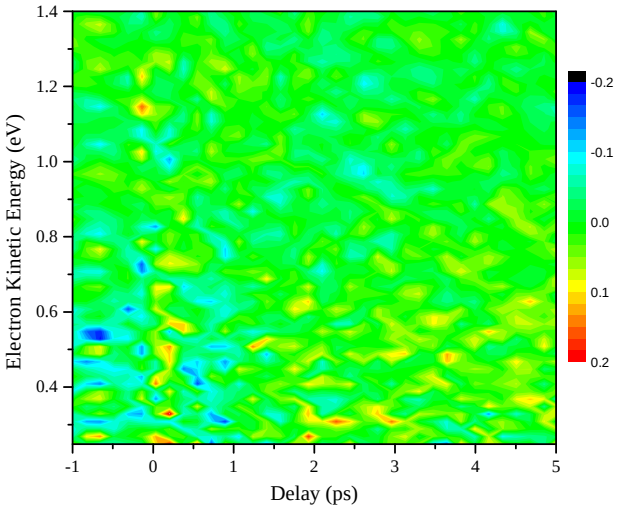

Figure B.4: Enlarged portion of the experimental spectra from Figure 5.3 in Chapter 5 in which each energy slice has been normalised to its maximum intensity.

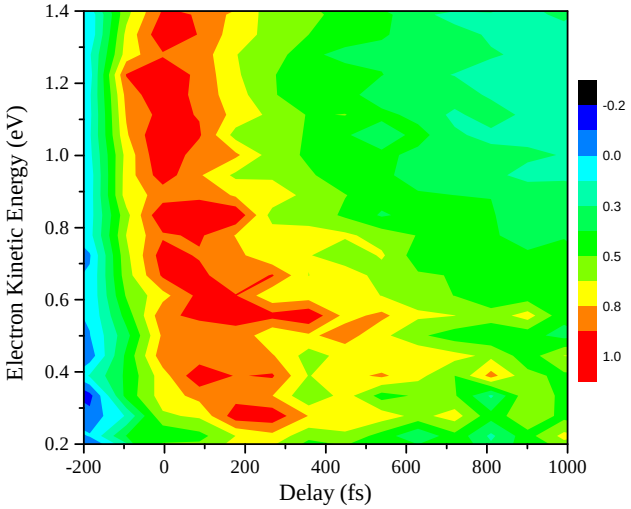

B.2.1 Global Fit

$$S(e\mathrm{KE}, t) = \sum_i g(t) \otimes c_i(e\mathrm{KE}) e^{-t/\tau_i} \tag{B.1}$$

When $t = 0$, this expression can be rewritten,

$$S(e\mathrm{KE}, 0) = \sum_i g(t) \otimes c_i(e\mathrm{KE}), \tag{B.2}$$

showing that the photoelectron spectrum of the initial excited state population is the sum of the decay associated spectra.

B.2.2 *Ab initio calculations*

Table B.3: Ground and excited state CASSCF/CASPT2 absolute energies for the model GFP chromophore anion and radical.

Structure	State	CASSCF (au)	CASPT2 energy (au)	reference weight[a]
FC	S_0	-641.58927	-643.44721	0.61
	S_1	-641.45926	-643.34034	0.60
	D_0	-641.54655	-643.33445	0.62
FS	S_0	-641.58238	-643.44597	0.61
	S_1	-641.46749	-643.34726	0.60
	D_0	-641.54238	-643.33390	0.62
TI	S_0	-641.53817	-643.40090	0.61
	S_1	-641.48565	-643.35810	0.60
	D_0	-641.52780	-643.31457	0.62

Table B.4: Table showing summary of wavefunction printout of CASSCF calculation from MOLCAS (2, fully occupied; 0, empty; u, spin up; d, spin down). [a] Showing contributions with a weight >0.05

Structure	State	Configuration	Coefficient	Weight[a]
FC	S_0	22222200000	-0.91210	0.83192
	S_1	22222ud0000	0.89274	0.79699
	D_0	22222u00000	-0.87599	0.76736
FS	S_0	22222200000	-0.90627	0.82133
	S_1	22222ud0000	-0.88658	0.78602
	D_0	22222u00000	-0.86119	0.74164
TI	S_0	22222200000	0.91354	0.83455
	S_1	22222ud0000	-0.91818	0.84306
	D_0	22222u00000	0.87890	0.77247

B.2.3 Geometries

```
  21
MOLPRO CASSCF FC OPT - 6-31G*
C    -0.0000002370  -0.1756586901  -3.6449534381
C    -0.0000115581  -1.2130418447  -2.6244916432
C    -0.0000090666  -0.9261949528  -1.3009138326
C     0.0000032666   0.4084248508  -0.8010151223
C     0.0000141330   1.4464387280  -1.7931161790
C     0.0000144860   1.1910978861  -3.1306844949
O    -0.0000020672  -0.4224742499  -4.8507991840
H    -0.0000210319  -2.2334389368  -2.9685878637
H    -0.0000177546  -1.7295936096  -0.5882556776
H     0.0000253239   2.4712517863  -1.4548318753
H     0.0000221027   1.9886546445  -3.8540971652
C     0.0000022601   0.7588204306   0.5612333256
C    -0.0000090123   0.0145864480   1.7284391915
N    -0.0000147168  -1.3859353746   1.8506379738
C    -0.0000033488  -1.6395162620   3.1082289545
N     0.0000612231  -0.4992745364   3.8927942288
C     0.0000014912   0.6103725689   3.0527359257
H     0.0000054025  -2.6205746547   3.5408467743
H    -0.0001295696  -0.4471726834   4.8829690575
O    -0.0000335734   1.7633833931   3.4396250818
H     0.0000062283   1.8194887882   0.7585874641


  21
MOLPRO FS OPT  CASSCF 6-31G*
C     0.2082302009  -0.0000077759  -3.6389737034
C     1.2174367975  -0.0000054089  -2.6214614587
C     0.9025713827   0.0000060232  -1.2596434070
C    -0.4431325006   0.0000162234  -0.8095029566
C    -1.4634473202   0.0000136133  -1.8328037023
C    -1.1717283031   0.0000029398  -3.1430252226
O     0.4389442661  -0.0000181655  -4.8621477481
H     2.2454018470  -0.0000130344  -2.9397817537
H     1.6880562790   0.0000071428  -0.5324911536
H    -2.4947607709   0.0000212380  -1.5170024342
H    -1.9517335747   0.0000017132  -3.8856008629
C    -0.8637766943   0.0000285421   0.5783029127
C    -0.0376888343   0.0000132371   1.7413909392
N     1.3424252424  -0.0000065649   1.7999541788
C     1.6683570282  -0.0000208791   3.0581587177
N     0.5591033865   0.0000534331   3.8808614950
C    -0.5784438741  -0.0000011350   3.0918784704
H     2.6676568923  -0.0000171618   3.4405228977
H     0.5450671299  -0.0002194297   4.8723971240
O    -1.7311563816  -0.0000456147   3.5056430495
H    -1.9197597083   0.0000398743   0.7753873181


  21
MOLPRO 5 Degrees OPT  CASSCF 6-31G*
C     0.2077584595   0.0156167349  -3.6384506798
```

```
C     1.2169651816  -0.0254692388  -2.6216764537
C     0.9021472124  -0.0499800831  -1.2600775026
C    -0.4429283660  -0.0316421648  -0.8094055256
C    -1.4631135982   0.0100926852  -1.8316733985
C    -1.1717425567   0.0317158363  -3.1419323124
O     0.4386056533   0.0376449605  -4.8614091835
H     2.2446723077  -0.0400660380  -2.9404716912
H     1.6875872651  -0.0804121396  -0.5334758883
H    -2.4941712598   0.0232621539  -1.5153279472
H    -1.9517105829   0.0633500608  -3.8838671511
C    -0.8633394081  -0.0645419647   0.5788968309
C    -0.0377012867  -0.0219036326   1.7412331310
N     1.3424910122  -0.0074303261   1.7993581099
C     1.6684458865   0.0294567621   3.0569649385
N     0.5592513458   0.0396515567   3.8798040023
C    -0.5783002247   0.0078670180   3.0915042466
H     2.6677073275   0.0479466886   3.4390015641
H     0.5452790271   0.0677465991   4.8709426534
O    -1.7308689585   0.0071571788   3.5056019382
H    -1.9193700973  -0.0635496671   0.7758737953


 21
MOLPRO 10 Degrees OPT  CASSCF 6-31G*
C     0.2062603676   0.0313086480  -3.6367275521
C     1.2153813537  -0.0532443862  -2.6222013010
C     0.9006507514  -0.1025972988  -1.2613627284
C    -0.4425833379  -0.0642424645  -0.8091459387
C    -1.4620435024   0.0220479288  -1.8281364347
C    -1.1716286560   0.0660835596  -3.1385451778
O     0.4377306073   0.0747263713  -4.8590520576
H     2.2422573900  -0.0837480568  -2.9424845354
H     1.6858315355  -0.1647388269  -0.5363956956
H    -2.4922987025   0.0503762985  -1.5102510080
H    -1.9515005489   0.1305734463  -3.8784252233
C    -0.8622439611  -0.1286735823   0.5807032192
C    -0.0377612678  -0.0431233221   1.7406808397
N     1.3425533676  -0.0122072270   1.7972145861
C     1.6687355809   0.0610424053   3.0530176015
N     0.5599717524   0.0786959993   3.8765156016
C    -0.5777410721   0.0148086477   3.0903618956
H     2.6679522277   0.0991411588   3.4337946901
H     0.5462490142   0.1365758303   4.8663646578
O    -1.7298119407   0.0120980651   3.5057147859
H    -1.9183798744  -0.1276876689   0.7774885460


 21
MOLPRO 20 Degrees OPT  CASSCF 6-31G*
C     0.1994797572   0.0573036372  -3.6300732532
C     1.2057277287  -0.1343394165  -2.6255244709
C     0.8906726472  -0.2286601376  -1.2676789491
C    -0.4434401030  -0.1275035003  -0.8086654274
C    -1.4562944205   0.0699813869  -1.8126802468
C    -1.1692839636   0.1548718482  -3.1243151770
```

```
O     0.4350805769   0.1396941033  -4.8500312429
H     2.2276007625  -0.2141018981  -2.9530012094
H     1.6726813249  -0.3691032970  -0.5498510634
H    -2.4817097888   0.1477952936  -1.4878065438
H    -1.9469795369   0.3002373757  -3.8548281840
C    -0.8603584253  -0.2420199582   0.5890388473
C    -0.0391209136  -0.0761023698   1.7379127075
N     1.3407517661   0.0060423601   1.7838206099
C     1.6704226915   0.1425652402   3.0329725959
N     0.5661554813   0.1510646211   3.8634060296
C    -0.5732882922   0.0172450205   3.0884022662
H     2.6697720560   0.2279061198   3.4059659185
H     0.5550977010   0.2590533892   4.8490807362
O    -1.7215977601  -0.0077781532   3.5127662856
H    -1.9165003019  -0.2597122279   0.7856777598


  21
MOLPRO 30 Degrees OPT  CASSCF 6-31G*
C     0.2119493752  -0.0471382262  -3.5938744553
C     1.0715622207  -0.5824858764  -2.5685296715
C     0.6882616622  -0.5984806416  -1.2300590464
C    -0.5377567742  -0.0587729915  -0.8091971568
C    -1.3642591176   0.5278335925  -1.8126801156
C    -1.0395298410   0.5202135172  -3.1271271248
O     0.5222954275  -0.0518602144  -4.8006413507
H     2.0135496997  -0.9992108591  -2.8784904458
H     1.3499741079  -1.0117540314  -0.4940540328
H    -2.3020074711   0.9573747010  -1.5007055948
H    -1.6950739760   0.9437087815  -3.8682451742
C    -0.9827052296  -0.0253760686   0.6218584645
C    -0.1024608259   0.0623528442   1.7150111235
N     1.2267094004   0.4643639957   1.6808814126
C     1.6493318470   0.4754438272   2.9068395160
N     0.6730912532   0.0745205783   3.8001909335
C    -0.4976006931  -0.1695081189   3.0951421942
H     2.6476288835   0.7071678150   3.2180292642
H     0.7210164321   0.0961674295   4.7905233510
O    -1.5597381747  -0.5074493785   3.6008802751
H    -1.9047332188  -0.5441432205   0.8400376660


  21
MOLPRO 40 Degrees OPT  CASSCF 6-31G*
C     0.2152512154  -0.0475525561  -3.5663800396
C     0.9622332778  -0.7660869522  -2.5580868071
C     0.5532423028  -0.7888076217  -1.2333266751
C    -0.5926576024  -0.0949439060  -0.8006076651
C    -1.2865481520   0.6763964963  -1.7801197810
C    -0.9419600879   0.6858078578  -3.0893468130
O     0.5529898434  -0.0459812340  -4.7626740265
H     1.8392518666  -1.2994027419  -2.8794670508
H     1.1282080662  -1.3320235736  -0.5075706080
H    -2.1507836622   1.2299711271  -1.4539981877
H    -1.5053310330   1.2455829906  -3.8153449624
```

```
C    -1.0281820188  -0.0559014314   0.6306952917
C    -0.1243646909   0.0712711735   1.7014949376
N     1.1802143445   0.5465598530   1.6238349046
C     1.6444362348   0.5710213044   2.8333523409
N     0.7233625708   0.1121335525   3.7559579358
C    -0.4586455549  -0.1885225188   3.0880395827
H     2.6394437631   0.8541601264   3.1121562273
H     0.8044457462   0.1270990065   4.7441790030
O    -1.4807448799  -0.5871597213   3.6327691340
H    -1.8834931621  -0.6756926786   0.8681058175


  21
MOLPRO 50 Degrees OPT  CASSCF 6-31G*
C     0.2129947750  -0.0435301137  -3.5453839941
C     0.8207076719  -0.9326484036  -2.5742820908
C     0.3999315666  -0.9556398637  -1.2583802532
C    -0.6330945164  -0.1122875260  -0.7918249039
C    -1.1788337143   0.8158298947  -1.7337195832
C    -0.8194364637   0.8418298562  -3.0364043037
O     0.5656848850  -0.0354527564  -4.7338501938
H     1.6077849701  -1.5775628815  -2.9225313799
H     0.8704060032  -1.6199764803  -0.5578103939
H    -1.9465784437   1.4811118567  -1.3784774778
H    -1.2723799595   1.5239379782  -3.7342159914
C    -1.0541347381  -0.0748971663   0.6357394078
C    -0.1336432825   0.0717826669   1.6922237811
N     1.1622533565   0.5658951231   1.5809627082
C     1.6549668831   0.6003819321   2.7785273822
N     0.7624540595   0.1309936064   3.7225398686
C    -0.4321549690  -0.1875955254   3.0817577074
H     2.6519577113   0.8996224452   3.0333640381
H     0.8654126165   0.1486649896   4.7086108236
O    -1.4340758349  -0.6002664340   3.6560366719
H    -1.8836073676  -0.7257804979   0.8838317154


  21
MOLPRO 60 Degrees OPT  CASSCF 6-31G*
C     0.2052193993  -0.0449801392  -3.5346377571
C     0.6372483826  -1.0788488734  -2.6096936262
C     0.2181219082  -1.0841739540  -1.2967563298
C    -0.6497649624  -0.0879578439  -0.7840004429
C    -1.0246295687   0.9629651292  -1.6849941427
C    -0.6570950090   0.9873196264  -2.9829021458
O     0.5599346654  -0.0462069250  -4.7199336131
H     1.2959018680  -1.8370130829  -2.9941904416
H     0.5575246900  -1.8532059832  -0.6279722169
H    -1.6632182572   1.7351120629  -1.2939717621
H    -0.9753504572   1.7704876016  -3.6479820265
C    -1.0651208548  -0.0526507675   0.6372957093
C    -0.1338235786   0.0726393880   1.6892694751
N     1.1763828653   0.5237624850   1.5582120305
C     1.6850079592   0.5482078218   2.7493599577
N     0.7894726016   0.1111675140   3.7046627624
```

```
C    -0.4232173167  -0.1733442788   3.0780722990
H     2.6935461601   0.8189604375   2.9910613897
H     0.9033418918   0.1297371399   4.6894599970
O    -1.4299434303  -0.5529455323   3.6702408626
H    -1.9243887639  -0.6627313042   0.8825223076


  21
MOLPRO 70 Degrees OPT  CASSCF 6-31G*
C     0.1894854871  -0.0499562051  -3.5382619409
C     0.3923424909  -1.1956755856  -2.6655717251
C    -0.0059274109  -1.1671644414  -1.3484299026
C    -0.6370573630  -0.0297218637  -0.7787282906
C    -0.7997647757   1.1120686113  -1.6360659137
C    -0.4351082609   1.1168347304  -2.9330915840
O     0.5323341310  -0.0733024387  -4.7252372935
H     0.8700062841  -2.0588475284  -3.0935334282
H     0.1627799013  -2.0197147209  -0.7168974000
H    -1.2602176601   1.9820210614  -1.2033999926
H    -0.5816958202   1.9772906679  -3.5615026261
C    -1.0552507794   0.0142723288   0.6355978962
C    -0.1235807232   0.0719393935   1.6931504292
N     1.2223863467   0.3996474977   1.5579530481
C     1.7308852138   0.3918059856   2.7496683329
N     0.7986291301   0.0476609902   3.7069743338
C    -0.4343491852  -0.1360022858   3.0803097357
H     2.7588514510   0.5769202960   2.9905346134
H     0.9118531705   0.0673616850   4.6917911115
O    -1.4715691720  -0.4187603730   3.6769365228
H    -1.9961439732  -0.4603713319   0.8703438709


  21
MOLPRO 80 Degrees OPT  CASSCF 6-31G*
C     0.1717209341  -0.0399179849  -3.5523045871
C     0.1305824442  -1.2466963533  -2.7407890160
C    -0.2365894894  -1.2005012261  -1.4156478965
C    -0.6049098790   0.0147191210  -0.7773721424
C    -0.5458498433   1.2063733667  -1.5826045374
C    -0.1917848711   1.2002777928  -2.8814685100
O     0.4948650716  -0.0738408602  -4.7438580972
H     0.4085469638  -2.1685140644  -3.2196973182
H    -0.2507197187  -2.1010156184  -0.8297630213
H    -0.8116101550   2.1301731936  -1.1013310894
H    -0.1605622133   2.1022260390  -3.4665125930
C    -1.0249866028   0.0656479005   0.6320820258
C    -0.1079575991   0.0540681880   1.7011014789
N     1.2699126104   0.2016345919   1.5713551218
C     1.7638827684   0.1696880064   2.7691772764
N     0.7876226728  -0.0204480209   3.7249167187
C    -0.4534359750  -0.0712906790   3.0888737743
H     2.8046090265   0.2365353126   3.0169816991
H     0.8938862288   0.0179035853   4.7099384092
O    -1.5235187627  -0.2012209285   3.6819566794
H    -2.0481952332  -0.1846636436   0.8569184663
```

```
  21
MOLPRO 80 Degrees OPT  CASSCF 6-31G*
C     0.1632101605   0.0154634352  -3.5632276045
C     0.0176229201  -1.2317572675  -2.8290119601
C    -0.3320963668  -1.2370592379  -1.4978455231
C    -0.5839736217  -0.0382006434  -0.7788227006
C    -0.4299462137   1.1937293801  -1.5120466928
C    -0.0850391613   1.2384627377  -2.8118206833
O     0.4756933070   0.0291277873  -4.7578244747
H     0.2071572880  -2.1425322434  -3.3683433625
H    -0.4252993392  -2.1681405997  -0.9698703590
H    -0.6097184625   2.1055721206  -0.9717502040
H     0.0229813446   2.1691868678  -3.3399657424
C    -1.0033106886  -0.0436401210   0.6294832507
C    -0.0992066190  -0.0111336016   1.7065287002
N     1.2862550786   0.0264929487   1.5835145488
C     1.7681407330   0.0517960638   2.7869033895
N     0.7736217219   0.0084530523   3.7413734771
C    -0.4629531046  -0.0065429546   3.0955097534
H     2.8089648172   0.0707163110   3.0422221070
H     0.8754290677   0.1087671675   4.7224636046
O    -1.5444799220  -0.0127189258   3.6825847896
H    -2.0560383150  -0.0688289421   0.8493285299
```

Appendix C

Photoactive Yellow Protein

C.0.4 Vertical Detachment Energy Calculations

Calculated VDEs for the coumaric acid isomers were calculated by Andreas Iskra for the requirements of his undergraduate masters project. Tables C.1 and C.2 are a summary of his work which is pertinent to this thesis.

Geometries of the coumaric acid anions were optimised using B3LYP/6-311++G(d,p) and VDE were calculated using EPT/6-311++G(2df,p). All calculations were done using the GAUSSIAN09 software package. Optimised geometries in XYZ format can be found below.

The VDE for $D_1 \leftarrow S_0$ was calculated by adding the energies of the excited states of the neutral to the fundamental VDEs ($D_0 \leftarrow S_0$). The energies of the first excited state of the radical are calculated using TD-DFT with B3LYP/6-311++G(2df,p) based on B3LYP/6-31++(d,p) optimised anion geometry.

Table C.1: Table showing the calculated VDE for the phenolate and carboxylate isomers of oCA^-, mCA^- and pCA^-. Calculations performed by A. Iskra.

Chromophore	Theory (eV)	
	Phenoxide	Carboxylate
oCA^-	2.76	4.61
mCA^-	2.74	4.85
pCA^-	2.98	4.64

Table C.2: Table showing the calculated $D_1 \leftarrow S_0$ VDE for oCA^-, mCA^- and pCA^-. Calculations performed by A. Iskra.

Chromophore	Theory (eV)
oCA^-	3.85
mCA^-	3.70
pCA^-	3.85

pCA anion

C	-2.38144200	-1.25551700	0.00008600
C	-1.02124700	-1.06946400	0.00011600
C	-0.43113100	0.23292100	0.00007800
C	-1.33940100	1.33567600	0.00004100
C	-2.70469400	1.17393600	0.00001600
C	-3.32421400	-0.14202300	-0.00002500
H	-2.80817000	-2.25604600	0.00014300
H	-0.36867300	-1.94058200	0.00019000
H	-0.91910100	2.34186600	0.00005200
H	-3.37129400	2.03318000	0.00000700
C	0.97052500	0.47161800	0.00006000
H	1.27004400	1.52067600	0.00008700
C	2.01279900	-0.43085500	-0.00006600
H	1.84831700	-1.50276600	-0.00009200
C	3.37811900	0.01236800	-0.00004200
O	-4.57326000	-0.31293200	-0.00017800
O	4.28123200	-1.04554800	-0.00005100
H	5.15128600	-0.61720500	-0.00004300
O	3.82224100	1.16459500	-0.00001300

mCA anion

C	-2.27648600	1.74014600	-0.00008200
C	-0.91318500	1.43031300	-0.00018100
C	-0.54051400	0.06194800	-0.00014800
C	-1.52932300	-0.93738100	-0.00001600
C	-2.94856000	-0.65893900	0.00007800
C	-3.26175100	0.75327800	0.00006600
H	-2.57964400	2.78773400	-0.00010000
H	-0.16621100	2.21740700	-0.00037100
H	-1.23347300	-1.98506700	0.00003500
C	0.84655900	-0.37029000	-0.00017700
H	1.00472800	-1.44855700	-0.00035900
C	1.96842600	0.39900200	0.00012300
H	1.92615100	1.48229700	0.00031200
C	3.29194200	-0.19912700	0.00001400
O	4.29008100	0.75553400	0.00027200
H	5.11979000	0.25220900	0.00026900
O	3.59386700	-1.38810000	-0.00020400
O	-3.83130500	-1.57321500	0.00017900
H	-4.31513000	1.02653300	0.00017500

```
oCA anion
 C                -2.53514000   -1.72436200    0.00011000
 C                -1.19469500   -1.38357000    0.00013300
 C                -0.74686900   -0.03752500    0.00007400
 C                -1.73153700    1.05902200   -0.00001900
 C                -3.12721100    0.64038700   -0.00011500
 C                -3.50318800   -0.68281000   -0.00000800
 H                -0.45172200   -2.17925300    0.00013600
 H                -3.86821300    1.43649200   -0.00022700
 C                 0.63926600    0.31428700    0.00004800
 H                 0.82891700    1.38671900    0.00019900
 C                 1.73249400   -0.51707100   -0.00020600
 H                 1.63701200   -1.59818200   -0.00036100
 C                 3.07986200   -0.00677500    0.00001200
 O                 4.02538000   -1.02972900   -0.00015100
 H                 4.87730000   -0.56617900    0.00012300
 O                 3.47645200    1.15827100    0.00019700
 H                -4.56262600   -0.94085000   -0.00002100
 H                -2.84474100   -2.76630700    0.00005700
 O                -1.41356000    2.27871500   -0.00005600
```

C.0.5 Simulated Detachment Spectra Calculations

Geometries

Photodetachment spectra were simulated using GAUSSIAN09 and Ezspectrum. Ground state anion and radical geometries were optimised for all the coumaric acid isomers (ortho, meta, and para) using B3LYP/aug-cc-pVDZ. The XYZ coordinates of these geometries can be found below.

```
oCA Anion S0
 C                     2.53209  -1.72713  -0.00017
 C                     1.19179  -1.38261  -0.00026
 C                     0.74786  -0.03431  -0.00036
 C                     1.73519   1.0607   -0.00094
 C                     3.13057   0.63755   0.00002
 C                     3.50358  -0.68748   0.00012
 H                     0.44524  -2.18039  -0.00015
 H                     3.87811   1.43375   0.00043
 C                    -0.63965   0.31837  -0.00008
 H                    -0.83037   1.39463  -0.00025
 C                    -1.73312  -0.51338   0.00035
 H                    -1.63676  -1.5986    0.00049
 C                    -3.08287  -0.00394   0.00062
 O                    -4.02563  -1.03241   0.00006
 H                    -4.87686  -0.57029  -0.0003
 O                    -3.48225   1.15746  -0.00011
 H                     4.56656  -0.94933   0.0005
 H                     2.84064  -2.77359  -0.00005
 O                     1.42047   2.2796    0.00049


oCA Radical D0
 C                     2.54872  -1.6865    0.00001
 C                     1.18698  -1.38636   0.
 C                     0.73099  -0.06044   0.
 C                     1.73056   1.03172   0.00001
 C                     3.14036   0.66128   0.00002
 C                     3.52759  -0.65479   0.00002
 H                     0.47043  -2.20735  -0.00001
 H                     3.85986   1.47963   0.00003
 C                    -0.66726   0.31836  -0.00001
 H                    -0.86509   1.39125  -0.00001
 C                    -1.72698  -0.52598  -0.00002
 H                    -1.62418  -1.61037  -0.00002
 C                    -3.10773  -0.0025   -0.00003
 O                    -4.01766  -1.01898   0.
 H                    -4.89602  -0.60595   0.00001
 O                    -3.43846   1.16594  -0.00001
 H                     4.58538  -0.9203    0.00003
 H                     2.8689   -2.72853   0.00001
 O                     1.3838    2.23214   0.00001
```

mCA-1 Anion S0

C	2.28197	1.74002	0.00001
C	0.91643	1.43541	0.00003
C	0.54029	0.0664	0.00003
C	1.52647	-0.93514	0.00003
C	2.95381	-0.66921	0.00009
C	3.26336	0.75036	0.00002
H	2.58982	2.79356	-0.00001
H	0.16564	2.22745	0.00003
H	1.22613	-1.9891	0.00001
C	-0.84951	-0.35872	0.00001
H	-1.01614	-1.44257	0.00002
C	-1.97248	0.4085	-0.00002
H	-1.93376	1.49866	-0.00004
C	-3.29584	-0.20036	-0.00004
O	-4.2953	0.74755	-0.00005
H	-5.11277	0.21938	-0.00005
O	-3.58496	-1.3883	-0.00002
O	3.82632	-1.57801	-0.00004
H	4.32554	1.01926	-0.00002

mCA-1 Radical D0

C	-2.29051	1.73995	0.00001
C	-0.93359	1.37352	-0.00005
C	-0.53407	0.00492	-0.00005
C	-1.52137	-0.97152	-0.00004
C	-2.93418	-0.6357	-0.00014
C	-3.28144	0.77484	0.00002
H	-2.55614	2.79751	0.00005
H	-0.17772	2.15741	-0.00005
H	-1.26676	-2.03182	-0.00001
C	0.87469	-0.4051	-0.00004
H	1.05859	-1.4822	-0.00004
C	1.95657	0.39703	-0.00003
H	1.89477	1.48413	-0.00002
C	3.31539	-0.18464	-0.00001
O	4.26767	0.78996	0.0001
H	5.12799	0.34012	0.00017
O	3.59425	-1.36684	0.00006
O	-3.81804	-1.53015	0.00006
H	-4.34067	1.0313	0.00009

mCA-2 Anion S0

C	-2.651961	-0.918431	0.000031
C	-1.214442	-0.784452	0.000013
C	-0.560204	0.45896	0.000007
C	-1.3133	1.661971	0.000011
C	-2.71203	1.579212	0.000014
C	-3.362789	0.349269	0.000019
O	-3.249752	-2.037789	0.00001
H	-0.63988	-1.712424	0.000007
H	-0.803787	2.626277	0.000007
C	0.889051	0.590418	-0.000003

```
 H                     1.270012   1.616124 -0.000006
 C                     1.828759  -0.393335 -0.000009
 H                     1.562272  -1.448515 -0.000007
 C                     3.247725  -0.075221 -0.000019
 O                     4.030747  -1.21405 -0.00003
 H                     4.943474  -0.888288 -0.00004
 O                     3.784242   1.026335 -0.000027
 H                    -3.304056   2.499697  0.000012
 H                    -4.45478   0.300816  0.000018


mCA-2 Radical D0
 C                     2.640637 -0.895228 -0.000013
 C                     1.194805 -0.794527 -0.000015
 C                     0.548191  0.438801 -0.000007
 C                     1.343878  1.615461 -0.000001
 C                     2.752376  1.560473 -0.000003
 C                     3.401954  0.343474 -0.000011
 O                     3.21343 -2.016538 -0.000026
 H                     0.646343 -1.735643 -0.000022
 H                     0.84726  2.586416  0.000004
 C                    -0.913235  0.589061 -0.000005
 H                    -1.29132  1.614455 -0.000008
 C                    -1.832704 -0.394227 -0.000003
 H                    -1.574183 -1.452156  0.000001
 C                    -3.273342 -0.064028 -0.000006
 O                    -4.036847 -1.191438  0.000045
 H                    -4.963475 -0.902409  0.000073
 O                    -3.75799  1.050444  0.000024
 H                     3.322479  2.489968  0.000001
 H                     4.48879  0.264069 -0.000013


pCA Anion S0
 C                    -2.3797   -1.25625  -0.00002
 C                    -1.01896  -1.06714  0.
 C                    -0.43232   0.23755  -0.00012
 C                    -1.34309   1.33864   0.00003
 C                    -2.70912   1.17338   0.00001
 C                    -3.32654  -0.14467  -0.0006
 H                    -2.8053   -2.26224   0.0002
 H                    -0.36282  -1.94066   0.00014
 H                    -0.92372   2.3496    0.0002
 H                    -3.37982   2.03534   0.00026
 C                     0.97044   0.47741  -0.00013
 H                     1.27002   1.53068  -0.00015
 C                     2.01262  -0.42616  -0.00012
 H                     1.84615  -1.50206  -0.00007
 C                     3.38087   0.01395  -0.00015
 O                    -4.5735   -0.31855   0.00053
 O                     4.27886  -1.05118   0.00017
 H                     5.14905  -0.62602   0.00031
 O                     3.8298    1.16163   0.00002
```

```
pCA Radical D0
 C                    -2.349271  -1.278444   0.000024
 C                    -0.996511  -1.077445  -0.000029
 C                    -0.442923   0.244887 -0.000002
 C                    -1.33947   1.358403 -0.00003
 C                    -2.699561   1.184267  0.000023
 C                    -3.28522  -0.153735  0.000344
 H                    -2.781202  -2.279209 -0.00005
 H                    -0.327038  -1.937007 -0.000116
 H                    -0.916687   2.364351 -0.000122
 H                    -3.388812   2.028663 -0.000055
 C                     0.97552   0.50165 -0.000068
 H                     1.282236   1.55054 -0.000085
 C                     1.975478  -0.420432 -0.000125
 H                     1.794102  -1.493791 -0.000117
 C                     3.386083   0.012199 -0.000208
 O                    -4.520115  -0.330242 -0.000052
 O                     4.23073  -1.055869  0.000032
 H                     5.13413  -0.700318  0.000167
 O                     3.784423   1.160749 -0.000015
```

Bibliography

1. McKay, A. R., Sanz, M. E., Mooney, C. R. S., Minns, R. S., Gill, E. M., Fielding, H. H. "Development of a new photoelectron spectroscopy instrument combining an electrospray ion source and photoelectron imaging" *Review of Scientific Instruments* **2010**, *81*.

2. Mooney, C. R. S., Sanz, M. E., McKay, A. R., Fitzmaurice, R. J., Aliev, A. E., Caddick, S., Fielding, H. H. "Photodetachment Spectra of Deprotonated Fluorescent Protein Chromophore Anions" *Journal Of Physical Chemistry A* **2012**, *116*, 7943–7949.

3. Mooney, C. R. S., Parkes, M. A., Zhang, L., Hailes, H. C., Simperler, A., Bearpark, M. J., Fielding, H. H. "Competition between photodetachment and autodetachment of the $2^1\pi\pi^*$ state of the green fluorescent protein chromophore anion" *The Journal of Chemical Physics* **2014**, *140*.

4. Mooney, C. R. S., Parkes, M. A., Zhang, L., Hailes, H. C., Bochenkova, A. V., Fielding, H. H. "Tuning the electron emission properties of the deprotonated green fluorescent protein chromophore anion" *In Preparation* **2014**.

5. Mooney, C. R. S., Horke, D. A., Chatterley, A. S., Simperler, A., Fielding, H. H., Verlet, J. R. R. "Taking the green fluorescence out of the protein: dynamics of the isolated GFP chromophore anion" *Chemical Science* **2013**, *4*, 921–927.

6. Mooney, C. R. S., Parkes, M. A., Iskra, A., Fielding, H. H. "Controlling Radical Formation in the Photoactive Yellow Protein Chromophore" *Angewandte Chemie International Edition* **2015**, DOI:10.1002/anie.201500549.

7. Shimomura, O., Johnson, F. H., Saiga, Y. "Extraction, purification and properties of aequorin, a bioluminescent protein from luminous hydromedusan, aequorea" *Journal of Cellular and Comparative Physiology* **1962**, *59*, 223.

8. Tsien, R. Y. "The Green Fluorescent Protein" *Annual Review of Biochemistry* **1998**, *67*, 509.

9. Patterson, G. H., Knobel, S. M., Sharif, W. D., Kain, S. R., Piston, D. W. "Use of the green fluorescent protein and its mutants in quantitative fluorescence microscopy" *Biophysical Journal* **1997**, *73*, 2782–2790.

10. Chalfie, M., Tu, Y., Euskirchen, G., Ward, W. W., Prasher, D. C. "Green fluorescent protein as a marker for gene-expression" *Science* **1994**, *263*, 802–805.

11. Lippincott-Schwartz, J., Snapp, E., Kenworthy, A. "Studying protein dynamics in living cells" *Nature Reviews Molecular Cell Biology* **2001**, *2*, 444.

12. Inouye, S., Tsuji, F. I. "Aequorea green fluorescent protein - expression of the gene and fluorescence characteristics of the recombinant protein" *FEBS letters* **1994**, *341*, 277–280.

13. Heim, R., Prasher, D. C., Tsien, R. Y. "Wavelength Mutations And Posttranslational Autoxidation Of Green Fluorescent Protein" *Proceedings of the National Academy of Sciences of the United States Of America* **1994**, *91*, 12501.

14. Tsien, R. "Constructing and Exploiting the Fluorescent Protein Paintbox (Nobel Lecture)" *Angewandte Chemie International Edition* **2009**, *48*, 5612–5626.

15. Cubitt, A. B., Heim, R., Adams, S. R., Boyd, A. E., Gross, L. A., Tsien, R. Y. "Understanding, Improving And Using Green Fluorescent Proteins" *Trends In Biochemical Sciences* **1995**, *20*, 448.

16. Heim, R., Cubitt, A. B., Tsien, R. Y. "Improved green fluorescence" *Nature* **1995**, *373*, 663–664.

17. Heim, R., Tsien, R. Y. "Engineering green fluorescent protein for improved brightness, longer wavelengths and fluorescence resonance energy transfer" *Current Biology* **1996**, *6*, 178 – 182.

18. Yokoe, H., Meyer, T. "Spatial dynamics of GFP-tagged proteins investigated by local fluorescence enhancement" *Nature Biotechnology* **1996**, *14*, 1252.

19. Yang, F., Moss, L., Phillips, G. "The molecular structure of green fluorescent protein" *Nature Biotechnology* **1996**, *14*, 1246.

20. Niwa, H., Inouye, S., Hirano, T., Matsuno, T., Kojima, S., Kubota, M., Ohashi, M., Tsuji, F. I. "Chemical nature of the light emitter of the Aequorea green fluorescent protein" *Proceedings of the National Academy of Sciences of the United States Of America* **1996**, *93*, 13617.

21. Ward, W. W., Bokman, S. H. "Reversible denaturation of aequorea green-fluorescent protein - physical separation and characterization of the renatured protein" *Biochemistry* **1982**, *21*, 4535–4540.

22. Creemers, T. M. H., Lock, A. J., Subramaniam, V., Jovin, T. M., Volker, S. "Three photoconvertible forms of green fluorescent protein identified by spectral hole-burning" *Nature Structural Biology* **1999**, *6*, 557.

23. Chattoraj, M., King, B. A., Bublitz, G. U., Boxer, S. G. "Ultra-fast excited state dynamics in green fluorescent protein: Multiple states and proton transfer" *Proceedings of the National Academy of Sciences of the United States Of America* **1996**, *93*, 8362.

24. Ward, W. W., Prentice, H. J., Roth, A. F., Cody, C. W., Reeves, S. C. "Spectral perturbations of the aequorea green-fluorescent protein" *Photochemistry and Photobiology* **1982**, *35*, 803.

25. Lossau, H., Kummer, A., Heinecke, R., Pöllinger-Dammer, F., Kompa, C., Bieser, G., Jonsson, T., Silva, C. M., Yang, M. M., Youvan, D. C., Michel-Beyerle, M. E. "Time-resolved spectroscopy of wild-type and mutant Green Fluorescent Proteins reveals excited state deprotonation consistent with fluorophore-protein interactions" *Chemical Physics* **1996**, *213*, 1.

26. Fang, C., Frontiera, R. R., Tran, R., Mathies, R. A. "Mapping GFP structure evolution during proton transfer with femtosecond Raman spectroscopy" *Nature* **2009**, *462*, 200.

27. Kennis, J. T. M., Larsen, D. S., van Stokkum, N. H. M., Vengris, M., van Thor, J. J., van Grondelle, R. "Uncovering the hidden ground state of green fluorescent protein" *Proceedings of the National Academy of Sciences of the United States Of America* **2004**, *101*, 17988.

28. Zimmer, M. "Green fluorescent protein (GFP): Applications, structure, and related photophysical behavior" *Chemical Reviews* **2002**, *102*, 759.

29. Webber, N. M., Meech, S. R. "Electronic spectroscopy and solvatochromism in the chromophore of GFP and the Y66F mutant" *Photochemical & Photobiological Sciences* **2007**, *6*, 976–981.

30. He, X., Bell, A. F., Tonge, P. J. "Isotopic labeling and normal-mode analysis of a model green fluorescent protein chromophore" *Journal of Physical Chemistry B* **2002**, *106*, 6056–6066.

31. Dong, J., Solntsev, K. M., Tolbert, L. M. "Solvatochromism of the green fluorescence protein chromophore and its derivatives" *Journal of the American Chemical Society* **2006**, *128*, 12038–12039.

32. Litvinenko, K. L., Webber, N. M., Meech, S. R. "An ultrafast polarisation spectroscopy study of internal conversion and orientational relaxation of the chromophore of the green fluorescent protein" *Chemical Physics Letters* **2001**, *346*, 47–53.

33. Litvinenko, K. L., Webber, N. M., Meech, S. R. "Internal conversion in the chromophore of the green fluorescent protein: Temperature dependence and isoviscosity analysis" *Journal of Physical Chemistry A* **2003**, *107*, 2616–2623.

34. Webber, N. M., Litvinenko, K. L., Meech, S. R. "Radiationless relaxation in a synthetic analogue of the green fluorescent protein chromophore" *Journal of Physical Chemistry B* **2001**, *105*, 8036.

35. Vengris, M., van Stokkum, I. H. M., He, X., Bell, A. F., Tonge, P. J., van Grondelle, R., Larsen, D. S. "Ultrafast excited and ground-state dynamics of the green fluorescent protein chromophore in solution" *Journal of Physical Chemistry A* **2004**, *108*, 4587–4598.

36. Weber, W., Helms, V., McCammon, J. A., Langhoff, P. W. "Shedding light on the dark and weakly fluorescent states of green fluorescent proteins" *Proceedings of the National Academy of Sciences of the United States Of America* **1999**, *96*, 6177–6182.

37. Nielsen, S. B., Lapierre, A., Andersen, J. U., Pedersen, U. V., Tomita, S., Andersen, L. H. "Absorption spectrum of the green fluorescent protein chromophore anion in vacuo" *Physical Review Letters* **2001**, *87*.

38. Forbes, M. W., Jockusch, R. A. "Deactivation Pathways of an Isolated Green Fluorescent Protein Model Chromophore Studied by Electronic Action Spectroscopy" *Journal of the American Chemical Society* **2009**, *131*, 17038.

39. Forbes, M. W., Nagy, A. M., Jockusch, R. A. "Photofragmentation of and electron photodetachment from a GFP model chromophore in a quadrupole ion trap" *International Journal of Mass Spectrometry* **2011**, *308*, 155–166.

40. Horke, D. A., Verlet, J. R. R. "Photoelectron spectroscopy of the model GFP chromophore anion" *Physical Chemistry Chemical Physics* **2012**, *14*, 8511–8515.

41. Toker, Y., Rahbek, D. B., Klaerke, B., Bochenkova, A. V., Andersen, L. H. "Direct and indirect electron emission from the green fluorescent protein chromophore" *Physical Review Letters* **2012**, *109*.

42. Epifanovsky, E., Polyakov, I., Grigorenko, B., Nemukhin, A., Krylov, A. I. "Quantum Chemical Benchmark Studies of the Electronic Properties of the Green Fluorescent Protein Chromophore. 1. Electronically Excited and Ionized States of the Anionic Chromophore in the Gas Phase" *Journal of Chemical Theory and Computation* **2009**, *5*, 1895.

43. Zuev, D., Bravaya, K. B., Makarova, M. V., Krylov, A. I. "Effect of microhydration on the electronic structure of the chromophores of the photoactive yellow and green fluorescent proteins" *Journal Of Chemical Physics* **2011**, *135*, 194304.

44. Bravaya, K. B., Krylov, A. I. "On the photodetachment from the Green Fluorescent Protein Chromophore" *Journal of Physical Chemistry A* **2013**, *117*, 11815–11822.

45. Epifanovsky, E., Polyakov, I., Grigorenko, B., Nemukhin, A., Krylov, A. I. "The effect of oxidation on the electronic structure of the green fluorescent protein chromophore" *Journal of Chemical Physics* **2010**, *132*, 115104.

46. Martin, M. E., Negri, F., Olivucci, M. "Origin, nature, and fate of the fluorescent state of the green fluorescent protein chromophore at the CASPT2//CASSCF resolution" *Journal of the American Chemical Society* **2004**, *126*, 5452–5464.

47. Bravaya, K. B., Bochenkova, A. V., Granovskii, A. A., Nemukhin, A. V. "Modeling of the Structure and Electronic Spectra of Green Fluorescent Protein Chromophore" *Russian Journal of Physical Chemistry B* **2008**, *2*, 671.

48. Bravaya, K. B., Khrenova, M. G., Grigorenko, B. L., Nemukhin, A. V., Krylov, A. I. "Effect of Protein Environment on Electronically Excited and Ionized States of the Green Fluorescent Protein Chromophore" *Journal of Physical Chemistry B* **2011**, *115*, 8296–8303.

49. Das, A., Hasegawa, J., Miyahara, T., Ehara, M., Nakatsuji, H. "Electronic excitations of the green fluorescent protein chromophore in its protonation states: SAC/SAC-CI study" *Journal of Computational Chemistry* **2003**, *24*, 1421–1431.

50. Laino, T., Nifosi, R., Tozzini, V. "Relationship between structure and optical properties in green fluorescent proteins: a quantum mechanical study of the chromophore environment" *Chemical Physics* **2004**, *298*, 17–28.

51. Sinicropi, A., Andruniow, T., Ferre, N., Basosi, R., Olivucci, M. "Properties of the emitting state of the green fluorescent protein resolved at the CASPT2//CASSCF/CHARMM level" *Journal of the American Chemical Society* **2005**, *127*, 11534–11535.

52. Toniolo, A., Olsen, S., Manohar, L., Martinez, T. "Conical intersection dynamics in solution: the chromophore of Green Fluorescent Protein" *Faraday Discussions* **2004**, *127*, 149–163.

53. Huang, T.-w., Yang, L., Zhu, C., Lin, S. H. "Absorption and fluorescence spectra of the neutral and anionic green fluorescent protein chromophore: Franck-Condon simulation" *Chemical Physics Letters* **2012**, *541*, 110–116.

54. Dong, J., Solntsev, K. M., Tolbert, L. M. "Solvatochromism of the green fluorescence protein chromophore and its derivatives" *Journal of the American Chemical Society* **2006**, *128*, 12038–12039.

55. Voityuk, A. A., Michel-Beyerle, M. E., Rosch, N. "Protonation effects on the chromophore of green fluorescent protein. Quantum chemical study of the absorption spectrum" *Chemical Physics Letters* **1997**, *272*, 162.

56. Voityuk, A., Michel-Beyerle, M., Rosch, N. "Structure and rotation barriers for ground and excited states of the isolated chromophore of the green fluorescent protein" *Chemical Physics Letters* **1998**, *296*, 269.

57. Voityuk, A., Michel-Beyerle, M., Rosch, N. "Quantum chemical modeling of structure and absorption spectra of the chromophore in green fluorescent proteins" *Chemical Physics* **1998**, *231*, 13–25.

58. Helms, V., Winstead, C., Langhoff, P. W. "Low-lying electronic excitations of the green fluorescent protein chromophore" *Journal of Molecular Structure-Theochem* **2000**, *506*, 179–189.

59. Sprenger, W. W., Hoff, W. D., Armitage, J. P., Hellingwerf, K. J. "The eubacterium ectothiorhodospira-halophila is negatively phototactic, with a wavelength dependence that fits the absorption-spectrum of the photoactive yellow protein" *Journal of Bacteriology* **1993**, *175*, 3096–3104.

60. Meyer, T. E. "Isolation and characterization of soluble cytochromes, ferredoxins and other chromophoric proteins from the halophilic phototrophic bacterium ectothiorhodospira-halophila" *Biochimica et Biophysica Acta* **1985**, *806*, 175–183.

61. van Beeumen, J. J., Devreese, B. V., van Bun, S. M., Hoff, W. D., Hellingwerf, K. J., Meyer, T. E., Mcree, D. E., Cusanovich, M. A. "Primary structure of a photoactive yellow protein from the phototrophic bacterium ectothiorhodospira-halophila, with evidence for the mass and the binding-site of the chromophore" *Protein Science* **1993**, *2*, 1114–1125.

62. Dux, P., Rubinstenn, G., Vuister, G. W., Boelens, R., Mulder, F. A. A., Hard, K., Hoff, W. D., Kroon, A. R., Crielaard, W., Hellingwerf, K. J., Kaptein, R. "Solution structure and backbone dynamics of the photoactive yellow protein" *Biochemistry* **1998**, *37*, 12689–12699.

63. Meyer, T. E., Yakali, E., Cusanovich, M. A., Tollin, G. "Properties of a water-soluble, yellow protein isolated from a halophilic phototrophic bacterium that has photochemical activity analogous to sensory rhodopsin" *Biochemistry* **1987**, *26*, 418–423.

64. Hoff, W. D., van Stokkum, I. H. M., van Ramesdonk, H. J., van Brederode, M. E., Brouwer, A. M., Fitch, J. C., Meyer, T. E., van Grondelle, R., Hellingwerf, K. J. "Measurement and global analysis of the absorbency changes in the photocycle of the photoactive yellow protein from ectothiorhodospira-halophila" *Biophysical Journal* **1994**, *67*, 1691–1705.

65. Changenet-Barret, P., Espagne, A., Katsonis, N., Charier, S., Baudin, J. B., Jullien, L., Plaza, P., Martin, M. M. "Excited-state relaxation dynamics of a PYP chromophore model in solution: influence of the thioester group" *Chemical Physics Letters* **2002**, *365*, 285–291.

66. Hellingwerf, K. J., Hendriks, J., Gensch, T. "Photoactive Yellow Protein, a new type of photoreceptor protein: Will this "yellow lab" bring us where we want to go?" *Journal Of Physical Chemistry A* **2003**, *107*, 1082–1094.

67. Changenet-Barret, P., Espagne, A., Plaza, P., Hellingwerf, K. J., Martin, M. M. "Investigations of the primary events in a bacterial photoreceptor for photomotility: photoactive yellow protein (PYP)" *New Journal OF Chemistry* **2005**, *29*, 527–534.

68. Genick, U. K., Soltis, S. M., Kuhn, P., Canestrelli, I. L., Getzoff, E. D. "Structure at 0.85 angstrom resolution of an early protein photocycle intermediate" *Nature* **1998**, *392*, 206–209.

69. Meyer, T. E., Devanathan, S., Woo, T., Getzoff, E. D., Tollin, G., Cusanovich, M. A. "Site-specific mutations provide new insights into the origin of pH effects and alternative spectral forms in the photoactive yellow protein from Halorhodospira halophila" *Biochemistry* **2003**, *42*, 3319–3325.

70. Brudler, R., Meyer, T. E., Genick, U. K., Devanathan, S., Woo, T. T., Millar, D. P., Gerwert, K., Cusanovich, M. A., Tollin, G., Getzoff, E. D. "Coupling of hydrogen bonding to chromophore conformation and function in photoactive yellow protein" *Biochemistry* **2000**, *39*, 13478–13486.

71. Gromov, E. V., Burghardt, I., Hynes, J. T., Koeppel, H., Cederbaum, L. S. "Electronic structure of the photoactive yellow protein chromophore: Ab initio study of the low-lying excited singlet states" *Journal of Photochemistry and Photobiology A-Chemistry* **2007**, *190*, 241–257.

72. Nielsen, I. B., Boye-Peronne, S., El Ghazaly, M. O. A., Kristensen, M. B., Nielsen, S. B., Andersen, L. H. "Absorption spectra of photoactive yellow protein chromophores in vacuum" *Biophysical Journal* **2005**, *89*, 2597–2604.

73. Rajput, J., Rahbek, D. B., Aravind, G., Andersen, L. H. "Spectral Tuning of the Photoactive Yellow Protein Chromophore by H-Bonding" *Biophysical Journal* **2010**, *98*, 488–492.

74. Putschoegl, M., Zirak, P., Penzkofer, A. "Absorption and emission behaviour of trans-p-coumaric acid in aqueous solutions and some organic solvents" *Chemical Physics* **2008**, *343*, 107–120.

75. Rahbek, D. B.; Ph.D. thesis; Department of Physics and Astronomy, University of Aarhus, Denmark; 2012.

76. Lee, I. R., Lee, W., Zewail, A. H. "Primary steps of the photoactive yellow protein: Isolated chromophore dynamics and protein directed function" *Proceedings of the National Academy of Sciences of the United States of America* **2006**, *103*, 258–262.

77. Zuev, D., Bravaya, K. B., Crawford, T. D., Lindh, R., Krylov, A. I. "Electronic structure of the two isomers of the anionic form of p-coumaric acid chromophore" *Journal of Chemical Physics* **2011**, *134*, 34310.

78. Sergi, A., Gruning, M., Ferrario, M., Buda, F. "Density Functional study of the photoactive yellow protein's chromophore" *Journal of Physical Chemistry B* **2001**, *105*, 4386–4391.

79. Rocha-Rinza, T., Christiansen, O., Rajput, J., Gopalan, A., Rahbek, D. B., Andersen, L. H., Bochenkova, A. V., Granovsky, A. A., Bravaya, K. B., Nemukhin, A. V., Christiansen, K. L., Nielsen, M. B. "Gas Phase Absorption Studies of Photoactive Yellow Protein Chromophore Derivatives" *Journal of Physical Chemistry A* **2009**, *113*, 9442–9449.

80. Gromov, E. V., Burghardt, I., Koeppel, H., Cederbaum, L. S. "Electronic structure of the PYP chromophore in its native protein environment" *Journal of the American Chemical Society* **2007**, *129*, 6798–6806.

81. Condon, E. "A theory of intensity distribution in band systems" *Physical Review* **1926**, *28*, 1182–1201.

82. Franck, J., Dymond, E. G. "Elementary processes of photochemical reactions" *Transactions of the Faraday Society* **1926**, *21*, 536–542.

83. Hollas, M. J. *High Resolution Spectroscopy*, 2nd ed.; Wiley: Chichester, 1998.

84. Zewail, A. H. "Femtochemistry: Atomic-Scale Dynamics of the Chemical Bond Using Ultrafast Lasers (Nobel Lecture)" *Angewandte Chemie International Edition* **2000**, *39*, 2586–2631.

85. Weinkauf, R., Schermann, J., de Vries, M., Kleinermanns, K. "Molecular physics of building blocks of life under isolated or defined conditions" *European Physical Journal D* **2002**, *20*, 309–316.

86. Suenram, R., Lovas, F. "Millimeter Wave Spectrum of Glycine" *Journal of Molecular Spectroscopy* **1978**, *72*, 372–382.

87. Hendricks, J., Lyapustina, S., deClercq, H., Snodgrass, J., Bowen, K. "Dipole bound, nucleic acid base anions studied via negative ion photoelectron spectroscopy" *Journal of Chemical Physics* **1996**, *104*, 7788–7791.

88. Rizzo, T. R., Park, Y. D., Levy, D. H. "A molecular-beam of tryptophan" *Journal of the American Chemical Society* **1985**, *107*, 277–278.

89. Cable, J. R., Tubergen, M. J., Levy, D. H. "Electronic spectroscopy of small tryptophan peptides in supersonic molecular-beams" *Journal of the American Chemical Society* **1988**, *110*, 7349–7355.

90. Cable, J. R., Tubergen, M. J., Levy, D. H. "Laser desorption molecular-beam spectroscopy - the electronic-spectra of tryptophan peptides in the gas-phase" *Journal of the American Chemical Society* **1987**, *109*, 6198–6199.

91. Miller, T., Zegarski, B., Sears, T., Bondybey, V. "Gas-phase Emission-spectra of Supercooled Organic Ions" *Journal of Physical Chemistry* **1980**, *84*, 3154–3156.

92. Powers, D., Hopkins, J., Smalley, R. "Laser Production of Jet-Cooled Radicals - Methoxy and Methoxy-Argon" *Journal of Physical Chemistry* **1981**, *85*, 2711–2713.

93. de Hoffmann, E., Stroobant, V. *Mass Spectrometry: Principles and Applications*; Wiley, 2007.

94. Fenn, J. B., Mann, M., Meng, C. K., Wong, S. F., Whitehouse, C. M. "Electrospray ionization for mass-spectrometry of large biomolecules" *Science* **1989**, *246*, 64–71.

95. Tanaka, K., Waki, H., Ido, Y., Akita, S., Yoshida, Y., Yoshida, T., Matsuo, T. "Protein and polymer analyses up to m/z 100 000 by laser ionization time-of-flight mass spectrometry" *Rapid Communications in Mass Spectrometry* **1988**, *2*, 151–153.

96. Nielsen, S. B. "Gas-phase studies of chromophore molecules in an electrostatic storage ring" *Physica Scripta* **2004**, *T110*, 332–335.

97. Wang, X.-B., Wang, L.-S. "Development of a low-temperature photoelectron spectroscopy instrument using an electrospray ion source and a cryogenically controlled ion trap" *Review of Scientific Instruments* **2008**, *79*, 73108.

98. Lecointre, J., Roberts, G. M., Horke, D. A., Verlet, J. R. R. "Ultrafast Relaxation Dynamics Observed Through Time-Resolved Photoelectron Angular Distributions" *Journal of Physical Chemistry A* **2010**, *114*, 11216–11224.

99. Talbot, F., Tabarin, T., Antoine, R., Broyer, M., Dugourd, P. "Photodissociation spectroscopy of trapped protonated tryptophan" *Journal of Chemical Physics* **2005**, *122*, 74310.

100. Larraillet, V., Antoine, R., Dugourd, P., Lemoine, J. "Activated-Electron Photodetachment Dissociation for the Structural Characterization of Protein Polyanions" *Analytical Chemistry* **2009**, *81*, 8410–8416.

101. Boyarkin, O., Mercier, S., Kamariotis, A., Rizzo, T. "Electronic spectroscopy of cold, protonated tryptophan and tyrosine" *Journal of the American Chemical Society* **2006**, *128*, 2816–2817.

102. Rizzo, T. R., Stearns, J. A., Boyarkin, O. V. "Spectroscopic studies of cold, gas-phase biomolecular ions" *International Reviews in Physical Chemistry* **2009**, *28*, 481–515.

103. Chingin, K., Balabin, R. M., Frankevich, V., Barylyuk, K., Nieckarz, R., Sagulenko, P., Zenobi, R. "Absorption of the green fluorescent protein chromophore anion in the gas phase studied by a combination of FTICR mass spectrometry with laser-induced photodissociation spectroscopy" *International Journal of Mass Spectrometry* **2011**, *306*, 241–245.

104. Frankevich, V., Barylyuk, K., Chingin, K., Nieckarz, R., Zenobi, R. "Native Biomolecules in the Gas Phase? The Case of Green Fluorescent Protein" *ChemPhysChem* **2013**, *14*, 929–935.

105. Wang, X., Woo, H., Wang, L. "Vibrational cooling in a cold ion trap: Vibrationally resolved photoelectron spectroscopy of cold C_{60}^- anions" *Journal of Chemical Physics* **2005**, *123*, 51106.

106. Gerlich, D., Horning, S. "Experimental Investigations of Radiative Association Processes as Related to Interstellar Chemistry" *Chemical Reviews* **1992**, *92*, 1509–1539.

107. Wang, Y., Tsai, C., Lee, Y., Chang, H., Jiang, J., Asvany, O., Schlemmer, S., Gerlich, D. "Investigations of protonated and deprotonated water clusters using a low-temperature 22-pole ion trap" *Journal of Physical Chemistry A* **2003**, *107*, 4217–4225.

108. Stearns, J. A., Guidi, M., Boyarkin, O. V., Rizzo, T. R. "Conformation-specific infrared and ultraviolet spectroscopy of tyrosine-based protonated dipeptides" *Journal of Chemical Physics* **2007**, *127*.

109. Fenn, J. B. "Electrospray wings for molecular elephants (Nobel lecture)" *Angewandte Chemie-International Edition* **2003**, *42*, 3871.

110. Yamashita, M., Fenn, J. B. "Negative-Ion Production With The Electrospray Ion-Source" *Journal of Physical Chemistry* **1984**, *88*, 4671.

111. Yamashita, M., Fenn, J. B. "Electrospray Ion-Source - Another Variation On The Free-Jet Theme" *Journal of Physical Chemistry* **1984**, *88*, 4451.

112. Iribarne, J. V., Thomson, B. A. "Evaporation Of Small Ions From Charged Droplets" *Journal of Chemical Physics* **1976**, *64*, 2287.

113. Dole, M., Mack, L. L., Hines, R. L., Mobley, R. C., Ferguson, L. D., Alice, M. B. "Molecular Beams of Macroions" *The Journal of Chemical Physics* **1968**, *49*, 2240.

114. Sannes-Lowery, K. A., Hu, P. F., Mack, D. P., Mei, H. Y., Loo, J. A. "HIV 1 Tat peptide binding do to TAR RNA by electrospray ionization mass spectrometry" *Analytical Chemistry* **1997**, *69*, 5130.

115. Eppink, A. T. J. B., Parker, D. H. "Velocity map imaging of ions and electrons using electrostatic lenses: Application in photoelectron and photofragment ion imaging of molecular oxygen" *Review of Scientific Instruments* **1997**, *68*, 3477–3484.

116. Horke, D. A., Roberts, G. M., Lecointre, J., Verlet, J. R. R. "Velocity-map imaging at low extraction fields" *Review of Scientific Instruments* **2012**, *83*.

117. Neumark, D. M. "Slow Electron Velocity-Map Imaging of Negative Ions: Applications to Spectroscopy and Dynamics†" *The Journal of Physical Chemistry A* **2008**, *112*, 13287–13301.

118. Gebhardt, C. R., Rakitzis, T. P., Samartzis, P. C., Ladopoulos, V., Kitsopoulos, T. N. "Slice imaging: A new approach to ion imaging and velocity mapping" *Review of Scientific Instruments* **2001**, *72*, 3848–3853.

119. Dribinski, V., Ossadtchi, A., Mandelshtam, V. A., Reisler, H. "Reconstruction of abel-transformable images: The Gaussian basis-set expansion abel transform method" *Review of Scientific Instruments* **2002**, *73*, 2634–2642.

120. Garcia, G. A., Nahon, L., Powis, I. "Two-dimensional charged particle image inversion using a polar basis function expansion" *Review of Scientific Instruments* **2004**, *75*, 4989–4996.

121. Bordas, C., Paulig, F., Helm, H., Huestis, D. "Photoelectron imaging spectrometry: Principle and inversion method" *Review of Scientific Instruments* **1996**, *67*, 2257–2268.

122. Roberts, G. M., Nixon, J. L., Lecointre, J., Wrede, E., Verlet, J. R. R. "Toward real-time charged-particle image reconstruction using polar onion-peeling" *Review of Scientific Instruments* **2009**, *80*.

123. Whitaker, B. J. *Imaging in Molecular Dynamics: Technology and Applications*; Cambridge University Press, 2003.

124. Frisch, Schlegel, Scuseria, Robb, Cheeseman, Scalmani, Barone, Mennucci, Petersson, Nakatsuji, Caricato, Li, Hratchian, Izmaylov, Bloino, Zheng, Sonnenberg, Hada, Ehara, Toyota, Fukuda, Hasegawa, Ishida, Nakajima, Honda, Kitao, Nakai, Vreven, Jr., M., Peralta, Ogliaro, Bearpark, Heyd, Brothers, Kudin, Staroverov, Kobayashi, Normand,

Raghavachari, Rendell, Burant, Iyengar, Tomasi, Cossi, Rega, Millam, Klene, Knox, Cross, Bakken, Adamo, Jaramillo, Gomperts, Stratmann, Yazyev, Austin, Cammi, Pomelli, Ochterski, Martin, Morokuma, Zakrzewski, Voth, Salvador, Dannenberg, Dapprich, Daniels, Farkas, Foresman, Ortiz, Cioslowski, , Fox; *GAUSSIAN 09, Revision A*; 2009; Gaussian Inc.: Wallingford CT.

125. Werner, H.-J., Knowles, P. J., Knizia, G., Manby, F. R., Schütz, M., Celani, P., Korona, T., Lindh, R., Mitrushenkov, A., Rauhut, G., Shamasundar, K. R., Adler, T. B., Amos, R. D., Bernhardsson, A., Berning, A., Cooper, D. L., Deegan, M. J. O., Dobbyn, A. J., Eckert, F., Goll, E., Hampel, C., Hesselmann, A., Hetzer, G., Hrenar, T., Jansen, G., Köppl, C., Liu, Y., Lloyd, A. W., Mata, R. A., May, A. J., McNicholas, S. J., Meyer, W., Mura, M. E., Nicklass, A., O'Neill, D. P., Palmieri, P., Pflüger, K., Pitzer, R., Reiher, M., Shiozaki, T., Stoll, H., Stone, A. J., Tarroni, R., Thorsteinsson, T., Wang, M., Wolf, A.; *MOLPRO, version 2010.1, a package of ab initio programs*; 2010; see http://www.molpro.net.

126. Karlstrom, G., Lindh, R., Malmqvist, P., Roos, B., Ryde, U., Veryazov, V., Widmark, P., Cossi, M., Schimmelpfennig, B., Neogrady, P., Seijo, L. "MOLCAS: a program package for computational chemistry" *Computational Materials Science* **2003**, *28*, 222–239.

127. Cederbaum, L. S. "One-body Green's function for atoms and molecules: theory and application" *Journal of Physics B: Atomic and Molecular Physics* **1975**, *8*, 290.

128. Zakrzewski, V. G., Ortiz, J. V. "Semidirect algorithms in electron propagator calculations" *International Journal of Quantum Chemistry* **1994**, 23–27.

129. Møller, C., Plesset, M. "Note on an approximation treatment for many-electron systems" *Physical Review* **1934**, *46*, 0618–0622.

130. Olsen, J. "The CASSCF Method: A Perspective and Commentary" *International Journal of Quantum Chemistry* **2011**, *111*, 3267–3272.

131. Hartree, D. R. "The wave mechanics of an atom with a non-Coulomb central field Part III Term values and intensities in series an optical spectra" *Proceedings of the Cambridge Philosophical Society* **1928**, *24*, 426–437.

132. Ditchfie, R., Hehre, W. J., Pople, J. A. "Self-consistent molecular-orbital methods .9. extended gaussian-type basis for molecular-orbital studies of organic molecules" *Journal of Chemical Physics* **1971**, *54*, 724.

133. Dunning, T. H. "Gaussian-basis sets for use in correlated molecular calculations .1. the atoms boron through neon and hydrogen" *Journal of Chemical Physics* **1989**, *90*, 1007.

134. Simons, J. "Molecular anions" *Journal of Physical Chemistry A* **2008**, *112*, 6401–6511.

135. Voliani, V., Bizzarri, R., Nifosi, R., Abbruzzetti, S., Grandi, E., Viappiani, C., Beltram, F. "Cis-trans photoisomerization of fluorescent-protein chromophores" *Journal of Physical Chemistry B* **2008**, *112*, 10714–10722.

136. Paige, J. S., Wu, K. Y., Jaffrey, S. R. "RNA Mimics of Green Fluorescent Protein" *Science* **2011**, *333*, 642–646.

137. Zhan, L.; Master's thesis; Department of Chemistry, University College London, United Kingdom; 2013.

138. Bajic, S. "Electrospray and atmospheric pressure chemical ionization mass spectrometer and ion source" *Patent Number US5756994A* **1998**.

139. Paul, W. "Electromagnetic traps for charged and neutral particles" *Angewandte Chemie-International Edition in English* **1990**, *29*, 739–748.

140. Mathieu, É "Mémoire sur le mouvement vibratoire d'une membrane de forme elliptique" *Journal de Mathématiques Pures et Appliqués* **1868**, *13*, 137–203.

141. Chernushevich, I. V. "Duty cycle improvement for a quadrupole-time-of-flight mass spectrometer and its use for precursor ion scans" *European Journal of Mass Spectrometry* **2000**, *6*, 471–479.

142. Alexander, J. D., Graham, L., Calvert, C. R., Kelly, O., King, R. B., Williams, I. D., Greenwood, J. B. "Determination of absolute ion yields from a MALDI source through calibration of an image-charge detector" *Measurement Science & Technology* **2010**, *21*, 45802.

143. Dahl, D. A. "SIMION for the personal computer in reflection" *International Journal of Mass Spectrometry* **2000**, *200*, 3–25.

144. Hager, J. W. "A new linear ion trap mass spectrometer" *Rapid Communications in Mass Spectrometry* **2002**, *16*, 512–526.

145. Chandler, D. W., Houston, P. L. "Two-dimensional imaging of state-selected photodissociation products detected by multiphoton ionization" *Journal of Chemical Physics* **1987**, *87*, 1445–1447.

146. Vrakking, M. J. J. "An iterative procedure for the inversion of two-dimensional ion/photoelectron imaging experiments" *Review of Scientific Instruments* **2001**, *72*, 4084–4089.

147. Manzhos, S., Loock, H. P. "Photofragment image analysis using the Onion-Peeling Algorithm" *Computer Physics Communications* **2003**, *154*, 76–87.

148. Sanov, A., Mabbs, R. "Photoelectron imaging of negative ions" *International Reviews in Physical Chemistry* **2008**, *27*, 53–85.

149. Roberts, G. M., Lecointre, J., Horke, D. A., Verlet, J. R. R. "Spectroscopy and dynamics of the 7,7,8,8-tetracyanoquinodimethane radical anion" *Physical Chemistry Chemical Physics* **2010**, *12*, 6226–6232.

150. Tian, Z., Wang, X.-B., Wang, L.-S., Kass, S. R. "Are Carboxyl Groups the Most Acidic Sites in Amino Acids? Gas-Phase Acidities, Photoelectron Spectra, and Computations on Tyrosine, p-Hydroxybenzoic Acid, and Their Conjugate Bases" *Journal of the American Chemical Society* **2009**, *131*, 1174–1181.

151. Cooper, J., Zare, R. N. "Angular distribution of photoelectrons" *Journal of Chemical Physics* **1968**, *48*, 942.

152. Jungmann, J. H., Gijsbertsen, A., Visser, J., Visschers, J., Heeren, R. M. A., Vrakking, M. J. J. "A new imaging method for understanding chemical dynamics: Efficient slice imaging using an in-vacuum pixel detector" *Review of Scientific Instruments* **2010**, *81*.

153. Hanstorp, D., Gustafsson, M. "Determination of the Electron-Affinity of Iodine" *Journal of Physics B* **1992**, *25*, 1773–1783.

154. *Angstrom WS-7 Wavemeter Specifications*; `http://www.highfinesse.com/en/wavelengthmeter/ws7.php`; Accessed: 2015-02-01.

155. Mock, R. S., Grimsrud, E. P. "The photodetachment-modulated pulsed electron-capture detector - iodide-specific and bromide-specific detection for the trace analysis of halocarbon mixtures - photodetachment cross-sections of the halides" *Analytical Chemistry* **1988**, *60*, 1684–1694.

156. Wilm, M., Mann, M. "Analytical properties of the nano-electrospray ion source" *Analytical Chemistry* **1996**, *68*, 1–8.

157. Wilm, M., Mann, M. "Electrospray and taylor-cone theory, doles beam of macromolecules at last" *International Journal of Mass Spectrometry* **1994**, *136*, 167–180.

158. Misteli, T., Spector, D. L. "Applications of the green fluorescent protein in cell biology and biotechnology" *Nature Biotechnology* **1997**, *15*, 961–964.

159. Bonsma, S., Purchase, R., Jezowski, S., Gallus, J., Konz, F., Volker, S. "Green and red fluorescent proteins: Photo- and thermally induced dynamics probed by site-selective spectroscopy and hole burning" *ChemPhysChem* **2005**, *6*, 838–849.

160. Andersen, L. H., Bluhme, H., Boye, S., Jorgensen, T. J. D., Krogh, H., Nielsen, I. B., Nielsen, S. B., Svendsen, A. "Experimental studies of the photophysics of gas-phase fluorescent protein chromophores" *Physical Chemistry Chemical Physics* **2004**, *6*, 2617.

161. Andersen, L. H., Lapierre, A., Nielsen, S. B., Nielsen, I. B., Pedersen, S. U., Pedersen, U. V., Tomita, S. "Chromophores of the green fluorescent protein studied in the gas phase" *European Physical Journal D* **2002**, *20*, 597.

162. Bogdanov, A. M., Mishin, A. S., Yampolsky, I. V., Belousov, V. V., Chudakov, D. M., Subach, F. V., Verkhusha, V. V., Lukyanov, S., Lukyanov, K. A. "Green fluorescent proteins are light-induced electron donors" *Nature Chemical Biology* **2009**, *5*, 459–461.

163. Niwa, H., Inouye, S., Hirano, T., Matsuno, T., Kojima, S., Kubota, M., Ohashi, M., Tsuji, F. I. "Chemical nature of the light emitter of the Aequorea green fluorescent protein" *Proceedings of the National Academy of Sciences of the United States of America* **1996**, *93*, 13617–13622.

164. Conyard, J., Kondo, M., Heisler, I. A., Jones, G., Baldridge, A., Tolbert, L. M., Solntsev, K. M., Meech, S. R. "Chemically Modulating the Photophysics of the GFP Chromophore" *Journal of Physical Chemistry B* **2011**, *115*, 1571–1576.

165. Boye, S. V., Nielsen, I. B., Nielsen, S. B., Krogh, H., Lapierre, A., Pedersen, H. B., Pedersen, S. U., Pedersen, U. V., Andersen, L. H. "Gas-phase absorption properties of a green fluorescent protein-mutant chromophore: The W7 clone" *Journal of Chemical Physics* **2003**, *119*, 338–345.

166. Olsen, S., Smith, S. C. "Bond selection in the photoisomerization reaction of anionic green fluorescent protein and kindling fluorescent protein chromophore models" *Journal of the American Chemical Society* **2008**, *130*, 8677–8689.

167. Sawin, K. E., Nurse, P. "Photoactivation of green fluorescent protein" *Current Biology* **1997**, *7*, R606–R607.

168. Elowitz, M. B., Surette, M. G., Wolf, P. E., Stock, J., Leibler, S. "Photoactivation turns green fluorescent protein red" *Current Biology* **1997**, *7*, 809–812.

169. Zheng, W. J., Nilles, J. M., Thomas, O. C., Bowen, K. H. "Photoelectron spectroscopy of nickel-benzene cluster anions" *Journal of Chemical Physics* **2005**, *122*, 44306.

170. Yang, X., Wang, X. B., Vorpagel, E. R., Wang, L. S. "Direct experimental observation of the low ionization potentials of guanine in free oligonucleotides by using photoelectron spectroscopy" *Proceedings of the National Academy of Sciences of the United States of America* **2004**, *101*, 17588–17592.

171. Tao, J. M., Perdew, J. P., Staroverov, V. N., Scuseria, G. E. "Climbing the density functional ladder: Nonempirical meta-generalized gradient approximation designed for molecules and solids" *Physical Review Letters* **2003**, *91*, 146401.

172. Mozhayskiy, V. A., Krylov, A. I.; 2012; ezSpectrum version 3.0.

173. Gunion, R. F., Gilles, M. K., Polak, M. L., Lineberger, W. C. "Ultraviolet photoelectron-spectroscopy of the phenide, benzyl and phenoxide anions, with abinitio calculations" *International Journal of Mass Spectrometry and Ion Processes* **1992**, *117*, 601.

174. Flores-Moreno, R., Melin, J., Dolgounitcheva, O., Zakrzewski, V. G., Ortiz, J. V. "Three Approximations to the Non-local and Energy-Dependent Correlation Potential in Electron Propagator Theory" *International Journal of Quantum Chemistry* **2010**, *110*, 706–715.

175. Mooney, C. R. S., Sanz, M. E., McKay, A. R., Fitzmaurice, R. J., Aliev, A. E., Caddick, S., Fielding, H. H. "Photodetachment Spectra of Deprotonated Fluorescent Protein Chromophore Anions - Supporting Information" *Journal of Physical Chemistry A* **2012**, *116*, 7943–7949.

176. West, C. W., Hudson, A. S., Cobb, S. L., Verlet, J. R. R. "Communication: Autodetachment versus internal conversion from the S-1 state of the isolated GFP chromophore anion" *Journal of Chemical Physics* **2013**, *139*.

177. Mandal, D., Tahara, T., Webber, N. M., Meech, S. R. "Ultrafast fluorescence of the chromophore of the green fluorescent protein in alcohol solutions" *Chemical Physics Letters* **2002**, *358*, 495–501.

178. Mandal, D., Tahara, T., Meech, S. R. "Excited-state dynamics in the green fluorescent protein chromophore" *Journal of Physical Chemistry B* **2004**, *108*, 1102–1108.

179. Rajput, J., Rahbek, D. B., Andersen, L. H., Rocha-Rinza, T., Christiansen, O., Bravaya, K. B., Erokhin, A. V., Bochenkova, A. V., Solntsev, K. M., Dong, J., Kowalik, J., Tolbert, L. M., Petersen, M. A., Nielsen, M. B. "Photoabsorption studies of neutral green fluorescent protein model chromophores in vacuo" *Physical Chemistry Chemical Physics* **2009**, *11*, 9996–10002.

180. Dong, J., Solntsev, K. M., Tolbert, L. M. "Activation and Tuning of Green Fluorescent Protein Chromophore Emission by Alkyl Substituent-Mediated Crystal Packing" *Journal of the American Chemical Society* **2009**, *131*, 662–670.

181. Frizler, M., Yampolsky, I. V., Baranov, M. S., Stirnberg, M., Guetschow, M. "Chemical introduction of the green fluorescence: imaging of cysteine cathepsins by an irreversibly locked GFP fluorophore" *Organic & Biomolecular Chemistry* **2013**, *11*, 5913–5921.

182. Baranov, M. S., Lukyanov, K. A., Borissova, A. O., Shamir, J., Kosenkov, D., Slipchenko, L. V., Tolbert, L. M., Yampolsky, I. V., Solntsev, K. M. "Conformationally Locked Chromophores as Models of Excited-State Proton Transfer in Fluorescent Proteins" *Journal of the American Chemical Society* **2012**, *134*, 6025–6032.

183. Lincke, K., Solling, T., Andersen, L. H., Klaerke, B., Rahbek, D. B., Rajput, J., Oehlenschlaeger, C. B., Petersen, M. A., Nielsen, M. B. "On the absorption of the phenolate chromophore in the green fluorescent protein-role of individual interactions" *Chemical Communications* **2010**, *46*, 734–736.

184. Nielsen, M. B., Andersen, L. H., Rocha-Rinza, T. "Absorption tuning of the green fluorescent protein chromophore: synthesis and studies of model compounds" *Monatshefte für Chemie* **2011**, *142*, 709–715.

185. Paige, J. S., Nguyen-Duc, T., Song, W., Jaffrey, S. R. "Fluorescence Imaging of Cellular Metabolites with RNA" *Science* **2012**, *335*, 1194.

186. Linderberg, C. J., Öhrn, Y. *Propagators in Quantum Chemistry*; John Wiley and Sons: Hoboken, NJ, 2004.

187. Zakrzewski, V. G., Dolgounitcheva, O., Zakjevskii, A. V., Ortiz, J. V. In *Annual Reports in Computational Chemistry, Vol 6*; Wheeler, RA, Ed.; Annual Reports in Computational Chemistry, Vol. 6; Elsevier: Sara Burgerhartstraat 25, PO BOX 211, 1000 AE Amsterdam, Netherlands, 2010; pp 79–94.

188. Yanai, T., Tew, D. P., Handy, N. C. "A new hybrid exchange-correlation functional using the Coulomb-attenuating method (CAM-B3LYP)" *Chemical Physics Letters* **2004**, *393*, 51–57.

189. Bochenkova, A. V., Andersen, L. H. "Ultrafast dual photoresponse of isolated biological chromophores: link to the photoinduced mode-specific non-adiabatic dynamics in proteins" *Faraday Discussions* **2013**, *163*, 297–319.

190. A. V. Bochenkova, B. Klærke, D. B. Rahbek, J. Rajput, Y. Toker, and L. H. Andersen "UV excited-state photoresponse of biochromophore negative ions" *unpublished* **2014**.

191. Meech, S. R. "Excited state reactions in fluorescent proteins" *Chemical Society Reviews* **2009**, *38*, 2922–2934.

192. Kummer, A. D., Kompa, C., Niwa, H., Hirano, T., Kojima, S., Michel-Beyerle, M. E. "Viscosity-dependent fluorescence decay of the GFP chromophore in solution due to fast internal conversion" *Journal of Physical Chemistry B* **2002**, *106*, 7554–7559.

193. Gepshtein, R., Huppert, D., Agmon, N. "Deactivation mechanism of the green fluorescent chromophore" *Journal of Physical Chemistry B* **2006**, *110*, 4434–4442.

194. Altoe, P., Bernardi, F., Garavelli, M., Orlandi, G., Negri, F. "Solvent effects on the vibrational activity and photodynamics of the green fluorescent protein chromophore: A quantum-chemical study" *Journal of the American Chemical Society* **2005**, *127*, 3952–3963.

195. Stolow, A., Bragg, A., Neumark, D. "Femtosecond time-resolved photoelectron spectroscopy" *Chemical Reviews* **2004**, *104*, 1719–1757.

196. Verlet, J. R. R. "Femtosecond spectroscopy of cluster anions: insights into condensed-phase phenomena from the gas-phase" *Chemical Society Reviews* **2008**, *37*, 505–517.

197. Filippi, C., Zicchedduu, M., Buda, F. "Absorption Spectrum of the Green Fluorescent Protein Chromophore: A Difficult Case for ab Initio Methods?" *Journal of Chemical Theory and Computation* **2009**, *5*, 2074.

198. Veryazov, V., Widmark, P. O., Serrano-Andres, L., Lindh, R., Roos, B. O. "MOLCAS as a development platform for quantum chemistry software" *International Journal of Quantum Chemistry* **2004**, *100*, 626–635.

199. Aquilante, F., De Vico, L., Ferre, N., Ghigo, G., Malmqvist, P.-A., Neograd y, P., Pedersen, T. B., Pitonak, M., Reiher, M., Roos, B. O., Serrano-Andres, L., Urban, M., Veryazov, V., Lindh, R. "Software News and Update MOLCAS 7: The Next Generation" *Journal of Computational Chemistry* **2010**, *31*, 224–247.

200. Kukura, P., McCamant, D. W., Yoon, S., Wandschneider, D. B., Mathies, R. A. "Structural Observation of the Primary Isomerization in Vision with Femtosecond-Stimulated Raman" *Science* **2005**, *310*, 1006–1009.

201. Ormo, M., Cubitt, A. B., Kallio, K., Gross, L. A., Tsien, R. Y., Remington, S. J. "Crystal structure of the Aequorea victoria green fluorescent protein" *Science* **1996**, *273*, 1392.

202. Smith, A. L. "Role of autoionization in molecular photoelectron spectra" *Philosophical Transactions of the Royal Society of London Series A-Mathematical and Physical Sciences* **1970**, *268*, 169.

203. Iskra, A.; Master's thesis; Department of Chemistry, University College London, United Kingdom; 2013.

204. Seidel, R., Thuermer, S., Winter, B. "Photoelectron Spectroscopy Meets Aqueous Solution: Studies from a Vacuum Liquid Microjet" *Journal of Physical Chemistry Letters* **2011**, *2*, 633–641.

Acronyms

4HCA *trans*-4-hydoxycinnamyl.

ADE adiabatic detachment energy.

aug-MCQDPT2 augmented Multi-configurational quasi-degenerate second order perturbation.

BASEX basis set expansion.

BBO β-barium borate.

BOA Born-Oppenheimer approximation.

CAM coulomb attenuating method.

CAS complete active space.

CASPT2 multi-configurational second-order perturbation theory.

CASSCF complete active space self consistent field.

CCD Charge Coupled Device.

CFP cyan fluorescent protein.

CI configuration interaction.

CIS configuration interaction singles.

CIS(D) configuration interaction singles and doubles.

DC Direct Current.

DF-HBI difluoro-hydroxybenzylidene-imidazolinone.

DF-HBI$^-$ deprotonated difluoro-hydroxybenzylidene-imidazolinone anion.

DFT density functional theory.

DM-HBI dimethoxy-benzylidene-imidazolinone.

DM-HBI$^-$ deprotonated dimethoxy-benzylidene-imidazolinone anion.

DNA deoxyribonucleic acid.

EAa adiabatic electron affinity.

eBE electron binding energy.

EI electron ionisation.

eKE photoelectron kinetic energy.

ELISA electrostatic storage ring for atomic physics.

EOM equations-of-motion.

EPT Electron Propagator Theory.

ESI electrospray ionisation.

ESPT excited state protein transfer.

FC Franck-Condon.

FS fluorescent state.

FT-ICR Fourier transform ion cyclotron resonance.

FWHM full-width half maximum.

GFP green fluorescent protein.

GGA Meta-generalized Gradient Approximation.

HBI$^-$ deprotonated *p*-hydroxybenzylidene-imidazolinone.

HF Hartree-Fock.

HF-SCF HF SCF.

HOMO Highest Occupied Molecular Orbital.

IC internal conversion.

IR infra-red.

ISC intersystem crossing.

IVR Intramolecular Vibrational Energy Redistribution.

KDP potassium dihydrogen phosphate.

LUMO Lowest Unoccupied Molecular Orbital.

MALDI matrix-assisted laser-desorption ionisation.

mCA *meta*-coumaric acid.

mCA$^-$ deprotonated *meta*-coumaric acid.

mCA$^-$-1 *s-cis trans meta*-Coumaric acid.

mCA$^-$-2 *s-trans trans meta*-Coumaric acid.

mCMe$^-$ deprotonated *meta*-methyl-coumaric acid.

MCP multichannel plate.

MM molecular mechanics.

MO molecular orbital.

MP Møller-Plesset.

nanoESI nanospray electrospray ionisation.

NMR nuclear magnetic resonance.

oCA *ortho*-coumaric acid.

oCA$^-$ deprotonated *ortho*-coumaric acid.

oCMe$^-$ deprotonated *ortho*-methyl-coumaric acid.

OVGF outer valence Green's function.

PAD photoelectron angular distribution.

pBASEX polar basis set expansion.

PC personal computer.

pCA *para*-coumaric acid.

pCA$^-$ deprotonated *para*-coumaric acid.

PCM polarisation continuum model.

pCM *trans*-methyl-*p*-coumarate.

pCM$^-$ deprotonated *trans*-methyl-*p*-coumarate.

pCMe$^-$ deprotonated *para*-methyl-coumaric acid.

pCT *trans*-thiophenyl-*p*-ccoumarate.

pCT$^-$ deprotonated *trans*-thiophenyl-*p*-coumarate.

PEEK polyether ether ketone.

PEI photoelectron imaging.

PES potential energy surface.

PES photoelectron spectroscopy.

pHBDI *p*-hydroxybenzylidene-imidazolinone.

pHBDI$^-$ deprotonated p-hydroxybenzylidene-imidazolinone anion.

PS potential switch.

PYP Photoactive Yellow Protein.

Q-ToF quadrupole time-of-flight.

QMF quadrupole mass filter.

RF radio frequency.

RNA ribonucleic acid.

SAC symmetry adapted cluster.

SAC-CI SAC-CI.

SCF Self-Consistent Field.

SOC scaled opposite spin.

SOS scaled opposite spin.

TD-DFT time dependent DFT.

TI twisted intermediate.

TOF Time-of-Flight.

TRPES time-resolved photoelectron spectroscopy.

TTL Transistor-Transistor Logic.

UCL University College London.

UV ultraviolet.

VAD vibrational autodetachment.

VDE vertical detachment energy.

VEE vertical excitation energy.

VMI velocity map imaging.